Imperial College London

Towards Scalable Steady LoRa Networks: Performance Prospects from Link Level to System Level

Yathreb Bouazizi

A dissertation submitted in partial fulfilment
of the requirements for the degree of

Doctor of Philosophy
of
Imperial College London.

Department of Computing
Imperial College London

July 2023

Copyright

The copyright of this thesis rests with the author. Unless otherwise indicated, its contents are licensed under a Creative Commons Attribution-Non Commercial 4.0 International Licence (CC BY-NC).

Under this licence, you may copy and redistribute the material in any medium or format. You may also create and distribute modified versions of the work. This is on the condition that: you credit the author and do not use it, or any derivative works, for a commercial purpose.

When reusing or sharing this work, ensure you make the licence terms clear to others by naming the licence and linking to the licence text. Where a work has been adapted, you should indicate that the work has been changed and describe those changes.

Please seek permission from the copyright holder for uses of this work that are not included in this licence or permitted under UK Copyright Law.

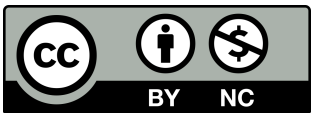

© Yathreb Bouazizi

Statement of Originality

This is to certify that the intellectual content of this thesis is the product of my own work unless explicitly stated and referenced. All the assistance received in preparing this thesis sources have been acknowledged.

London, July 2023 **Yathreb Bouazizi**

Acknowledgement

The research presented in this thesis was conducted as part of a multidisciplinary project. Being part of this project was a fabulous opportunity to collaborate with people of different backgrounds and cultures, discovering, sharing, and growing. I want to acknowledge the financial support from Singapore Ministry of National Development that made this research possible.

To begin with, I am immensely grateful to my main supervisor, Prof. Julie McCann, for the endless guidance, the confidence, the flexibility, and the freedom to explore research topics. She has been incredibly generous sharing her knowledge and expertise and supporting her students.

I am deeply grateful to my second supervisor, Dr. Fatma Benkhelifa, for the valuable technical support, mentorship, encouragement, and pastoral care she generously provided me during the difficult episodes of the PhD.

I am thankful to Prof. Hesham ElSawy for the valuable technical discussions, the critical reading and the constructive feedback at the beginning of my work.

I express my sincere appreciation to my labmates for their help in the experimental aspects of the thesis. I extend my appreciation to our partner teams at HDB and A*Star for their assistance during the time spent in Singapore.

I want to thank my friend Takoua for her advice and experience sharing. My sincere thanks go also to my friends Imen, Dima, and Hanen, with whom I shared my journey in Singapore and without whom the terrible Covid-19 lockdown would have been tougher to come through.

I am very grateful to my sister Oumeyma, my fiancé Abder and my brothers Ahmed and Oussema for their comprehension, unconditional love, unwavering support, and endless encouragement.

Dedication

To my parents Rafika and Tarek, who have always considered my education as the worthiest of all investments, with whom I share the thirst of knowledge, and I have shared the ambition to pursue my PhD studies. Their endless love, sacrifices, and belief in my abilities have always been my driving force to persevere and thrive.

To my sister Mima, who has always been there for me, caring, providing wise counsel, and telling me that no matter how cloudy the day might be, the sun will rise, and no matter how rocky the road might be, amazing things are always waiting for us... just around the corner.

To my nephew Yazan whom I have seen blossoming as the chapters of this thesis have been.

To the perseverant who I have been and will always be.

Abstract

With a plethora of applications perpetually expanding to shore up different business use cases, the IoT ecosystem is continuously growing to underpin a wide variety of "Things". In response to this growth, the Low Power Wide Area Networks (LPWAN) paradigm has emerged, encompassing an array of technologies designed to extend network coverage, support low data rates, and consume less power. Among the LPWAN, LoRa has particularly attracted the attention of research and industrial communities thanks to the opportunity it offers to stakeholders to build private IoT infrastructures while reconciling range, power, and cost. However, with an unplanned deployment model and uncoordinated communications in the license-free spectrum, LoRa could face scalability issues. Characterising the scalability of LoRa networks and revealing what impacts it and how it trades with other performance KPIs are fundamental steps in engineering well-provisioned LoRa networks.

Unlike its licensed counterparts, LoRa is a new technology with a patented physical layer that relies on several tuneable parameters. While beneficial to answer the requirements of different IoT scenarios, these parameters bring more challenges to LoRa modelling, performance estimation, and scalability characterisation. This thesis explores LoRa and provides a comprehensive picture of its link-level and system-level performance. From a link-level perspective, we deeply investigate LoRa signal theory and modulation scheme. Our study reveals and quantifies the non-orthogonality of LoRa modulation. From a network-level standpoint, we use the outcome of the link-level analysis to devise meticulous, more accurate analytical frameworks to evaluate the performance of large-scale LoRa networks. The proposed analytical frameworks uniquely join stochastic

geometry and queueing theory to reflect both device-level and network-level, account for the access restriction to the shared medium, which is a significant challenge for license-free technologies, and comprehensively evaluate the interplay between different performance indicators in LoRa-based IoT networks under both static and dynamic SF allocations.

Contents

Copyright **2**

Statement of Originality **3**

Acknowledgement **4**

Dedication **5**

Abstract **6**

List of Tables **15**

List of Figures **16**

List of Abbreviations **20**

List of Symbols **23**

1 Introduction **24**

1.1 General Context 24

1.2 LPWAN, LoRa, and the Massive Connectivity Era 25

1.3 Motivation and Research Questions 27

1.4 Objectives and Methodology 28

1.4.1 Objectives 28

1.4.2 Link-Level Analysis 29

1.4.3 System-Level Analysis 29

1.5 Stochastic Geometry for Wireless Networks Modelling and Analysis 30

1.5.1 Overview and Usefulness of Stochastic Geometry 32
1.5.2 Theory of PP: Definitions and Formalisms 33
1.5.3 PP Categories 35
1.5.4 PP Essential Theorems 35
1.6 DTMC for Device-Level Modelling 36
1.6.1 Application Areas of DTMC 36
1.6.2 Key Definitions 37
1.6.3 Main Theorems 38
1.7 Thesis Contributions 38
1.8 List of Publications 42
Published 43
Under review 43
Under preparation 43
1.9 Thesis Outline 44

2 Background and Preliminaries **45**
2.1 LPWAN: Licensed and License-free Technologies 45
2.1.1 Narrow Band-IoT 45
2.1.2 Sigfox 47
2.1.3 LoRa 48
2.2 LoRa Physical Layer 49
2.2.1 Overview of LoRa Modulation 49
2.2.2 Transmission Parameters 49
2.2.3 Frame Structure 50
2.3 LoRaWAN 51
2.3.1 Architecture 51
2.3.2 Regulatory Constraints 52
2.3.3 Device Classes 52
2.3.4 LoRa Adaptive Data Rate (ADR) 53
2.4 Recapitulation of LPWAN Technical Differences 53

2.5 An Application-Level Approach to Enable LPWAN Comparison: LoRa Vs NB-IoT . . . 55
2.5.1 Motivation and Contribution . . . 55
2.5.2 IoT Applications Profiles . . . 56
2.5.3 Profiles Characteristics and Communication Requirements . . . 57
2.5.4 Performance Assessment Metrics . . . 59
2.5.5 Experimental Setup . . . 59
2.5.6 Data Analysis and Results . . . 62
2.5.7 Discussion . . . 68
2.6 Chapter Summary . . . 69

3 LoRa/LoRaWAN Related Work and State of the Art 70
3.1 Introduction . . . 70
3.2 LoRa Physical Layer and SF-Orthogonality . . . 71
3.3 Performance Evaluation Approaches of LoRa Networks: Benefits and Challenges . . . 73
3.4 Stochastic Geometry for LoRa Networks Scalability Analysis . . . 76
3.5 DTMC for LoRa Device Modelling . . . 79
3.6 Chapter Summary . . . 80

4 LoRa Modulation: Waveforms Properties and Orthogonality Conditions 82
4.1 Motivation and Contribution . . . 82
4.2 LoRa Waveforms and Properties . . . 83
4.2.1 Technical Description of LoRa Modulation . . . 83
4.2.2 LoRa Waveform in Continuous-Time Domain . . . 85
4.2.3 LoRa Waveform in Discrete-Time Domain . . . 87
4.3 LoRa Cross-Correlation Functions . . . 88
4.3.1 Continuous-Time Domain . . . 88
4.3.2 Discrete-Time Domain . . . 91
4.4 LoRa Cross-Correlation Factors Analysis . . . 92
4.4.1 Maximum, Mean, and CDF . . . 92
4.4.2 Impact of Bandwidth . . . 95

4.4.3 Impact of Temporal Displacement . . . 96
4.4.4 Orthogonality Conditions . . . 99
4.5 LoRa BER Analysis . . . 99
4.5.1 LoRa Physical Layer Matlab Simulator . . . 99
4.5.2 Simulated BER Results . . . 100
4.6 Experimental Validation . . . 103
4.6.1 Experimental Setup . . . 103
4.6.2 PDR Analysis . . . 105
4.7 Discussion . . . 108
4.8 Chapter Summary and Key Findings . . . 109

5 Stochastic Geometry based Modelling and Analysis of Multi-Gateway LoRa Networks 111

5.1 Motivation and Contribution . . . 111
5.2 System Model . . . 113
5.2.1 Spatial Distribution . . . 113
5.2.2 Propagation Model . . . 114
5.2.3 Medium access . . . 114
5.2.4 Spreading Factor Allocation . . . 115
5.3 Spatiotemporal Analysis . . . 115
5.3.1 SF-Dependent Collision Overlap Time . . . 115
5.3.2 Transmission Success Probability . . . 117
5.3.3 Special Cases . . . 119
5.4 Numerical Results and Discussion . . . 119
5.4.1 Simulation Setup . . . 119
5.4.2 Validation of the Spatiotemporal Model . . . 120
5.4.3 Impact of Gateway Density . . . 123
5.4.4 Impact of Nodes Density . . . 123
5.4.5 Impact of Contention Window . . . 125
5.4.6 Impact of Power Allocation . . . 125
5.5 Discussion, Limitations and Future Extensions . . . 129

5.6 Chapter Summary and Key Findings 130

6 Scalability, Reliability, and Latency in Duty-Cycled LoRa Networks with Static SF Allocation 133

6.1 Motivation and Contribution 133
6.2 System Model 134
6.2.1 Spatial Distribution 134
6.2.2 Propagation model 134
6.2.3 Channel Access and Queuing Model 135
6.2.4 LoRa Duty-Cycling 135
6.2.5 LoRa β_{q_1,q_2} – SF Orthogonality 135
6.2.6 SF Allocation 136
6.3 Spatiotemporal Framework 136
6.3.1 Macroscopic Coverage Analysis with Stochastic Geometry . 137
6.3.2 Microscopic Device-Level Queuing Theory Analysis 138
6.3.3 Iterative Algorithm and KPIs 142
6.4 Numerical Results 143
6.4.1 Monte Carlo Simulation Setting 143
6.4.2 Validation of the Analytical Framework 143
6.4.3 Network Scalability-Stability Analysis 145
6.4.4 Average Delay Analysis 146
6.5 Discussion, Limitations and Future Extensions 147
6.6 Chapter Summary and Key Findings 148

7 Dynamic SF-Adaptive Duty-Cycled LoRa Networks: Scalability, Reliability, and Latency Trade-offs 149

7.1 Motivation and Contribution 149
7.2 System Model and Assumptions 150
7.2.1 Spatial Distribution and Propagation Model 150
7.2.2 Channel Access and Queuing Model 151
7.2.3 LoRa Physical Parameters and Network Operations 152
7.2.4 Methodology of Analysis 154

7.2.5 Main Assumptions . . . 155
7.3 Spatiotemporal Framework . . . 157
7.3.1 Coverage Probability . . . 157
7.3.2 Microscopic Device-Level Queuing Theory Analysis . . . 158
7.3.3 Iterative Algorithm for SG-QT Interdependence . . . 163
7.3.4 Performance Assessment Metrics . . . 163
7.4 Numerical Results . . . 166
7.4.1 Impact of SF Adaptation Cardinality N . . . 166
7.4.2 Distance-Oblivious Analysis (M=1, N=6) . . . 170
7.4.3 Distance-Aware Analysis . . . 177
7.5 Discussion, Limitations and Future Extensions . . . 182
7.6 Chapter Summary and Key Findings . . . 183

8 Conclusion and Future Work **185**
8.1 Summary of Thesis Achievements . . . 185
8.2 Ongoing and Future Works . . . 188
8.2.1 Energy Harvesting for Self-Powered Green LoRa Networks . 188
8.2.2 System-Level Optimisation: . . . 190
8.2.3 Meta Distribution in LoRa networks: . . . 191
8.2.4 3D-SG Models: . . . 191

Bibliography **192**

AppendixA Appendices for Chapter 4 **217**
A.1 Proof of Theorem. 4.1 By Dr. Fatma Benkhelifa (co-author in [P1]) . 217
A.2 Proof of Theorem. 4.2 . . . 218
A.3 Tables of LoRa Cross-Correlation Factors . . . 219

AppendixB Appendices for Chapter 5 **221**
B.1 Proof of Lemma 5.1 . . . 221
B.2 Proof of Corollary 5.1 . . . 222
B.3 Proof of Theorem 5.1 . . . 222
B.4 Proof of Theorem 5.2 . . . 223

AppendixC Appendices for Chapter 6 **224**

C.1 Proof of Theorem. 6.1 224

AppendixD Attributions **225**

List of Tables

2.1 Comparison of LPWA Technologies [51, 52, 53, 54]. 54
2.2 Applications Profiles. 57
2.3 Profiles technical requirements. 58
2.4 Deployment locations in London and their respective geographical characteristics. 61
2.5 Deployment locations in Singapore and their respective geographical characteristics. 62
2.6 Signal quality (in dBm). 63
2.7 Packet Delivery Ratio(PDR) for LoRa and NB-IoT in London. 66
2.8 Packet Delivery Ratio(PDR) for LoRa and NB-IoT in Singapore. 66
2.9 Mean Delay time(seconds) of LoR and NB-IoT in London. 67
2.10 Average energy consumed per node per profile (mWh) of LoRa and NB-IoT in London. 67

4.1 LoRa Orthogonality Conditions. 99
4.2 SF SNR thresholds. 102

5.1 Packet Time on Air [128]. 120
5.2 SF-based Power Allocation 120

6.1 LoRa *Spreading Factor* (SF) Orthogonality Coefficients β_{q_1,q_2} 136

A.1 Maximum of cross-correlations functons in continuous time domain. . 219
A.2 Maximum of cross-correlation functions in discrete time domain. . . . 219
A.3 Mean of crosscorrelation functions in continuous time domain. 220
A.4 Mean of crosscorrelation functions in discrete time domain. 220

List of Figures

1.1 Massive IoT applications. 25
1.2 Wireless technologies. 26
1.3 Methodology of the proposed analysis. 31
1.4 Advantages of the proposed methodology. 32
1.5 Manchester case study. Dense urban environment, where the 44.46% of the area is occupied by buildings [7]. 33
1.6 Point process types [20, 21]. 35

2.1 NB-IoT Deployment Options 46
2.2 LoRa frame structure. 50
2.3 LoRa Network Architecture. 51
2.4 LoRa/NB-IoT sensor node mounted in a water-proof box. 60
2.5 Deployment locations in London. 61
2.6 Examples of deployment locations in Punggol HDB estate. 62
2.7 LoRa Average delay in Singapore. 65
2.8 Recommendations for HDB. 68

4.1 Illustration of Up-Chirp LoRa Waveform. 84
4.2 Spectrogram of a LoRa symbols sequence $\{0, 50, 75, 125\}$ modulated with $SF_1 = 7$ and $B = 125$ KHz. 85
4.3 Phase variation with time for two LoRa symbols modulated using the same SF with $f_{min} = 0$. 86
4.4 Maximum of cross-correlation factors between SFs in the continuous/discrete time domains with $\tau = 0$ and $f_d = 0$. 92

4.5 Mean of cross-correlation factors between SFs in the continuous/discrete time domains with $\tau = 0$ and $f_d = 0$. 93
4.6 Empirical Cumulative distribution function (ECDF) of the magnitude of cross-correlation in the continuous time domain for $SF_1 = 7$. 94
4.7 Cross-Correlation factors for $SF_1 = 7$. 95
4.8 Maximum of cross-correlation between SFs in continuous time domain with $\tau = 0$ and $f_d = 0$ for different B_1 and B_2. 96
4.9 Maximum of cross-correlation factors between SFs in discrete time domain with $\tau = 0$ and $f_d = 0$ for different B_1 and B_2. 97
4.10 Maximum cross-correlation functions versus time delay τ/T_1. 98
4.11 LoRa Physical transmitter and receiver chains. 100
4.12 LoRa coded BER performance under AWGN for different SFs. 101
4.13 FFT amplitude spectrum of a received signal modulated with $SF_1 = 7$ under (a) only *Additive White Gaussian Noise* (AWGN) channel ($SNR = 0$ dB) and (b)-(e) different interference scenarios with *Signal to Interference Ratio* (SIR)= 0 dB. 103
4.14 LoRa BER performance under interference from different SFs with $\tau = 0$ and $f_d = 0$ for different B_1 and B_2. 104
4.15 Experimental setup using Semtech SX1280 2.4GHz transceivers. 104
4.16 Experimental analysis of packet delivery ratio (PDR) for $B_1 = B_2 = 203$ MHz, $SF_1 \in \{5, \ldots, 12\}$ and $SF_2 \in \{5, \ldots, 12\}$. 105
4.17 Experimental analysis of packet delivery ratio (PDR) for different $B_1 = B_2$. 106
4.18 Experimental analysis of packet delivery ratio (PDR) for $B_1 = 4B_2$ and $B_1 = 0.25B_2$. 107
4.19 Experimental analysis of packet delivery ratio (PDR) for $B_1 = 2B_2$ and $B_1 = 0.5B_2$. 108

5.1 HDB map: NUS urban analytics lab [158]. 112
5.2 Transmission success probability (P_{Succ}) versus different SINR thresholds (γ_{th}) for a Multi-Gateway topology. 114
5.3 Collision Overlap time between two LoRa transmissions. 117

5.4 Transmission success probability (P_{Succ}) versus different SINR thresholds (γ_{th}) for Single Gateway topology. 121
5.5 Transmission success probability (P_{Succ}) versus different SINR thresholds (γ_{th}) for a Multi-Gateway topology. 122
5.6 Transmission success probability under Intra-Cluster and Inter-Cluster Interference (P_{Succ}) of SF= 7 versus different SINR thresholds (γ_{th}) for different λ_G. 123
5.7 Transmission success probability versus SINR thresholds for different λ_{ED} in a single LoRa cell. 124
5.8 Transmission success probability versus SINR thresholds for different contention window sizes in a single LoRa cell. 126
5.9 Transmission success probability versus SINR thresholds under Per-SF interference and same power allocation in a single LoRa cell with λ_{ED} = 200 nodes/km^2. 127
5.10 Transmission success probability versus SINR thresholds under Per-SF interference and SF-based power allocation in a single *Long Range* (LoRa) cell with λ_{ED} = 200 nodes/km^2. 128

6.1 DTMC of a LoRa node transmitting with SF_q. 138
6.2 Coverage Probability. 144
6.3 Stability Frontiers. 145
6.4 End-To-End Latency. 147

7.1 LoRa Network discretised into M = 4 equiprobable regions. 152
7.2 Methodology of the proposed analysis. 156
7.3 Two-dimensional DTMC of a LoRa node under Adaptive SF for N = 3. 159
7.4 Impact of adaptation cardinality N on stability frontiers (λ_L, a). 167
7.5 Impact of adaptation cardinality N on coverage probability, a = 0.01 packets/slot, d = 0.3, b = 0.8. 168
7.6 Impact of adaptation cardinality N on average delay, λ_L = 500 nodes/Km^2, b = 0.8 ,d = 0.3. 169
7.7 Impact of SFs orthogonality assumption on stability frontiers (λ_L, a). . . 170

7.8 Impact of SFs orthogonality assumption N on stability frontiers, (λ_L, a)-plane. 172
7.9 Impact of nodes density on SF activity distribution, $a = 0.015$ (packets/slot). 174
7.10 Impact of nodes density on the Per-SF Coverage probability$a = 0.015$ (packets/slot) 174
7.11 Impact of packet arrival rate on SF activity distribution, $\lambda_L = 10^3$ nodes/km^2. 175
7.12 Impact of traffic arrival rate on Per-SF Coverage probability $\lambda_L = 10^3$ nodes/km^2. 175
7.13 Global (SF-Averaged) coverage probability for $\lambda_L = 10^3$ nodes/km^2 and $a = 0.02$ packet/slot. 176
7.14 Average delay for $\lambda_L = 10^3$ nodes/km^2 and $a = 0.02$ packet/slot. 176
7.15 Per-SF Activity distribution and coverage in different regions for $a = 0.01$ packet/slot, $\lambda_L = 10^3$ nodes/km^2, b) $a = 0.01$ packet/slot). 178
7.16 Global (SF-Averaged) coverage probability in different regions for $a = 0.01$ packet/slot, $\lambda_L = 10^3$ nodes/km^2. 178
7.17 Average delay in different regions for $\lambda_L = 10^3$ nodes/km^2 $a = 0.01$ packet/slot. 179
7.18 ζ-Stability region, $M = 6$, $a = 0.01$ packet/slot, $\lambda_L = 10^3$ nodes/km^2. . . 180
7.19 Coverage ζ-Operativity region for $P^* = 80\%$, $M = 6$, $a = 0.01$ packet/slot, $\lambda_L = 10^3$ nodes/km^2. 181
7.20 Delay ζ-Operativity region for $W^* = 10$ slots, $M = 6$, $a = 0.01$ packet/slot, $\lambda_L = 10^3$ nodes/km^2. 181

List of Abbreviations

IoT Internet of things

M2M Machine to Machine

LPWA Low power wide area

LPWAN Low Power Wide Area Networks

LoRa Long Range

LoRaWAN Long Range Wide Area Network

LR-WPAN Low Rate Wireless Personal Area Network technology

MAC Medium Access Control

ISM Industrial Scientific and Medical

CSS Chirp Spread Spectrum

SF Spreading Factor

BW Band Width

FEC Forward Error Correction

CR Coding Rate

DC Duty Cycle

LBT Listen Before Talk

ToA Time-on-Air

UP Uplink

DL Downlink

ACK Acknowledgment

QoS Quality of service

KPI Key Performance Indicator

PDF Probability Density Function

CDF Cumulative Distribution Function

SG Stochastic Geometry

PP Point Process

PPP Poisson Point Process

MCP Matérn Cluster Process

PGFL Probability Generating Functional

QT Queuing Theory

DTMC Discrete Time Markov Chain

QBD Quasi Birth and Death

MAM Matrix Analytic Method

TPM Transition Probability Matrix

i.i.d. independent and identically distributed

FIFO First In First Out

ED End-Device

EIB Equal-Interval-Based

EAB Equal-Area-Based

SNR Signal to Noise Ratio

SIR Signal to Interference Ratio

SINR Signal to Interference and Noise Ratio

RSSI Received Signal Strength Indicator

PDR Packet Delivery Ratio

BER Bit Error Rate

AWGN Additive White Gaussian Noise

DFT Discrete Fourier Transform

FSCM Frequency Shifting Chirp Modulation

FSK Frequency Shift Keying

BPSK binary phase shift keying

SE Spectral Efficiency

EE Energy Efficiency

TDMA Time Division Multiple Access

CSMA Carrier Sense Multiple Access

FTDMA Frequency Time Division Multiple Access

NB-IoT Narrow Band-IoT

3GPP 3rd Generation Partnership Project

5G Fifth Generation

B5G Beyond Fifth Generation

6G Sixfth Generation

GSM Global System for Mobile Communication

UAV Unmanned Aerial Vehicular

LTE Long Term Evolution

LTE-M Long-Term Evolution Machine Type

PRBs Physical Resource Blocks

NPUSCHs Narrowband Physical Uplink Shared CHannels

NPRACHs Narrowband Physical Random Access Channels

NPDCCH Narrowband Physical Downlink Control Channel

MC Monte Carlo

List of Symbols

Symbol/Function	Description
$\mathbb{P}$	Probability operator
$\mathbb{E}_{\mathcal{X}}$	Expectation measure
$\mathcal{L}_{\mathcal{X}}(s) = \mathbb{E}_{\mathcal{X}}\{e^{-sX}\}$	Laplace Transform of a random variable $\mathcal{X}$
$\overline{(.)}$	Complement operator
$[.]^T$	Transpose operator
$\mathbb{1}_S$	Indicator function
$\boldsymbol{e}$	All ones column vector of appropriate length
$\mathbf{0}$	All zeros matrix of appropriate size
c	Speed of light
f_c	Carrier frequency
α	Frequency dependant factor = $c/(4\pi f_c)^2$
η	Path loss exponent
${}_2F_1(\cdot)$	Gaussian hypergeometric function
NF	Noise floor

CHAPTER 1

Introduction

1.1 General Context

The research conducted in this thesis was part of a collaborative multidisciplinary project supported by Singapore Ministry of National Development (MND) under the challenge of the Land and Livability Innovation Research Program. The project brings together academia through Imperial College London, research institutes through the Agency of Science, Technology and Research of Singapore (A*STAR)[1], and government through the Housing and Development Board (HDB) of Singapore[2]. The scope of the project was smart sensing and predictive modeling for urban habitat optimization. It spans a variety of applications, such as lift monitoring, water harvesting systems, rainfall prediction, waste management systems, pipeline monitoring, smart grids, and aims to assist HDB in optimizing their smart urban infrastructures. The thesis focus was on the communication side of the project, particularly on potential connectivity solutions to carry HDB applications.

[1] https://www.a-star.edu.sg

[2] The Housing and Development Board (HDB) is Singapore's public housing authority. It plans and develops Singapore's housing estates https://www.hdb.gov.sg/cs/infoweb/homepage.

1.2 LPWAN, LoRa, and the Massive Connectivity Era

Internet of things (IoT) forms a ubiquitous ecosystem where communication, information, and operational technologies meet. This ecosystem comprises a myriad of physical devices, sensors, actuators, and daily life objects that are spatially dispersed and interacting using various wireless connectivity solutions. In recent years, rapid growth in has been witnessed the IoT market as the number of interconnected devices that exchange data is expected to exceed 75 billion by 2025 [1]. This growth is mainly attributed to the emergence of a plethora of IoT and sensor-based industries such as smart homes, smart factories, smart agriculture, logistics and tracking, and smart cities as illustrated in Fig. 1.1.

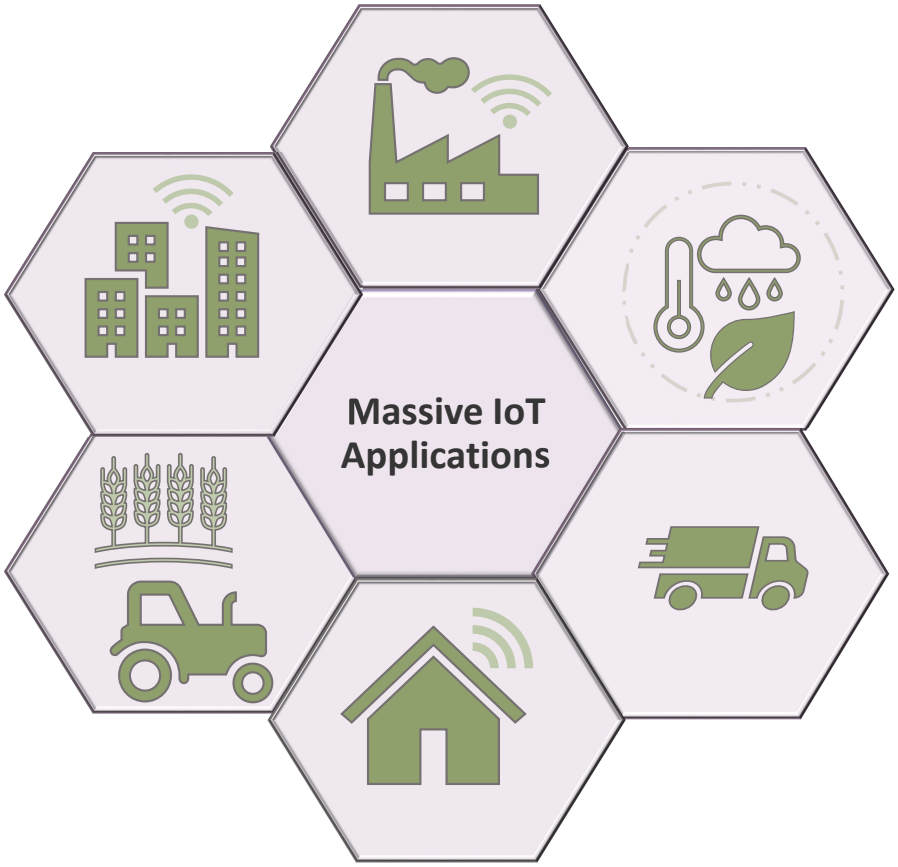

Fig. 1.1: Massive IoT applications.

To address the massive-connectivity challenges arising from the IoT growth, a new IoT paradigm, namely the *Low Power Wide Area Networks* (LPWAN) has

appeared and been continuously evolving. The LPWAN paradigm embraces a number of technologies that share common goals centered on achieving extended network coverage, reducing devices' cost and complexity, and minimizing energy consumption. These technologies are, therefore, designed to enable the transmission of small bursts of data from 1000s of devices located over long distances from the gateway. The devices can be deployed in harsh environments requiring them to be battery-powered with an expected battery longevity of several years. In the context of smart city projects, LPWAN could shore up a large array of applications, including environment monitoring, infrastructure monitoring, transportation, and metering. To optimally perform their tasks, these applications need to be carried by appropriate wireless connectivity solutions that fit their communication needs and meet their *Quality of service* (QoS) requirements. Optimizing the tasks of these applications helps efficiently manage city resources, achieves more sustainability, and provides citizens with greater convenience and better life quality.

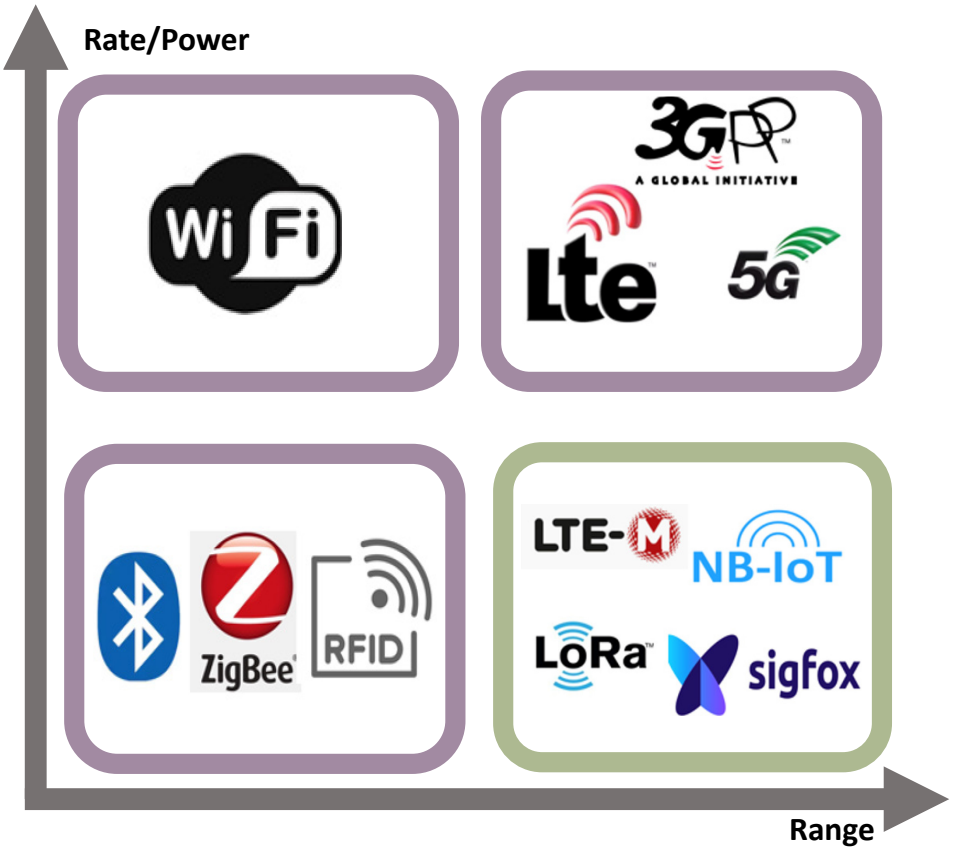

Fig. 1.2: Wireless technologies.

Among the LPWA technologies currently in the market, *Long Range* (LoRa) is a promising solution that has particularly attracted the attention of both academic communities and industrial stakeholders as it supports ad hoc sensor deployments while reconciling low-power, low-cost, and long-range requirements. In light of the prospective leading role of LoRa in the IoT market and the opportunity it offers to stakeholders, like HDB, to build and control their private sensing infrastructures, the focus of this thesis is primarily on LoRa-based IoT networks.

1.3 Motivation and Research Questions

Unlike its licensed competitors (*Long-Term Evolution Machine Type* (LTE-M), *Narrow Band-IoT* (NB-IoT), ...) which inherit the mature protocol stack and well-established infrastructure of conventional cellular networks, LoRa is a new technology. It was developed by a French startup company, Cycleo, and acquired by Semtech in 2012. In 2015, *LoRa Alliance* [2] was founded, an association that maintains the collaborative development of LoRa/*Long Range Wide Area Network* (LoRaWAN). With the foundation of this association LoRa has been perpetually gaining more popularity. This popularity has come along with questions about whether LoRa can live up to the claimed performance. Concerns about LoRa scalability have, then, started to rise, and research efforts have been devoted to address the challenges related to these concerns. To deploy scalable LoRa networks that meet QoS requirements of the smart sensing applications they carry, it is substantial to first model the LoRa network, predict, and analyse its performance in terms of various *Key Performance Indicator* (KPI)s such as reliability, scalability, stability, latency, and energy consumption. A meticulous LoRa network model should account for different degrees of uncertainty coming from the unreliable wireless medium and reflect, at the same time, the technology peculiarities.

LoRa's peculiarities stem essentially from its patented physical layer that adapts its configurations to applications requirements by relying on several tuneable parameters like *Spreading Factor* (SF), *Coding Rate* (CR), transmit power, and *Band Width* (BW) [3]. While these parameters endow LoRa with the flexibility to cope

with different smart sensing use-cases and IoT scenarios, they bring more challenges into its modelling and performance analysis. Understanding how tuning these adaptive parameters impact various performance interplays is essential to harness maximum performance gains in LoRa networks and pave the way for a wide industrial adoption of LoRa. All the characteristics we described above emphasise the need to explore LoRa and further motivate a more in-depth investigation of this technology.

Our research focus on LoRa has been driven by three main questions all of which we try to provide answers to throughout this dissertation:

The first question wishes to understand for which IoT applications could LoRa successfully cater. While basic, this question is of tremendous importance for IoT developers, users, and stakeholders like HDB[3].

The second question is, where LoRa is selected for a specific IoT application and adopted for a large deployment, how would LoRa scale? Can we characterise and foresee this scalability? What system parameters affect the scalability? And how does it trade-off with other performance KPIs such as reliability, stability, latency, and even sustainability? Tying them back to the origin, these sub-questions have immanently led us to a fundamental, yet impactful third question:

Exactly how orthogonal is LoRa modulation?

1.4 Objectives and Methodology

1.4.1 Objectives

With the above research questions in mind, we set the research objectives of this thesis to comprehensively cover LoRa performance from link level to system level: The first objective tackles the link level by delving into LoRa physical layer and signal theory, to discern its behaviours, reveal its properties, and quantify the

[3]The Housing and Development Board (HDB) is Singapore's public housing authority. It plans and develops Singapore's housing estates https://www.hdb.gov.sg/cs/infoweb/homepage.

orthogonality between its resources (SFs). The second objective concerns the system-level performance; modelling the network, characterising the scalability, and analysing the performance trade-offs under different SF allocations whether static or adaptive.

1.4.2 Link-Level Analysis

The first step in our methodology relies on a comprehensive analysis of LoRa signal theory. It aims to propose a quantification of how LoRa resources (SF) statistically impact each other in the case of packet transmission overlap (i.e. how orthogonal are they?). The interaction between SFs governs the interference between them, impacting as a result, their performance. Therefore, characterising and quantifying the orthogonality of LoRa SFs is a crucial step towards a more accurate performance prediction and optimisation of LoRa networks.

Our approach to quantifying LoRa orthogonality starts by first formulating LoRa waveform expressions in both continuous and discrete time domains. Using the developed waveforms expressions, we derive cross-correlation functions between the same and different SFs accounting for different system parameters (i.e. sampling rate, BW, initial frequency) and various signal displacement cases (i.e., time delay, frequency shift). To further support the orthogonality quantification approach and assess its impact on LoRa link-level performance, first, we developed a MATLAB-based simulator for LoRa physical layer. The developed simulator is used to calculate simulated bit error statistics. Second, we deployed a small-scale experiment to study *Packet Delivery Ratio* (PDR) performance.

1.4.3 System-Level Analysis

Moving from the link level to the system level, our goal is to provide analytical tools that accurately represent LoRa technology and can be exploited to comprehensively assess the performance of LoRa networks under different resource (SF) allocation strategies (static and adaptive). System-level performance evaluation approaches

are fundamental to gain insights into the performance tradeoffs of IoT networks. Evaluating the tradeoffs between different performance metrics requires capturing both network-level and device-level spatial and temporal dynamics. For this reason, our methodology relies on the joint use of two mathematical tools: *Stochastic Geometry* (SG) and *Queuing Theory* (QT). While QT is used to model the device behaviour and the different protocol phases, SG models the macroscopic scale of the network and captures the interactions between the spatially dispersed devices. The interaction between the devices comes from their susceptibility to interference due to the random access to the shared wireless medium. To have a more realistic and practical modelling of the interference in LoRa networks, we use the orthogonality quantification outcome of our study about LoRa physical layer characterisation and link-level analysis.

The proposed methodology has the advantage of bridging the gap between coverage-oriented analysis and standalone queuing approaches, adopts realistic interference modelling, and accounts for LoRa regulatory constraints regarding access to the shared wireless medium. Thereby, performance metrics are derived to study the network scalability, stability reliability, and latency. A summary of the adopted methodology is sketched in Fig. 1.3. The usefulness of this methodology is illustrated in Fig. 1.4. The following sections give an overview of the tools that we use to implement the proposed methodology.

1.5 Stochastic Geometry for Wireless Networks Modelling and Analysis

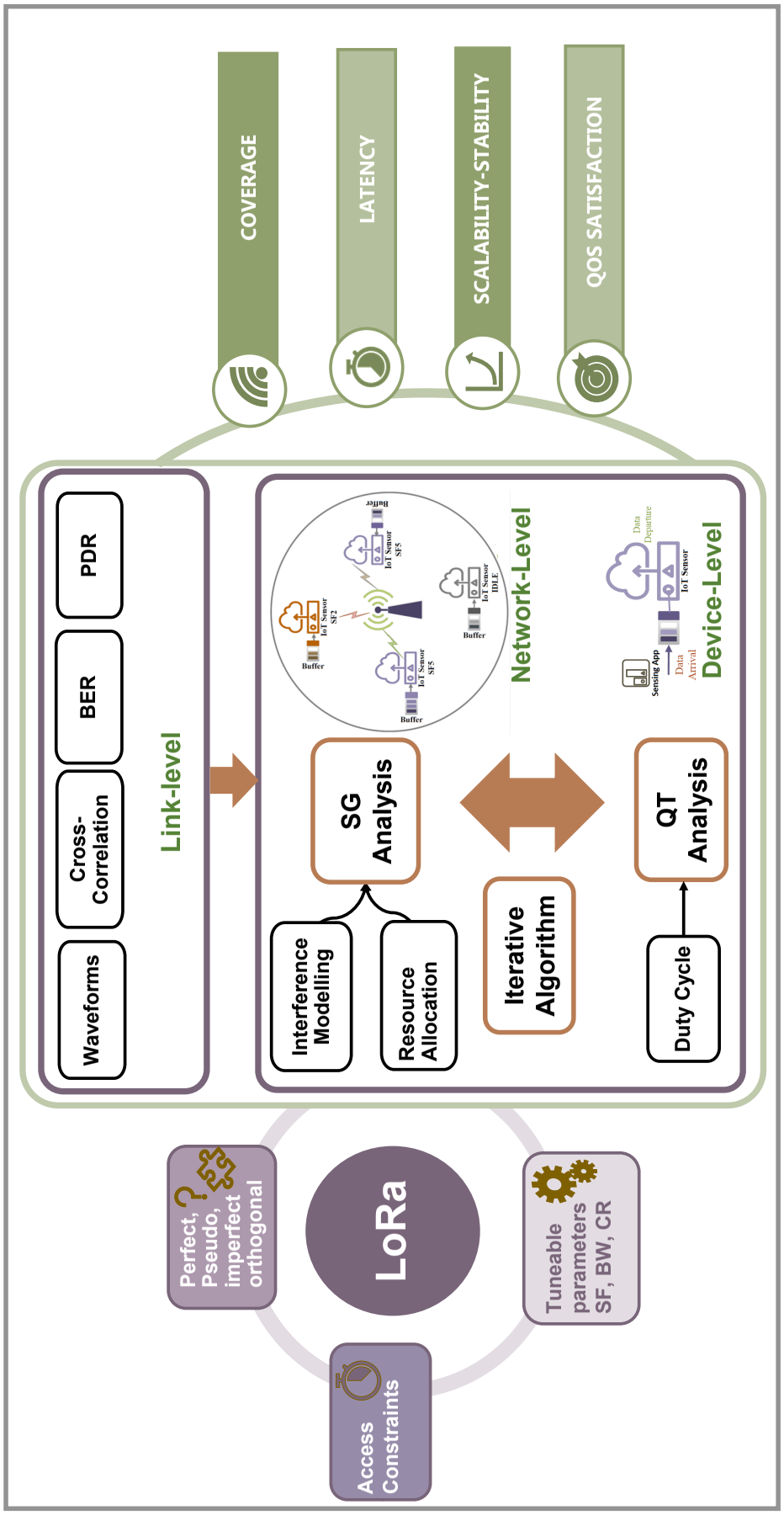

Fig. 1.3: Methodology of the proposed analysis.

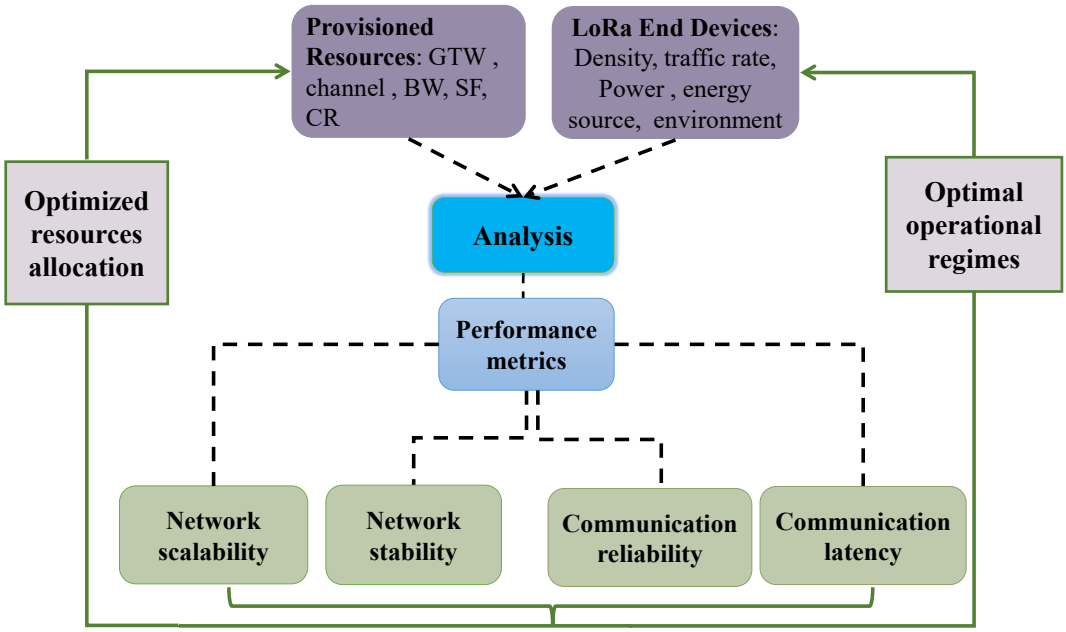

Fig. 1.4: Advantages of the proposed methodology.

1.5.1 Overview and Usefulness of Stochastic Geometry

SG is a field of applied probability that studies random spatial patterns in a $\mathbb{R}^n$ plane [4]. SG has been used to provide tractable statistical models that help analyse and understand, in a probabilistic way, systems behaviours in different fields. In the field of wireless communications, SG has received a growing interest as a powerful tool that captures various degrees of uncertainty naturally existing within the wireless network such as the nodes spatial distributions, the distance to the serving gateway, the uncertainty of radio communication channels [5], and lays solid foundations for system-level performance analysis and optimisation [6].

From a SG perspective, the gateway and the nodes in a wireless network are interpreted as interacting randomly spread points in the space namely point processes (PPs). The ability of *Point Process* (PP)-based abstraction to accurately model cellular networks has been empirically validated in [7]. Authors in [7] used a large data sets obtained from OFCOM[4] for the deployments of two operators

[4]OFCOM is the independent regulator and competition authority for the United Kingdom (UK) communications industries.

(O_2 and Vodafone) in two cities (Manchester and London). With the aid of these empirical data sets, the authors in [7] concluded that PP-based model is sufficiently accurate for modeling dense urban environments. In light of its usefulness,

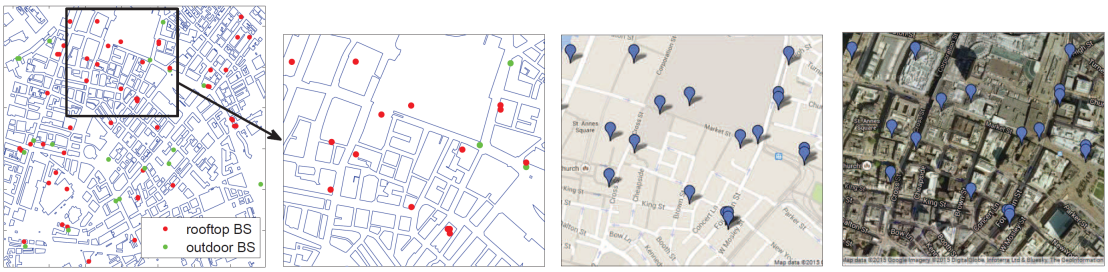

Fig. 1.5: Manchester case study. Dense urban environment, where the 44.46% of the area is occupied by buildings [7].

accuracy, and tractability, SG has been widely recalled to analyse both terrestrial and non-terrestrial wireless communications systems including cognitive ad-hoc networks [8], IoT-enabled cellular networks [9, 10], uncoordinated massive IoT networks [11], wireless-powered IoT networks [12], satellite communications [13], and *Unmanned Aerial Vehicular* (UAV) post-disaster cellular networks [14]. SG has been also shown to play an important role in characterising and analyzing novel paradigms and new enabling concepts emerging as part of the evolution to *Fifth Generation* (5G), *Beyond Fifth Generation* (B5G) and *Sixfth Generation* (6G) networks [15]. Such concepts include millimeter and terahertz communications [16, 17], joint communication and sensing [18], and reflective intelligent surfaces [19].

1.5.2 Theory of PP: Definitions and Formalisms

The core of stochastic geometry as a mathematical tool is the point process.

Definition 1.1. ***Point Process:*** *A PP is a countable random collection of points occupying a measure space that is commonly the Euclidean space* $\mathbb{R}^d$.

A PP has a two-fold interpretation [20]:

Random set: A PP can be perceived as a countable random set $\Phi = \{x_1, x_2, ...x_n\} \subset \mathbb{R}^d$ where each element x_i is considered as a random variable.

Random measure: A PP can be interpreted as a random counting measure N that enumerates the number of random points that fall in a specific set $S \subset \mathbb{R}^d$, where $N(S)$ is a random variable with positive integer values.

Definition 1.2. ***Marked Point Process:*** *The concept of marking consists on assigning marks to the points of an initial point process. These marks provide additional information about the points. In the context of wireless networks they can be transmission parameters like time, power, network tier, etc.*

The most eminent and commonly used PP in SG frameworks is the *Poisson Point Process* (PPP). Its popularity comes from its zero-interaction characteristic that yields an analytical flexibility, therefore a tractability in the results.

Definition 1.3. ***Poisson Point Process (PPP):*** *A PP $\Phi = \{x_1, x_2, ...x_N\}$ is a PPP if and only if the number of points inside any compact set $S \subset \mathbb{R}^d$ is a Poisson random variable, and the numbers of points in disjoint sets are independent [5].*

Definition 1.4. ***Homogeneous PPP:*** *A homogenous PPP $\Phi = \{x_1, x_2, ...x_N\} \subset \mathbb{R}^d$ with intensity λ has the following properties:*

- *λ is uniform i.e. does not depend on the location.*
- *Φ is stationary i.e. invariant with translation.*
- *The probability that a number of points n exists in a bounded region $B \subset \mathbb{R}^d$ in given by: $P(N(B) = n) = \frac{\lambda|B|}{n!}$ where $|B|$ is the volume in $\mathbb{R}^d$ and N is the random counting measure.*
- $\mathbb{E}(N(B)) = \lambda|B|$

Homogeneous PPP are widely adopted in SG-based analysis thanks to the known forms of their *Probability Generating Functional* (PGFL).

Definition 1.5. ***Independent thinning:*** *An independently thinned PPP is formed by randomly and independently selecting points from a primary PPP.*

1.5.3 PP Categories

Based on their degree of repulsion, point processes are classified into three main categories:

- **Repulsive:** The points in this category are over dispersed compared to the neutral one. The most famous process among this category is the Matern Hard Core Type 1 which can be constructed from a basic homogeneous PPP by carrying a thinning [20]. This thinning consists on removing nodes which have neighbors within the hard core distance(Fig. 1.6a).
- **Neutral:** This family comprises essentially homogeneous PPP where a full spatial randomness is assumed and the points have no interaction between each other (Fig. 1.6.b)
- **Clustered:** These processes are less dispersed and can be obtained by independent replication and displacement of an initial process points(Fig. 1.6. c).

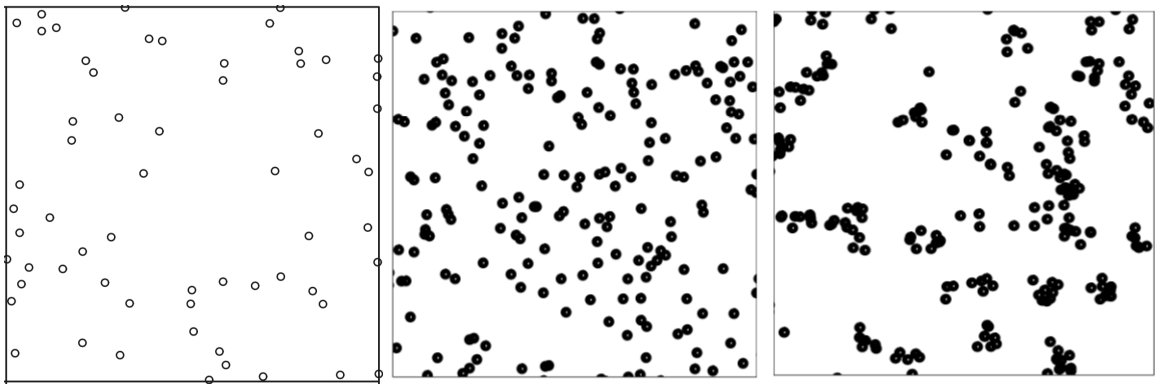

(a) Matern Hard core (b) Homogeneous PPP (c) Cluster PP

Fig. 1.6: Point process types [20, 21].

1.5.4 PP Essential Theorems

The tractability of SG as a mathematical tool is mainly attributed to the following theorems:

Theorem 1.1. ***Campbell's theorem*** *[22] Let* $\Phi = \{x_1, x_2, ...x_N\} \subset \mathbb{R}^d$ *be a PP ,* $f : \mathbb{R}^d \to \mathbb{R}$ *be a measurable function and* Λ *an intensity measure on* $\mathbb{R}^d$*, then:*

$$\mathbb{E}_\Phi\Big[\sum_{xi\in\mathbf{\Phi}} f(xi)\Big] = \int_{R^d} (f(x)\Lambda(dx))$$

Campbell's theorem transforms an expectation over a random summation to an integral involving the PP intensity function. The integration boundaries represent the boundaries of the region where the PP exists [22].

Theorem 1.2. ***Probability Generating Functional (PGFL)*** *[22] Let* $\Phi = \{x_1, x_2, ...x_N\} \subset \mathbb{R}^d$ *be a PPP ,* $f : \mathbb{R}^d \to \mathbb{R}$ *be a measurable function and* Λ *an intensity measure on* $\mathbb{R}^d$*, then:*

$$\mathbb{E}_\Phi\Big[\prod_{xi\in\mathbf{\Phi}} f(xi)\Big] = \exp\Big\{\Big\{-\int_{R^d}(1 - f(x)\Lambda(dx))\Big\}\Big\}$$

PGFL transforms an expectation over a product to an integral over the PP domain involving the PP intensity function. Note that, unlike Campbell's theorem, which is general, a PGFL does not necessarily exist [22].

1.6 DTMC for Device-Level Modelling

1.6.1 Application Areas of DTMC

Markov processes play an important role in many areas including but not limited to computer science [23], manufacturing engineering [24], neuroscience[25], psychology [26] and notably telecommunications [27]. They have been particularly used in cellular, wireless sensor and IoT networks to devise performance evaluation methods, power allocation, congestion-control, and scheduling schemes [10, 28, 29, 30]. In the next subsection we define Markov processes and outline key concepts and main theorems that will be useful for the queuing theory part of the methodology proposed in Subsection. 1.4.3.

1.6.2 Key Definitions

Definition 1.6. ***Markov chain:*** *A Markov chain is a stochastic process* $\boldsymbol{X} = \{X1, X2, X3, ...\}$ *with state space* $\mathcal{S} = \{i_0, i_1, ...i_n\}$ *such that:*

$$\mathbb{P}\{X_n = i_n | X_0 = i_0, ..., X_{n-1} = i_{n-1}\} = \mathbb{P}\{X_n = i_n | X_{n-1} = i_{n-1}\} \tag{1.1}$$

This means that the probability to transit from one state to the other depends only on the current state i.e. future states are fully captured by the present state and are not impacted by the previous states. We say that Markov chains are "memoryless" discrete time processes.

Definition 1.7. *We say that a state* j *is accessible or reachable from state* i *if and only if there exists some integer* $n \geq 0$ *such that* $P^n_{i,j} = \mathbb{P}\{X_n = j | X_0 = i\} \geq 0$. *If* j *is accessible from* i *and vice versa, states* i *and* j *are said to communicate.*

Definition 1.8. *A state is said to be absorbing if once the process enters it does not leave it [27].*

Definition 1.9. *A state is said to be transient if once the process enters it might not return to it [27].*

Definition 1.10. *A state is said to be recurrent if once the system enters it will definitely return to it again [27].*

Definition 1.11. *A Markov chain is called irreducible if all the states communicate. This means that regardless of the current state we can reach any other state in finite time [27].*

Definition 1.12. ***Steady State Distribution:*** *The steady state distribution also called stationary, static, invariant or equilibrium is the conditions where regardless of the current state, the next state will be the same.*

Definition 1.13. ***Transition Probability:*** *A transition probability is the rate at which the chain transitions from one state to the other in discrete time.*

Definition 1.14. ***Transition Probability Matrix (TPM):*** *Each Markov process is characterised by a square matrix that represents the transition probabilities between its different states. This matrix is called the Transition Probability Matrix* (TPM). *A TPM can be presented by a transition diagram.*

Definition 1.15. ***QBD:*** *Quasi Birth and Death* (QBD) *are matrix generalisation of birth-and-death processes which are skip-free Markov processes where the chain can move up or down by only one level .i.e. to only an adjacent state [31]. QBD is the most commonly used process to model discrete time queues.*

1.6.3 Main Theorems

Theorem 1.3. ***Loynes theorem:*** *According to Loynes theorem, a network is considered stable if the average service rate of a randomly selected device is higher that its average arrival rate [32, 33].*

Theorem 1.4. ***Little's law:*** *Little's law is an important theorem in queuing theory. It states that the average number in the system is equal to the arrival rate multiplied by the mean waiting time in the system [33, p. 5.4.5].*

1.7 Thesis Contributions

In line with the defined research questions and the established objectives, the contributions of this thesis are summarized herein: **Section. 2.5:** In this section of Chapter. 2, we present, as preliminary, our approach to compare LoRa and NB-IoT in real deployment conditions and against realistic application profiles based on a taxonomy of IoT applications that we have developed. This study was mainly motivated by a user-oriented thinking about the best technology for a specific application. We can describe this study as the catalyst that has further motivated our focus on LoRa. The outcome of this preliminary study will be submitted to IEEE IoT magazine [O1] and its main contributions are:

- A taxonomy of IoT applications and requirements is derived based on a literature review about IoT traffic characterisation and a consultation of IoT practitioners. Though not exhaustive, the proposed taxonomy confines the broadness of IoT into an applications suite that is agnostic to hardwares and

protocols. Therefore, this taxonomy can serve IoT experimental evaluations and benchmarking approaches.

- The developed taxonomy is used to evaluate the performance of LoRa and NB-IoT against realistic application profiles through two experimental setups that try to ensure fairness at different levels: hardware, deployment conditions, applications, and metrics.
- The collected data from the experimental setups is used to calculate and compare the application-level metrics, PDR, delay and energy consumption of LoRa and NB-IoT giving insights about their appropriateness for the application profiles.
- In light of this study some recommendations have been advised to HDB regarding which technology works for which application in the context of sensing and monitoring applications at HDB estates.

Chapter. 4: In this chapter, we deeply examine LoRa physical layer and provide a comprehensive refined analysis of its signal theory. The outcome of this chapter was published in IEEE Internet of Things Journal (IEEE IoT) [P1] and its main contributions are summarised below:

- We present general expressions of LoRa waveforms in continuous and discrete time domains and outline a number of their proprieties. The presented expressions account for diverse configuration parameters (BW, SF, etc.) and different signal displacements (time delay shift, frequency shift, etc.) which makes them general and can scale down to special cases existing in the literature. Using the waveforms expressions, we derive, likewise general, analytical expressions of LoRa cross-correlation functions between same and different SFs.
- We analyse the orthogonality between LoRa SFs by studying the cross-correlation functions and quantify their mean, maximum, and *Cumulative Distribution Function* (CDF) in both the discrete and continuous time domains. The impact of the temporal displacement and the bandwidth on the quantified mean and maximum cross-correlation is investigated.

- This chapter reveals how LoRa modulation is not perfectly orthogonal and how its orthogonality is highly affected by physical features like the SF, the BW, and the time delay.
- For same BWs, the largest maximum cross-correlation occurs for the same SF and is equal to 100% due to same symbols. The maximum cross-correlation between different SFs is less than 26%, and 20% before and after sampling, respectively and is shown to decrease as the difference between SFs increases. Whereas, for different BWs, we observe that the largest maximum cross-correlation is no longer observed for the same SF but rather depends on the ratios of the BWs.
- We performed simulated bit error rate and experimental PDR evaluations that have interestingly shown performance trends aligned with the maximum cross-correlation functions analyses.

Chapter. 5: In this chapter we propose to model and analyse *Uplink* (UP) communications in single-gateway and multi-gateway LoRa networks using tools from SG. A *Matérn Cluster Process* (MCP) is leveraged to reflect LoRa deployment model. A random start time distribution is used to reflect LoRa uncoordinated transmissions and to calculate the overlap time in events of packets collision. The outcome of this chapter was presented in IEEE Global Communication Conference-2020 (IEEE GLOBECOM) [P2] and its main contributions are:

- We derive tractable expressions for the UP transmission success probability in single-gateway and multi-gateway LoRa networks. The derived expressions are used to study the performance of the network under both assumptions of orthogonality (perfect and imperfect) and to investigate the impact of different system parameters such as power, nodes density, and gateway density on the performance of different SFs.
- The results show that the transmission success probability decreases as the SF increases and that the orthogonality assumption impacts the predicted coverage performance of different SFs and influences the impact of system parameters such as the density and the start time distribution.

- The results reveal that interfering SF degrading the performance the most depends on the decoding threshold range and the power allocation scheme. Assigning the power incrementally with the SF mitigates the near-far problem stemming from the distance-based SF allocation improving, therefore, the performance of higher SFs. However, this power allocation coupled with the long *Time-on-Air* (ToA) make higher SFs the most detrimental to coverage performance. When SFs are allocated the same power, the most detrimental SF on the coverage performance varies with the *Signal to Interference and Noise Ratio* (SINR) regime. For low SINR thresholds, lower SFs are the culprit behind performance deterioration, while it is the inverse for high SINR regime.
- The analysis has confirmed that the impact of interference (Co-SF and Inter-SF) on the performance of each of the SFs is profoundly governed by the SF allocation scheme, the density regime, and the transmission time distribution among the nodes.

Chapter. 6: In this chapter we study the scalability, reliability and latency of LoRa networks with statically allocated SFs. The results of this chapter were published in IEEE Wireless Communication Letters (IEEE WCL) [P3] and its main contributions are:

- Using SG, we derive the coverage probability of different SFs while adopting a more realistic and practically useful interference scenario using the orthogonality quantification outcome of Chapter. 6.
- Using QT, we have been able to model LoRa-device behaviours accounting for the traffic dynamics and the regulatory constraints regarding access to the shared medium.
- We derive metrics to characterise the coverage and the latency performance.
- By combining SG and QT we study the trade-off between stability and scalability through the joint limits of device density and traffic intensity per device.

Chapter. 7: In this chapter, we propose to investigate dynamic LoRa networks by extending the study in Chapter. 6 from static SF to adaptive SF. The proposed analysis has been submitted to IEEE Transaction on Communications (IEEE TCOM) [R1] and its main contributions are:

- We propose a probabilistic spreading factor adaptation scheme whose performance is studied using stochastic geometry and queuing theory. Using the devised analytical framework, we derive performance metrics that quantify the scalability, reliability and latency of LoRa network while accounting for the location dependent queues states.
- We thoroughly study the impact of different system design parameters including the density, the traffic arrival rate, the adaptation cardinality, the SF-Up and SF-Down rates on the SFs distribution, the stability-scalability frontiers, the coverage, and the delay.
- The evolution of SFs distribution and coverage with density and traffic arrival rate have demonstrated regimes where each of the SFs dominates and where the SF adaptation improves the network performance.
- We identify operating regimes that achieve a stable and adequately provisioned network according to the QoS requirements of the IoT applications.
- Our results highlight the importance of properly quantifying the imperfect orthogonality of LoRa SFs in deriving more accurate performance metrics, therefore determining preciser performance boundaries of LoRa networks.
- Our results reveal the existence of adaptation parameters (cardinality, SF-Up probability b, SF-Down probability d,...) that minimize the average packet delay or maximize the coverage probability.

1.8 List of Publications

This section lists the publication produced throughout this thesis:

Published

[P1] Fatma Benkhelifa, **Yathreb Bouazizi**, and Julie A. McCann. "How Orthogonal is LoRa Modulation?" In: *IEEE Internet of Things Journal* 9.20 (2022), pp. 19928–19944. DOI: 10.1109/JIOT.2022.3173060.

[P2] **Yathreb**. **Bouazizi**, Fatma Benkhelifa, and J. McCann. "Spatiotemporal Modelling of Multi-Gateway LoRa Networks with Imperfect SF Orthogonality". In: *GLOBECOM 2020 - 2020 IEEE Global Communications Conference*. 2020, pp. 1–7. DOI: 10.1109/GLOBECOM42002.2020.9322640.

[P3] **Yathreb Bouazizi**, Fatma Benkhelifa, Hesham ElSawy, and Julie A. McCann. "On the Scalability of Duty-Cycled LoRa Networks with Imperfect SF Orthogonality". In: *IEEE Wireless Communications Letters* (2022), pp. 1–1. DOI: 10.1109/LWC.2022.3200912.

Under review

[R1] **Yathreb Bouazizi**, Fatma Benkhelifa, Hesham ElSawy, and Julie A. McCann. "SF-Adaptive Duty-Cycled LoRa Networks: Scalability, Reliability, and Latency Tradeoffs". In: *IEEE Transactions on Communications* (Under review).

Under preparation

[O1] **Yathreb Bouazizi**, Boon Wong, Breza Micheal, and Julie A. McCann. "Taxonomy and Communication Requirements of IoT Applications: LoRa Versus NB-IoT Case Study". In: *IoT magazine* (To submit).

[O2] **Yathreb Bouazizi**, Fatma Benkhelifa, and Julie A. McCann. "Harvesting Energy for Self-Powered Green LoRa Networks". In: *IEEE GLOBECOM Conference 2024* (To submit).

1.9 Thesis Outline

The remainder of this dissertation is structured as follows: In Chapter. 2, the first part presents the background to LPWAN and LoRa while the second part is dedicated to the application-based approach we propose to enable the comparison of LPWAN. Preliminary experimental results of this approach applied to compare LoRa and NB-IoT are presented and discussed. Each chapter in this thesis starts with a motivation section and is concluded with a summary. In Chapter. 3, we discuss the related works relevant to the different chapters of the thesis. In Chapter. 4, we present our approach to study LoRa link-level performance and quantify its orthogonality. Chapter. 5, Chapter. 6, and Chapter. 7 propose system-level performance evaluation frameworks based on SG or SG and QT. Chapter. 5, Chapter. 6, and Chapter. 7 are structured as follows: First, we describe the system model with its conceptual choices and assumptions. Second, we detail the analytical framework and the derived performance assessment metrics. Then we present and analyse selected numerical results. A discussion section is included at the end of each chapter to point out the limitations and how they can be addressed as future extensions.

CHAPTER 2

Background and Preliminaries

This chapter introduces LPWAN with a focus on the three leading technologies currently in the market LoRa, NB-IoT, and Sigfox, drills down into the technical details of LoRa physical and *Medium Access Control* (MAC) layers, then presents our preliminary experimental comparative study of LoRa and NB-IoT.

2.1 LPWAN: Licensed and License-free Technologies

Several *Low power wide area* (LPWA) technologies are currently available in the market. Each technology has its own set of characteristics, network topologies, and deployment strategies. LPWA technologies can be broadly classified into two categories according to the used spectrum. Technologies operating in the licensed spectrum are standardized by the *3rd Generation Partnership Project* (3GPP), and licence-free technologies operating in the sub-GHz frequency bands. In the subsequent sections, we present the technical features of the three famous LPWA technologies LoRa, NB-IoT, and Sigfox.

2.1.1 Narrow Band-IoT

NB-IoT, which name stands for Narrow Band Internet of Things, is a licensed 3GPP initiated LPWA solution. It was proposed as part of Release 13 in 2016 [34].

It inherits the frequency bands, the networking stack and the deployment model of conventional cellular networks, especially *Long Term Evolution* (LTE). The main idea behind NB-IoT is to optimize traditional cellular networks and adapt their design so that they can better accommodate IoT and *Machine to Machine* (M2M) services which have fundamentally peculiar traffic characteristics compared to ordinary mobile services. The use of cellular licensed spectrum allows NB-IoT to control interference better and to provide better QoS. NB-IoT has two main types of UP channels: *Narrowband Physical Uplink Shared CHannels* (NPUSCHs) which are used for data transmission, and *Narrowband Physical Random Access Channels* (NPRACHs), which are responsible for the initial connection-less random access procedure.

NB-IoT offers three deployment modes [34, 35] illustrated in Fig. 2.1:

- Stand-Alone: In this deployment option, the NB-IoT carrier can replace a *Global System for Mobile Communication* (GSM) carrier and the power at the gateway is dedicated to NB-IoT which allows longer coverage ranges.
- In-band: In this deployment option, the NB-IoT carrier co-exists within LTE *Physical Resource Blocks* (PRBs) and the power is shared between both LTE and NB-IoT.
- Guard-band: In this deployment option, the NB-IoT carrier exploits the guard bands of the LTE spectrum.

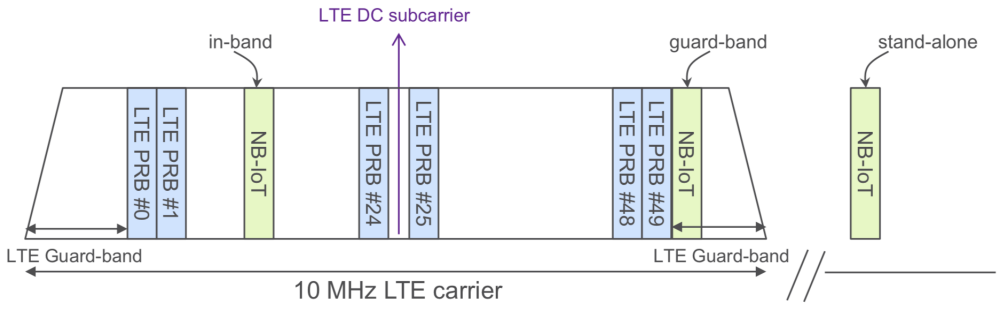

Fig. 2.1: NB-IoT Deployment Options [34].

The 3GPP had prior cellular-IoT solutions: EC-GSM-IoT and eMTC. Compared to these technologies, NB-IoT comes with a set of enhancements centred mostly around: power efficiency, coverage extension and complexity reduction. To

enhance coverage, NB-IoT implements a link adaptation mechanism that relies on grouping the devices according to their propagation environments into a number of Coverage Classes (CC), also called Coverage Enhancement Levels (ECLs). Based on the attributed CC to the device, appropriate coverage enhancement mechanisms like blind re-transmission and Transmission Time Interval (TTI) bundling are used [36].

To reduce the power consumption of NB-IoT devices, 3GPP has introduced two main features [37, 38]:

- Power Saving Mode (PSM): As a connection-based technology, NB-IoT uses Radio Resource Connection (RRC) to establish links between the device and the base station. An RRC has two possible states, either connected or IDLE. When the device is in the latter state, it can disconnect the radio and go to deep sleep mode, where it becomes, yet, registered but unreachable by the base station. The device can quit this mode, wake up and resume the connection with less overhead than a newly established one.
- Extended Discontinuous Reception (eDRx): This mechanism is designed for downlink communications efficient management, it is based on DRx cycles, and it allows NB-IoT devices to monitor discontinuously the *Narrowband Physical Downlink Control Channel* (NPDCCH). When the device is in an eDRx state, it remains synchronized and can be reached by any downlink message from the network.

2.1.2 Sigfox

Sigfox is a license-free LPWA technology developed and patented by a French company in 2009 [39]. In its first releases, it supported only uplinks then its protocol was enhanced to become bidirectional. Sigfox operates in Sub-1 GHz ISM bands and obeys its duty cycling limitations. This technology adopts an operator-based business model where only Sigfox operators can deploy a Sigfox network. Sigfox base stations are based on software-defined radios and are connected to Sigfox Backend servers using IP-backhauling links.

Sigfox can be considered an ultra-narrow band technology where a basic modulation scheme, the BPSK, is adopted. The BPSK modulation, although robust since its band-limited signal is immune to noise, it drastically limits the data rates supported by Sigfox because it allows only to modulate 1 bit per symbol. As a result, a Sigfox device can send only a few bits per day with a maximum UP throughput of 100 bps. A Sigfox UP message has a width of only 100 Hz and a maximum size of 12 bytes [39].

Sigfox access mechanism is based on dual time-frequency randomness using Random *Frequency Time Division Multiple Access* (FTDMA). As the narrow band signal can be weakened by flat fading, frequency hopping is performed continuously inside a band too large compared to the signal bandwidth. This continuity in the carrier frequency selection is cost-efficient since it decreases the precision requirement of the oscillator [40]. Because of its limited *Downlink* (DL), Sigfox gateway does not acknowledge received messages. Instead, each transmission can be repeated up to 3 consecutive times in different carrier frequencies to increase the probability of successful reception.

2.1.3 LoRa

LoRa belongs, like Sigfox, to the family of license-free technologies. Initially, LoRa was developed to use the sub-GHz band. The exact range varies between the regions. In EU, LoRa uses the *Industrial Scientific and Medical* (ISM) frequency bands like 433 MHz and 863 – 870 MHz, while it uses 915 – 928 MHz, 902 – 928 MHz, and 915 – 928 MHz respectively in Australia, North America, and Asia, [41]. New chips operating in the 2.4 GHz frequency band have been recently introduced into the market [42]. Unlike Sigfox, LoRa deployments are not necessarily administrated by an operator allowing stakeholders to acquire and deploy proprietary gateways. LoRa and LoRaWAN are sometimes used interchangeably. The name of the technology LoRa refers, in reality, to the physical layer stack whereas, LoRaWAN refers to the network layer protocol maintained by the LoRa Alliance.

As this thesis focuses primarily on LoRa, next in Section. 2.2 and Section. 2.3,

we further drill down into the technical details of LoRa physical and MAC layers. Section. 2.2 and Section. 2.3 give the technical background needed for Chapter. 4, Chapter. 5, Chapter. 6, and Chapter. 7.

2.2 LoRa Physical Layer

2.2.1 Overview of LoRa Modulation

LoRa physical layer stands on a patented modulation based on a Chirp Spread Spectrum (CSS) technique [43]. This technique modulates the exchanged data sequence by a series of chirp signals. Chirp signals are frequency-modulated pulses where the frequency is monotonically increasing or decreasing during a chirp duration, leading to an Up-Chirp or a Down-Chirp. The narrowband signal is multiplied by the wider-band chirp signal to give a waveform spread through the entire bandwidth. As such, LoRa modulation achieves signals with high ($BW \times Time$), which improves the technology's resilience to frequency-selective fading, Doppler effect [44] and narrowband interference [45] from coexisting license-free technologies. More in-depth explanations of LoRa modulation and technical details about its waveforms will be presented in Chapter. 4.

2.2.2 Transmission Parameters

LoRa modulation supports adaptive configurations, making the bit rate vary with each combination of transmission parameters. The effective bit rate (in kbits/s) is obtained by equation Eq. 2.1 [46]:

$$\mathrm{R}_b = \frac{4 \quad \mathrm{SF} \quad \mathrm{BW}}{(4 + \mathrm{CR}) \quad 2^{\mathrm{SF}}}, \tag{2.1}$$

where:

- **SF:** The spreading factor $\mathrm{SF} \in \{5, 6, ..., 12\}$ controls the chirp rate, i.e. how fast the signal is spread across the bandwidth.

- **CR**: is the coding rate scheme. CR $\in \{0, 1, 2, 3, 4\}$ defines the number of bits used for error correction. A CR= 0 means that no forward error correction (FEC) is applied.
- **BW:** The used bandwidth $BW \in \{125, 250, 500\}$ Khz.

Added to the SF, CR, BW, LoRa also supports variable transmit power and carrier frequencies. Lora networks can be designed to trade data rates for coverage and energy efficiency based on this tweakable set of transmission parameters. Increasing the SF improves the processing gain, which enhances the coverage at the expense of longer packet time on air and higher energy consumption. Increasing the CR decreases the rate for a more robust transmission that can better endure interference but, at the same time, consumes more energy. Doubling the BW doubles the data rate. These tweakable parameters make LoRa flexible to satisfy the requirements of an extensive array of IoT applications and smart sensing scenarios.

2.2.3 Frame Structure

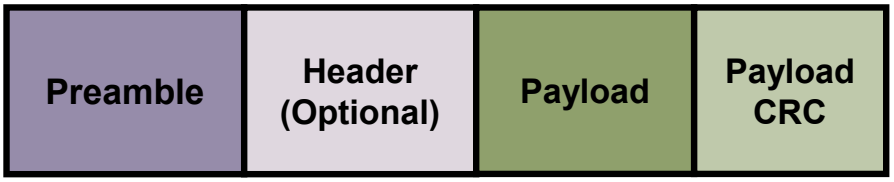

Fig. 2.2: LoRa frame structure.

A LoRa frame is composed as illustrated in Fig. 2.2 by a preamble that serves to synchronise the receiver with the transmitter. The preamble consists of a minimum of 8 symbols. The preamble starts by a sequence of up-chirps that shows the start of the frame. The remaining symbols of the preamble are programmable. Optionally the preamble is followed by a header that contains information about the payload length and the *Forward Error Correction* (FEC) CR whenever the explicit mode for data transmission is activated. In the implicit mode the header is deactivated [47].

2.3 LoRaWAN

To overcome the overhead caused by dedicated channel allocation, LoRa default device class relies on an Aloha-like medium access scheme where nodes access to channels without prior synchronisation or listening. This full random access technique simplifies the protocol stack at the node and provides energy gain but makes the technology suffer from overlapping transmissions due to a lack of coordination between the nodes.

2.3.1 Architecture

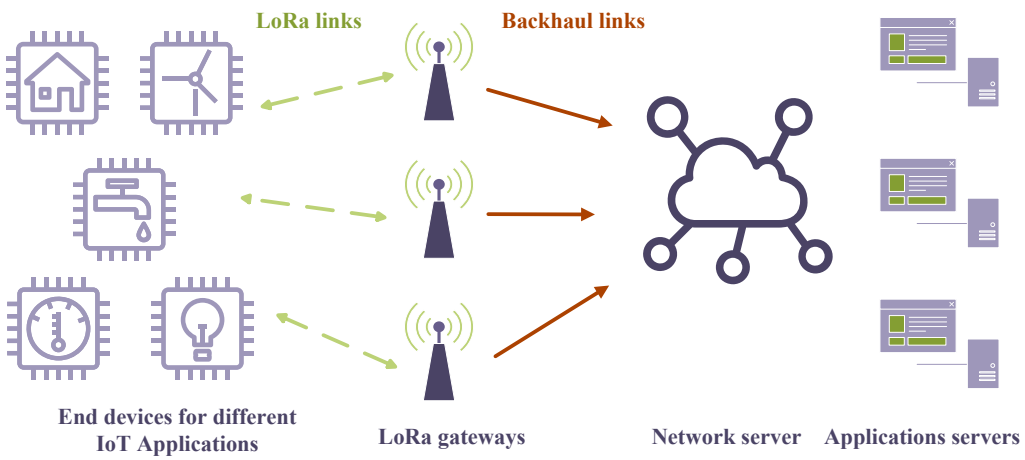

Fig. 2.3: LoRa Network Architecture.

LoRaWAN relies on a star network architecture where LoRa devices are connected to LoRa gateways via single-hop links. The gateways are connected via backhauling links to a network server that is in turn connected to applications servers. Network servers can be private or belong to public providers like Semtech network or The Things network. Fig. 2.3 illustrates the star topology of a LoRa network.

2.3.2 Regulatory Constraints

LoRaWAN is subject to regions-specific regulatory constraints to ensure fair access to the shared wireless medium between the nodes. These regulatory constraints mandate which specific ISM frequency band LoRaWAN networks designers need to set for their deployments and how it should be implemented, i.e. the mandatory channels, the maximum radiated power and the maximum time the device can be on. These regulations are often imposed via two main regimes, either duty cycling or *Listen Before Talk* (LBT). In Europe, the *Duty Cycle* (DC) regime is exclusively adopted where a node can be active only for a specific time duration. LoRaWAN DC is correlated with the transmission ToA and can be 1% or 10%. For 1% DC, a LoRa device can be active for up to 36 seconds during an hour. Other regions such as South Korea and Japan impose, instead, the activation of the LBT functionality as a collision avoidance mechanism where a LoRa device needs to monitor the channel to transmit only whenever it is not occupied. Detailed explanations of these regulations across different regions can be found in [48].

2.3.3 Device Classes

To answer different IoT use cases LoRa offers three device' classes[49]:

Class A: It is the default class that should be supported by all devices in a LoRa network. It has the most energy-efficient operational mode. When operating in this class, a LoRa device is able to receive downlink messages from the gateway only after sending an UP message. Two receiver windows can be open after an UP message. The first window duration, channel and rate are determined based on the previous UP communication parameters whereas the second window is offset from the first one by a default period of one second. The first receiver window is mandatory, but the second can be canceled once the downlink message is successfully received during the first open window. The standard prescribes that the first receive window (RX1) can be opened on the same channel that was used in the UP, while the second window is opened on the dedicated DL channel,

centered at 869.525 MHz.

Class B: Added to the basic functionalities of class A, class B devices are bidirectional and synchronized with the network thanks to beacon frames sent by the gateway. The DL reception is not conditioned by a prior UP transmission, it has instead scheduled receiver windows during which the device will be listening to the gateway.

Class C: Class C LoRa devices are bidirectional and whenever they are not locked to a transmission, they continuously listen to the medium for any arriving messages from the gateway. That is why this type of device works better for applications with high DL traffic such as firmware over-the-air updates and remote centralized control. The high energy consumption induced by the continuous channel sensing may restrict the deployment to areas with available mains power.

2.3.4 LoRa Adaptive Data Rate (ADR)

ADR is a resource optimisation mechanism based on dynamic power and SF adjustment s. It is activated by setting the ADR bit in the packet to one and relies on an interaction between both the network server and the node. When the ADR is activated, the network, based on information collected about the signal quality and using proper MAC commands, regulates the power and the SF of the transmission downward. Meanwhile the node believes that packets are not reaching the gateway when it detects many transmissions with no DL feedback, and so automatically adjusts the spreading factor and the used power upward to enhance the coverage range [50].

2.4 Recapitulation of LPWAN Technical Differences

After having presented LPWAN, detailed the technical features of three of the main technologies LoRa, NB-IoT and Sigfox, we summarize, in Tab. 2.1, the technical differences between them.

	LoRa	Sigfox	NB-IoT
Spectrum	ISM Sub-GHz EU:868	ISM Sub-GHz	LTE Band
Band Width	125 kHz, 250 kHz, 500 kHz	UP: 100 Hz DL: 600 Hz	180 kHz
Modulation	CSS and FSK	BPSK	QPSK
Medium Access	Pure Aloha	Pure Aloha	OFDMA SC-FDMA
Max Coverage	Rural: 15 Km Urban: 5 Km	Rural: 50 Km Urban: 10 Km	Rural:>15 Km Urban: 5 Km
Max Coupling Loss (db)	155	162	164
Max Data Rate	50 kbps	UP: 100 bps DL: 600 bps	250 kbps
Max Payload (bytes)	242	12	1600
Network Topology	Star	Star	Star
Standardization	LoRa alliance	Ongoing	3GPP
Protocol Stack	Specific stack Mac options for each device class	Proprietary Stack	A simplified optimal version of LTE Stack
Synchronisation	No	No	Yes
Deployment	Private	Operator-based	Operator-based

Table 2.1: Comparison of LPWA Technologies [51, 52, 53, 54].

Adopting a basic modulation, the main limiting factor of Sigfox is its very low data rate. By inheriting the cellular infrastructure, NB-IoT inherits the blessings that come along with, but also the challenges stemming from the naturally different patterns between cellular services and IoT traffics. LoRa, on the other hand, sits in between as it is a license-free technologies that offers decent data rate and signal penetration which makes it a compelling solution for a number of smart sensing industries. LoRa and NB-IoT can be considered as the most competitive technologies in the LPWA market. Next, in Section. 2.5, we present our approach to compare these two technologies against realistic applications profiles.

2.5 An Application-Level Approach to Enable LPWAN Comparison: LoRa Vs NB-IoT

In this section we present our high level application-based approach to compare LPWAN. The approach is applied to compare LoRa and NB-IoT against realistic application profiles in two environments with different urban layouts: Imperial South Kensington Campus in London and HDB Punggol Northshore estate[1].

2.5.1 Motivation and Contribution

As it has been previously introduced, the research works conducted in the context of my PhD were part of a collaborative project with HDB Singapore. HDB estates compromise an array of sensing and monitoring services where nodes are sometimes deployed in harsh environments. Such harsh environments require to have battery-powered nodes that last for a long duration with minimal human intervention. With the HDB strategy of smart sustainable living in mind, our aim was to explore alternative connectivity technologies that could provide HDB with reliable, effective, and sustainable sensing infrastructures.

As we have seen in the previous sections, various emerging technologies are available in the market giving an array of choices to stakeholders like HDB. However, this variety renders challenging the decision of a stakeholder about the best and most effective technology for its applications. With the scarcity of resources dealing with comparative studies of LPWA technologies under real operating conditions, the choice becomes even more difficult. Most of the existing studies dealing with comparative analysis of LPWA technologies are reviews [35, 51, 52, 53, 55] where the comparison is carried out based on the technologies, technical specifications and data-sheets. Few studies in which empirical comparison has been performed [38, 56, 57] often abstract application characteristics and restrict

[1]The Housing and Development Board (HDB) is Singapore's public housing authority. It plans and develops Singapore's housing estates https://www.hdb.gov.sg/cs/infoweb/homepage.

their focus to a specific environment [56] or a unique metric such as coverage [57] or energy consumption [38].

Stakeholders like HDB would simply ask the following questions: "Will my application work on this specific set of processors, communication protocols, and gateways?" "Which technology would better satisfy the QoS requirements of my application?" Although simple, these questions could not find answers in typical IoT benchmarking approaches [58, 59, 60]. The reason is that typical IoT benchmarking approaches like TPCX [58], IoTMark [59] or SecureMark-TLS [60] often address the question from a micro component-based perspective that fails to give an accurate picture of system's performance when it comes to real deployment scenarios. Motivated by this gap and adopting user-oriented thinking, we propose a taxonomy of IoT applications based on their traffic characteristics and communication requirements. The derived taxonomy is then used to compare LoRa and NB-IoT against realistic application profiles and in real deployment conditions.

2.5.2 IoT Applications Profiles

The first step in designing the applications profiles consisted on reviewing the literature body about the classification of IoT applications and their traffic characteristics. In [61] a study of M2M traffic characteristics in smart city environment is presented. The authors outlined three types of traffic distributions, Poisson for periodic reporting, beta for synchronised traffic and deterministic for scheduled events. Authors in [62] presented a detailed survey about IoT areas, highlighted the principal services in each area and described their characteristics in terms of data transmission rate, average network size, energy sources, and QoS. In [63], the authors proposed an aggregation scheme of potential applications in smart cities and surveyed existing smart city projects. The study in [64] employed a network analytical approach to empirically classify the behaviour of IoT devices based on a number of attributes including their traffic characteristics. More smart city projects have been investigated [65, 66, 67, 68, 69] with a focus on the technical require-

ments of the involved applications. Multiple factors influence the applications technical requirements including the traffic behaviour, the application longevity and its potential deployment locations. In [70, 71, 72, 73], the authors qualitatively highlighted the requirements of some IoT applications in terms of bandwidth, power consumption, reliability and delay tolerance.

We validated the results of the literature review with a questionnaire [2] distributed among IoT research teams and industrial practitioners that implement and operate IoT applications. Noting that the aim of our questionnaire was not to collect statistically representative quantitative data but qualitative information about the limits of the applications in terms of packet sizes and data transmission rate as well as its QoS requirement. We designed a set of profiles, that map the applications commonly encountered in smart city and urban habitat projects. The profiles are summarized in Tab. 2.2.

Application Profile	**Packet Profile** Bytes	**Rate Profile** Msg/hour
P1: Environment Monitoring	45	20
P2: Building Automation	45	5
P3: Non-Critical Infrastructure Monitoring	100	5
P4: Critical Infrastructure Monitoring	100	8 (Regular)
P5: Critical Infrastructure Monitoring	1024	0.04 (Event)
P6: Smart Metering (Single transmission)	400	0.04
P7: Smart Metering (Fragmented)	12	2.83

Table 2.2: Applications Profiles.

2.5.3 Profiles Characteristics and Communication Requirements

The characteristics of the applications profiles given in Tab. 2.2, their potential deployment environment, the criticality of the data they report all together impact the choice of the most suitable technology for them. A wrong choice of technology can lead to cost inefficiency, technical incompatibility with the

[2] https://docs.google.com/forms/d/11Inr0XVWSSREAjSOhXLSaMY77D-u0SIH7beA5AqtmS0/viewform?edit_requested=true

application requirements and even transmission issues. Below, we describe the characteristics of the profiles in Tab. 2.2:

- **Environment Monitoring:** This category covers applications with periodic monitoring and communication such as temperature, humidity, air quality and rain flow monitoring. The applications in this profile can be delay-tolerant. Their most important constraint is energy consumption.
- **Building Automation:** This category encompasses applications related to building structures for systems like lighting control, heating and ventilation remote monitoring. These applications are less energy-constrained as grid power is usually available in buildings. Their traffic rate is not high and require medium to high quality of service.
- **Infrastructure Monitoring:** This category includes infrastructure monitoring where no time-critical data is transmitted. Typical applications among this category are waste management systems and smart parking areas.
- **Critical Infrastructure Monitoring:** This category includes applications like factory assembly lines, water mains, or gas pipeline monitoring. Periodic and event-based reporting may be required. These profiles require a high degree of reliability and a minimal delay for predictive maintenance to trigger an alarm in bounded time.
- **Smart metering:** Smart metering is a category of applications where one reporting message is sent per day. Since these meters can run of mains power, they do not have very constrained energy requirements.

Application Profile	**Tolerable Delay** secs	**Reliability** (%)
Environment Monitoring	5-30	36-95
Building Automation	<5	36-100
Non-Critical Infrastructure Monitoring	5-30	36-95
Critical Infrastructure Monitoring	<5	>95
Smart Metering	>30	Best effort

Table 2.3: Profiles technical requirements.

Tab. 2.3 summarises the technical requirement of the applications profiles described

above. The values in Tab. 2.3 were obtained from the literature review and the survey previously detailed [70, 71, 72, 73][3].

2.5.4 Performance Assessment Metrics

To compare the performance of LoRa and NB-IoT against the application profiles in Tab. 2.2, we define the following application-level metrics:

- **Reliability:** This metric is measured by the *Packet Delivery Ratio* (PDR). PDR is defined as the ratio of the number of packets successfully delivered over the total number of sent packets. PDR is measured at the gateway or the application server by recording all the messages received from a given node using specific profile.
- **Energy Efficiency:** This metric used energy consumption logged on the nodes.
- **Delay:** This metric is calculated from the time the sensor generates a message to the time the message is received. The calculation of this metric is performed offline from logs captured on both the node and the gateway assuming they are synchronised.

2.5.5 Experimental Setup

The experimental setups and nodes deployments for this preliminary study have been prepared in collaboration with teams from Imperial College London, A*Star[4] and APAQ[5] (Appendix D). We deployed the nodes in different locations in two urban areas: Imperial South Kensington Campus in London and HDB Punggol Northshore in Singapore. Each deployment location has specific geographical characteristics ranging from deep underground to open areas. In the sequel we detail the hardware structure of the deployed nodes and the characteristics of their deployment locations.

[3] Noting that the minimum reliability is difficult to quantify and was set to 36% according to the maximum achievable throughput per slot for a slotted aloha system [74]

[4] https://www.a-star.edu.sg

[5] https://www.apaq-group.com/

A. Hardware Infrastructure

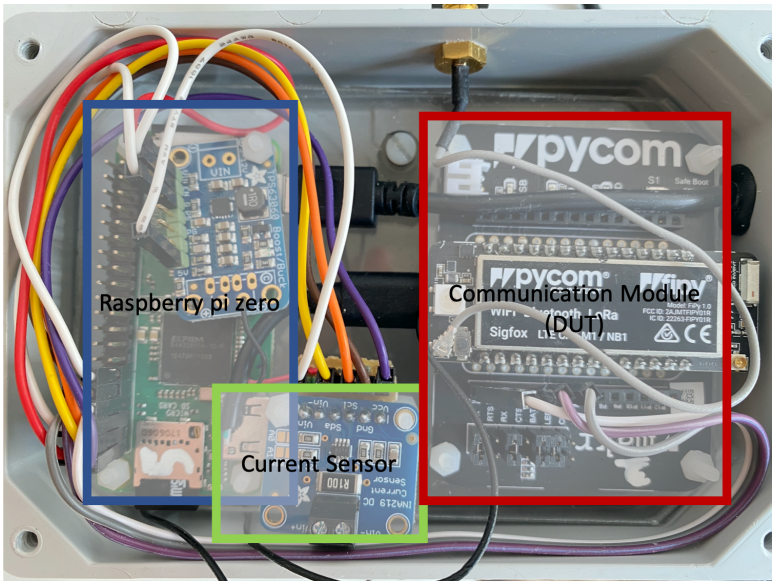

Fig. 2.4: LoRa/NB-IoT sensor node mounted in a water-proof box.

To conduct our experiments, we assembled the LoRa/NB-IoT sensor node as a BentoBox [75]. Each BentoBox is composed as shown in Fig. 2.4 of:

- 1 Raspberry Pi Zero
- 1 Pycom FiPy communication module Mounted on a Pycom Extension Board
- 1 Adafruit 1NA219 voltage/current sensor breakout board
- 1 LoRa 868/915 MHz antenna kit
- 1 LTE-M antenna kit
- 1 battery pack

The hardware was designed using a Pycom FiPy module for communication which has a single processor to control LoRa and NB-IoT radio chips. Given that, all aspects of the node except for the radios are the same. The Adafruit INA219 current sensor breakout board is used to measure the node's current consumption. Dummy data was generated in the scripts running in the nodes based on the packet size and the transmission frequency of the applications summarized in Tab. 2.2. The generated data is then transmitted using LoRa and NB-IoT.

B. Testbed deployment in London

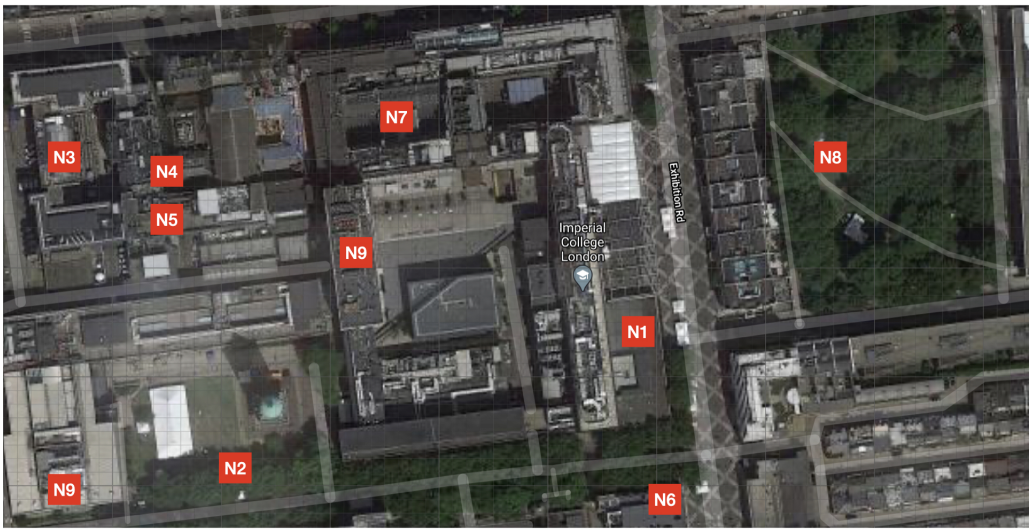

Fig. 2.5: Deployment locations in London.

We deployed our nodes in 9 different locations across Imperial College South Kensington campus. The characteristics of the deployment locations are summarized in Tab. 2.4.

Node	Geographical Characteristics
LN1	Deep indoor environment, windowless, surrounded by rooms
LN2	Windowed indoor above ground level
LN3	Underground manhole, Shielded by a metal lid and concrete
LN4	Underground with LTE network, with windows
LN5	Deep underground with no LTE network, Windowless
LN6	Densely surrounded by tall buildings above ground level
LN7	Enclosed space on rooftop, close to LoRa basestation
LN8	Garden environment at ground level, Surrounded by foliage
LN9	Open rooftop environment

Table 2.4: Deployment locations in London and their respective geographical characteristics.

C. Testbed deployment in Singapore

We deployed our nodes in 8 different locations across the Punggol Northshore HDB estate. The characteristics of the deployment locations are summarized in

Tab. 2.5 and examples of the locations are shown in Fig. 2.6.



(a) LoRa Gateway (b) SN_1 (c) SN_3

Fig. 2.6: Examples of deployment locations in Punggol HDB estate.

Node	Geographical Characteristics
SN1	Garden environment in building basement
SN2	Building open sky terrace
SN3	Deep underground environment in a water retention tank
SN4	Underground environment, treatment room
SN5	Open space with vegetation, sky garden
SN6	Enclosed space in the building , Riser room
SN7	Rooftop, open area in line of sight with LoRa GTW
SN8	Playground

Table 2.5: Deployment locations in Singapore and their respective geographical characteristics.

2.5.6 Data Analysis and Results

To analyse the collected data, a Matlab script was created to parse the data collected from the nodes and the gateway. The parsed data is then used to calculate the performance metrics detailed in Subsection. 2.5.4.

Signal Quality: As highlighted in Section. 2.4, NB-IoT is an operator-based technology for which the gateways' locations are not disclosed. LoRa is, instead, an operator-free technology where anyone can deploy gateways. To characterise the signal quality, we use the *Received Signal Strength Indicator* (RSSI) of LoRa DL messages and the Channel Signal Quality (CSQ) available before every NB-IoT

transmission. The Channel Signal Quality (CSQ is converted to dBm. The signal quality across different locations in London and Singapore are shown, respectively, in Tab. 2.6a and Tab. 2.6b. NB-IoT signal quality was better in Singapore than in London, while LoRa signal quality was overall better in London than in Singapore. This can be explained by the fact that NB-IoT coverage is omnipresent in Singapore, while at the time of the experiment, our gateway was the only LoRa gateway in the area. Moreover, the urban layout of the deployment area in Singapore is characterised by very high-rising buildings, which makes it harsher compared to the deployment area in London. LoRa has shown a comparable signal quality to NB-IoT (SN7) when the node is deployed close to the gateway.

Node	Signal Strength(dBm)	
	LoRa	NB-IoT
LN1	-101	-77
LN2	-87	-73
LN3	-89	-71
LN4	-109	-63
LN5	-104	X
LN6	-82	-65
LN7	-61	-65
LN8	-87	-59
LN9	-77	-61

(a) London deployment Locations.

Node	Signal Strength(dBm)	
	LoRa	NB-IoT
SN1	-101	-57
SN2	-104	-60
SN3	-122	-77
SN4	-112	-86
SN5	-92	-54
SN6	-112	-61
SN7	-47	-49
SN8	-77	-56

(b) Singapore deployment Locations.

Table 2.6: Signal quality (in dBm).

Packet Delivery Ratio: Tab. 2.7 and Tab. 2.8 show the obtained PDR for both protocols in the two setups. The PDR for NB-IoT is shown to be consistently higher than 90% whenever the connection to the network is successful and stable. In Singapore's setup, P5, which corresponds to critical event reporting with 1 kbytes packet size, was the most challenging profile for NB-IoT with a performance ranging from no reception at all in challenging locations such as SN6 and a PDR of 20% in overground open locations such as SN8.

LoRa PDR performance is shown to be quite significantly impacted by the location of the node and the application profile. First, from Tab. 2.7 and Tab. 2.8,

we see that LoRa fails for P5 and P6 in both London and Singapore because these application profiles have packet sizes that exceed the maximum payload limit. LoRa's best PDR performance is obtained in overground open area locations such as SN7 and SN8, and LN9 where the nodes are close to the gateway or in near line-of-sight with it. A PDR comparable to NB-IoT is obtained in LN9. In Singapore, NB-IoT has shown better performance in underground and deep underground environments (SN3 and SN4), while these two locations were the most challenging for LoRa. We obtained the opposite behaviour for the deep underground location in London (LN5), as LoRa successfully delivered a few packets. However, NB-IoT was unable to establish a connection with the network. The omnipresent NB-IoT connectivity in Singapore could be the reason for that.

Delay: Tab. 2.9 and Fig. 2.7 show the mean delay between packet reception and generation for each of the profiles and locations in London and Singapore, respectively. The delay for LoRa is less than 3 seconds for most of the profiles and locations in London. In the case of LN5, SN3 and SN4, which are underground and deep underground, the delay is high as the node in these harsh locations keeps trying to re-transmit. Higher average delays reaching 5 seconds for some locations have been shown in Singapore. For NB-IoT, the delay is less than 17 seconds regardless of the location, except for specific profiles. In Singapore, challenging profiles P4 and P5, with respective packet sizes of 400 and 1024 bytes, gave average delays exceeding 20 sec for some locations. It is worth noting that the delay for NB-IoT considers the connection time, which explains its high values compared to LoRa. Fig. 2.7 clearly illustrates the delay overhead caused by the connection establishment for NB-IoT.

Energy: Tab. 2.10 shows the average total energy consumed per packet(mWh) by each of the two technologies for each of the profiles across different locations. The energy consumption results account for only the energy used to transmit the packet. It does not take into account duty-cycling. Examining this table, we can see that LoRa consumes less energy compared to NB-IoT even when both provide comparable PDR performance. The energy consumed by LoRa is impacted by the locations and is shown to increase as the signal becomes weaker. This illustrates

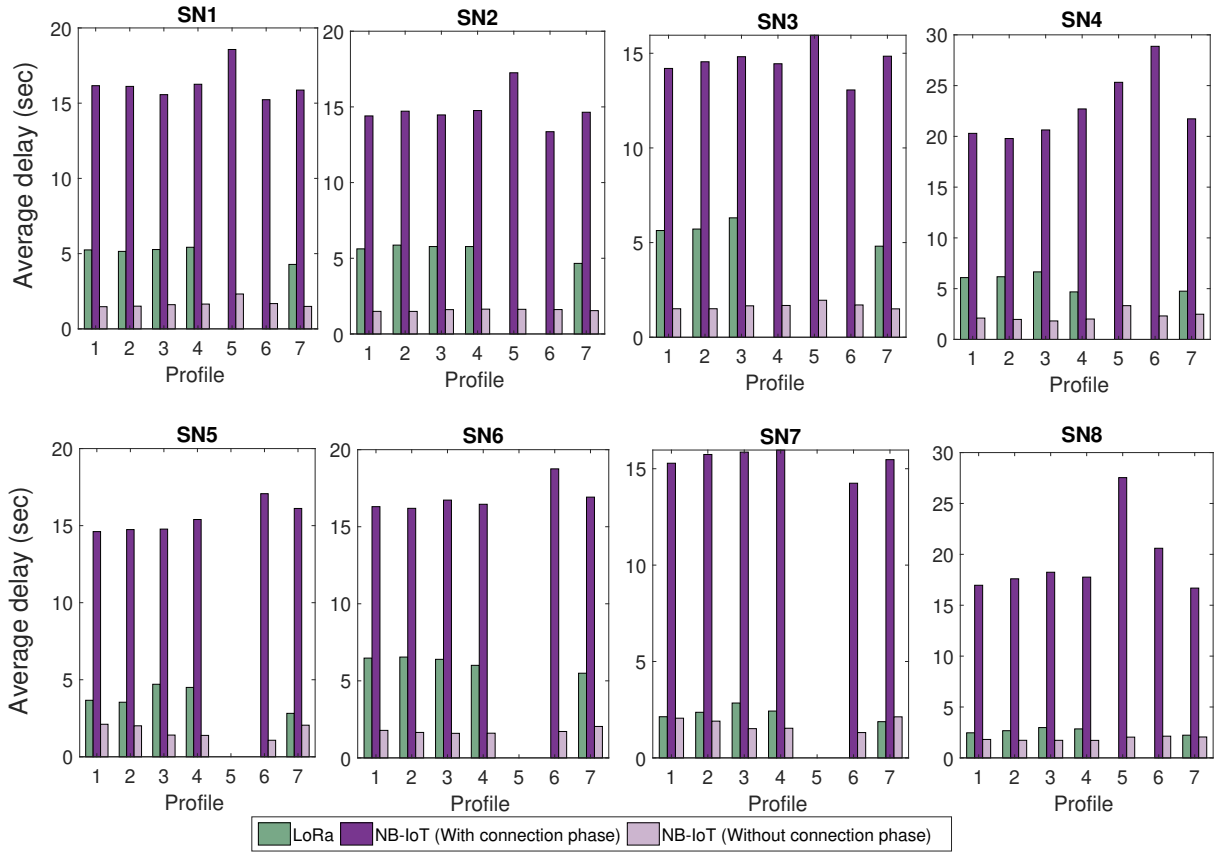

Fig. 2.7: LoRa Average delay in Singapore.

how LoRa adapts its power and SF to improve the coverage of the node in response to signal deterioration. The results in Tab. 2.10 and Tab. 2.7 evince a tradeoff between energy and reliability (PDR).

	LN1		LN2		LN3		LN4		LN5		LN6		LN7		LN8		LN9	
	lora	nbiot	lora	nbiot	lora	nbiot	lora	nbiot	lora	nbiot	lora	nbiot	lora	nbiot	lora	nbiot	lora	nbiot
P1	0.60	0.96	0.61	0.96	0.73	0.93	0.05	0.96	0.04	X	0.82	0.96	0.79	0.97	0.86	0.93	0.90	0.94
P2	0.61	0.95	0.58	0.97	0.73	0.93	0.06	0.96	0.10	X	0.81	0.96	0.81	0.96	0.86	0.93	0.89	0.94
P3	0.01	0.96	0.37	0.97	0.57	0.93	X	0.96	X	X	0.66	0.96	0.67	0.97	0.57	0.94	0.76	0.94
P4	0.01	0.95	0.66	0.97	0.58	1.00	X	0.98	X	X	0.83	0.99	0.80	0.99	0.78	0.95	0.75	0.96
P5	X	1.00	X	1.00	X	1.00	X	1.00	X	X	X	1.00	X	1.00	X	1.00	X	1.00
P6	X	1.00	X	1.00	X	1.00	X	0.93	X	X	X	1.00	X	1.00	X	1.00	X	0.93
P7	0.81	0.95	0.87	0.98	0.80	0.99	0.65	0.98	0.04	X	0.91	0.99	0.98	1.00	0.92	0.96	0.99	0.96

Table 2.7: Packet Delivery Ratio(PDR) for LoRa and NB-IoT in London.

	SN1		SN2		SN3		SN4		SN5		SN6		SN7		SN8	
	lora	nbiot	lora	nbiot	lora	nbiot	lora	nbiot	lora	nbiot	lora	nbiot	lora	nbiot	lora	nbiot
P1	0.47	0.99	0.37	0.99	0.07	0.99	0.15	0.97	0.34	0.99	0.17	0.99	0.53	0.99	0.64	0.97
P2	0.42	0.99	0.32	0.99	0.03	1	0.15	0.97	0.4	0.99	0.18	0.99	0.65	1	0.57	0.99
P3	0.2	0.99	0.10	0.99	0.05	0.99	0.03	0.96	0.18	1	0.02	0.99	0.42	0.99	0.42	0.97
P4	0.3	0.99	0.20	0.99	X	0.99	0.02	0.95	0.63	0.99	0.03	0.99	0.75	0.99	0.8	0.98
P5	X	1.00	X	1.00	X	1.00	X	1.00	X	X	X	1.00	X	1.00	X	1.00
P6	X	1.00	X	1.00	X	1.00	X	1	X	X	X	1.00	X	1.00	X	0.84
P7	0.61	1	0.54	1	0.01	0.1	0.3	0.97	0.53	0.97	0.3	0.99	0.55	1	0.65	1

Table 2.8: Packet Delivery Ratio(PDR) for LoRa and NB-IoT in Singapore.

	LN1		LN2		LN3		LN4		LN5		N6		LN7		LN8		LN9	
	lora	nbiot	lora	nbiot	lora	nbiot	lora	nbiot	lora	nbiot	lora	nbiot	lora	nbiot	lora	nbiot	lora	nbiot
P1	2.99	13.15	2.12	13.35	1.72	13.82	3.81	13.94	552.19	X	1.79	14.02	1.73	14.15	2.02	14.09	1.68	13.86
P2	3.00	13.23	2.15	13.15	1.73	20.61	3.80	13.14	616.61	X	1.80	14.22	1.73	14.27	2.33	14.06	1.65	13.97
P3	1.79	12.92	1.49	13.14	1.81	20.56	X	13.77	X	X	1.37	13.96	1.36	14.25	1.38	14.20	1.36	13.85
P4	1.79	13.42	1.41	13.49	1.51	12.52	X	11.93	X	X	1.37	14.28	1.36	14.76	1.42	17.80	1.38	15.28
P5	X	13.67	X	13.99	X	11.82	X	12.19	X	X	X	14.81	X	14.59	X	14.02	X	14.23
P6	X	13.21	X	13.83	X	15.65	X	11.64	X	X	X	17.07	X	14.80	X	14.01	X	17.26
P7	2.18	13.55	1.47	13.28	1.37	12.58	2.78	11.89	141.07	X	1.34	14.20	1.50	14.71	1.38	14.26	1.60	14.86

Table 2.9: Mean Delay time(seconds) of LoR and NB-IoT in London.

	LN1		LN2		N3		LN4		LN5		LN6		LN7		LN8		LN9	
	lora	nbiot	lora	nbiot	lora	nbiot	lora	nbiot	lora	nbiot	lora	nbiot	lora	nbiot	lora	nbiot	lora	nbiot
P1	1.00	4.09	0.76	4.28	0.59	4.78	0.90	4.44	1.19	X	0.56	4.83	0.80	4.90	0.71	4.24	0.62	4.19
P2	0.81	4.34	0.76	4.25	0.61	4.82	1.09	4.67	2.34	X	0.57	4.73	0.79	4.70	0.71	4.92	0.76	4.13
P3	1.98	4.11	1.02	4.23	1.70	4.42	7.23	4.91	2.35	X	0.86	4.99	0.92	4.96	0.88	5.31	0.91	4.14
P4	1.63	4.79	0.79	4.21	1.42	3.51	7.11	4.30	1.04	X	0.57	4.41	0.90	4.98	0.61	4.85	0.93	4.39
P5	X	4.51	X	4.60	X	4.24	X	5.01	X	X	X	5.39	X	5.65	X	5.33	X	4.33
P6	X	4.46	X	4.52	X	4.86	X	5.26	X	X	X	5.89	X	5.67	X	5.24	X	4.84
P7	0.84	4.95	0.67	4.01	0.62	3.39	0.93	4.30	1.04	X	0.51	4.47	0.69	4.80	0.66	4.77	0.68	3.93

Table 2.10: Average energy consumed per node per profile (mWh) of LoRa and NB-IoT in London.

2.5.7 Discussion

The preliminary study presented in this chapter was initiated during the first year of the PhD while getting into the world of LPWAN. During the first year, we have been able to deploy the experiment in London. Then, as COVID-19 has hit, the procurement and administrative procedures of the deployment in Singapore had been delayed. It was only by the beginning of the fourth year that we were able to collect the data from the deployment in Singapore.

Based on the results of the preliminary study and the characteristics of the applications, some recommendations have been shared with HDB about which technology fits which application in the context of HDB estates. These recommendations are summarized in Fig. 2.8. NB-IoT is more suitable for applications that embed a certain degree of criticality making them demanding in terms of reliability and network throughput. For HDB urban estates, fire alarms, lift monitoring alerts, building maintenance alerts, control systems monitoring like water tanks are among these categories. On the other side, LoRa is more convenient for applications with relaxed constraints about reliability and stricter constraints regarding battery lifetime as it is more energy saving, this could apply for applications like street lights, air quality management, soil, humidity, and temperature monitoring, water quality monitoring, and odour sensing for the case of Pneumatic Waste Conveyance System (PWCS) which typically have small packet sizes.

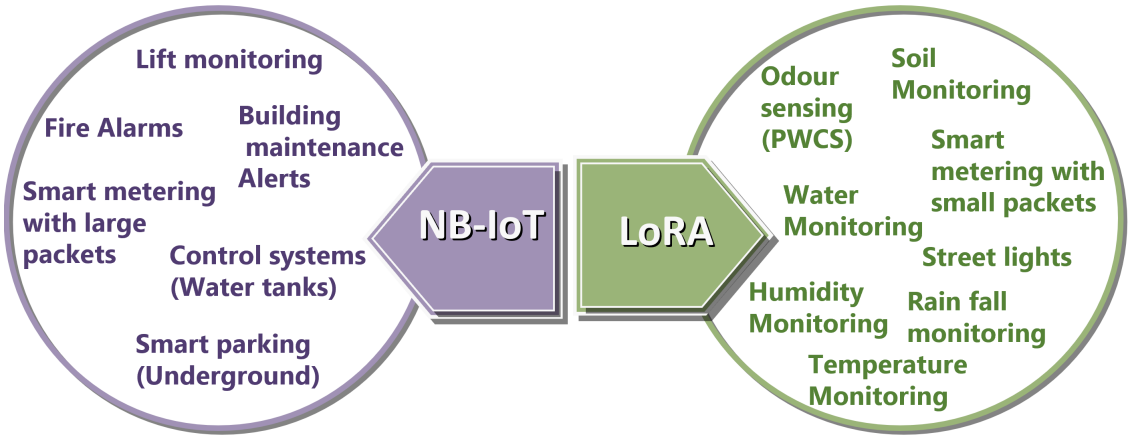

Fig. 2.8: Recommendations for HDB.

It is worth highlighting that due to their fundamental technical differences, LoRa and NB-IoT cannot directly compete. Judging from our results, no single technology is likely to dominate the market at the moment. Each of these technologies has use cases and scenarios in which it can win. The choice between them will depend on the needs of users, the requirements of their projects in terms of privacy, security, criticality of applications, the timeliness and reliability of data delivery, and of course costs.

We believe that the IoT market would converge towards heterogeneity and co-existence, where different technologies complement each other. We can imagine scenarios where two technologies like LoRa and NB-IoT cohabit the same hardware infrastructure similarly to our bentobox in Fig. 2.4 and based on the nature of the application and the characteristics of its traffic, dynamic switching between them can be performed to optimize energy efficiency and extend the application's longevity. For example, a sensing node can perform its less critical daily reporting with LoRa to save power, then send critical messages over NB-IoT to ensure high data reliability. Such cooperation would foster IoT interoperability and harness more long-term benefits. Initial efforts encouraging these hybrid multi-RAT infrastructures were made in [76].

2.6 Chapter Summary

In the first part of this chapter, we have presented technical overviews of the three famous LPWA technologies, LoRa, NB-IoT, and Sigfox, then we drilled down into the details of LoRa physical and MAC layers to provide the needed background for the remaining chapters of the thesis. In the second part, we present a preliminary study that we have conducted to compare the performance of LoRa and NB-IoT following our application-level approach. At the end of the chapter, we discussed the results of the comparative study and the recommendations we advised to HDB.

CHAPTER 3

LoRa/LoRaWAN Related Work and State of the Art

3.1 Introduction

The comparative preliminary study conducted in the previous chapter has shown that LoRa PDR is highly affected by transmission parameters and conditions compared to NB-IoT that has shown a more consistent PDR performance whenever the connection to the cellular network is successful. NB-IoT high reliability was primarily due to NB-IoT being a connection-based technology. However, the connection establishment has been shown to cause significant delay and energy overheads. Therefore LoRa has demonstrated better, more promising performance in terms of energy consumption.

Energy consumption is a crucial factor in the sustainability strategies of stakeholders like HDB. Reducing energy consumption was considered as the prime action area in HDB green towns program[1]. The results of the preliminary experimental study presented in Chapter. 2 have then sharpened our research focus: Exploring LoRa, understanding its behaviours, quantifying the impact of transmission parameters and conditions on its performance, and characterising the

[1]The green towns program is a 10-years plan to make HDB towns more sustainable and liveable. https://www.hdb.gov.sg/about-us/our-role/smart-and-sustainable-living/Green-Towns-Programme

performance trade-offs within LoRa networks were our areas of research focus throughout the PhD. In the spirit of these research focus areas, we explored the LoRa/LoRaWAN state-of-the-art.

The state-of-the-art for LoRa/LoRaWAN is broad and miscellaneous. We choose to review it based on the following four categories which are the most relevant to the thesis's scope:

1. Characterisation of LoRa physical layer performance and SF orthogonality.
2. Performance evaluation of LoRa/LoRaWAN networks using different approaches: experimental, simulation, and analytical.
3. A zoom on the analytical approach and the use of stochastic geometry for LoRa scalability analysis.
4. *Discrete Time Markov Chain* (DTMC) for LoRa device-level modelling.

3.2 LoRa Physical Layer and SF-Orthogonality

As a proprietary technology, LoRa physical layer specifications are closed; there is no public documentation available that explains the technical details behind this technology, including the waveform and signal theory, the modulation/coding and the demodulation/decoding processes. In this section, we explore research works that have focused on characterising LoRa physical layer.

The first category in this direction addresses the signal theory of LoRa, where few studies attempted to describe the LoRa waveforms and inspect their orthogonality. In [77], LoRa modulation was described as *Frequency Shifting Chirp Modulation* (FSCM). The paper investigated LoRa waveforms orthogonality. However, their investigation was limited to chirps in the discrete-time domain for synchronous transmissions using the same SFs. The performance of LoRa modulation was compared using simulations to *Frequency Shift Keying* (FSK) modulation in both AWGN and frequency-selective channels. The results of the comparison

have shown that LoRa and FSK exhibited similar performance in AWGN while LoRa outperforms FSK in frequency-selective channels. Similarly, [78] tackled the same-SF orthogonality scenario for only continuous synchronous transmissions. The performance of LoRa was compared by simulations to *binary phase shift keying* (BPSK). It has been shown that LoRa is more robust against interference than BPSK, which is the modulation scheme used by Sigfox (Subsection. 2.1.2). In [79], LoRa spectral properties have been studied for both continuous and discrete cases. However, in line with the existing works in the literature, the paper addressed only the same SF. In [79], LoRa was described as M-array modulation shown to be orthogonal for the same SFs as long as $M = 2^{SF}$ is asymptotically large. Additionally, the paper restrictively examined spectral properties. It did not give a complete picture of LoRa performance in terms of metrics such as *Bit Error Rate* (BER) or PDR.

The second category focuses, instead, on theoretical BER analyses where many efforts have been devoted to study LoRa BER performance in different environments and under different channel conditions. In [80], due to the analytical complexity, a Monte Carlo approximation is recalled to obtain bit and symbol error rates of non-coherently detected LoRa signals in an AWGN. The study has also compared the theoretical BER performance of LoRa and Sigfox. In [81], approximate BER expressions based on a Gaussian approximation have been proposed to study the performance of uncoded LoRa in AWGN and Rayleigh Fading channels under non-coherent detection. The BER performance of both codded and uncoded LoRa signals under coherent and non-coherent detections have been theoretically studied in [82, 83]. The improved approximate expressions proposed in [82, 83] are based on Gaussian Q-function and algebraic formulas.

As the vulnerability of LoRa to interference started to be accused of limiting its scalability, recent works have started to analyse LoRa BER performance in the presence of interference. Most research works assumed, however, a "perfect orthogonality" scenario under which only interference from the same SF is considered [84, 85, 86]. In [84], the authors extended their work in [81] to account for the same SF interference. They were able, as a result, to study the BER performance under the

joint impact of *Signal to Noise Ratio* (SNR) and SIR, evincing a correlation between them. In [87], the authors adopted the interference model proposed in [84] and improved it by extending the random shift between the desired and interferer LoRa signals from an integer number of samples to a uniform distribution. In [86], the authors propose a semi-analytical approximate expression of LoRa symbol error rate under coherent and non-coherent detections in two scenarios. First, they studied the performance of a LoRa signal over either an AWGN or a multi-path frequency selective fading channel. Then, they examined the particular scenario of a desired LoRa signal over an AWGN suffering from an interfering signal with the same SF.

3.3 Performance Evaluation Approaches of LoRa Networks: Benefits and Challenges

The performance characterization of LoRa networks has been carried out using different approaches ranging from experimental, simulation-based, to analytical. While the three approaches are naturally complementary to draw a complete picture of LoRa performance, each of them comes with its benefits and challenges.

The experiment-based approach has the advantage of mimicking real application scenarios. Many LoRa experimental testbeds have been deployed for several application scenarios and in different signal propagation conditions. The impact of indoor, semi-indoor, and outdoor environments on LoRa's coverage performance was evaluated in [88, 89, 90]. LoRa has also been tested for the monitoring of underground environments such as mines [91]. The resilience of LoRa to the Doppler shift was investigated in [44]. LoRa has been tested for maritime applications and monitoring of critical infrastructures in [92, 93], respectively. In [94], the feasibility of LoRa/LoRaWAN for smart metering has been tested. In [95, 96, 97, 98] smart agriculture infrastructures based on LoRa/LoRaWAN were proposed. In [99], a LoRa/LoRaWAN network was deployed to monitor radiation in the European Organization for Nuclear Research (CERN). LoRa nodes were

installed in metallic waste containers to monitor radioactivity. The results of [99] showcased a promising packet reception rate that is impacted by the placement of the nodes under or inside the container. A promising performance has also been obtained in [100] where LoRa with a custom MAC layer has been implemented to monitor school buildings. The study shows that LoRa provides a more reliable, more robust and less expensive solution compared to IEEE 802.15.4, which is a *Low Rate Wireless Personal Area Network technology* (LR-WPAN).

However, such field deployments are often hampered by practical implementation constraints. These constraints entail: (i) spatial limitations due to deployment areas being often small and confined in regions like buildings, parks, and gardens, (ii) temporal limitations as the experiments cannot span an extended period, and (iii) scale limitations due to the high costs required for the deployment of many devices during a test phase. A second challenge of experimental approaches is the lack of detailed documentations and guidelines that infinitesimally describe the setup so researchers can reproduce them. In [101], a survey on evaluation approaches in wireless sensor networks, the authors illustrate that the proportion of experimental papers that allow the conditions of experiments to reproduce remains very low (< 11 %). The implementation constraints and the lack of reproducibility impede experimental approaches from leveraging generalizable results that can be extrapolated to draw statistically meaningful conclusions about large-scale deployments. Recently, researchers have started to focus on this issue, and efforts are put forward to design approaches and methodologies that could guide the reproducibility and the repeatability of experiment-based analyses in wireless ad-hoc networks [102][103].

The second approach, which relies on discrete-time simulators, has been widely used to: evaluate LoRaWAN data extraction rate and energy consumption [104, 105, 106, 107, 108, 109], assess and enhance LoRa rate control scheme [110, 111, 112, 113, 114, 115], and explore alternative medium access techniques [116, 117]. In [118], the authors survey and compare different open-source discrete-time simulators used for LoRa/LoRaWAN performance assessment. The most used simulators are *LoRaSim*, *FLORA*, and *NS-3* [118]. *LoRaSim* was first proposed in

[104] as a custom-built simulator implemented based on *SimPy* to evaluate two metrics; data extraction rate and network energy consumption. Multiple attempts have, since then, followed to improve and extend it [114, 115, 117, 119, 120]. In [113], *FLoRa*, an open-source simulator based on *OMNeT++* is presented and used to evaluate LoRa link adaptation mechanism. In [121], *FLoRa* was leveraged to examine the scalability of LoRa networks in rural and urban environments. Alternatively, LoRa/LoRaWAN modules have been also developed in *NS-3* [108, 109, 116]. Simulation-based approaches are known for their flexibility to test different setups. However, this flexibility often comes with long running times and heavy computational resources, making them onerous to reproduce.

Alternatively, analytical approaches are a third category of interest in modelling and analysing the performance of LoRa networks. Analytical approaches are particularly useful in evaluating different network configurations while being, unlike discrete-time simulations, time-saving. Therefore, they enable the understanding of the inter-plays between various system parameters. Such understanding provides guidelines to select optimal operational regimes for large-scale networks which are, otherwise, challenging to analyse using simulations or experiments. The main challenge for analytical approaches is balancing tractability and accuracy. An analytical model can be perfectly accurate yet too complex to derive meaningful statistical measures useful for analysing the network performance trends. At the same time, a tractable model requires assumptions and conceptual choices that could not perfectly shape the modelled technology or protocol. Thus, modelling tools need to be appropriately selected, and assumptions need to be judiciously made in the pursuit of such a balance.

Various analytical frameworks have been devised to study different aspects related to LoRa's performance [122, 123, 124, 125, 126, 127, 128, 129, 130, 131, 132, 133, 134, 135, 136, 137, 138, 139, 140]. These frameworks rely often on different fields of probability theory. Using a classic probability-based approach relying essentially on an elementary evaluation of the distributions, LoRa throughput has been analysed for both single-gateway [122, 123] and multi-gateway [124] topologies. In [125], the authors developed a mathematical model for LoRaWAN acknowledged

transmissions and extended it to account for LoRa capture capabilities in [126]. In [127], the authors used the results of their work [84] to devise a scalability framework that jointly incorporates noise-limited and interference-limited coverage regions. To maintain the tractability of their elementary formulations, research works relying on classic (*Geometry-less*) probability-based approaches often simplify the studied use case by considering only two or a few concurrently transmitting nodes. They also tend to combine interference into a single random variable [141] neglecting, therefore, important parameters such as the geometry of the network, the distance of the nodes to their serving gateways, the fading, etc. In the next section, we will further expand the analytical approaches that specifically use the concept of geometric probability, namely stochastic geometry, which has emerged as a compelling paradigm to model and analyze different types of wireless networks. The usefulness and technical background of stochastic geometry have been detailed in Section. 1.5.

3.4 Stochastic Geometry for LoRa Networks Scalability Analysis

There is particularly a growing body of literature focusing on coverage analysis and SF allocation recalling tools from stochastic geometry [128, 129, 130, 131, 132, 133, 134, 135, 136, 137, 138, 139, 140]. However, most of these studies [128, 129, 130, 132, 134, 135, 139] assume perfect SF-orthogonality and exclusively limit their investigations to the impact of interference from the nodes using the same SF. From this perspective, a LoRa network can be interpreted as the aggregation of independent sub-networks, each operating in a different SF. Under the perfect orthogonality assumption, the scalability of a single-gateway LoRa network in terms of coverage probability was studied in [128]. The outage condition in [128] was formulated based only on the dominant interfering signal to simplify the analytical burden. The work in [129] leveraged the concept of Poisson rain process [142], where a node is born to perform a transmission and dies immediately after

and proposed a space-time density to study a single gateway network under only co-SF interference. In [130], the performance of multi-gateway LoRa networks coexisting with other unlicensed radio technologies were studied in terms of coverage probability and area spectrum efficiency using only six nodes per cluster. Similarly, [131] studied LoRa performance when coexisting with an underlying IoT network. SG has been further recalled to design optimal annuli-based division of the network [132], to study the energy efficiency of LoRa networks [133], to explore energy harvesting opportunities in LoRa networks [135] and to evaluate alternative random access schemes such as *Time Division Multiple Access* (TDMA) and *Carrier Sense Multiple Access* (CSMA) [140]. While the focus of [128, 129, 130, 131, 132, 133] was uniform LoRa deployments, the authors in [134, 135] choose to investigate the performance of non-uniform deployments respectively in single-gateway and multi-gateway typologies, yet always under the perfect orthogonality assumption.

Fewer studies tackled LoRa performance while accounting for the impact of the same and different SFs. In [136, 137], the performance of a single-gateway LoRa network under imperfect orthogonality was studied. [137] has the advantage of accounting for interference time dependence through a formulated collision time distribution based on the difference between uniform start times. In [138], the authors modelled a multi-gateway LoRa network using two different cluster processes: MCP and Matérn hard-core Process and studied the network performance under both assumptions of orthogonality (perfect and imperfect) without taking into account the partial temporal overlap between the asynchronous LoRa transmissions. However, most of the works which run their investigations under an imperfect orthogonality assumption used in their outage probability formulations, disjoint (SNR, SIR) conditions with specific co-subchannel rejection thresholds between each two SFs. Such outage formulation neglects the correlation between SNR and SIR as it conjectures that the SIR thresholds remain the same regardless of the noise level. Furthermore, considering these constant restrictive SIR thresholds implicitly assumes that the desired packet is overlapped with a single interfering SF. This assumption is far to be realistic since a LoRa gateway can receive multiple packets coming from devices using various SFs.

Two more concerns can be raised regarding these co-rejection thresholds. First, they are empirical, not unique and heterogeneous among different research papers in the literature. Indeed, the thresholds presented in [143] were derived and empirically validated for the case of only one interferer and were adopted in [138]. Different thresholds were obtained in [54] and were used in [137]. Second, considering the interference from only one SF-packet can overlook and underestimate LoRa capture capabilities.

For simplification reasons, LoRa scalability analysis and performance optimisation are often carried out assuming static SF allocations that can be either distance-dependant [128, 129, 131, 132, 133, 134, 135, 136, 137, 138], or distance-independent [144, 145, 146]. The first category divides the cell into a set of annuli using specific geometric layouts such as *Equal-Interval-Based* (EIB), *Equal-Area-Based* (EAB), Pathloss-Based, Power-Based etc..., and assigns SFs incrementally as we move outwards away from the cell center. The second category follows probabilistic distributions where the SFs are attributed randomly to the nodes and independently from their distances to the gateway. The concern raised by such static distributions is whether they reflect the arrangement of nodes in practical deployment scenarios. We can take the example of a device deployed near a LoRa gateway that may experience higher channel variations due to surrounding buildings or vegetation. The same device can also be subject to more aggressive interference depending on the concurrently transmitting nodes and their communication parameter settings (power, SF, CR, etc...). As a result, the node needs to increment its SF to improve packet reception by the gateway. Due to the mathematical complexity involved, dynamic rate/SF is typically evaluated by simulations [110, 111, 112] which are time-consuming and fail to provide much insight into network design.

Using the static SF distributions described above, most research efforts focus on spatial coverage analysis [128, 129, 132, 134, 135, 137, 138] and ignore the temporal component of the node traffic. That is, the spatial coverage analysis assumes randomly deployed LoRa nodes with *saturated data buffers*. Such assumptions fail to track the node protocol state; the temporal evolution of packet generation,

accumulation, departure, and, moreover, the possibility of several retransmission attempts. Further, DC imposed by regulations is often overlooked. Temporal traffic dynamics are typically characterised using DTMC. In the next section we examine the body of literature where DTMC models are leveraged to study LoRadevice-level behaviours.

3.5 DTMC for LoRa Device Modelling

A small body of LoRa/LoRaWAN literature involves temporal dynamics where DTMC models are leveraged to characterize and analyse metrics such as throughput, latency, energy, and / or to propose optimised transmission policies for LoRa nodes [147, 148, 149, 150, 151]. The work in [147] analyzed the MAC-layer performance of class-A LoRaWAN devices where LoRa is approximated as a multi-channel Aloha. Along the same line, [148] analysed the throughput and delay of slotted Aloha-based LoRa. The trade-off delay / energy in class A LoRa devices was investigated in [149]. The authors in [150] proposed a DTMC to optimize the performance of class-A LoRaWAN devices while accounting for DC regulatory constraints. A discrete period of one hour was used in the proposed DTMC and LoRa DC was interpreted as a commodity that is recharged during the node sensing cycle and consumed during packet transmission. In [151], the authors proposed a DTMC to estimate the delay of confirmed downlink frames in a Class B LoRaWAN device.

The main limitation of such DTMC-standalone models is that they are often based on simplified collision models that neglect LoRa physical features and the network spatial parameters (e.g. capture effect, nodes density, fading, network geometry, and mutual interference). For instance, the analysis carried out [147, 148] assumed perfect orthogonality between LoRa SFs. Such an assumption implies that only packets transmitted with the same SF collide. This perception of a LoRa network fails to represent the real interplay between SFs that are, in reality, not perfectly orthogonal. The assumption of perfect orthogonality adopted in [147, 148] has been shown to overestimate the network performance by making the

coverage analysis optimistic. Further, treating LoRa like Aloha [147, 148, 149, 150, 151] where collision means packet loss overlooks LoRa capture capabilities. LoRa capture effect is the ability of a LoRa gateway to still, under some conditions, recover a LoRa signal even when it suffers from collisions.

A second constraint of these approaches is that they tend to be node-centric, as they propose either to analyse the performance of a single device regardless of its environment or to consider a very limited number of concurrently existing devices (up to 10 in [148]). Such environment-unawareness would question the validity of the analysis for larger-scale deployments especially that by mission LoRa is intended for massive connectivity scenarios. Following this node-centric approach, [148, 149, 150] neglected the physical layer attributes such as the channel conditions, the distance to the gateway, and interference coming from concurrently transmitting nodes. Added to the physical layer obliviousness and the environment-unawareness, the approaches adopted in [148, 149, 150] assumed buffer-less devices. This restrictive and less realistic assumption implies that sensed data during the node's duty cycle state will not be queued but discarded and lost.

3.6 Chapter Summary

In this chapter, we have reviewed LoRa/LoRaWAN state-of-the-art and related work. With a thorough exploration of the LoRa/LoRaWAN state-of-the-art, a number of research gaps that merit being further investigated can be pointed-out.

First, we notice that there is no consensus about LoRa modulation nomenclature. Some researchers tend to use it interchangeably with the *Chirp Spread Spectrum* (CSS) modulation [54, 88, 152], which is quite different as it is not necessarily band-limited compared to LoRa modulation. Some other researchers refer to it as chirp modulation [90] or frequency modulation [153], or wide-band linear frequency modulation [95], and some others assigned to it novel names such as frequency shift chirp modulation (FSCM) [77]. Likewise, the description of LoRa

is heterogeneous across the literature. Initially, it was treated as an orthogonal modulation. Then, as LoRa's orthogonality started to be questioned, new attributes have emerged "imperfect", "quasi", and "pseudo" orthogonal to describe it. Yet no research has clearly quantified *"How orthogonal is LoRa modulation?"*. Thus, a comprehensive description of LoRa waveforms, a rigorous analysis of its signal theory and a characterisation of its orthogonality are required to delineate its behaviours. Enabling, therefore, a better understanding of the technology's expected performance when it is adopted in real deployments.

A second category of research gaps concerns LoRa scalability analyses and enhancements. Characterising LoRa network scalability restrictively in terms of the number of supported end devices overlook the traffic dynamics of the nodes, the evolution of the packets in the device buffer, and the possibility of retransmissions. A comprehensive scalability analysis framework should account for various random factors in the network and capture both its spatial and traffic dynamics. Likewise, it should capture different LoRa physical features as well as the regulatory constraints LoRa devices are subject to. Capturing spatial and temporal dynamics allows us to cover a more comprehensive array of network performance KPIs and analyse their trade-offs. Further, static SF allocations have been widely adopted in the scalability analytical frameworks, which is not the case for dynamic adaptive allocation. To the best of our knowledge, no spatiotemporal analytical frameworks have been leveraged to analyse dynamic LoRa networks with adaptive SF.

Addressing these gaps is essential towards wide adoption of LoRa in the IoT industries. With this intention, the next chapters' research efforts have been carried out. Chapter. 4 addresses the first category of research gaps while Chapter. 5, Chapter. 6, Chapter. 7 focus on the second category.

CHAPTER 4

LoRa Modulation: Waveforms Properties and Orthogonality Conditions

4.1 Motivation and Contribution

With a closed physical layer and an open-standard upper layer, LoRa forms a quasi-closed ecosystem that has attracted growing interest and spurred researchers' efforts to explore this technology, reveal its unknown facts, and testify whether it holds its performance promises claimed by the technology owners. To this end, as detailed in Section. 3.2, several research works have proposed to reverse-engineer LoRa [143, 154, 155, 156], and analyse its performance in terms of Bit error statistics under different channel conditions [82, 83, 84, 85, 87]. However, fewer of them have investigated the signal theory fundamentals. Yet, by restrictively assuming perfect orthogonality between the SFs [77, 78, 79], they steered their focus on the same spreading factor use-case, and none of them provided a theoretical characterisation of how different LoRa spreading factors are orthogonal. Such characterisation had remained untapped in the literature.

In this chapter, we propose to theoretically quantify the imperfect-orthogonality of different LoRa SFs in both continuous and discrete time under different cases of

displacements (temporal and frequency shifts) while accounting for different LoRa physical features like the bandwidth, the sampling rate, and the initial frequency. We delve into LoRa modulation and provide a deep, comprehensive analysis of its signal theory to answer the fundamental question about how orthogonal is LoRa modulation. The contribution to the knowledge of this chapter can be used in several ways. For instance, a proper characterisation of imperfect orthogonality between different LoRa SFs is crucial to understand the behaviour of LoRa systems and unveil the statistical impact the SFs have on each other's performance in events of collision and interference. Researchers can therefore evaluate the performance of LoRa networks more accurately and develop optimal resource allocation schemes and efficient transmission policies that minimise interference between different SFs. This concrete characterisation also plays a primordial role in identifying implementation scenarios where LoRa could be vulnerable to jamming and interception. The analysis proposed in this chapter can spark potential new directions for designing collision recovery techniques, leveraging constructive-interference-empowered transmissions, and devising more robust waveforms with improved security, *Spectral Efficiency* (SE), and *Energy Efficiency* (EE).

4.2 LoRa Waveforms and Properties

4.2.1 Technical Description of LoRa Modulation

Being a derivative of Chirp Spread Spectrum techniques, LoRa modulation relies on varying the frequency over time. The frequency is swept over the entire bandwidth $B = [f_{min}, f_{max}]$. That is, the frequency starts at an initial time t_0 from an initial frequency f_k and whenever the maximum frequency f_{max} is reached, it is wrapped to start from the minimum frequency f_{min}. This sweeping process is repeated until the transmission time of the symbol ends. Noting that the frequency sweeping ends at the same initial frequency f_k. The key parameter in LoRa modulation is

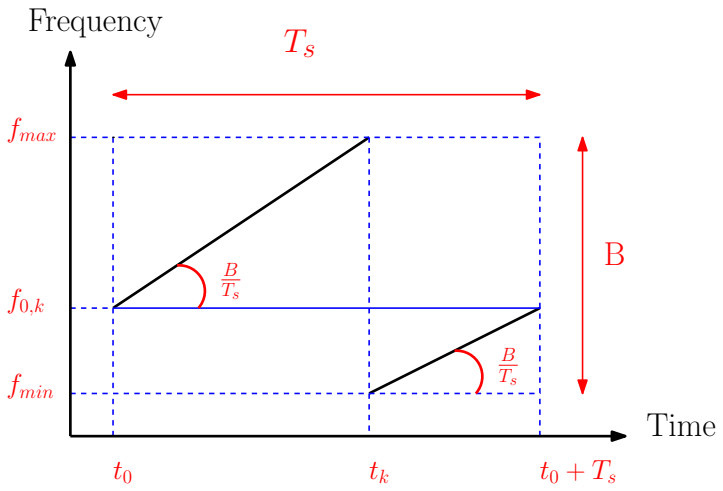

Fig. 4.1: Illustration of Up-Chirp LoRa Waveform.

the SF, an integer number belonging to the space $\{5, \ldots, 12\}$. The SF shapes the modulating signal by specifying the following parameters:

- **Symbol duration:** A symbol modulated with SF has a duration $T_s = 2^{\mathrm{SF}} \times T$ where $T = \frac{1}{B}$ is the chip rate.
- **Number of symbols:** A LoRa device transmitting at SF has 2^{SF} symbols $k \in \{0, 1, 2, \ldots, 2^{\mathrm{SF}} - 1\}$. Each symbol k conveys SF bits. These symbols are mapped to 2^{SF} chirps obtained by cyclically shifting the initial raw chirp. The chirp period is equal to the symbol duration.
- **Initial frequency:** The interval $[f_{min}, f_{max}]$ is discretised into 2^{SF} points, each associated to one of the 2^{SF} symbols. These discrete points define the initial frequency f_k expressed as $f_k = f_{min} + k\frac{B}{2^{\mathrm{SF}}}$
- **Shrink time:** The shrink time t_k defines the time point where the frequency reaches f_{max} and is wrapped to f_{min}. It is given by $t_k = T\left(2^{\mathrm{SF}} - k\right)$

To better understand the impact of the above parameters, let us examine Fig. 4.1 and Fig. 4.2. Fig. 4.1 depicts the frequency variation of a symbol $k \in \{0, 1, 2, \ldots, 2^{\mathrm{SF}} - 1\}$. It clearly illustrates the linear variation with time and the rollover when f_{max} is reached. Fig. 4.2 shows the spectrogram of a sequence of chirps corresponding to the symbols $\{0, 50, 75, 125\}$ modulated using SF= 7 and

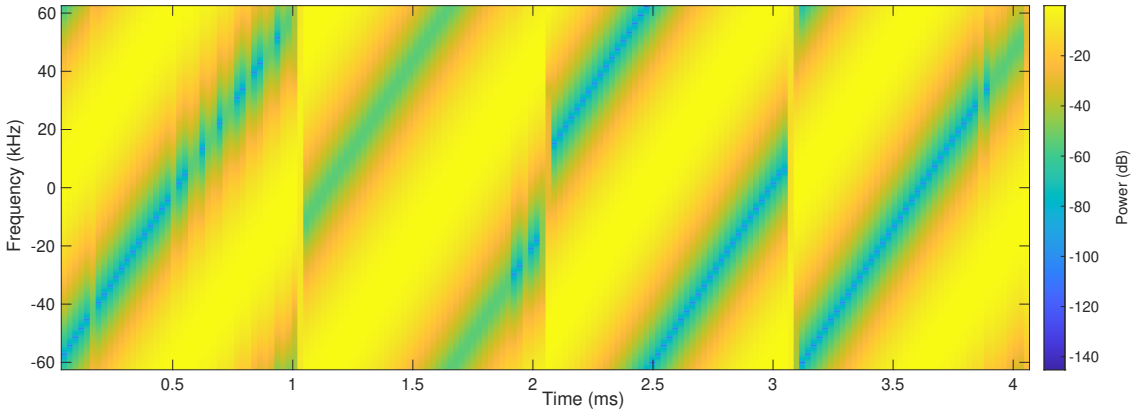

Fig. 4.2: Spectrogram of a LoRa symbols sequence $\{0, 50, 75, 125\}$ modulated with $\mathrm{SF}_1 = 7$ and $B = 125$ KHz.

$B = 125KHz$. The figure shows how the initial frequency and the shrink time vary with the symbol. We can also see how the frequency sweeping starts and ends at the same initial frequency.

4.2.2 LoRa Waveform in Continuous-Time Domain

To describe LoRa wavefrom expression in the time domain, we start, first, by formulating the instantaneous frequency and phase corresponding to symbol k swept over the interval $[0, B]$ during the time interval $[t_0, t_0 + T_s]$. The instantaneous frequency is given as:

$$f_k(t) = \begin{cases} f_{min} + \frac{B}{2^{\mathrm{SF}}}\left(\frac{t-t_0}{T} + k\right), & \text{if } 0 \leq t - t_0 \leq t_k, \\ f_{min} + \frac{B}{2^{\mathrm{SF}}}\left(\frac{t-t_0}{T} + k - 2^{\mathrm{SF}}\right), & \text{if } t_k \leq t - t_0 \leq T_s, \end{cases} \tag{4.1}$$

$$= f_{min} + \frac{B}{2^{\mathrm{SF}}} \mod \left(\frac{t - t_0}{T} + k, 2^{\mathrm{SF}}\right), \tag{4.2}$$

where $\mod(x, y)$ is the modulo operator that gives the rest of the integer division between x and y.

Given an initial phase $\phi_k(t_0) = 0$, the instantaneous phase is obtained by integrating the frequency over time which gives the following expression:

$$\phi_k(t) = \phi_k(t_0) + 2\pi \int_{t_0}^{t} f_k(\tau) d\tau = \begin{cases} 2\pi\left(f_{min} + \frac{B}{2^{\mathrm{SF}}}\left(\frac{t-t_0}{2T} + k\right)\right)(t - t_0), & \text{if } 0 \leq t - t_0 \leq t_k, \\ 2\pi\left(f_{min} + \frac{B}{2^{\mathrm{SF}}}\left(\frac{t-t_0}{2T} + k - 2^{\mathrm{SF}}\right)\right)(t - t_0), & \text{if } t_k \leq t - t_0 \leq T_s. \end{cases} \tag{4.3}$$

Property 4.1. *The instantaneous phase of the LoRa modulated continuous waveform has a memoryless property, only if* $f_{min} \propto \frac{1}{2^{SF}T}$*, i.e.*

$$\phi_k(t_0 + T_s) = 2\pi\left(f_{min} + \frac{B}{2^{SF}}\left(\frac{t_0 + T_s - t_0}{2T} + k - 2^{SF}\right)\right)(t_0 + T_s - t_0) = f_{min}2^{SF}T \mod 2\pi. \tag{4.4}$$

This follows from the fact that $\frac{B}{2^{SF}}\left(\frac{T_s}{2T} + k - 2^{SF}\right)T_s$ *is an integer since* $BT_s = 2^{SF}$*.*

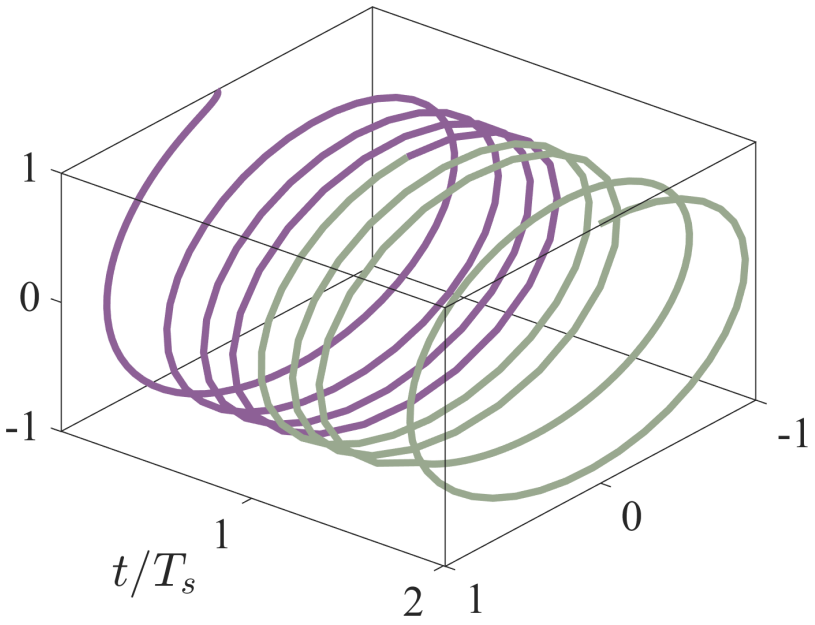

Fig. 4.3: Phase variation with time for two LoRa symbols modulated using the same SF with $f_{min} = 0$.

In Fig. 4.3 we visualised the variation in time of two consecutive symbols for $f_{min} = 0$. The graph illustrates the memoryless property as it shows how the phase starts and ends at the same value regardless of the symbol.

Using Eq. 4.3, the continuous waveform $s_k^C(t)$ corresponding to the k'th symbol of duration T_s is given by:

$$s_k^C(t) = \frac{1}{\sqrt{T_s}}e^{j\phi_k(t)} = \begin{cases} \frac{1}{\sqrt{T_s}}e^{2j\pi\left(f_{min}+\frac{B}{2^{SF}}\left(\frac{t-t_0}{2T}+k\right)\right)(t-t_0)}, & \text{if } 0 \le t - t_0 \le t_k, \\ \frac{1}{\sqrt{T_s}}e^{2j\pi\left(f_{min}+\frac{B}{2^{SF}}\left(\frac{t-t_0}{2T}+k-2^{SF}\right)\right)(t-t_0)}, & \text{if } t_k \le t - t_0 \le T_s. \end{cases} \tag{4.5}$$

Property 4.2. *If we assume that the transmitted symbols are independent and identically distributed* (i.i.d.) *with probability* $P(k) = \frac{1}{2^{SF}}$*, for* $k = 0, \ldots, 2^{SF} - 1$*, then the mean of the*

transmitted waveform using SF is:

$$E_k\left[s_k^{\mathcal{C}}(t))\right] = \frac{1}{2^{SF}} \sum_{k=0}^{2^{SF}-1} s_k^{\mathcal{C}}(t)$$
$$= \frac{e^{2j\pi\left(f_{min}+\frac{B}{2^{SF}}\left(\frac{t-t_0}{2T}+k_c-2^{SF}\right)\right)(t-t_0)}}{2^{SF}} \frac{e^{2j\pi B(t-t_0)}-1}{e^{2j\pi\frac{B}{2^{SF}}(t-t_0)}-1}, \tag{4.6}$$

where k_c is such that $t \leq T(2^{SF}-k_c)$. The absolute value of the mean is given by

$$|E_k[s_k^{\mathcal{C}}(t)]| = \frac{1}{2^{SF}} \left| \frac{\sin\left(\pi B(t-t_0)\right)}{\sin\left(\pi\frac{B}{2^{SF}}(t-t_0)\right)} \right|. \tag{4.7}$$

4.2.3 LoRa Waveform in Discrete-Time Domain

To obtain LoRa waveform in the discrete-time domain, the continuous waveform $s_k^{\mathcal{C}}(t)$ is sampled at a rate $1/T_d$. Choosing T_d to be equal to the chip rate T gives exactly 2^{SF} samples at time instants $t = nT$ where $n \in \{0, 1, \ldots, 2^{\mathrm{SF}}-1\}$. A higher sampling rate would provide $2^{\mathrm{SF}}\frac{T}{T_d}$ samples. The n'th sample of the continuous waveform $s_k^{\mathcal{C}}(t)$ is given by the following expression:

$$s_k^{\mathcal{D}}(nT_d) = \begin{cases} \frac{1}{\sqrt{2^{\mathrm{SF}}}} e^{2j\pi\left(f_{min}+\frac{B}{2^{\mathrm{SF}}}\left(\frac{nT_d-t_0}{2T}+k\right)\right)(nT_d-t_0)}, & \text{if } 0 \leq n\frac{T_d}{T} - \frac{t_0}{T} \leq 2^{\mathrm{SF}}-k-1, \\ \frac{1}{\sqrt{2^{\mathrm{SF}}}} e^{2j\pi\left(f_{min}+\frac{B}{2^{\mathrm{SF}}}\left(\frac{nT_d-t_0}{2T}+k-2^{\mathrm{SF}}\right)\right)(nT_d-t_0)}, & \text{if } 2^{\mathrm{SF}}-k \leq n\frac{T_d}{T} - \frac{t_0}{T} \leq 2^{\mathrm{SF}}-1. \end{cases} \tag{4.8}$$

Special Cases: Below are few special cases for which the expression in Eq. 4.8 is further simplified:

- $T_d = T$ and t_0 is a multiple of T, i.e. $t_0/T = m_0$

$$s_k^{\mathcal{D}}(nT) = \frac{1}{\sqrt{2^{\mathrm{SF}}}} e^{2j\pi f_{min}(n-m_0)T} e^{2j\pi\left(\frac{n-m_0}{2}+k\right)\frac{n-m_0}{2^{\mathrm{SF}}}}. \tag{4.9}$$

- $T_d = T$, $t_0/T = m_0$, and f_{min} is a multiple of B

$$s_k^{\mathcal{D}}(nT) = \frac{1}{\sqrt{2^{\mathrm{SF}}}} e^{2j\pi\left(\frac{n-m_0}{2}+k\right)\frac{n-m_0}{2^{\mathrm{SF}}}} \tag{4.10}$$

.

4.3 LoRa Cross-Correlation Functions

In this section, we propose to derive, in both continuous and discrete time domains, the cross-correlation between two LoRa waveforms transmitting two symbols k_1 using SF_1, and k_2 using SF_2 over bandwidths B_1 and B_2, respectively. The symbol transmission times and the chip rates are respectively $T_{s,j}$ and $T_j = 1/B_j$, with $j = 1, 2$. The starting frequencies of symbols k_1 and k_2 are f_1 and f_2, respectively. Noting that the SFs play interchangeable roles. So, for clarity and without loss of generality, we take $SF_1 < SF_2$ and $SF_2 = SF_1 + s$, with $s \in \{1, \ldots, 7\}$. Our aim is to derive tractable expressions of the cross-correlation functions, analyse their properties, and examine the conditions ensuring orthogonality. Before delving into the technical formulations we recall the two following definitions:

- **Auto-correlation:** Auto-correlation is a statistical metric that measures the degree of similarity between a signal and its delayed version. Considering a continuous periodic signal $x(t)$ of period T, the auto-correlation of $x(t)$ is expressed as:

$$\mathcal{R}_{xx}(\tau) = \int_{t_0}^{t_0+T} x(t)\,(x(t-\tau))^*\,dt.$$

- **Cross-Correlation:** Cross-correlation is a statistical metric that measures the degree of similarity between two signals. For two continuous periodic signals $x(t)$ and $y(t)$ of periods T, the cross-correlation is expressed as:

$$\mathcal{R}_{xy}(\tau) = \int_{t_0}^{t_0+T} y(t)\,(x(t-\tau))^*\,dt.$$

4.3.1 Continuous-Time Domain

First, we study the continuous time domain. The cross-correlation function between the two continuous waveforms is defined as:

$$\mathcal{R}^{C}_{k_1,k_2}(\tau, f_d) = \int_{t_0+\tau}^{t_0+T_{s,1}} s^{C}_{k_1}(t)\left(s^{C}_{k_2}(t-\tau)\right)^*\,dt. \tag{4.11}$$

where τ is the time delay (TD) and f_d is the frequency differential shift (DFS) between the starting frequencies, i.e. $f_d = f_2 - f_1$.

Theorem 4.1. *The cross-correlation between two continuous transmitted waveforms is obtained as (4.12),*

$$\mathcal{R}^{\mathcal{C}}_{k_1,k_2}(\tau, f_d) = \begin{cases} \mathcal{K}_{a_{12}}\left(b_{k_1,k_2} - B_1, \tau, T_{s,1}\right), \\ \quad if \quad t_{k_1} \le \tau < T_{s,1} \le \tau + t_{k_2}, \\ \mathcal{K}_{a_{12}}\left(b_{k_1,k_2} - B_1, \tau, \tau + t_{k_2}\right) + e^{-2j\pi B_2 \tau}\mathcal{K}_{a_{12}}\left(b_{k_1,k_2} - B_1 + B_2, \tau + t_{k_2}, T_{s,1}\right), \\ \quad if \quad t_{k_1} \le \tau < \tau + t_{k_2} < T_{s,1}, \\ \mathcal{K}_{a_{12}}\left(b_{k_1,k_2}, \tau, t_{k_1}\right) + \mathcal{K}_{a_{12}}\left(b_{k_1,k_2} - B_1, t_{k_1}, T_{s,1}\right), \\ \quad if \quad \tau < t_{k_1} < T_{s,1} \le \tau + t_{k_2}, \\ \mathcal{K}_{a_{12}}\left(b_{k_1,k_2}, \tau, m_{k_1,k_2}(\tau)\right) \\ +e^{-2j\pi B_2 \tau u\left(t_{k_1} - \tau - t_{k_2}\right)}\mathcal{K}_{a_{12}}\left(b_{k_1,k_2} - B_c, m_{k_1,k_2}(\tau), M_{k_1,k_2}(\tau)\right)\mathbb{1}_{\{\left(t_{k_1} - \tau \neq t_{k_2}\right)} \\ +e^{-2j\pi B_2 \tau}\mathcal{K}_{a_{12}}\left(b_{k_1,k_2} - B_1 + B_2, M_{k_1,k_2}(\tau), T_{s,1}\right), \\ \quad if \tau < t_{k_1} \& \tau + t_{k_2} < T_{s,1}. \end{cases} \tag{4.12}$$

where

$$\mathcal{K}_{a_{12}}\left(b_{k_1,k_2}, t_1, t_2\right) = \begin{cases} \frac{e^{2j\pi c_{k_2}} e^{-j\pi \frac{b^2_{k_1,k_2}}{a_{12}}}}{\sqrt{T_{s,1}T_{s,2}}}\left[\operatorname{erf}\left(\sqrt{\frac{\pi a_{12}}{j}}\left(t_0 + t_2 + \frac{b_{k_1,k_2}}{a_{12}}\right)\right) - \operatorname{erf}\left(\sqrt{\frac{\pi a_{12}}{j}}\left(t_0 + t_1 + \frac{b_{k_1,k_2}}{a_{12}}\right)\right)\right], \\ \qquad if\, a_{12} \neq 0, \\ \frac{e^{2j\pi c_{k_2}} e^{j\pi b_{k_1,k_2}(2t_0 + t_1 + t_2)}}{\sqrt{T_{s,1}T_{s,2}}} sinc\left(\pi b_{k_1,k_2}(t_2 - t_1)\right)(t_2 - t_1), \\ \qquad if\, a_{12} = 0, \end{cases} \tag{4.13}$$

with the following intermediate variables defined for notation brevity: $\mu_j = \frac{B_j}{2^{SF_j}}$ *for* $j = 1, 2$, $a_{12} = \frac{\mu_1}{T_1} - \frac{\mu_2}{T_2}$, $b_{k_1,k_2} = f_1 + \mu_1 k_1 - f_2 - \mu_2 k_2 + \frac{\mu_2 \tau}{T_2}$, $c_{k_2} = \left(f_2 + \mu_2 k_2 - \frac{\mu_2 \tau}{2T_2}\right)\tau$, $m_{k_1,k_2}(\tau) = \min\left(t_{k_1}, \tau + t_{k_2}\right)$, $M_{k_1,k_2}(\tau) = \max\left(t_{k_1}, \tau + t_{k_2}\right)$, *and* $B_c = B_1 u\left(t_{k_2} + \tau - t_{k_1}\right) - B_2 u\left(t_{k_1} - t_{k_2} - \tau\right)$, $u(\cdot)$ *is the step function, and* $\mathbb{1}(\cdot)$ *is the indicator function.*

Proof. The proof is in Appendix Section. A.1 □

Special Cases: Below are few special cases for which the general expression in Eq. 4.12 is further simplified:

- **Same SF with no TD and with DFS:** If $\mathrm{SF}_1 = \mathrm{SF}_2 = \mathrm{SF}$, $B_1 = B_2 = B$, $\tau = 0$, and $f_d \neq 0$, the cross correlation function becomes:

$$\mathcal{R}^{C}_{k_1,k_2}(0, f_d) = \frac{e^{\frac{2j\pi}{2^{\mathrm{SF}}}\left(k_1-k_2-\frac{f_d 2^{\mathrm{SF}}}{B}\right)\left(\frac{t_0}{T}+2^{\mathrm{SF}}\right)}}{2j\pi}\left[\frac{1-e^{2j\pi\frac{f_d 2^{\mathrm{SF}}}{B}}}{k_1-k_2-\frac{f_d 2^{\mathrm{SF}}}{B}}\right. \tag{4.14}$$
$$\left.+\left(e^{-\frac{2j\pi}{2^{\mathrm{SF}}}\left(k_1-k_2-\frac{f_d 2^{\mathrm{SF}}}{B}\right)k_2}-e^{-\frac{2j\pi}{2^{\mathrm{SF}}}\left(k_1-k_2-\frac{f_d 2^{\mathrm{SF}}}{B}\right)k_1}\right)\left[\frac{\kappa_0}{k_1-k_2-\frac{f_d 2^{\mathrm{SF}}}{B}}-\frac{e^{2j\kappa_0\pi\frac{t_0}{T}}}{2^{\mathrm{SF}}+\kappa_0\left(k_1-k_2-\frac{f_d 2^{\mathrm{SF}}}{B}\right)}\right]\right].$$

- **Same SF with no TD and no DFS:** If $\mathrm{SF}_1 = \mathrm{SF}_2 = \mathrm{SF}$, $B_1 = B_2 = B$, $\tau = 0$, and $f_d = 0$, the cross correlation function scales down to:

$$\mathcal{R}^{C}_{k_1,k_2}(0,0) = \frac{e^{\frac{2j\pi}{2^{\mathrm{SF}}}(k_1-k_2)\left(\frac{t_0}{T}-k_1\right)}}{2j\pi}\left[\frac{e^{2j\pi\kappa_0\frac{t_0}{T}}}{2^{\mathrm{SF}}-|k_1-k_2|}+\frac{1}{|k_1-k_2|}\right]\left(1-e^{\frac{2j\pi}{2^{\mathrm{SF}}}(k_1-k_2)^2}\right), \tag{4.15}$$

  with $\kappa_0 = \frac{k_2-k_1}{|k_2-k_1|}$.

Corollary 4.1. *The argument of the cross-correlation between two continuous waveforms modulated using the same SF with no time delay and no differential frequency shift is equal to*

$$|\mathcal{R}^{C}_{k_1,k_2}(0,0)| = \frac{2^{SF}}{\pi}\frac{|\sin\left(\pi\frac{(k_1-k_2)^2}{2^{SF}}\right)|}{|k_1-k_2|\,(2^{SF}-|k_1-k_2|)} \tag{4.16}$$

and $\mathcal{R}^{C}_{k_1,k_2}$ is upper-bounded by $\frac{1}{\pi\left(\sqrt{\frac{2^{SF}}{2}}-\frac{1}{2}\right)}$ for $k_1 \neq k_2$, i.e:

$$\max_{k_1\neq k_2}|\mathcal{R}^{C}_{k_1,k_2}(0,0)| = \frac{1}{\pi\left(\sqrt{\frac{2^{SF}}{2}}-\frac{1}{2}\right)} \tag{4.17}$$

Proof. Examining Eq. 4.16, we can see that $|\mathcal{R}^{C}_{k_1,k_2}(0,0)|$ is symmetric around $\frac{2^{\mathrm{SF}}}{2}$. The numerator of Eq. 4.16 is an increasing function with respect to $|k_1 - k_2|$ whenever we have one of these conditions

$$\sqrt{2^{\mathrm{SF}}l} < |k_1-k_2| < \sqrt{2^{\mathrm{SF}}\left(l+\frac{1}{2}\right)},$$
$$\text{for } l = 0, 1, 2, \ldots, 2^{\mathrm{SF}}-5.$$

Otherwise, it is a decreasing function. The maximums of the numerator of Eq. 4.16 happens at

$$|k_1 - k_2| = \left\lfloor \sqrt{2^{\mathrm{SF}}\left(l + \frac{1}{2}\right)} \right\rfloor, \text{ for } l = 1, 2, 3, \ldots, 2^{\mathrm{SF}} - 3.$$

Also, the denominator of Eq. 4.16 is an increasing function for $0 \leq |k_1 - k_2| \leq 2^{\mathrm{SF}}/2$, and a decreasing function for $2^{\mathrm{SF}}/2 \leq |k_1 - k_2| \leq 2^{\mathrm{SF}} - 1$. So, the maximum of $|\mathcal{R}^{\mathcal{C}}_{k_1,k_2}(0,0)|$ should happen at $|k_1 - k_2| = \left\lfloor \sqrt{\frac{2^{\mathrm{SF}}}{2}} \right\rfloor$ and $|k_1 - k_2| = 2^{\mathrm{SF}} - \left\lfloor \sqrt{\frac{2^{\mathrm{SF}}}{2}} \right\rfloor$ □

Noting that the maximum is upper-bounded by 0.0909 for SF = 5, . . . , 12, and asymptotically vanishes as SF increases.

$$\frac{1}{\pi\left(\sqrt{\frac{2^{\mathrm{SF}}}{2}} - \frac{1}{2}\right)} \underset{SF=5\rightarrow 12}{=} \left[9.09, 6.17, 4.24, 2.94, 2.05, 1.44, 1.01, 0.71\right] \times 10^{-2}$$

4.3.2 Discrete-Time Domain

Next, we tackle the cross-corrleation between different SFs in the discrete time domain. We consider the sampling time T_d and we define the following shorthand parameters $B_1 = 2^{s_1}/T_d$, $B_2 = 2^{s_2}/T_d$, $m_0 = \frac{t_0}{T_d}$, and $m_1 = \frac{\tau}{T_d}$. For clarity and without loss of generality, we take $\mathrm{SF}_2 = \mathrm{SF}_1 + s_3$.

Theorem 4.2. *The cross correlation between two discrete waveforms modulated with different SFs is:*

$$\mathcal{R}^{\mathcal{D}}_{k_1,k_2}(\tau, f_d) = \begin{cases} \frac{e^{2j\pi c_{k_2}} e^{-j\pi a_{12}\left(\frac{b_{k_1,k_2}}{a_{12}}\right)^2}}{\sqrt{2^{SF_1} 2^{SF_2}}} \sum_{n'=m_1}^{2^{SF_1 - s_1} - 1} e^{j\pi a_{12}\left(n'T_d + \frac{b_{k_1,k_2}}{a_{12}}\right)^2}, & \text{if } a_{12} \neq 0, \\ \frac{e^{2j\pi c_{k_2}} e^{2j\pi b_{k_1,k_2} T_d m_1}}{\sqrt{2^{SF_1} 2^{SF_2}}} e^{j\pi\left(2^{SF_1 - s_1} - m_1 - 1\right) b_{k_1,k_2} T_d} & \\ \times \sin\left(\pi\left(2^{SF_1 - s_1} - m_1\right) b_{k_1,k_2} T_d\right) cosec\left(\pi b_{k_1,k_2} T_d\right), & \text{if } a_{12} = 0 \& b_{k_1,k_2} \neq 0, \\ \frac{e^{2j\pi c_{k_2}}}{\sqrt{2^{SF_1} 2^{SF_2}}} \frac{T_{s,1} - \tau}{T_d}, & \text{if } a_{12} = 0 \& b_{k_1,k_2} = 0, \end{cases} \tag{4.18}$$

Proof. The proof is in Appendix Section. A.2.

□

Corollary 4.2. *If both symbols are i.i.d., the mean of the cross correlation between two discrete transmitted waveforms with different SFs is:*

$$E_{k_1,k_2}\left[\mathcal{R}^{\mathcal{D}}_{k_1,k_2}\right] = \begin{cases} \frac{1}{\sqrt{2^{SF_1}2^{SF_2}}}, & \text{if } \tau = 0, \\ 0, & \text{if } \tau \neq 0. \end{cases} \tag{4.19}$$

Property 4.3. *The energy or the auto-correlation of the discrete waveforms is given by*

$$R_{k,k} = E_k = \sum_{n=m_0}^{2^{SF}+m_0-1} s^{\mathcal{D}}_k(nT)\left(s^{\mathcal{D}}_k\right)^*(nT) = 2^{SF}. \tag{4.20}$$

From Eq. 4.20, we can see that the energy is independent of the symbol.

4.4 LoRa Cross-Correlation Factors Analysis

4.4.1 Maximum, Mean, and CDF

In this subsection, we study the maximum, mean and CDF of the cross-correlation calculated using the expressions formulated in Section. 4.3. The analytical results have been further validated numerically. For the sake of more readability, a summary of the numerical values is also provided as tables in Section. A.3.

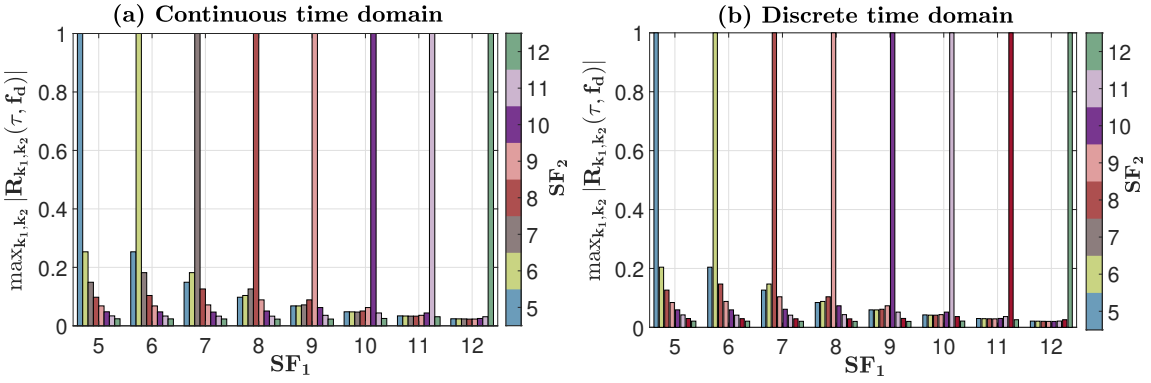

Fig. 4.4: Maximum of cross-correlation factors between SFs in the continuous/discrete time domains with $\tau = 0$ and $f_d = 0$.

In Fig. 4.4, we plot the maximum of the cross-correlation functions in the continuous and discrete time domain for $\tau = 0$ and $f_d = 0$. The figure shows that

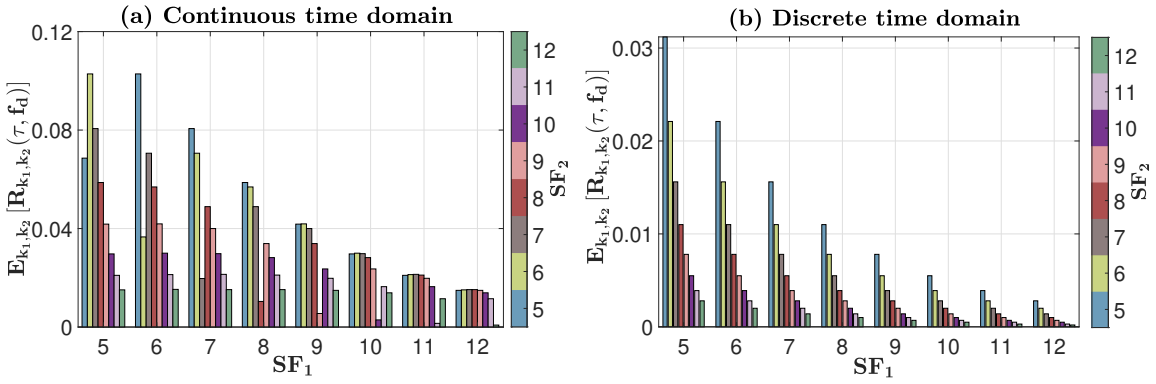

Fig. 4.5: Mean of cross-correlation factors between SFs in the continuous/discrete time domains with $\tau = 0$ and $f_d = 0$.

in both time domains (continuous and discrete), the maximum cross-correlation between the same SFs is more significant than the maximum cross-correlation between different SFs. Noting that the maximum cross-correlation for the same SF happens when the same symbol is transmitted, i.e. $k_1 = k_2$. It is also shown that the maximum cross-correlation decreases as the SF increases, which makes lower SFs more impactful. The closer SF_2 is to SF_1, the higher is its maximum cross-correlation. We notice that the maximum cross-correlation has slightly decreased in the discrete-time domain compared to the continuous-time domain. This decrease can be explained by the sampling time not being infinitesimally small enough to apply the Riemann integral, approximating the integrals by a sum expression for infinitesimally small steps.

In Fig. 4.5, we plot the mean of the cross-correlation functions between SFs in the continuous and discrete time domain, with $\tau = 0$ and $f_d = 0$. The figure shows that the mean cross-correlation is higher in the continuous time domain than in the discrete-time domain. We can also observe that in the continuous time domain, the mean of cross-correlation, unlike the maximum, is in most of the cases higher between different SFs than between same SFs. The difference gap between the same and different SFs become even more noticeable as the SF increases. The SF that leads to the highest mean cross-correlation is $\mathrm{SF}_2 = \{6, 5, 5\}$ for $\mathrm{SF}_1 = \{5, 6, 7\}$, respectively. For the discrete time domain, the mean cross-correlation exhibits rather a consistent behaviour and decreases with the SF whether it is the same or different.

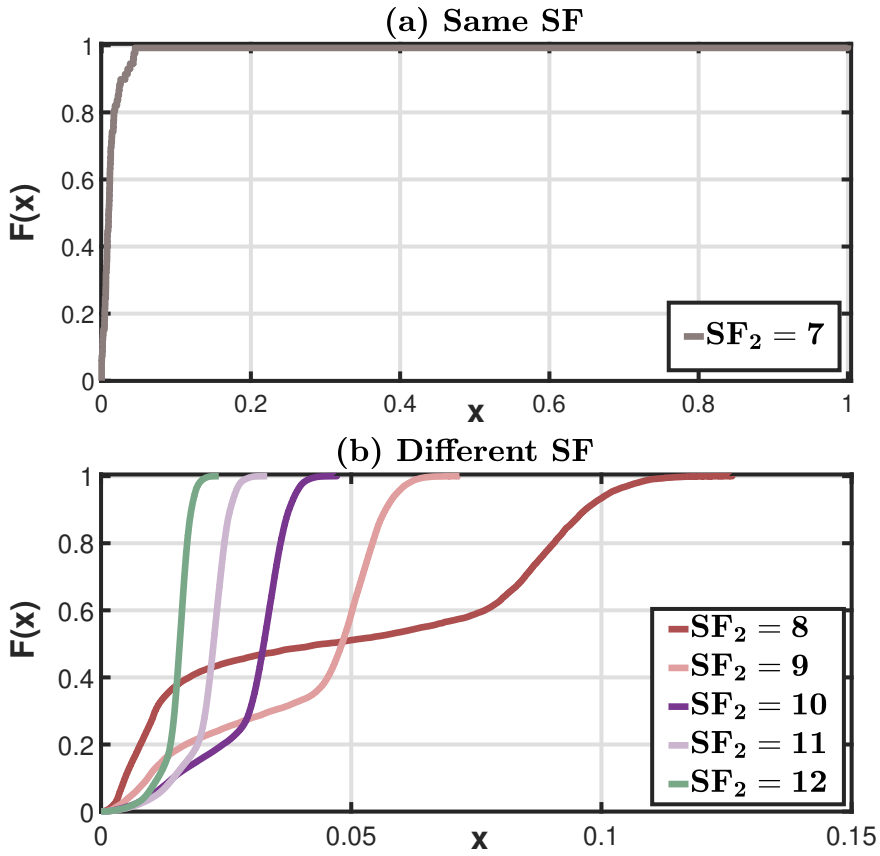

Fig. 4.6: Empirical Cumulative distribution function (ECDF) of the magnitude of cross-correlation in the continuous time domain for $SF_1 = 7$.

Fig. 4.6 shows the empirical cumulative distribution function (ECDF) of the cross-correlation magnitude in the continuous time domain for $SF_1 = 7$ and different SF_2. Examining Fig. 4.6, we can see that the probability of cross-correlation being higher than 0.04 is less than 3% for the same SF case. This observation can be explained by the fact that the cross-correlation reaches 1 for the same symbols; otherwise, the maximum cross-correlation is lower than 0.043 as it is further illustrated in Fig. 4.7. If we exclude the same symbol case, the cross-correlation values of $SF_1 = 7$ with different SFs spans a larger interval compared to the same SF case. These observations explain why we had the mean of cross-correlation of different SFs higher than that of same SF (see Fig. 4.5).

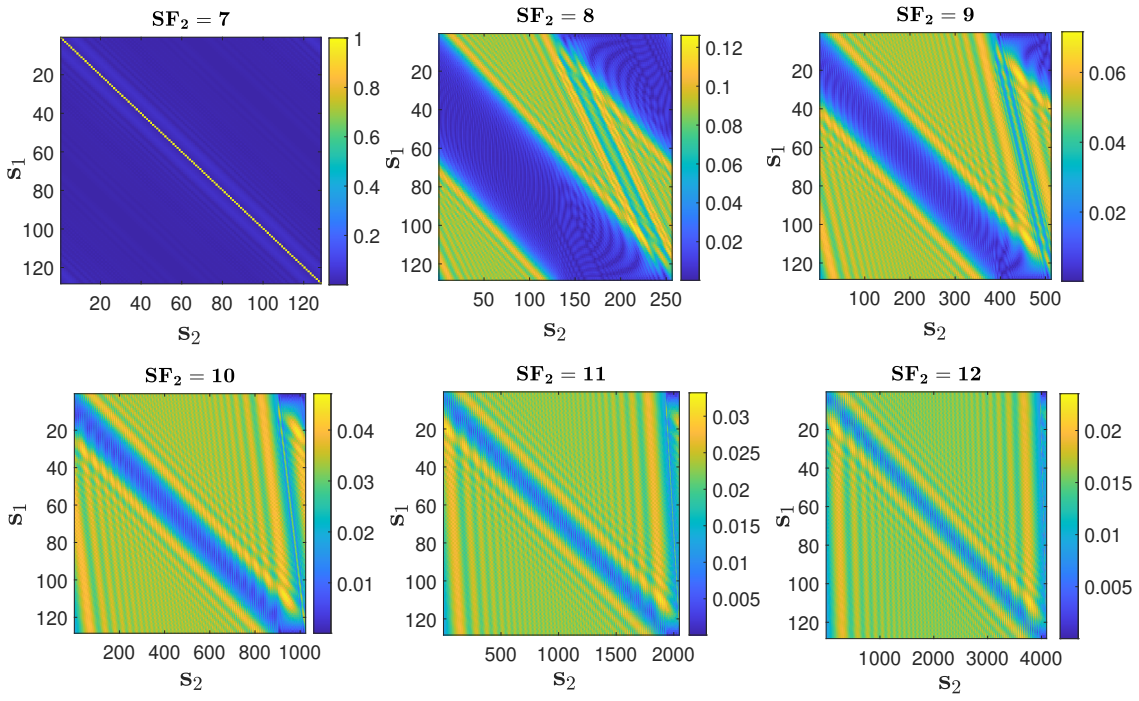

Fig. 4.7: Cross-Correlation factors for $SF_1 = 7$.

4.4.2 Impact of Bandwidth

In Fig. 4.8 and Fig. 4.9, we plot the maximum of the cross-correlation functions for different bandwidth values B_1 and B_2 in continuous and discrete time domains. We fixed the sampling rate for the discrete-time setup at $1/B_1$. Several interesting properties follow from the examination of these figures. Interestingly, in both time domains, the maximum cross-correlation is no longer the largest for the same SF. The SF leading to the highest maximum cross-correlation varies with the ratio $\frac{B_1}{B_2}$ as we obtain similar behaviours for the two pairs ($B_1 = 125$ kHz, $B_2 = 250$ kHz), and ($B_1 = 250$ kHz, $B_2 = 500$ kHz). If $B_2 > B_1$, the highest maximum cross-correlation occurs for $SF_2 = SF_1 + \frac{B_2}{B_1}$. Taking the example of $SF_1 = 5$ and $B_2 = 2 \times B_1$, the highest maximum cross-correlation is 0.7 and is obtained for $SF_2 = 7$ while the maximum cross-correlation of the remaining SF_2s is less than 0.4 (See Fig. 4.8 (a) and Fig. 4.9 (a)). If $B_2 < B_1$, the highest maximum cross-correlation is obtained for $SF_2 = \max\left(5, SF_1 - \frac{B_1}{B_2}\right)$ as it is shown in Fig. 4.8 (c), (d) and Fig. 4.9 (c), (d).

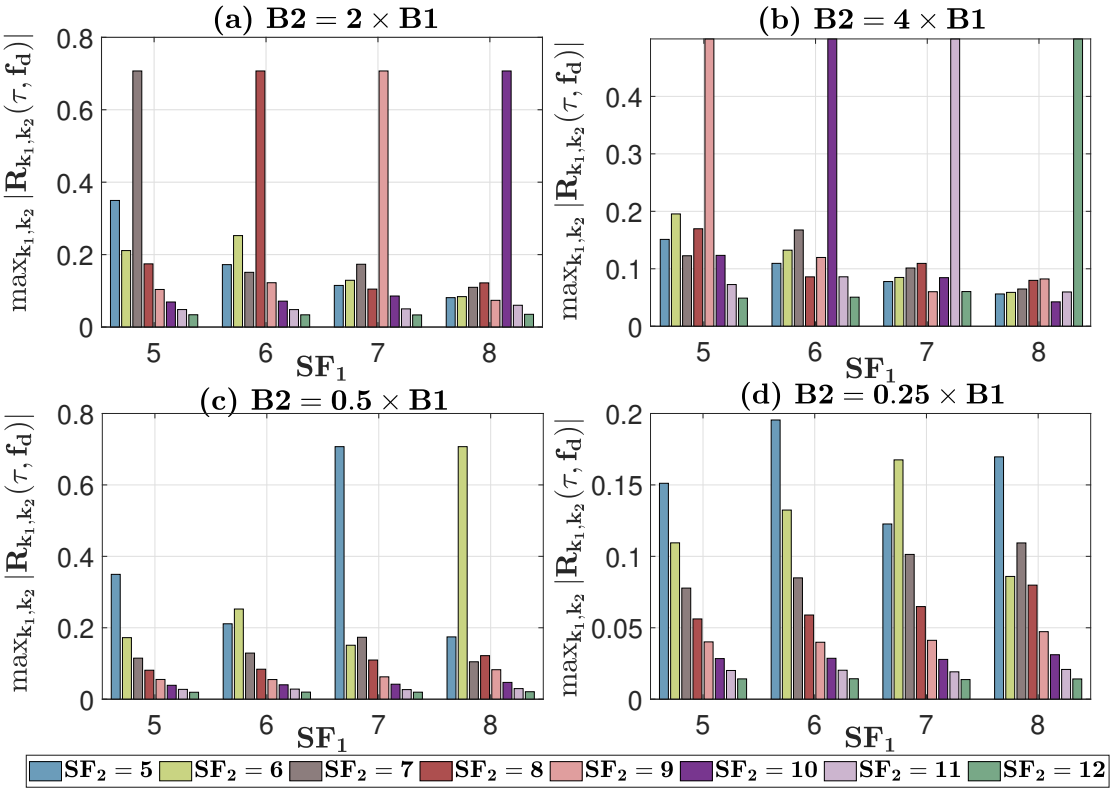

Fig. 4.8: Maximum of cross-correlation between SFs in continuous time domain with $\tau = 0$ and $f_d = 0$ for different B_1 and B_2.

4.4.3 Impact of Temporal Displacement

In Fig. 4.10, we plot the maximum of the cross-correlation functions versus the time delay for the same and different symbols in continuous and discrete time domains. We observe a couple of properties. From Fig. 4.10a and Fig. 4.10c, we find that for same symbols as the temporal displacement τ deviates from T_1, the maximum cross-correlation of different SFs becomes higher than that of same SFs in both continuous and discrete time domains. Two aspects worth analysing follow from this observation. First, the results illustrate LoRa resilience to multi-path fading where the gateway receives several time-shifted replicates of the main signal. Such resilience is particularly useful for outdoor urban environments or indoor environments where the signal is scattered from people, furniture, etc. Such observation further supports and motivates the adoption of LoRa not only for outdoor but also for indoor scenarios as it can be a promising alternative to WiFi/Bluetooth for smart home applications. Second, the results

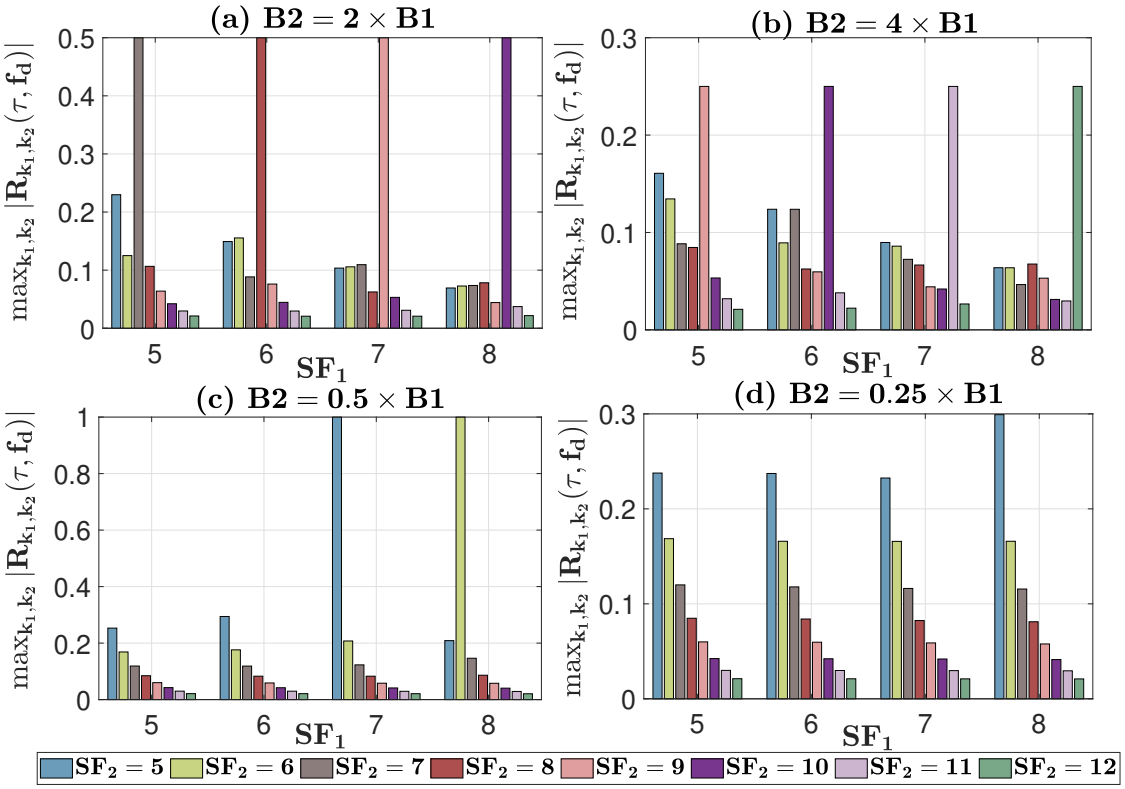

Fig. 4.9: Maximum of cross-correlation factors between SFs in discrete time domain with $\tau = 0$ and $f_d = 0$ for different B_1 and B_2.

prove that creating a constructive interference with the same SF requires perfect synchronisation between the two signals with a maximum temporal displacement of $T_1 = \frac{1}{B1}$.

For the same symbols modulated with different SFs, the maximum cross-correlation increases reaches a saturation that remains consistent over time, and then drops. This saturation is similarly observed for different symbols modulated using different SFs where the maximum cross-correlation follows the same values as the zero time delay scenario, up to a certain τ threshold that varies with the SF. These observations confirm that the results of maximum cross-correlation with zero delay can be extrapolated to study the performance of asynchronous transmissions. For different symbols, the maximum cross-correlation for the same SFs exceeds $\frac{1}{2}$ for $\tau \leq \tau_{thresh}$ where the threshold τ_{thresh} varies with the SF. This behaviour manifests the existence of temporal shift intervals during which overlapped LoRa transmissions are more prone to decoding errors. The high

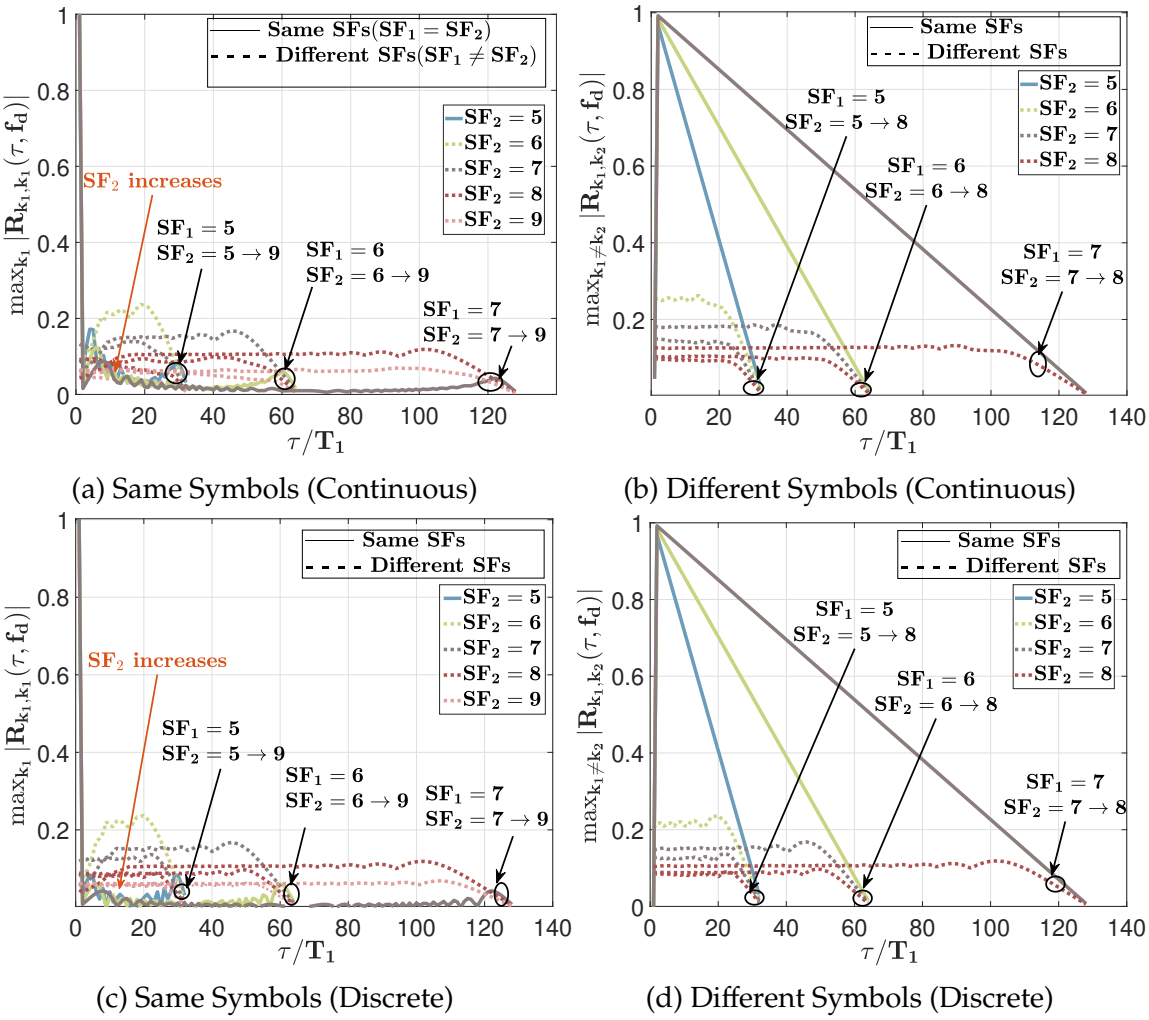

(a) Same Symbols (Continuous)

(b) Different Symbols (Continuous)

(c) Same Symbols (Discrete)

(d) Different Symbols (Discrete)

Fig. 4.10: Maximum cross-correlation functions versus time delay τ/T_1.

cross-correlation between two different symbols leads to two spikes with close amplitudes in the *Discrete Fourier Transform* (DFT) spectrum, making the distinction of the desired symbol challenging.

The plots of the same and different symbols reveal delay intervals where the cross-correlation is maximised. These results provide useful insights that can support the design of optimal transmission policies and resource allocation schemes. For instance, the same symbol results can help design scheduling policies that take advantage of constructive interference to improve the decoding capabilities of a LoRa system, boosting its reliability. The different symbols results, on the other side, provide a useful tool to understand LoRa vulnerability to inter-symbol interference (ISI) and how it can be mitigated.

4.4.4 Orthogonality Conditions

This section summarizes in Tab. 4.1 some of the conditions ensuring that two LoRa waveforms are orthogonal.

Time Domain	SFs	Bws	Time Shift	Freq Shift	Orthogonality Conditions
Continuous	$SF_1 = SF_2$	$B_1 = B_2$	$\tau = 0$	$f_d = 0$	SF even & $\lvert k_1 - k_2 \rvert \propto \sqrt{2^{SF}}$
				$f_d \neq 0$	SF even & $f_d \propto \frac{B}{2^{SF}}$ & $\lvert k_1 - k_2 - \frac{f_d 2^{SF}}{B} \rvert \propto \sqrt{2^{SF}}$
			$\tau \neq 0$	$f_d = 0$	SF even & $\tau \propto T$ & $\lvert k_1 - k_2 + \frac{\tau}{T} \rvert \propto \sqrt{2^{SF}}$
				$f_d \neq 0$	SF even & $\tau \propto T$ & $f_d \propto \frac{B}{2^{SF}}$ & $\lvert k_1 - k_2 + \frac{\tau}{T} - \frac{f_d 2^{SF}}{B} \rvert \propto \sqrt{2^{SF}}$
Discrete	$SF_1 = SF_2$	$B_1 = B_2$	$\tau = 0$	$f_d = 0$	$k_1 - k_2 \neq 0$
				$f_d \neq 0$	$f_d \propto \frac{B_1}{2^{SF_1}}$ & $k_1 - k_2 - f_d \frac{2^{SF_1}}{B_1} \neq 0$
			$\tau \neq 0$	$f_d = 0$	$\left(2^{SF_1} - \tau/T_1\right)\left(k_1 - k_2 + \frac{\tau}{T_1}\right) \propto 2^{SF_1}$
				$f_d \neq 0$	$f_d \propto \frac{B_1}{2^{SF_1}}$ & $\left(2^{SF_1} - \tau/T_1\right)\left(k_1 - k_2 + \frac{\tau}{T_1} - f_d \frac{2^{SF_1}}{B_1}\right) \propto 2^{SF_1}$

Table 4.1: LoRa Orthogonality Conditions.

4.5 LoRa BER Analysis

4.5.1 LoRa Physical Layer Matlab Simulator

Before having LoRa symbols generated using LoRa CSS modulation, the input bit sequence goes through a pipeline of operations at the transmitter side [43, 143, 154]. This pipeline includes:

- **Hamming coding:** LoRa adopts various error correction coding schemes that range from a simple parity check to an extended Hamming code of rate $\frac{4}{(4+CR)}$

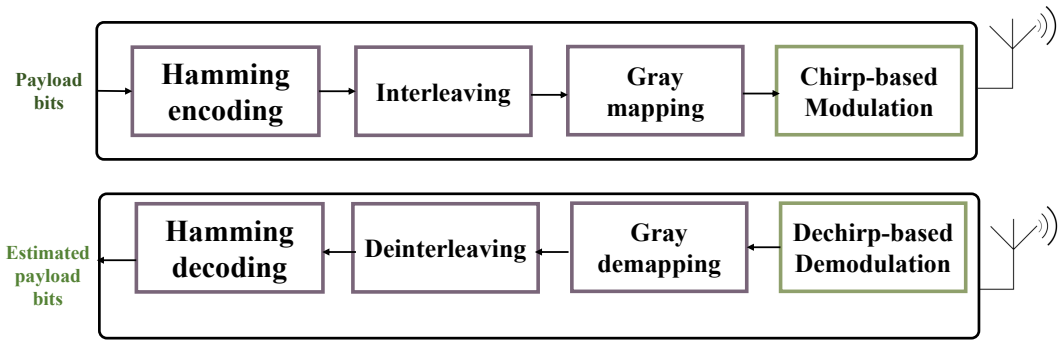

Fig. 4.11: LoRa Physical transmitter and receiver chains.

based on the chosen coding rate parameter CR$\in \{1, 2, 3, 4\}$. The parameter CR specifies the number of bits used for error correction.

- **Interleaving:** LoRa adopts an interleaving operation that aims to avoid the propagation of adjacent errors. The adopted interleaver is diagonal of size (SF $\times$ (CR + 4))[43].
- **Gray Coding:** The Gray coding operation maps the bit sequence into symbols while ensuring that each two consecutive symbols differ by one bit.

At the receiver side, the received message goes through the demodulation process, which is based on a down-chirping operation followed by a DFT [154], the corresponding inverses operations (Gray decoding, De-interleaving and Hamming decoding) are then performed on the demodulated signal to obtain the transmitted symbol. Fig. 4.11 shows the pipeline of operations at the transmitter side and their corresponding inverse at the receiver side. We built our LoRa's physical layer simulator on Matlab based on the processing pipeline explained above.

4.5.2 Simulated BER Results

We used the developed simulator to calculate the bit error statistics. In Fig. 4.12, we plot the BER performance of different spreading factors under an additive white Gaussian channel for the case of a 4/7 hamming coding scheme. The figure shows how a LoRa device sensitivity decreases with SF. Higher SFs can decode

signals with lower SNR.

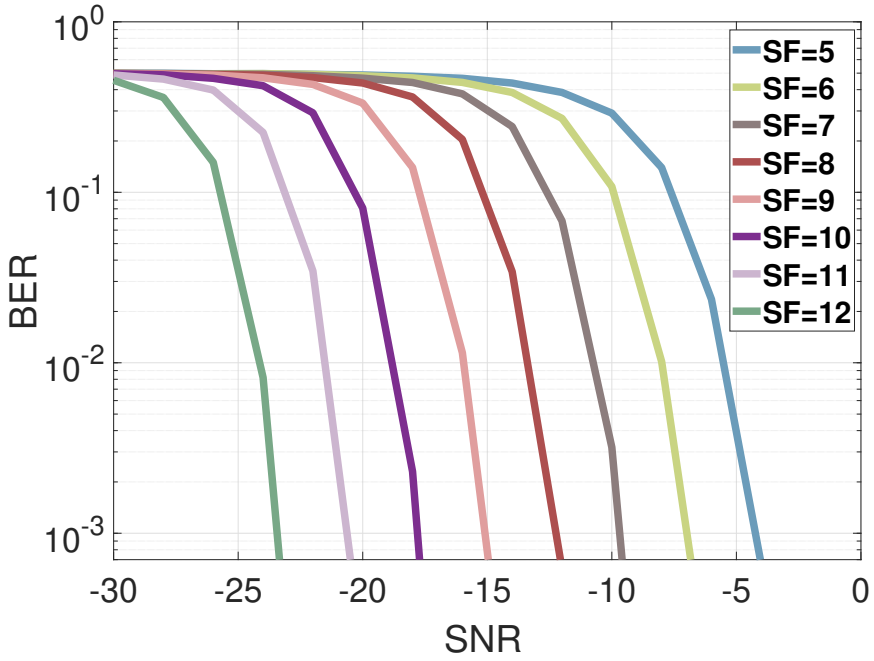

Fig. 4.12: LoRa coded BER performance under AWGN for different SFs.

Next, we examine LoRa bit error performance under both AWGN and interference from either the same or a different SF. To have our focus only on the modulation technique and the impact of non-orthogonality, we carry the BER analysis without considering the coding and interleaving operations so that their impacts are isolated. We consider a desired packet of size N bytes (25 for the following graphs) rounded to a number of blocks. The desired signal $S_0(nT)$ is modulated with SF_1 and impaired by an AWGN $W(nT)$ and an interfering signal $S_{int}(nT)$ modulated with SF_2. The SNR is fixed based on the sensitivity range of each SF (See Tab. 4.2), and the power of the interfering signal is set according to the SIR. The overall received signal $R(nT) = S_0(nT) + S_{int}(nT) + W(nT)$ goes through the demodulation process, which is based on a down-chirping operation followed by a DFT. The decoded symbol is detected by the position of the maximum in the DFT amplitude spectrum of R. Using this simulation setup we evaluate the BER for various combinations of (SF_1, SF_2, BW_1, BW_2) while varying the SIR and fixing the SNR.

SF	7	8	9	10	11	12
SNR Threshold(dB)	-6	-9	-12	-15	-17,5	-20

Table 4.2: SF SNR thresholds.

To illustrate the impact of interference on the demodulation process, we plot in Fig. 4.13, the DFT amplitude of the dechirped LoRa signal modulated using $SF_1 = 7$ under different interference scenarios. In Fig. Fig. 4.13(a), the LoRa chirp is sent through an AWGN channel (without interference). In contrast, in the remaining subplots, we have, in addition to the AWGN, a simultaneously transmitted interfering chirp modulated using SF_2 over bandwidth B_2 with a SIR value 0 dB. The figure highlights that the peak in the DFT amplitude spectrum is impacted by the two parameters SF_2 and B_2 used to modulate the interfering signal.

Examining the interference scenarios Fig. 4.13(b) and Fig. 4.13(d), we observe that the interfering signal gives ripples that remain safe and do not alter the decoding of the desired signal at the receiver. However, for the interference scenarios in Fig. 4.13(c) and Fig. 4.13(e), the interfering signal gives a second spike of comparable amplitude to the peak of interest, which makes the distinction of the desired symbol challenging, impacting as a result its decoding probability. The figures also illustrate that the amplitude peak competing with the desired one does not always come from the same-SF interfering signal, as shown in Fig. 4.13(e).

To evaluate the impact of LoRa SFs imperfect orthogonality and equate it to the obtained cross-correlation factors detailed in the previous section, we study the BER for different combinations of BWs and SFs in Fig. 4.14. We find that the behaviour of the BER is aligned with the behaviour of the maximum cross-correlation functions in the discrete time domain. By examining the subplots in Fig. 4.14, we can see how the SF with the dominant impact on the BER results is not always the same SF as the desired one (i.e. SF_1); it changes based on the BW ratio between the desired and the interfering SFs as it is previously shown in Fig. 4.9. The dominant interfering SF is the one that has the highest cross-correlation factors in Tab. A.2

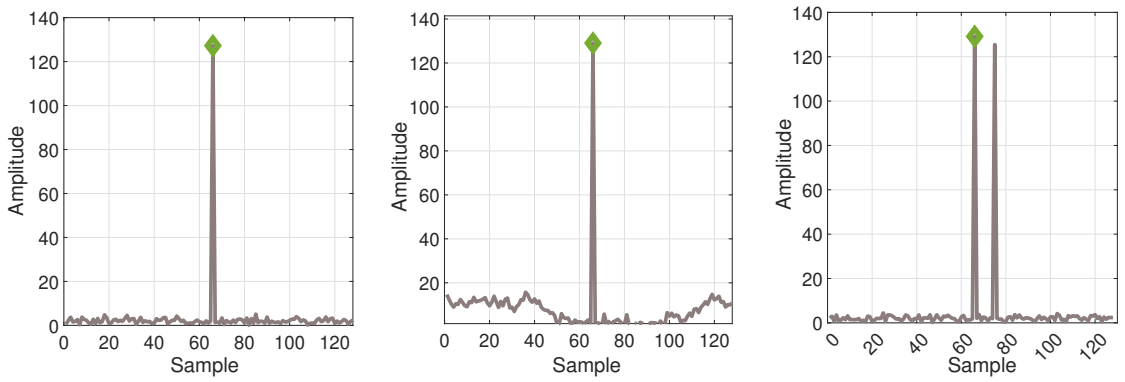

(a) Without Interference (b) $SF_2 = 6$, $B_2 = B_1$ (c) $SF_2 = 7$, $B_2 = B_1$

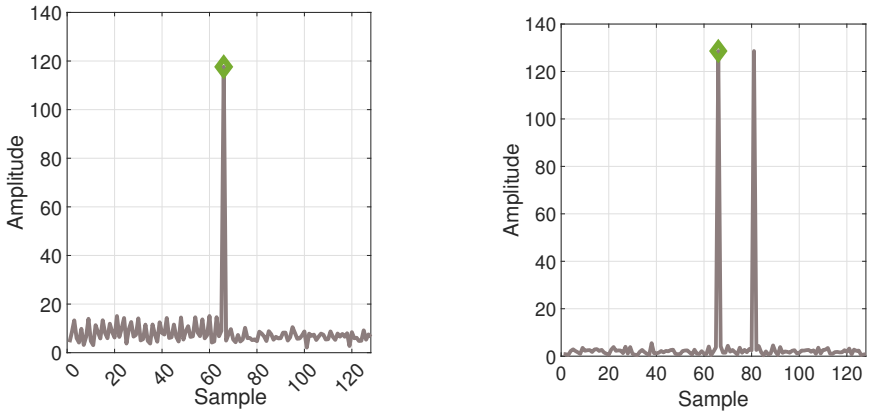

(d) $SF_2 = 7$, $B_2 = 2 \times B_1$ (e) $SF_2 = 9$, $B_2 = 2 \times B_1$

Fig. 4.13: FFT amplitude spectrum of a received signal modulated with $SF_1 = 7$ under (a) only AWGN channel ($SNR = 0$ dB) and (b)-(e) different interference scenarios with SIR= 0 dB.

4.6 Experimental Validation

4.6.1 Experimental Setup

In this section, we run a small experimental setup made up of three LoRa nodes (2 transmitters and 1 receiver) in Fig. 4.15. Each LoRa end user is represented by Semtech SX1280 2.4 GHz transceiver [157]. One transmitter is set to be the desired user and the second transmitter is set to be the interfering user. We set the transmit power of both transmitters to 22 dBm while we vary their SFs and BWs.

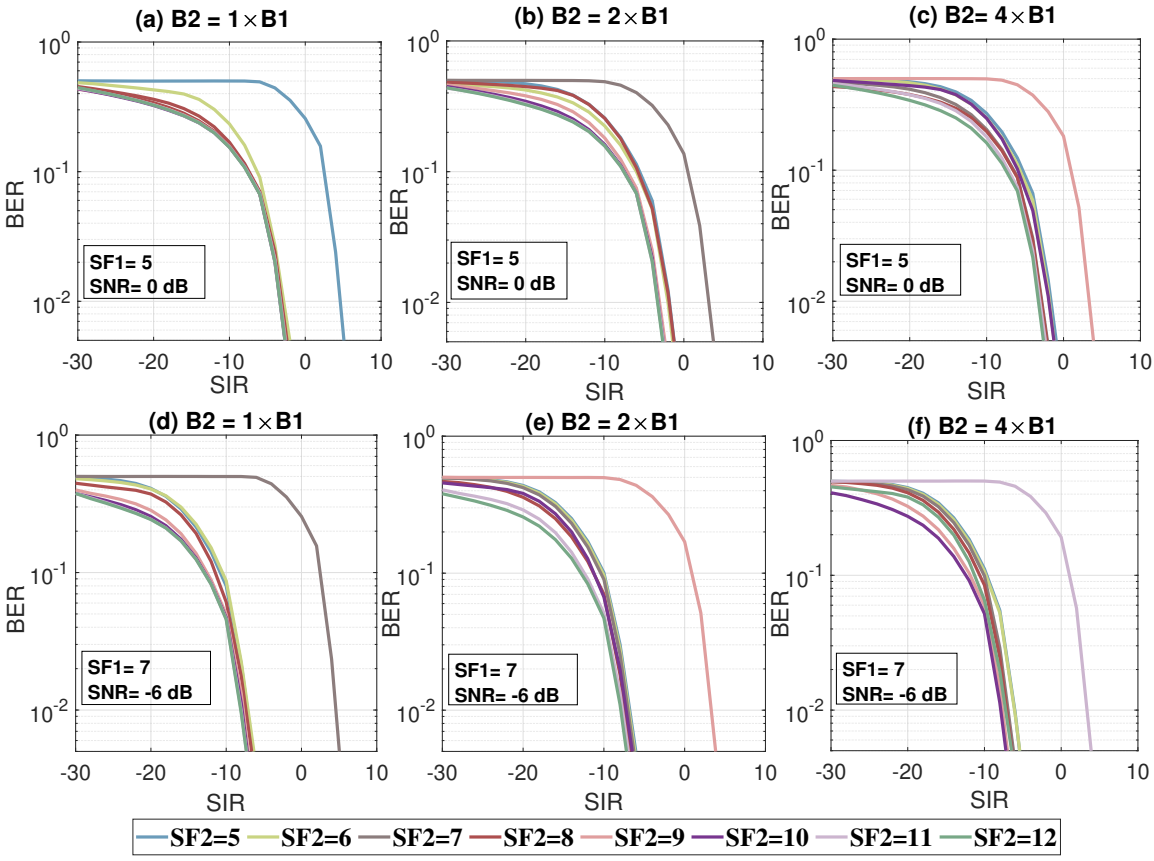

Fig. 4.14: LoRa BER performance under interference from different SFs with $\tau = 0$ and $f_d = 0$ for different B_1 and B_2.

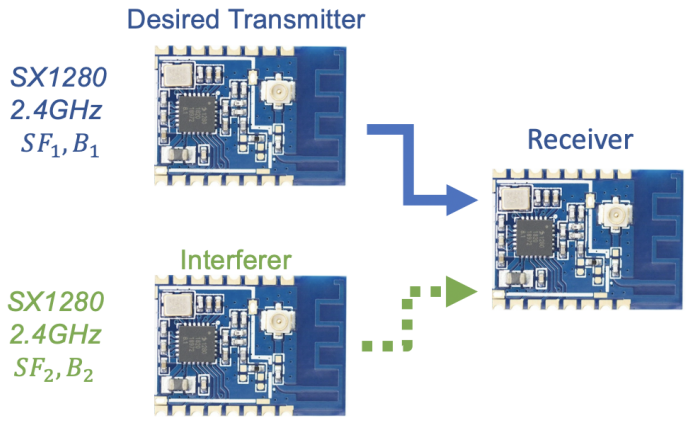

Fig. 4.15: Experimental setup using Semtech SX1280 2.4GHz transceivers.

4.6.2 PDR Analysis

We quantify the PDR metric by recording the number of correctly received packets over the number of transmitted packets.

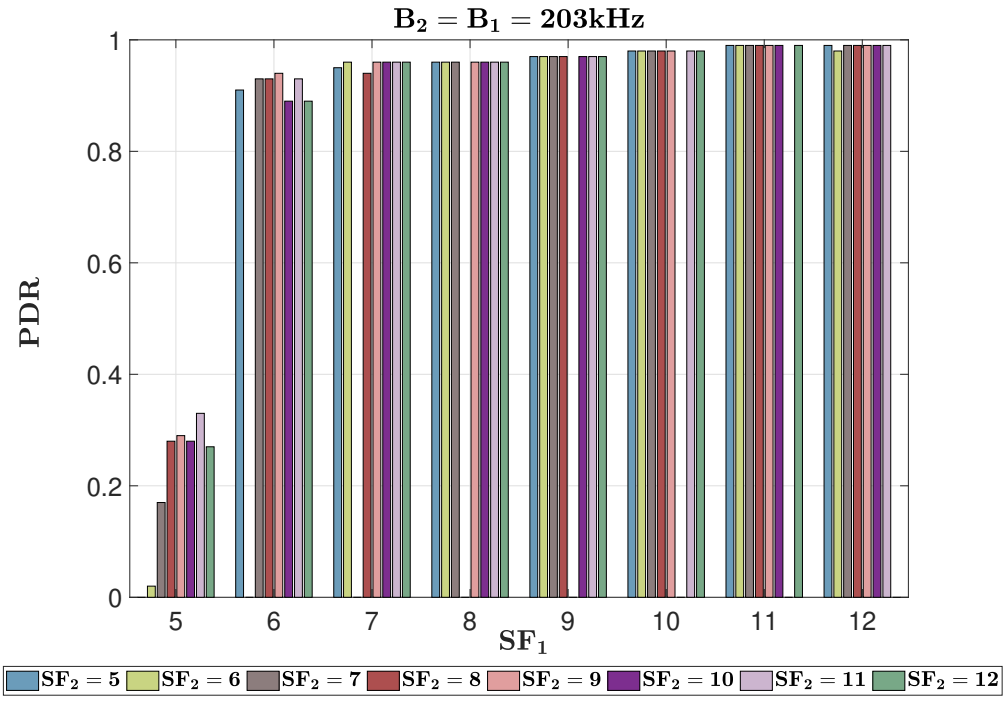

Fig. 4.16: Experimental analysis of packet delivery ratio (PDR) for $B_1 = B_2 = 203$ MHz, $SF_1 \in \{5, \ldots, 12\}$ and $SF_2 \in \{5, \ldots, 12\}$.

In Fig. 4.16, we plot the PDR results of different $SF_1 \in \{ 5, ..,12 \}$ under concurrent transmissions from interfering $SF_2 \in \{ 5, ..,12 \}$ using the same BW ($B_1 = B_2 = 203KHz$). For the sake of generalisability, the PDR is further evaluated for bandwidths (406 KHz, 812 KHz, 1624 KHz) in Fig. 4.17. Starting with the scenario where the desired transmitter and the interferer use the same BW, we observe in Fig. 4.16 and Fig. 4.17 that the PDR performance is drastically impacted by the same SF as the absent bars indicate an exactly zero PDR. This behaviour is highly aligned with the maximum cross-correlation factors in Fig. 4.4 (b) as well as the bit error results in Fig. 4.14(a),(d).

In Fig. 4.18 and Fig. 4.19, we plot the PDR results for the scenario where the desired transmitter and the interferer use different bandwidths. Fig. 4.19 shows

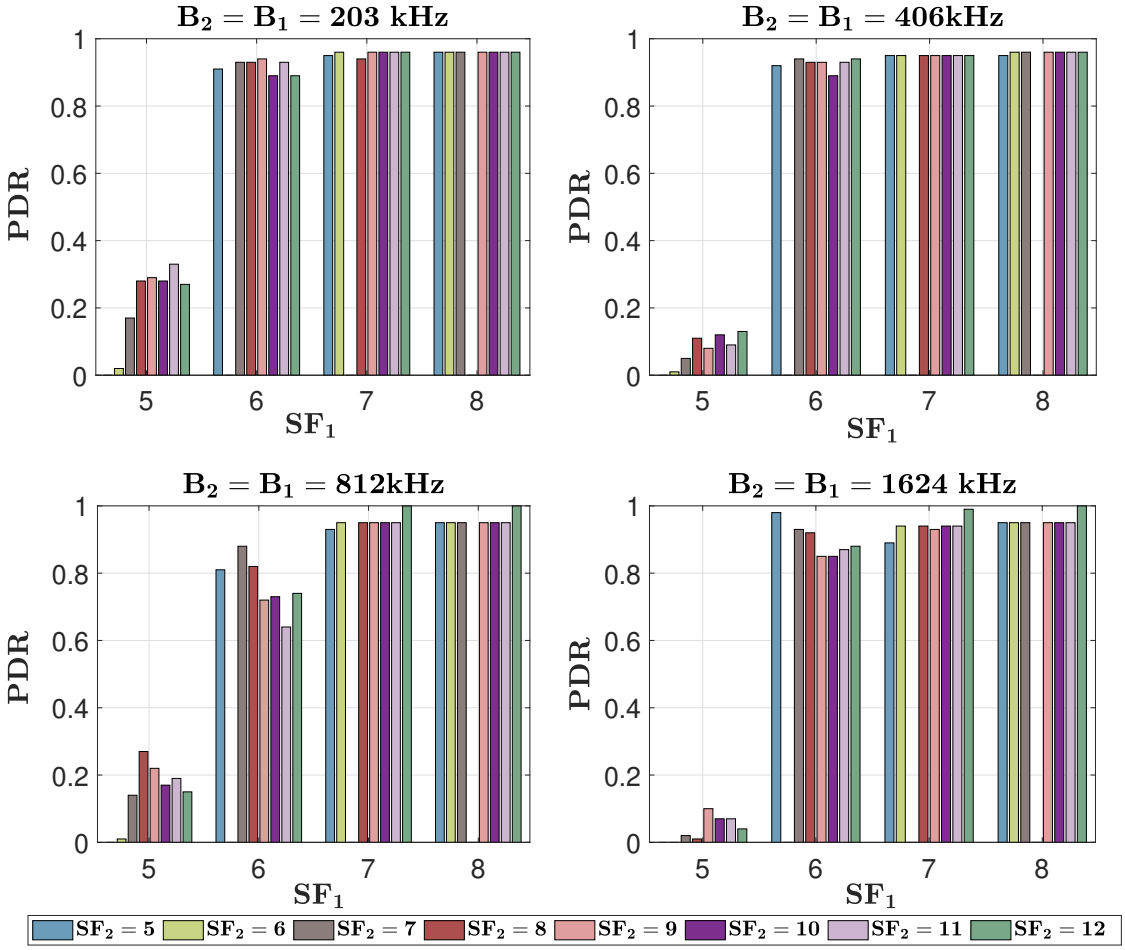

Fig. 4.17: Experimental analysis of packet delivery ratio (PDR) for different $B_1 = B_2$.

particularly the results for the ratio $\frac{B2}{B1} \in \{0.5, 2\}$ while Fig. 4.18 presents the results for the ratio $\frac{B2}{B1} \in \{0.25, 4\}$. Examining these figures, we intriguingly find out that ,when $B_2 > B_1$, the worst PDR performance is obtained for the scenarios where the difference between the desired and interfering SFs is exactly equal to the ratio between the bandwidths. For instance, for the ratio $\frac{B2}{B1} = 2$, we can clearly detect the missing bars indicating packet failure at $\mathrm{SF}_2 = \{7, 8, 9, 10\}$ for $\mathrm{SF}_1 = \{5, 6, 7, 8\}$, respectively. The missing bars are shifted to $\mathrm{SF}_2 = \{9, 10, 11, 12\}$ for the ratio $\frac{B2}{B1} = 4$. This behaviour recalls the results obtained for the maximum cross-correlation as it reaches its largest value for $\mathrm{SF}_2 = \mathrm{SF}_1 + \frac{B_2}{B_1}$. When $B_2 < B_1$, we notice that the PDR vanishes at $\mathrm{SF}_2 = \{5, 5, 5, 6\}$ for $\mathrm{SF}_1 = \{5, 6, 7, 8\}$ given $\frac{B2}{B1} = 0.5$. The PDR performance for $B_2 < B_1$ exhibits interestingly similar behaviour to the cross-correlation factors results detailed in Section. 4.4 as we find that the maximum

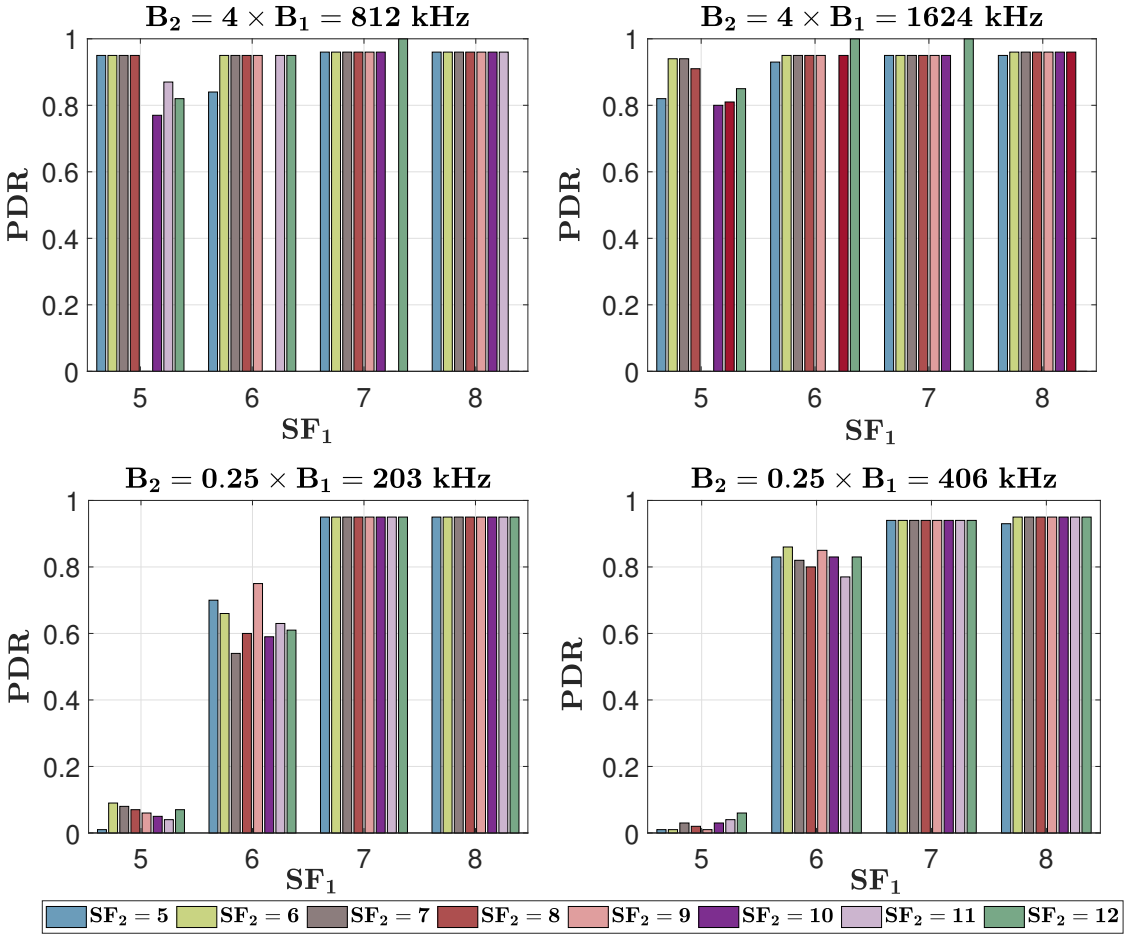

Fig. 4.18: Experimental analysis of packet delivery ratio (PDR) for $B_1 = 4B_2$ and $B_1 = 0.25B_2$.

cross-correlation is obtained for $\mathrm{S}F_2 = \max(5, \mathrm{SF}_1 - B_1/B_2)$,

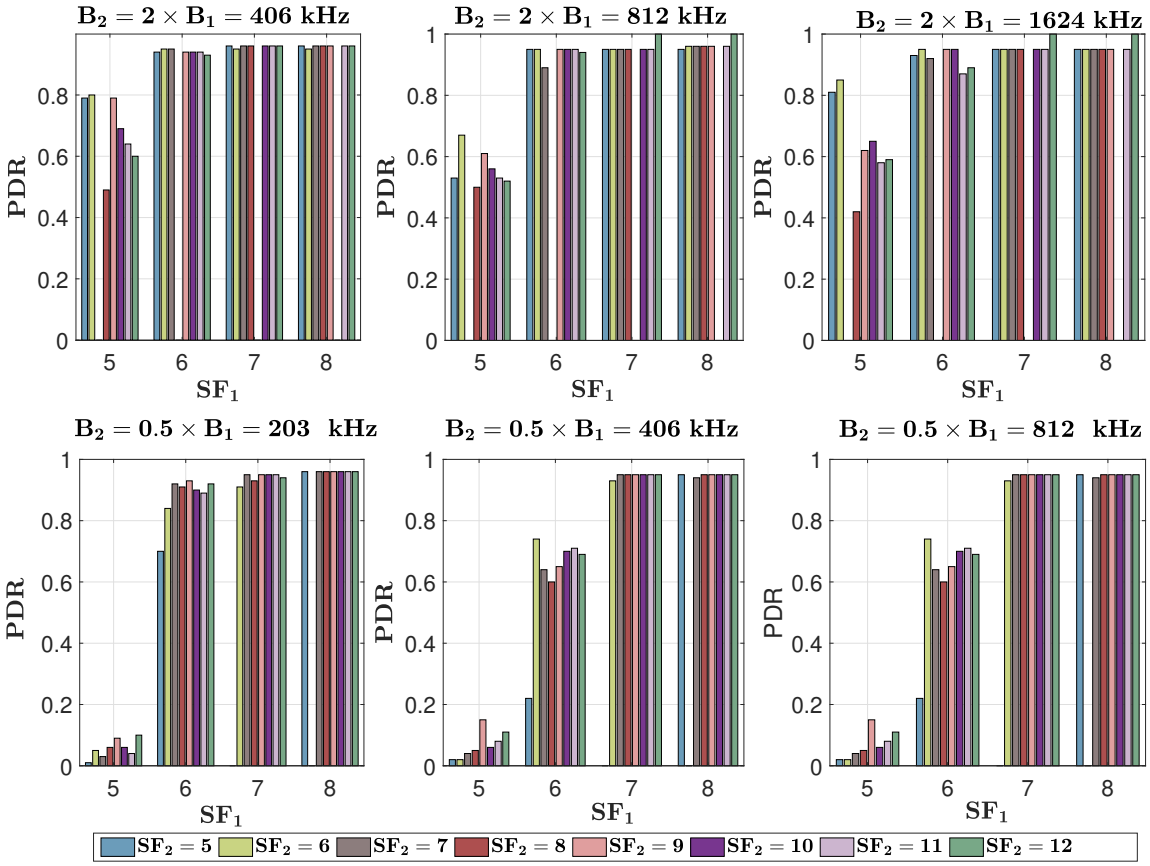

Fig. 4.19: Experimental analysis of packet delivery ratio (PDR) for $B_1 = 2B_2$ and $B_1 = 0.5B_2$.

4.7 Discussion

The analysis presented in this chapter, with its different components, waveform derivation, cross-correlation characterisation, simulated BER analysis, and experimental PDR analysis provides an in-depth view of LoRa link-level performance. However, while meticulous, link-level analyses are computationally gourmand and become limited when the network scales up to support thousands of devices which is the prime objective of LoRa and LPWA technologies. Analysing large-scale networks requires system-level evaluation approaches that account for relevant system functionalities and parameters. It is worth highlighting that ideally, link-level and system-level evaluations should not be carried out disjointly as they complement each other.

In the next chapters, we move from link-level to system-level, i.e. from small to large scale.

4.8 Chapter Summary and Key Findings

In this chapter, we characterise the orthogonality of LoRa same and different SFs by deriving cross-correlation functions that account for different LoRa tuneable physical features; the BW, the initial frequency, and the start time. The derived cross-correlation functions were further simplified for some special cases such as synchronous transmissions with zero frequency differential shift. Analysing the derived cross-correlation functions, we recapitulate some of the conditions ensuring orthogonality between LoRa SFs in Tab. 4.1.

Extensive numerical evaluations have been performed to study the maximum, mean and CDF of the cross-correlation functions, thoroughly investigating the impact of bandwidth and temporal displacement. To validate these numerical evaluations, we further studied the performance of simulated BER and experimental PDR. The obtained BER and PDR exhibit performance trends that are aligned with the behaviours observed in the maximum cross-correlation analysis.

Key Findings

Below we summarize the key findings of this chapter.

Analysing the impact of bandwidth, the following valuable findings are deduced:

- For two waveforms with the same bandwidths, the largest maximum cross-correlation is caused by the same SF; whereas, for transmissions with different bandwidths, the largest maximum cross-correlation is not always obtained by the same SF and, rather, varies with the ratio of bandwidths.
- For two waveforms with the same bandwidths, the closer the interfering SF is to the desired SF, the higher is their cross-correlation.

– For two waveforms with different bandwidths where $B_2 > B_1$, the largest maximum cross-correlation occurs at $\mathrm{SF}_2 = \mathrm{SF}_1 + \frac{B_2}{B_1}$, while for $B_1 < B_2$, the largest maximum cross-correlation occurs at $\mathrm{SF}_2 = \max\left(5, \mathrm{SF}_1 - \frac{B_1}{B_2}\right)$.

Analyzing the impact of the temporal displacement, the following attractive behaviours are showcased:

– For two waveforms carrying the same symbol, the maximum cross-correlation of different SFs becomes higher than that for the same SFs as soon as the temporal displacement deviates from the chip rate $T_1 = \frac{1}{B_1}$.
– The temporal displacement analysis of both same and different symbols evince delay intervals where the cross-correlation is maximised.

These results provide valuable insights into the design of constructive interference-enhanced transmission protocols boosting LoRa systems' reliability. They can also be adopted as a helpful analytical tool to understand and mitigate LoRa vulnerability to inter-symbol interference.

CHAPTER 5

Stochastic Geometry based Modelling and Analysis of Multi-Gateway LoRa Networks

The analysis of LoRa physical layer characteristics and link-level performance in Chapter. 4 provides deep insights into the behaviours of LoRa and the interaction between the SFs. However, it remains not sufficiently flexible to predict and analyse the performance of large-scale LoRa networks. In this chapter, we address the performance of UP transmissions in large-scale LoRa networks using tools from *Stochastic Geometry* (SG).

5.1 Motivation and Contribution

Wireless networks intrinsically inherit the unreliability of the wireless medium. Such unreliability is further exacerbated in grant-free unlicensed technologies like LoRa. Given their unplanned, unlicensed and uncoordinated nature, LoRa UP communications are impacted by several factors. These factors include not only the gateway placement and the radio environment with all the path-loss, the shadowing and the fading components, but also the inevitable interference from concurrently transmitting nodes. Interference in LoRa networks is affected

by the network topology and by the way the network resources, which are the time, the power, the BW, the channel and the SF, are allocated among the nodes. An efficient LoRa network engineering requires, as a first step, accurate modelling that reflects different LoRa peculiarities including the physical layer features, the medium access protocol, and the resource allocation mechanisms.



Fig. 5.1: HDB map: NUS urban analytics lab [158].

This chapter focuses on the modelling of LoRa networks using stochastic geometry. Specifically, a Matern cluster process is leveraged to depict multi-cell LoRa topologies. The choice of this specific point process is motivated by three main attributes: First, the unplanned operator-free deployment model of LoRa, second, the urban nomenclature of HDB[1] estates shown in Fig. 5.1, and third, the general clustered nature of the majority of smart sensing applications which come often aggregated in specific areas like buildings, parking spaces, parks and gardens. Accounting for the uncoordinated-nature of LoRa communications, random start times are added as independent marks to the ground spatial MCP. Using the start

[1]The Housing and Development Board (HDB) is Singapore's public housing authority. It plans and develops Singapore's housing estates https://www.hdb.gov.sg/cs/infoweb/homepage.

time distribution, a collision overlap function has been derived for both co-SF and inter-SF interference.

The derived collision overlap function is incorporated into the SINR formulation to equalise the interference power from either the same or a different SF. We devise our analytical model using SINR capture conditions rather than the separate (SNR, SIR) conditions [136, 137, 138]. While this modelling choice comes with extra tractability challenges, it has the advantage of making our approach general and capturing the correlation between the SIR and SNR[87, 159].

5.2 System Model

5.2.1 Spatial Distribution

The choice of the spatial point process plays an essential role in SG-based analysis as it impacts the degree of tractability of the final mathematical expressions. A *"convenient PP"* is a point process that combines tractability and practicality [5] while reflecting the specificity of the technology. As previously highlighted, LoRa operator-free deployment model allows IoT developers to acquire their own base stations and build private sensing infrastructures under their control. Such deployment strategy does not adopt interference exclusion regions commonly used in cellular networks, making MCP an excellent candidate to represent multi-gateway LoRa networks.

According to this cluster process, LoRa gateways L_i are distributed following a PPP $\Phi_G = \{y_i, i = 1, 2, \dots\}$ with intensity λ_G, where $y_i \in \mathbb{R}^2$ is the location of the i'th LoRa gateway. Each cluster C_i centred is at L_i and has a radius R. Within the area of each cluster, LoRa *End-Device* (ED)s are uniformly scattered around L_i and form a PPP $\Phi_{ED,i} = \{x_{ij}, j = 1, 2, \dots\}$ of intensity λ_{ED}, where $x_{ij} \in \mathbb{R}^2$ is the location of the j'th LoRa ED in the i'th cluster. The overall superposition of $\Phi_{ED,i}$ captures the position of all the children nodes and gives the desired MCP-based network.

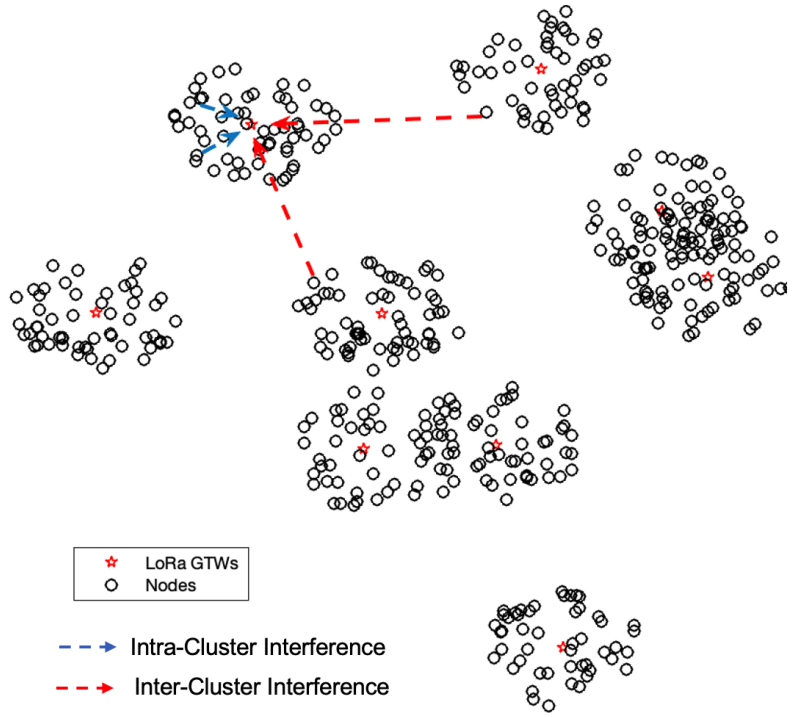

Fig. 5.2: Transmission success probability (P_{Succ}) versus different SINR thresholds (γ_{th}) for a Multi-Gateway topology.

5.2.2 Propagation Model

We consider a power law path-loss propagation model where the signal attenuates with the propagation distance at the rate $\alpha r^{-\eta}$, with $\eta > 2$ being the path-loss exponent and α being the frequency dependant factor. Additionally, we have Rayleigh block fading channels with unit mean exponentially distributed channel gains g_j, i.e. $g_j \sim exp(1)$. For tractability reasons, all channels are assumed to be i.i.d. in both space and time dimensions.

5.2.3 Medium access

LoRa adopts an Aloha-like MAC protocol where nodes send their packets independently without any prior coordination or synchronization. Each transmitting node is marked with a random independent mark that denotes its transmission start time and has to satisfy the duty cycle restriction a. By virtue of the independent thinning of a homogeneous PPP (Definition. 1.5), the subset of transmitting nodes form a

homogeneous PPP $\tilde{\Phi}_{ED,i}$ of intensity aλ_{ED}. The overall spatio-temporal model of the network can be interpreted as an independently marked process where the ground process is formed by the nodes positions and the marks represent the transmission start time of each node [142].

5.2.4 Spreading Factor Allocation

Each LoRa ED can be assigned to an SF in $\mathcal{S}$=$\{\mathbf{SF_1}, \ldots, \mathbf{SF_N}\}$, where N is the total number of available SFs. We adopt an EIB SF allocation scheme for which each cluster C_i is divided into N annuli A_q delimited by d_{q-1} and d_q, where $q \in Q$=$\{\mathbf{1}, \mathbf{2}, ..., \mathbf{N}\}$ is standing for the q'th SF. Each annulus A_q is of width $\omega = \frac{R}{N}$ and hence $d_{q-1} = (q-1)\omega$ and $d_q = q\omega$. The average nodes number in each annulus is $N_q = \lambda_{ED}\pi(d_q^2 - d_{q-1}^2)$.

5.3 Spatiotemporal Analysis

The received SINR at the typical LoRa gateway from a typical LoRa node, located at $r_0 = \|x_{00}\|$ and emitting with $\mathrm{SF}_{q_0 \in Q}$, is formulated as:

$$\mathrm{SINR}(r_0, q_0) = \frac{P_{q_0} g_{00} \alpha r_0^{-\eta}}{I_{intra} + I_{inter} + \sigma^2}, \tag{5.1}$$

where I_{intra} is the intra-cluster interference coming from active nodes within the same cluster, I_{inter} is the inter-cluster interference originating from transmitting nodes in other clusters, and σ^2 is the variance of AWGN. I_{intra} and I_{inter} account for interference from the same SF (Co-SF) and from different SFs (Inter-SF).

5.3.1 SF-Dependent Collision Overlap Time

As LoRa uses interleaving and repetition codes, we consider an averaging over the exchanged packet duration to account for the time dependence of the interference [142]. Unlike ordinary Aloha systems, LoRa has a variable packet duration since the ToA is linked to the SF used in the transmission. We denote the packet duration

using SF_q as l_q. The variable time-on-air leads to an SF-dependent collision overlap time.

We consider a typical LoRa node located at $x_{00} \in \tilde{\Phi}_{ED,0}$ emitting with SF $q_0 \in Q$ and communicating with a typical gateway placed at the origin. Without loss of generality, we assume that the typical LoRa node starts its desired transmission with SF= q_0 at $T_0 = 0$. The time-averaged intra-cluster and inter-cluster interference (I_{Intra} and I_{Inter}) experienced by the receiver are given by:

$$I_{Intra} = I_{intra}^{mean} = \frac{1}{l_{q_0}} \int_{T_0}^{T_0+l_{q_0}} I_{Intra}(t)dt = \sum_{q\in Q} \sum_{x\in\tilde{\Phi}_{ED,0}\setminus x_{00}} \mathbb{1}_{j,q} P_q \alpha \|x_{0j}\|^{-\eta} h_{q_0,q}(T_{ij}) g_{0j}, \quad (5.2)$$

$$I_{Inter} = I_{inter}^{mean} = \frac{1}{l_{q_0}} \int_{T_0}^{T_0+l_{q_0}} I_{Inter}(t))dt = \sum_{q\in Q} \sum_{y\in\Phi_G\setminus y_0} \sum_{x\in\ \tilde{\Phi}_{ED,i}} \mathbb{1}_{j,q} P_q \alpha \|y_i + x_{ij}\|^{-\eta} h_{q_0,q}(T_{ij}) g_{ij}, \quad (5.3)$$

where $\mathbb{1}_{j,q}$ is the indicator function of ED_j transmitting at SF q and $h_{q_0,q}(T_{ij})$ is the collision overlap time function between the LoRa node located at $x_{ij} \in \tilde{\Phi}_{ED,i}$ with random transmission start time T_{ij} and the typical user. $h_{q_0,q}(T_{ij})$ is expressed as:

$$h_{q_0,q}(T_{ij}) = \frac{1}{l_{q_0}} \int_{T_0}^{T_0+l_{q_0}} \mathbb{1}(\ x_{ij} \text{ overlaps with } x_{00}) \quad d(t). \quad (5.4)$$

Assuming all the active nodes (except the typical user) start transmitting randomly in a contention window $[-T_c, T_c]$, we derive the collision overlap time in the following lemma:

Lemma 5.1. *The collision overlap time function $h_{q_0,q}(T_{ij})$ between the desired node x_{00} and the interfering node x_{ij} transmitting with SF q at random time T_{ij} is*

$$h_{q_0,q}(T_{ij}) = \begin{cases} \frac{l_{q_0}-T_{ij}}{l_{q_0}}, & if\ \left(l_{q_0} - l_q\right)^+ \le T_{ij} \le l_{q_0}, \\ \frac{\min(l_{q_0},l_q)}{l_{q_0}}, & if\ -\left(l_q - l_{q_0}\right)^+ \le T_{ij} \le \left(l_{q_0} - l_q\right)^+, \\ \frac{l_q+T_{ij}}{l_{q0}}, & if\ -l_q \le T_{ij} \le -\left(l_q - l_{q_0}\right)^+, \\ 0, & if\ -T_c \le T_{ij} < -l_q \text{ or } l_{q_0} < T_{ij} \le T_c, \end{cases} \quad (5.5)$$

where $(t)^+ = max(t, 0)$.

Proof. The proof is in Appendix Section. B.1. □

Fig. 5.3 sketches the collision overlap scenarios between a desired and an interfering packet.

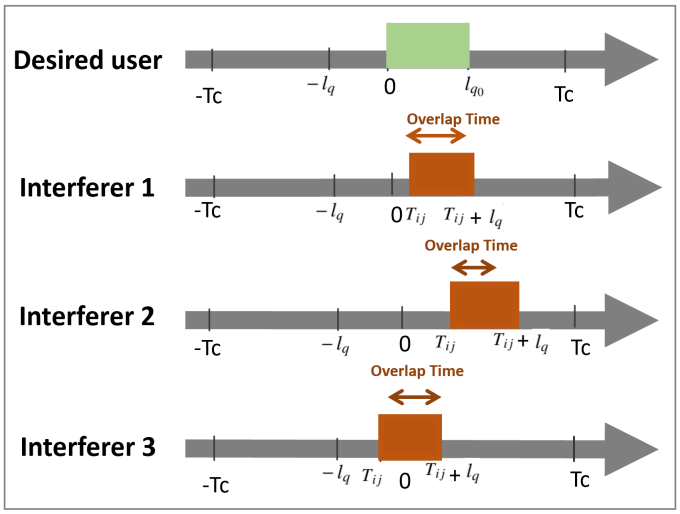

Fig. 5.3: Collision Overlap time between two LoRa transmissions.

Corollary 5.1. *Using Lemma 5.1, and assuming that the transmission starting time of the interfering node is uniformly distributed between* $[-T_c, T_c]$, $T_{ij} \overset{Dist}{=} U(-T_c, T_c)$, *we show that*

$$\mathbb{E}_{T_{ij}}\left[\frac{1}{1+uh_{q_0,q}\left(T_{ij}\right)}\right] = 1 - \frac{l_{q_0}+l_q}{2T_c} + \frac{\left|l_{q_0}-l_q\right|}{2T_c\left(1+u\frac{min\left(l_q,l_{q_0}\right)}{l_{q_0}}\right)} + \frac{l_{q_0}}{T_c u}\log\left(u\frac{min\left(l_q,l_{q_0}\right)}{l_{q_0}}+1\right). \tag{5.6}$$

Proof. The proof is given in Appendix Section. B.2. □

5.3.2 Transmission Success Probability

The typical LoRa gateway is able to receive and successfully decode the desired signal if its instantaneous SINR surpasses a reference decoding threshold γ_{th}. We define the transmission success probability as:

$$P_s(r_0, q_0) = \mathbb{P}\{\text{SINR}(r_0, q_0) \geq \gamma_{th}\} = exp(-\rho\sigma^2)\mathcal{L}_{I_{Intra}}(\rho)\mathcal{L}_{I_{Inter}}(\rho), \tag{5.7}$$

where $\rho = \frac{\gamma_{th} r_0^{\eta}}{P_{q_0}\alpha}$

To obtain the expression of the transmission success probability, we need first to derive the expressions of the Laplace transforms of I_{Intra} and I_{Inter}.

Theorem 5.1. *The Laplace transform of I_{Intra} is given by:*

$$\mathcal{L}_{I_{Intra}}(\rho) \approx \prod_{q\in Q} \exp\left(-2\pi a \lambda_{ED}\left(I_1(q) - I_2(q) - I_3(q)\right)\right), \tag{5.8}$$

$$I_1(q) = J_1(d_q) - J_1(d_{q-1}) \tag{5.9}$$

$$I_2(q) = J_2(d_q) - J_2(d_{q-1}) \tag{5.10}$$

$$I_3(q) = J_3(d_q) - J_3(d_{q-1}) \tag{5.11}$$

with functions $\mathcal{J}_1(\cdot)$ and $\mathcal{J}_2(\cdot)$ and $\mathcal{J}_3(\cdot)$ defined as:

$$\mathcal{J}_1(x) = \frac{(l_q + l_{q_0})}{4T_c} x^2, \tag{5.12}$$

$$\mathcal{J}_2(x) = \frac{min(l_q, l_{q_0})}{2T_c b(\eta+2)}\left(x^2\, {}_2F_1\left(1, -\frac{2}{\eta}; \frac{\eta-2}{\eta}; -bx^{-\eta}\right) + 2x^{\eta}\log\left(bx^{-\eta}+1\right)\right), \tag{5.13}$$

$$\mathcal{J}_3(x) = \frac{\left|l_{q_0} - l_q\right|}{2T_c b(\eta+2)}\left(x^{\eta+2}\, {}_2F_1\left(1, \frac{\eta+2}{\eta}; \frac{\eta+2}{\eta}+1; -\frac{x^{\eta}}{b}\right)\right), \tag{5.14}$$

where ${}_2F_1(\cdot)$ is the Gaussian hypergeometric function [160], and $b = \alpha P_q \frac{min(l_q, l_{q_0})}{l_{q_0}}\rho$.

Proof. The proof is in Appendix Section. B.3. □

Theorem 5.2. *The Laplace transform of I_{Inter} is given by:*

$$\mathcal{L}_{Inter}(\rho) \approx \prod_{q\in Q} \exp\Bigg[-2\pi\lambda_G a N_q \frac{\pi}{\eta \sin\left(\pi\frac{2}{\eta}\right)} \left(\alpha P_q \rho\right)^{\frac{2}{\eta}} \times \frac{1}{2Tc} \left(\frac{2\eta}{\eta+2} l_{q_0}\left(min(1, \frac{l_q}{l_{q_0}})\right)^{\frac{\eta+2}{\eta}} + \left(min(1, \frac{l_q}{l_{q_0}})\right)^{\frac{2}{\eta}} \left|l_{q_0} - l_q\right|\right)\Bigg]. \tag{5.15}$$

Proof. The proof is in Appendix Section. B.4. □

Using Eq. 5.8 and Eq. 5.15, the general expression of P_s is given in Eq. 5.16.

$$P_s(r_0, q_0) = \exp\left(-\rho\sigma^2\right) \prod_{q\in Q} \Bigg[\exp\left(-2\pi a\lambda_{ED}\left(I_1(q) - I_2(q) - I_3(q)\right)\right) \times \exp\left(\frac{-2\pi^2\lambda_G a N_q}{\eta \sin\left(\pi\frac{2}{\eta}\right)} \left(\alpha P_q \rho\right)^{\frac{2}{\eta}} \left(\frac{1}{2Tc}\frac{2\eta}{\eta+2} l_{q_0}\left(min(1, \frac{l_q}{l_{q_0}})\right)^{\frac{\eta+2}{\eta}} + \left(min(1, \frac{l_q}{l_{q_0}})\right)^{\frac{2}{\eta}} \left|l_{q_0} - l_q\right| \right) \right) \Bigg]. \tag{5.16}$$

5.3.3 Special Cases

Here, we deduce few special cases from the general expression of transmission success probability obtained in Eq. 5.16 that can scales down to other works in the literature:

- **Perfect Orthogonality:** If we consider perfect orthogonality, the transmission success probability simplifies to:

$$P_s(r_0, q_0) = \exp\left(-\rho\sigma^2\right) \exp\left(-2\pi a \lambda_{ED} \left(I_1(q_0) - I_2(q_0)\right)\right) \exp\left(\frac{-2\pi^2 \lambda_G a N_{q_0} l_{q_0} r_0^2 \gamma_{th}^{\frac{2}{\eta}}}{Tc(\eta+2)\sin\left(\pi\frac{2}{\eta}\right)}\right). \tag{5.17}$$

- **Single Gateway Topology:** For a single gateway topology, only Intra-cluster interference is considered:

$$P_s(r_0, q_0) = \exp\left(-\rho\sigma^2\right) \prod_{q \in Q} \exp\left(\left(-2\pi a \lambda_{ED} \left(I_1(q) - I_2(q) - I_3(q)\right)\right)\right). \tag{5.18}$$

- **Only one interfering SF:** Considering the q'th SF:

$$P_s(r_0, q_0) = \exp\left(-\rho\sigma^2\right) \exp\left(-2\pi a \lambda_{ED} \left(I_1(q) - I_2(q) - I_3(q)\right)\right)$$
$$\times \exp\left(\frac{-2\pi^2 \lambda_G a N_q}{\eta \sin \pi\frac{2}{\eta}} \left(\alpha P_q \rho\right)^{\frac{2}{\eta}} \left(\frac{1}{2Tc} \frac{2\eta}{\eta+2} l_{q_0} \left(min(1, \frac{l_q}{l_{q_0}})\right)^{\frac{\eta+2}{\eta}} + \left(min(1, \frac{l_q}{l_{q_0}})\right)^{\frac{2}{\eta}} |l_{q_0} - l_q|\right)\right). \tag{5.19}$$

- **Same Power Allocation:** Assuming all the SFs use the same power, $P_q = P_{q_0}$, and b in (Eq. 5.8) simplifies to $\frac{min(l_q, l_{q_0})}{l_{q_0}} \gamma_{th} r_0^{\eta}$.

5.4 Numerical Results and Discussion

5.4.1 Simulation Setup

The simulation parameters are fixed according to a typical LoRa network. According to [161], a typical metropolitan area of 100 km^2 can be covered by 30 gateways

and LoRa coverage radius for dense urban environment is about 2 km. Hence, unless otherwise mentioned, R= 2 km, λ_G = 0.3 nodes/km^2. The packet size is fixed to 25 bytes and its time-on-air is calculated, based on each SF Data Rate as shown in Tab. 5.1. Unless otherwise mentioned, the remaining simulation setup parameters are fixed to Tc = 1.5 sec, η = 3, a= 0.1 (10%), λ_{ED} = 100 nodes/km^2 and P_q = 14 dBm.

SF	7	8	9	10	11	12
ToA (sec)	0.036	0.064	0.113	0.204	0.365	0.682

Table 5.1: Packet Time on Air [128].

To analyze the impact of power allocation on the packet success probability, we tested two schemes: same power allocation and SF-based power allocation. For the first scheme, P_q = 14 dBm is used by all the SFs; while for the second, the power is attributed according to the used SF. Higher SFs are assigned higher powers following Tab. 5.2.

SF	7	8	9	10	11	12
P_q(dBm)	2	5	8	11	14	20

Table 5.2: SF-based Power Allocation

5.4.2 Validation of the Spatiotemporal Model

We start by verifying the tightness of the analytical expressions of both single-gateway and multi-gateway LoRa networks using *Monte Carlo* (MC) simulations. The simulations are conduced over a random, yet fixed, instantiation of the MCP LoRa network. While the nodes spatial instantiation remains fixed, the fading realisations, transmissions start times and the satisfaction of duty cycle constraints change over time. The desired node position is fixed based on the SF to evaluate at $r_0(q) = d_{q-1} + \frac{\omega}{2}$ and its transmission status remains equal to 1 (always active).

We can interpret each simulation step as a temporal observation window. During each window, the interfering nodes are determined based on the duty

cycle parameter a; once the DC is satisfied, the transmission start time of each node is randomly generated following a uniform distribution. The collision overlap time with the desired packet is then calculated and multiplied by the interfering power. Finally, the transmission success probability of each SF, under both perfect/imperfect SF orthogonality, is obtained by averaging over the number of simulations. Whenever indicated in the figures of this section, markers illustrate results obtained by MC, solid lines corresponds to imperfect orthogonality scenario i.e (Co-SF + Inter-SF) interference while dashed lines correspond to the impact of only Co-SF interference.

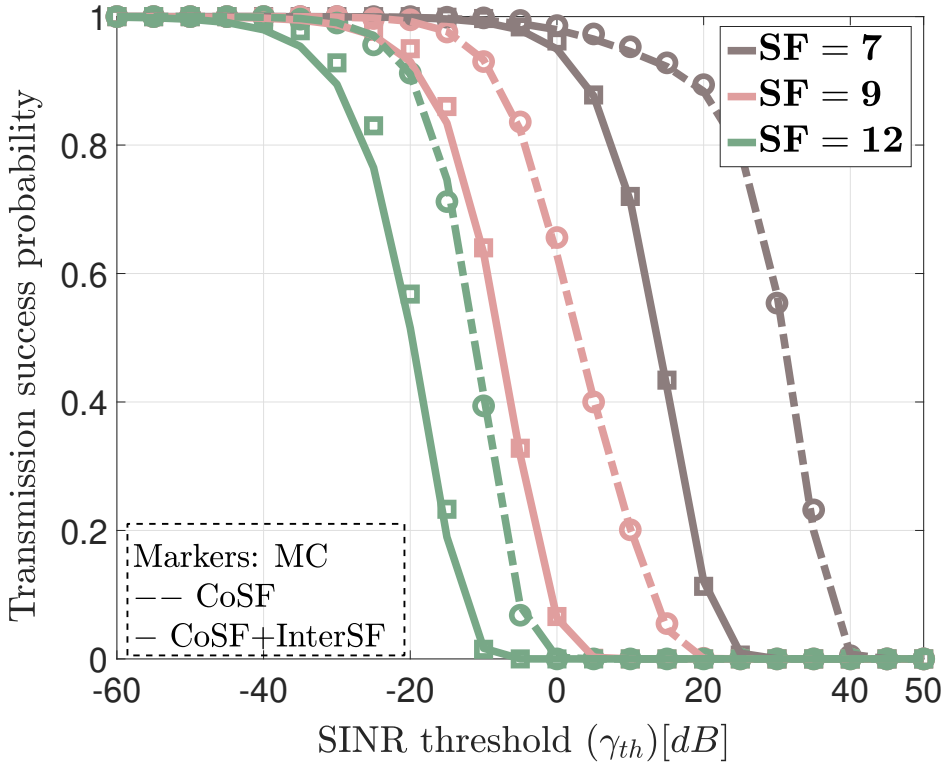

Fig. 5.4: Transmission success probability (P_{Succ}) versus different SINR thresholds (γ_{th}) for Single Gateway topology.

In Fig. 5.4 and Fig. 5.5 we plot the transmission success probability of each desired SF versus different SINR thresholds for, respectively, single-gateway and and multi-gateway LoRa topologies. Solid lines illustrate the impact of both interference types (Co-SF and Inter-SF), while dashed lines illustrate the impact of only Co-SF interference. First, the good match between analytical results (lines) and MC simulations (markers) validate the accuracy of the our theoretical analysis.

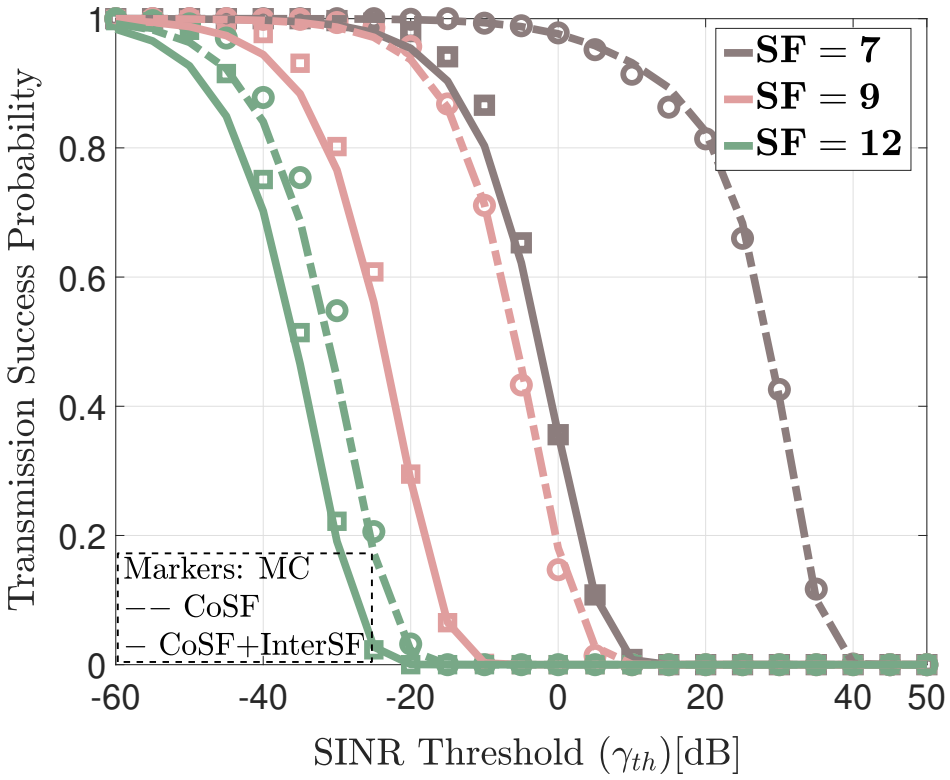

Fig. 5.5: Transmission success probability (P_{Succ}) versus different SINR thresholds (γ_{th}) for a Multi-Gateway topology.

Examining Fig. 5.4 and Fig. 5.5, we can see that for each SF, the probability of successful transmission under aggregated interference from different SFs is considerably lower than the result obtained by considering only Co-SF interference. The perfect orthogonality assumption, commonly used in the literature, results in an overestimation of the network performance which may impact its dimensioning and planning. As expected, packet transmission success decreases with SF. This decrease can be explained by the fact that higher SFs have a longer ToA which leads to longer overlap times with the desired packet exposing the node to more severe interference. Moreover, in the EIB SF allocation, high SFs are assigned to outer regions of the cell which makes them suffer from a near-far problem when interfering with lower SFs. This near-far problem worsens their capture probability.

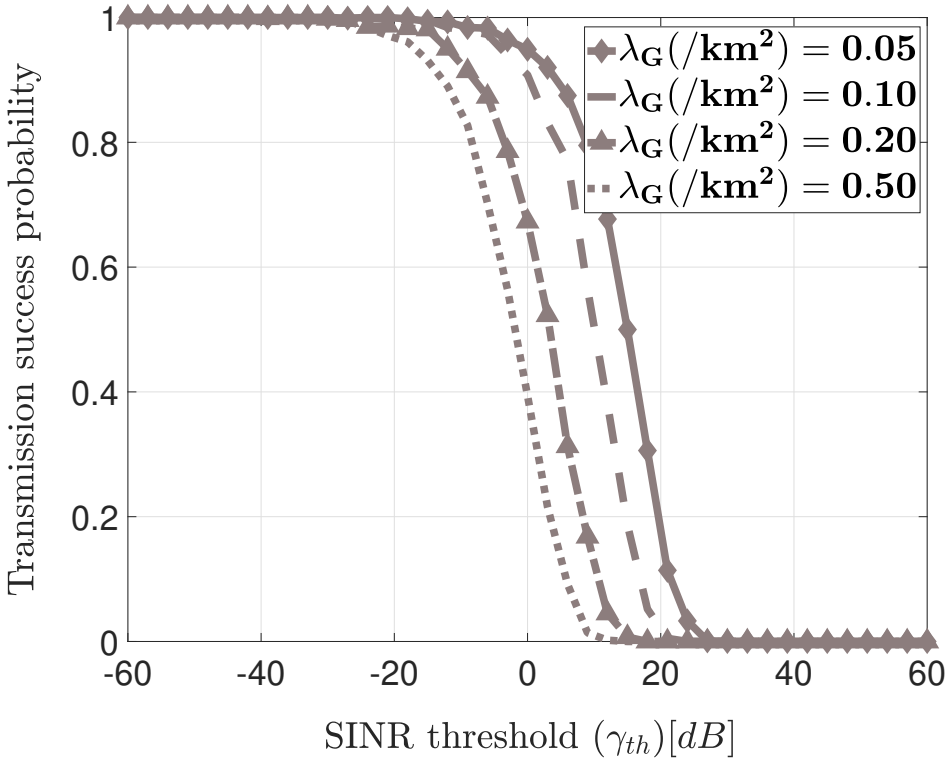

Fig. 5.6: Transmission success probability under Intra-Cluster and Inter-Cluster Interference (P_{Succ}) of SF= 7 versus different SINR thresholds (γ_{th}) for different λ_G.

5.4.3 Impact of Gateway Density

In Fig. 5.6, we study the impact of the gateway density on the transmission success performance of SF= 7. Increasing λ_G worsens the inter-cluster interference and deteriorates the transmission success probability. For a γ_{th} = 0 dB, multiplying λ_G by 10 (from λ_G = 0.05 to λ_G = 0.5) cuts down the transmission success probability by more than half.

5.4.4 Impact of Nodes Density

In Fig. 5.7, we plot the transmission success probability of different desired SFs under both aggregated interference and only co-SF interference, for different devices densities in a LoRa cluster. Higher nodes densities degrade all the SFs performance and its impact is more prominent for higher SFs as it appears for SF= 11 and SF= 12. As the nodes density increases, the required γ_{th} to achieve

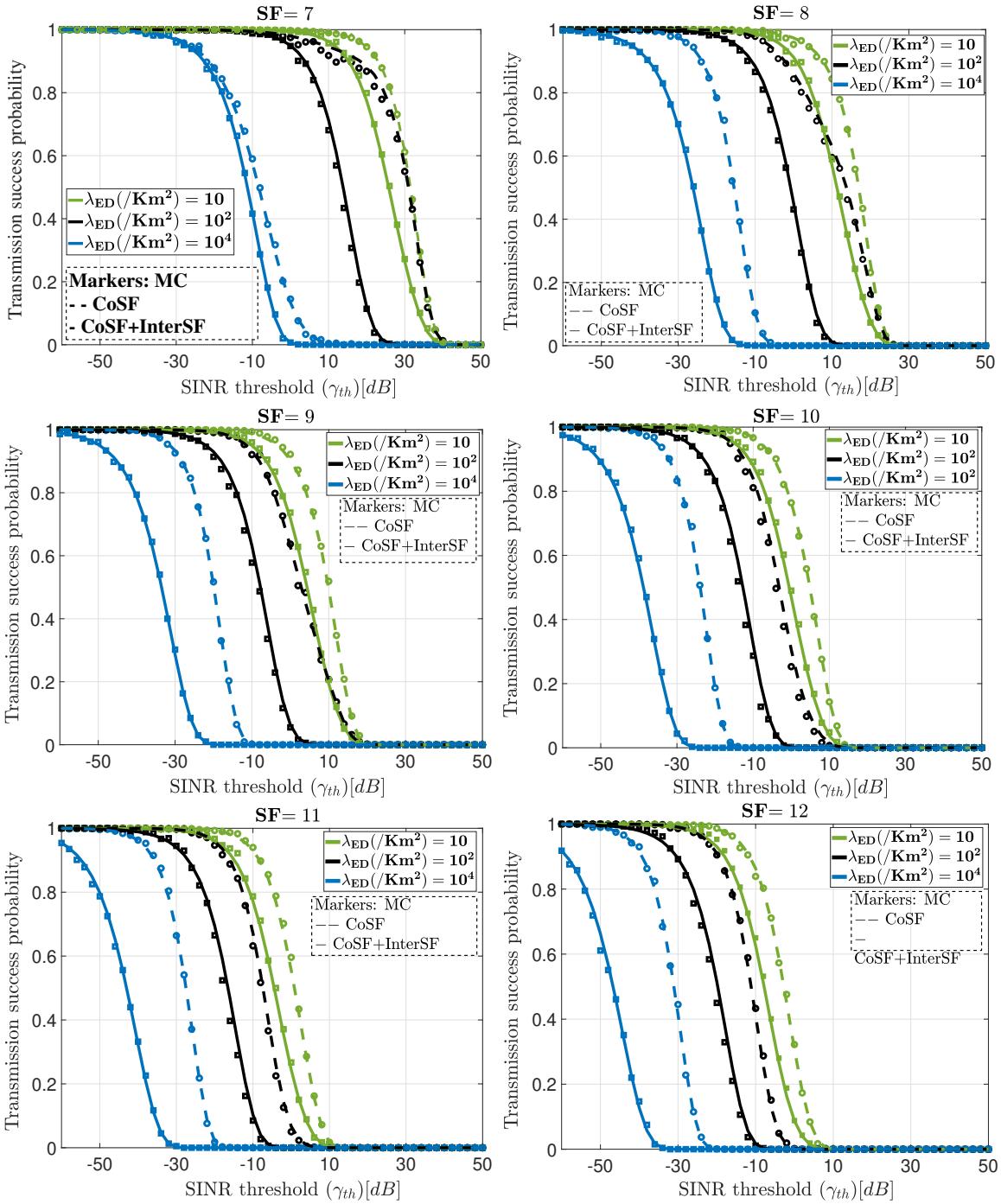

Fig. 5.7: Transmission success probability versus SINR thresholds for different λ_{ED} in a single LoRa cell.

a same reliability level decreases and varies among the SFs. Fixing a reliability level of 80%, the required decoding threshold for SF= 7 is $\gamma_{th} = \{20, 8, -18\}$ (dB) for $\lambda_{ED} \in \{10, 10^2, 10^4\}$ nodes/km^2, respectively. For a fixed density, to maintain a same reliability level, the capture threshold needs to be decreases as the SF increases. Comparing solid lines (Co-SF + Inter-SF) and dashed lines (Co-SF) in Fig. 5.7, it is found that the impact of inter-SF interference increases as the nodes density increases for SF$\geq$ 8. For SF= 7 which occupies the nearest annulus to the gateway and has the lowest ToA, the impact of Co-SF becomes dominant for a very highly loaded network ($\lambda_{ED} = 10^4$ nodes/km^2).

5.4.5 Impact of Contention Window

In Fig. 5.8, we track the transmission success probability of different SFs as the contention window size increases. Increasing the contention window size makes transmissions attempts spread over a larger interval which minimizes the collision probability, improving, as a result, the packet reception of different SFs. Examining the gap between solid and dashed lines, a small contention window size is found to have a detrimental effect on the performance of low SFs (SF= 7 and SF= 8) under the imperfect orthogonality assumption as it increases their exposure to overlap with higher SFs, therefore more Inter-SF interference. We can see that for a large contention window size, the perfect orthogonality assumption overestimates the performance of SF= 8 given a detection threshold of 10 dB by up to 10% while this amplification reaches more than 40% for a small contention window size. This observation highlights further the importance of orthogonality assumption on the performance analysis for the network.

5.4.6 Impact of Power Allocation

To assess the impact of SFs on one another performance, we plot in Fig. 5.9 and Fig. 5.10 the transmission success probability of each SF under interference from one specific interfering SF-set. In Fig. 5.9, we considered the same power allocated to all the nodes independently from the used SF, while in Fig. 5.10, we used the

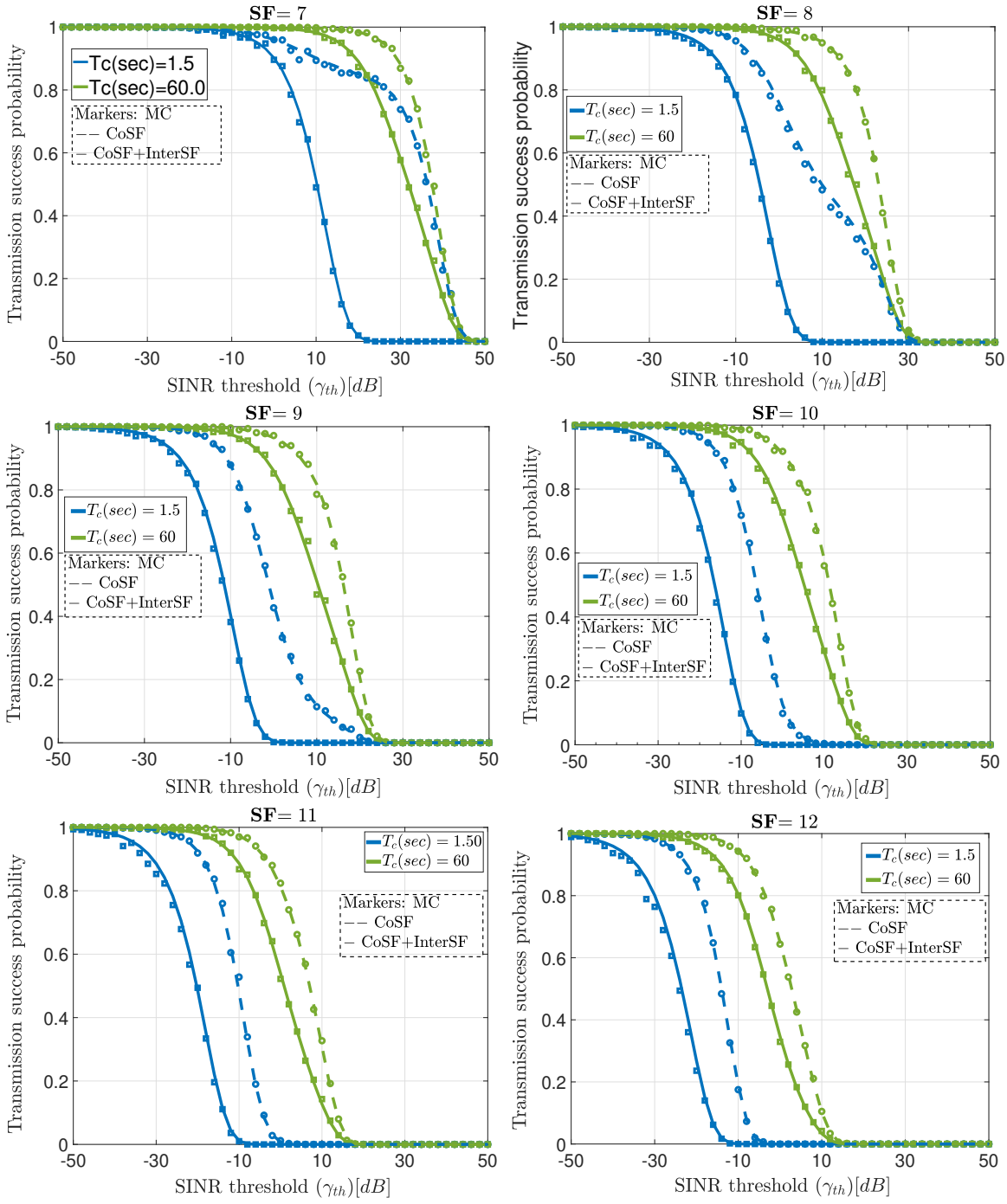

Fig. 5.8: Transmission success probability versus SINR thresholds for different contention window sizes in a single LoRa cell.

SF-based power allocation from Tab. 5.2 where higher power is assigned to higher SFs. Under SF-based power allocation, only one common behaviour for all the SFs is recognized: higher SFs deteriorates more the transmission success probability more regardless of the SINR threshold. The SF-based power allocation improves

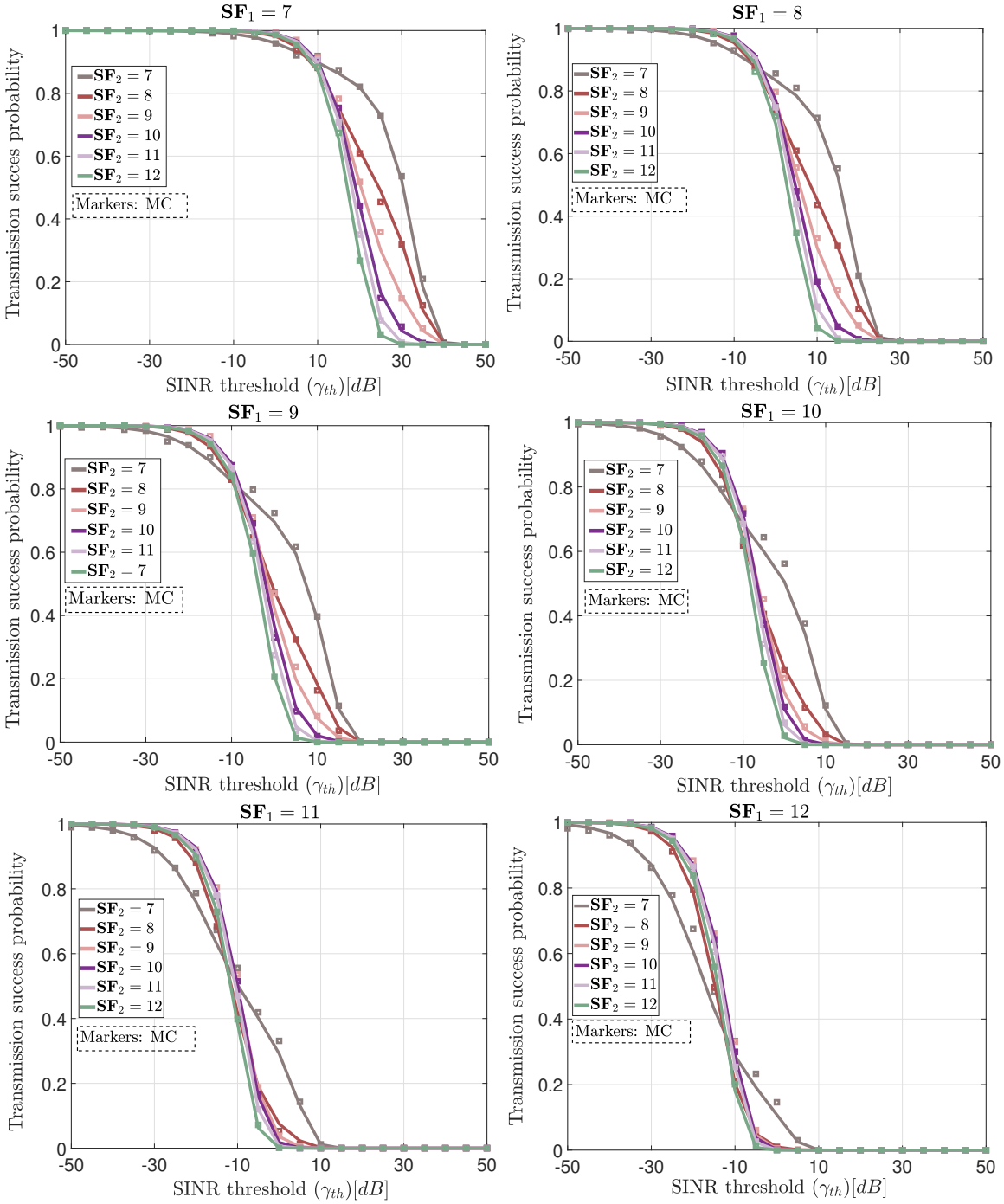

Fig. 5.9: Transmission success probability versus SINR thresholds under Per-SF interference and same power allocation in a single LoRa cell with λ_{ED} = 200 nodes/km^2.

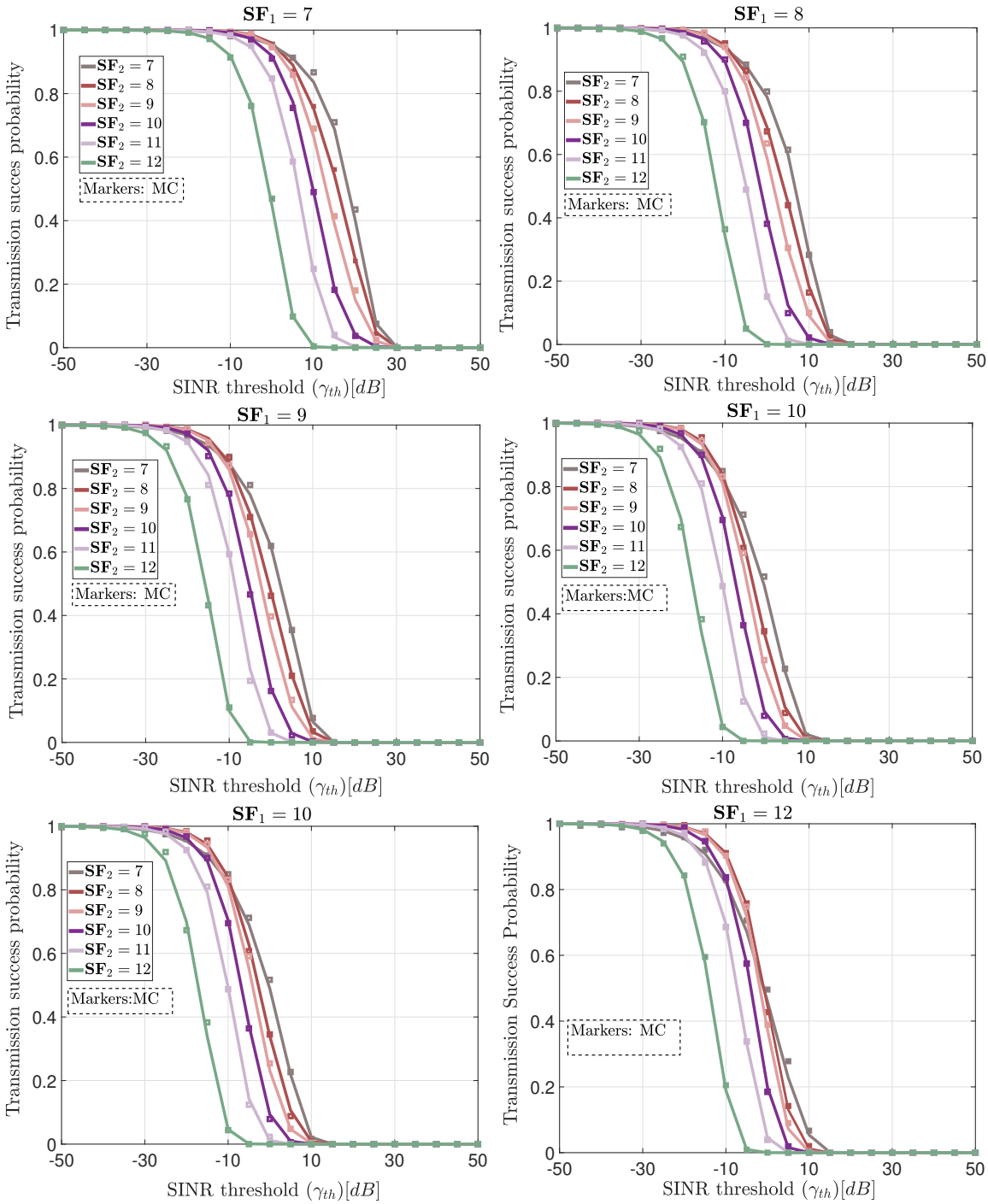

Fig. 5.10: Transmission success probability versus SINR thresholds under Per-SF interference and SF-based power allocation in a single LoRa cell with λ_{ED} = 200 nodes/km^2.

the performance of higher SFs as it mitigates the near-far problem higher SFs would suffer from but it decreases the performance of lower SFs compared to the same power allocation. Taking desired SF= 12, an SINR threshold of −10dB gives

a success probability of 30% regardless of the interfering SF when the same power is allocated to the SFs, whereas under the SF-based power allocation, the success probability overcomes 68% for SFs lower than 11.

Fig. 5.7, Fig. 5.8, Fig. 5.9, and Fig. 5.10 confirm that the decoding thresholds required for a reliability level are not fixed and do not depend only on the desired and interfering SFs, they are also impacted by the nodes density, the power allocation, the start time distribution. These thresholds decrease with the interfering SF, when the nodes density increase, and as the transmission start times of the nodes are spread across a short interval.

5.5 Discussion, Limitations and Future Extensions

Highly-Clustered Versus Overlapped Networks: Motivated by LoRa deployment model and the HDB private agglomerated urban nomenclature, the analytical framework proposed in this chapter relies on a MCP with a high clustering degree. This assumption makes the distance of a node to its cluster head much larger that the distance between the clusters heads (see Section. B.4). Given that, each LoRa node forms an offspring point associated to a gateway which is the head of the cluster it belongs to. This topology can be of interest for many applications and use-cases. HDB applications (building monitoring, lift monitoring, water harvesting system monitoring, pipeline monitoring, environment monitoring) are examples of them. However, since the packets transmitted from LoRa nodes can be received by multiple gateways, we can encounter cases where two or more clusters are overlapped. This could particularly happen in mobility scenarios or in the densification of an already deployed network. In such scenarios, a LoRa node could be nearer to a different cluster head than that it belongs to especially if it is at the edge of the cluster. This overlapping situation requires to account for the association of the node to its nearest gateway. For this, purpose, one needs to derive the *Probability Density Function* (PDF) of the distance to the nearest gateway. To address this challenge, the following reference provide a good start point [162].

Un-quantified LoRa Imperfect Orthogonality: In this chapter, we analysed the performance of LoRa networks under two scenarios: First, the perfect orthogonality scenario where we accounted for interference coming from only the same SF across different clusters. Second, the imperfect orthogonality scenario where we accounted for the aggregated interference coming from same or different SFs. While the first scenario represents an optimistic scenario, the latter is a worst case scenario as we treated the SFs equally , i.e without distinction about which SF impacts statistically the most an other SF. Yet, we tried to mitigate this limitation through the formulated collision overlap function. However, a more accurate quantification of how exactly orthogonal are LoRa SFs should lie between these two extreme scenarios (worst and best) and would provide preciser performance limits. In the next chapters, we address this limitation by adopting the results obtained from the link-level analysis of Chapter. 4.

Saturated LoRa Buffers: The analytical framework proposed in this chapter is a useful tool to analyse the transmission success probability and the coverage in LoRa networks. Yet, it does not reflect the dynamics of LoRa nodes (buffers) as it is oblivious to the protocol states. The nodes dynamics can be influenced by many factors including LoRa DC restrictions, packet failure and the possibility of packet re-transmissions. Therefore such coverage-only SG-based analysis, by assuming saturated buffers does not give any insights about useful metrics such as the average latency, the Pareto stability frontiers. Therefore, in the next chapters, we address this shortcoming by the joint use of QT and SG.

5.6 Chapter Summary and Key Findings

In this chapter, we characterise, using powerful tools from SG, the performance of uplink transmissions in multi-gateway LoRa networks modelled by a MCP. The proposed model considers a multi-cell topology, perfect/imperfect SF orthogonality scenarios, and random transmission start times. With all these factors taken into account, we initially developed the SF-dependent collision overlap time function for any start-time distribution. We then analyse the Laplace transforms

of Intra-cluster and Inter-cluster interference and formulate the UP transmission success probability. MC simulations validate the tightness of our analytical results. This chapter has thoroughly investigated the impact of SF orthogonality assumption, SF capture thresholds, power allocation as well as the nodes density and transmission start time distribution on the network reliability through the formulated transmission success probability metric.

Key Findings

Below we summarize the key findings of this chapter:

- The perfect orthogonality assumption between LoRa SFs overestimate the expected reliability level of the network compared to the imperfect orthogonality scenario. Taking the example of SF= 9 and a detection threshold of -30 dB, this amplification reaches 200% in a highly congested network (10^4 nodes/km^2) due to the impact of inter-SF interference.
- Given a detection threshold of 10 dB and a large contention window size, the perfect orthogonality assumption overestimates the performance of low SFs (SF= 7, SF= 8) by up to 12% while this amplification reaches more than 80% with a small contention window size.
- Analysing the impact of SFs on each others performance, the chapter has evinced that the interfering SF degrading the most the performance of a desired SF depends on the decoding threshold range and the power allocation scheme.
- We have found that assigning the power incrementally with the SF mitigates the near-far problem between low and high SFs arising from the distance-based EIB allocation. Therefore, the performance of higher SFs is improved. However, this power allocation coupled with the long ToA makes higher SFs the most detrimental to packet collision with the remaining SFs. On ther other side, when the SFs are allocated the same power, the most detrimental SF varies with the SINR regime. For low SINR thresholds, lower SFs are culprit for the performance deterioration.

- The analysis has confirmed, through the behaviors presented in Fig. 5.7 and Fig. 5.8, that the impact of interference (Co-SF and Inter-SF) on the performance of each of the SFs is deeply governed by the SF allocation scheme, the density regime, and the transmission time distribution among the nodes.
- LoRa decoding thresholds decrease with the SF, when the nodes density increases and as the transmission start times are less spread.

At the end of the chapter, we have discussed some of the limitations that could be addressed as future extensions of the proposed spatiotemporal model. In the next chapter, we address the limitation of saturated buffers by jointly incorporating SG with QT and the limitation of unquantified orthogonality by adopting the result of the link-level analysis carried out in Chapter. 4. The remaining limitations could be addressed in future works.

CHAPTER 6

Scalability, Reliability, and Latency in Duty-Cycled LoRa Networks with Static SF Allocation

6.1 Motivation and Contribution

In the previous chapter (Chapter. 5), SG was leveraged alone, under the assumption of saturated LoRa buffers, to study transmission success probability in single and multi-gateway LoRa networks. In this chapter, we take a step further in the scalability analysis of LoRa networks by incorporating the DTMC-based device-level modelling into the SG analysis. This approach bridges the gap between stand-alone QT approaches and SG-based scalability analysis allowing to account for both network spatial and temporal dynamics ,therefore, enabling a comprehensive assessment of the performance tradeoffs in large scale LoRa networks. We propose a novel inclusive spatiotemporal model where QT and SG are combined via a 2−D DTMC that tracks the node's data buffer and protocol state.

In this chapter and the next (Chapter. 7), we will focus on single-gateway LoRa topologies. The rationale behind this choice is to keep our focus on the trade-offs between the different performance metrics and the impact of LoRa physical features such as duty-cycle, imperfect orthogonality, and SF allocation. Noting

that single-gateway LoRa networks still have their significance for deployments in small-medium towns and for naturally-clustered sensing applications such as building, industrial, and agricultural monitoring. The significance of LoRa single-gateway deployments is manifested by the focus they have been receiving in many papers of LoRa/LoRaWAN state of the art [90, 92, 95, 123, 125, 126, 127, 129, 132, 133, 136, 137, 139, 144, 145, 163]. It is worth highlighting that the multi-gateway scenario can be, a straightforward yet a bit tedious, follow-up extension by recalling the stochastic geometry model we developed for multi-gateway LoRa topologies in Chapter. 5 .

6.2 System Model

6.2.1 Spatial Distribution

We consider a LoRa network where nodes are randomly scattered around a central gateway according to a homogeneous PPP Φ_L of intensity λ_L. Each node is assigned a spreading factor SF_q and shares the same bandwidth BW to communicate to the gateway. To account for the traffic requirements and DC states, let $\tilde{\Phi}_L$ be the thinned process of concurrently transmitting nodes. The subset of active nodes using SF_q is $\tilde{\Phi}_{L,q}$. We denote $\mathbf{\Delta} = [\delta_1, \ldots, \delta_q, \ldots, \delta_N]$ the activity vector of different SFs.

6.2.2 Propagation model

We consider a power-law path-loss propagation model where the signal attenuates with the propagation distance at the rate $\alpha r^{-\eta}$, $\eta > 2$ is the path-loss exponent, and α is the frequency dependant factor. Further, we have Rayleigh block fading channels with unit-mean exponentially distributed gains i.e. $g_i \sim exp(1)$. For tractability reasons, channel gains are assumed to be i.i.d. in both space and time dimensions.

6.2.3 Channel Access and Queuing Model

We assume a time-partitioned system. All nodes sense for the same application characterised by packet size L and per-slot data arrival probability a, which are linked to the sensing resolution and frequency, i.e. how often the updates will be sent to the application server. This traffic characterisation represents typical environmental and monitoring applications [164, 165]. In particular, at each device, packets of size L are generated according to a geometric distribution with parameter $a \in [0, 1]$. The generated packets are stored in a *First In First Out* (FIFO) queue. The head of the line packet is transmitted at the beginning of the time slot. As the aim of this chapter is to explore LoRa UP transmissions, we assume error-free DL communications.

6.2.4 LoRa Duty-Cycling

Let N be the total number of available SFs ranging from SF_1 to SF_N. Since LoRa symbol duration is expressed as $t_{s,q} = \frac{2^{SF_q}}{BW}$ as detailed in Chapter. 4, l_q the ToA of packet transmission using SF_q, doubles from SF_q to SF_{q+1}. We fix LoRa regulatory DC detailed in Subsection. 2.3.2 to 1% where each transmission during l_q is followed by a silent duration $99 \times l_q$. The adopted system slot is $T_1 = 100 \times l_1$ during which each node transmits no more than once $\forall$ SF_q [144]. As LoRa DC duration is a function of the ToA, each transmission using SF_q will be followed by n_q DC logical sub-states, $DC_q = \{DC_{q,1}, ..., DC_{q,n_q}\}$, with $n_q = 2^{q-1} - 1$ for $q > 1$ $n_1 = 0$.

6.2.5 LoRa β_{q_1,q_2} – SF Orthogonality

Given the non-perfect orthogonality of LoRa modulation confirmed in Chapter. 4, we examine a more realistic and practically more useful interference scenario, denoted hereinafter β_{q_1,q_2}-orthogonality, where each SF experiences interference from the concurrently transmitting SFs with an orthogonality coefficient β_{q_1,q_2}. These coefficients are outcome of the analysis carried in Chapter. 2, listed in

Section. A.3, and recalled below. Interference from same SFs and different SFs will be denoted hereinafter Co-SF and Inter-SF interference, respectively.

7	1					
8	0.104	1				
9	0.062	0.073	1			
10	0.041	0.043	0.052	1		
11	0.029	0.029	0.030	0.037	1	
12	0.021	0.020	0.020	0.021	0.026	1
SF_1 / SF_2	**7**	**8**	**9**	**10**	**11**	**12**

Table 6.1: LoRa SF Orthogonality Coefficients β_{q_1,q_2}

6.2.6 SF Allocation

In line with the commonly adopted SF allocation schemes in the literature, the SFs are allocated to the nodes following a distance-dependant scheme where each SF occupies a region of width [$d_{q-1} - d_q$] (e.g., EIB, EAB [136, 137, 138]).

6.3 Spatiotemporal Framework

Following the methodology explained in Section. 1.4, the proposed framework relies on integrated SG and QT models. SG allows us to derive the probability of coverage considering the spatial distribution of the nodes, while QT tracks the evolution of the nodes' MAC state and determines the activities of the nodes. These activities control the interference intensity that impact the coverage probability. Following subsections detail the SG and QT frameworks as well as the iterative solution to solve the interdependence between them.

6.3.1 Macroscopic Coverage Analysis with Stochastic Geometry

The received SINR at the gateway from a desired LoRa node located at $r_0 = \|x_0\|$ and using SF_{q_0} is given by:

$$\mathrm{SINR}(r_0, q_0) = \frac{\mathcal{P} g_0 \alpha r_0^{-\eta}}{\mathcal{I} + \sigma^2}, \tag{6.1}$$

where $\mathcal{P}$ the transmit power, $\mathcal{I}$ is the aggregate interference , and σ^2 is the variance of an AWGN. $\mathcal{I}$ is expressed as:

$$\mathcal{I} = \sum_{q \in Q} \sum_{x_j \in \tilde{\Phi}_{L,q} \setminus x_0} \mathcal{P} \alpha \|x_j\|^{-\eta} \beta_{q_0,q} g_j. \tag{6.2}$$

The impact of LoRa imperfect-orthogonality is captured via the orthogonality coefficients $\beta_{q_0,q}$ in Tab. 6.1.

A LoRa gateway successfully decodes a packet if the instantaneous SINR surpasses a capture threshold γ_q. We denote by $\Gamma = [\gamma_1, \gamma_2 ... \gamma_N]$ the capture threshold vector of different SFs. Considering these thresholds, the transmission success probability of a packet transmitted with SF_{q_0} from a node located at distance r_0 is given by:

$$p_s(r_0, q_0, \gamma_{q_0}) = \mathbb{P}\{\mathrm{SINR}(r_0, q_0) \geq \gamma_{q_0}\} = \exp\Big(-\rho_{q_0} \sigma^2\Big) \mathcal{L}_{\mathcal{I}}(\rho_{q_0}), \tag{6.3}$$

where $\rho_{q_0} = \frac{\gamma_{q_0} r_0^{\eta}}{\mathcal{P}\alpha}$.

Theorem 6.1. *Considering a distance-based SF allocation, the coverage probability, defined as the spatially averaged transmission success probability of SF_{q_0}, is expressed as:*

$$p_{q_0} = \int_{d_{q_0-1}}^{d_{q_0}} p_s(r_0, q_0, \gamma_{q_0}) \frac{2 r_0}{d_{q_0}^2 - d_{q_0-1}^2} dr_0, \tag{6.4}$$

with

$$p_s(r_0, q_0, \gamma_{q_0}) = \exp\Big(-\rho_{q_0} \sigma^2\Big) \prod_{q=1}^{N} \exp\Big(-2\pi \delta_q \lambda_L \Big(\mathcal{J}(d_q) - \mathcal{J}(d_{q-1})\Big)\Big), \tag{6.5}$$

$\mathcal{J}(x) = \frac{x^2}{2}\, {}_2F_1\left(1, \frac{2}{\eta}; 1 + \frac{2}{\eta}; -\frac{x^{\eta}}{b}\right)$, *and* $b = \alpha \rho_{q_0} \mathcal{P} \beta_{q_0,q}$.

Proof. The proof is in Appendix Chapter. C. □

6.3.2 Microscopic Device-Level Queuing Theory Analysis

Since a single packet can arrive and/or depart from a buffer at a given time slot, each device is characterised by a QBD process (Subsection. 1.6.2). The transition matrix of the DTMC tracks the number of packets at the device buffer and is given, for each SF_q, by :

$$\boldsymbol{P}_q = \begin{pmatrix} \boldsymbol{B}_q & \boldsymbol{C}_q & \mathbf{0} & \mathbf{0} & \mathbf{0} & \dots \\ \boldsymbol{E}_q & \boldsymbol{A}_{q,1} & \boldsymbol{A}_{q,0} & \mathbf{0} & \mathbf{0} & \ddots \\ \mathbf{0} & \boldsymbol{A}_{q,2} & \boldsymbol{A}_{q,1} & \boldsymbol{A}_{q,0} & \mathbf{0} & \ddots \\ \vdots & \ddots & \ddots & \ddots & \ddots & \ddots \end{pmatrix}, \tag{6.6}$$

where $\boldsymbol{A}_{q,0}$, $\boldsymbol{A}_{q,1}$ and $\boldsymbol{A}_{q,2}$ track the buffer when it increases by one level, stays in the same level, and decreases by one level, respectively. The matrices $\boldsymbol{B}_q$, $\boldsymbol{C}_q$, and $\boldsymbol{E}_q$ track the transition within level 0, from level 0 up to level 1, and from level 1 down to level 0, respectively.

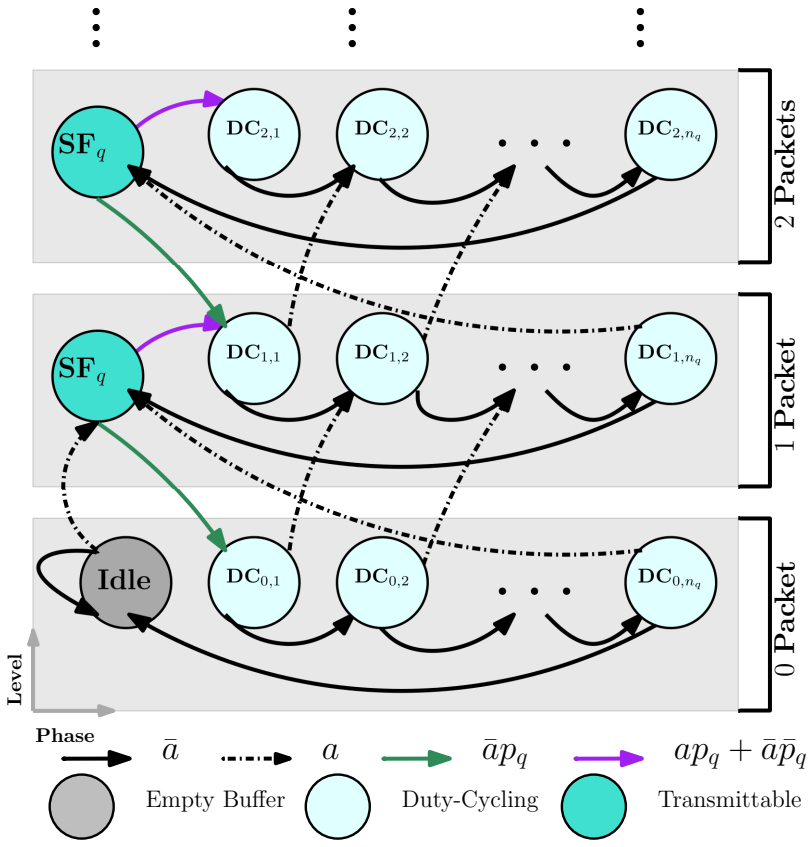

Fig. 6.1: DTMC of a LoRa node transmitting with SF_q.

Each device is perceived as a geometric inter-arrival times and PH service (Geo/PH/1) queue represented by the absorbing DTMC sketched in Fig. 6.1. We use the *Matrix Analytic Method* (MAM) [31, 166] to study the Geo/PH/1 queue depicting each LoRa device and construct the transition matrix $\boldsymbol{P}_q$. The PH-type parameters are given by the $(n_q + 1) \times (n_q + 1)$ matrix $\boldsymbol{F}_q$ defined in Eq. 6.7 and the $1 \times (n_q + 1)$ initialisation vector $\boldsymbol{\beta}_q = [0, 1, 0, \cdots, 0]$. $\boldsymbol{F}_q$ tracks the transition probabilities between phases until absorption. Noting that absorption in the context of our queuing analysis corresponds to transmission success i.e. packet departure from the nodes 's buffer. The absorption probabilities from the transient states phases are defined by the the vector $\boldsymbol{s}_q = \boldsymbol{e} - \boldsymbol{F}_q \boldsymbol{e}$. The transitions at level 0 are captured by $\boldsymbol{M}_{q,0}$.

$$\boldsymbol{F}_q = \begin{bmatrix} 0 & \bar{p}_q & 0 & \dots & 0 \\ 0 & 0 & 1 & \dots & 0 \\ \vdots & \ddots & \ddots & \ddots & \vdots \\ 0 & \dots & 0 & 0 & 1 \\ 1 & \dots & 0 & 0 & 0 \end{bmatrix}, \boldsymbol{M}_{q,0} = \begin{bmatrix} 1 & 0 & 0 & \dots & 0 \\ 0 & 0 & 1 & \dots & 0 \\ \vdots & \ddots & \ddots & \ddots & \vdots \\ 0 & \dots & 0 & 0 & 1 \\ 1 & 0 & \dots & 0 & 0 \end{bmatrix}. \tag{6.7}$$

The matrices forming $\boldsymbol{P}_q$ have, therefore, the following expressions: $\boldsymbol{A}_{q,1} = a\boldsymbol{s}_q\boldsymbol{\beta}_q + \bar{a}\boldsymbol{F}_q$, $\boldsymbol{A}_{q,2} = \bar{a}\boldsymbol{s}_q\boldsymbol{\beta}_q$, $\boldsymbol{A}_{q,0} = a\boldsymbol{F}_q$, $\boldsymbol{B}_q = \bar{a}\boldsymbol{M}_{q,0}$, $\boldsymbol{C}_q = a\boldsymbol{M}_{q,0}$, and $\boldsymbol{E}_q = \boldsymbol{A}_{q,2}$.

Before analysing the steady state distribution, we check the conditions that ensure stable queues (Theorem. 1.3). The stability check is conducted by studying the stationary distribution vector $\boldsymbol{\pi}_q$ of the matrix $\mathbf{A}_q = \mathbf{A_{q,0}} + \mathbf{A_{q,1}} + \mathbf{A_{q,2}}$. The stationary distribution $\boldsymbol{\pi}_q$ is the unique solution of the system of equations:

$$\begin{cases} \boldsymbol{\pi}_q \mathbf{A}_q = \boldsymbol{\pi}_q & \text{(6.8a)} \\ \boldsymbol{\pi}_q \mathbf{e} = 1 & \text{(6.8b)} \end{cases}$$

Noting that the normalisation condition in Eq. 6.8b serves to ensure the summation of the probabilities is equal to 1.

Lemma 6.1. *For a data buffer to be stable, it needs to satisfy:*

$$\boldsymbol{\pi}_q \mathbf{A_{q,2}} \mathbf{e} > \boldsymbol{\pi}_q \mathbf{A_{q,0}} \mathbf{e} \quad \textit{where} \quad \boldsymbol{\pi}_q = \mathbf{e}^T (\boldsymbol{s}_q \boldsymbol{\beta}_q + \boldsymbol{F}_q - \mathbf{I} + \mathbf{e}\mathbf{e}^T)^{-1}. \tag{6.9}$$

Proof. The proof of lemma 6.1 follows from solving the system of equations $\boldsymbol{\pi}_q = \boldsymbol{\pi}_q \mathbf{A}$ and $\boldsymbol{\pi}_q \mathbf{e} = 1$ by recalling [Lemma 1, [167]] and using the expressions of $\boldsymbol{A_{q,2}}$, $\boldsymbol{A_{q,1}}$, and $\boldsymbol{A_{q,0}}$. □

We define the invariant probability vector with regard to $\boldsymbol{P}_q$ as $\mathbf{x}_q = \begin{bmatrix} \mathbf{x}_{q,0} & \dots & \mathbf{x}_{q,i} \end{bmatrix}$ such that $\mathbf{x}_{q,i} = \begin{bmatrix} x_{q,i,0} & \dots & x_{q,i,n_q+1} \end{bmatrix}$, where $x_{q,i,m}$ is the probability of having i packets in the buffer while being at phase m of the DTMC for SF_q. We obtain $\mathbf{x}_q$ by solving the system of equations defined by:

$$\begin{cases} \mathbf{x}_q = \mathbf{x}_q \boldsymbol{P}_q & \text{(6.10a)} \\ \mathbf{x}_q \mathbf{e} = 1. & \text{(6.10b)} \end{cases}$$

Based on the outcome of the stability check (Eq. 6.9) the subsequent two analyses are carried out:

A. Stable LoRa System Analysis

If the outcome of the stability check (Eq. 6.9) is true then the system in Eq. 6.10a and Eq. 6.10b has a unique solution that is obtained using the MAM [31, 166]. The solution is given in the following theorem:

Theorem 6.2. *The steady state probabilities $\boldsymbol{x}_q$ of a LoRa node using SF_q is given by:*

$$\boldsymbol{x}_{q,i} = \begin{cases} \boldsymbol{x}_{q,0} \boldsymbol{C}_q \left(\boldsymbol{I} - \boldsymbol{A}_{q,1} - \boldsymbol{R}_q \boldsymbol{A}_{q,2} \right)^{-1} \times \boldsymbol{E}_q \left(\boldsymbol{I} - \boldsymbol{B}_q \right)^{-1}, & \text{if } i = 0, \\ \boldsymbol{x}_{q,0} \boldsymbol{C}_q \left(\boldsymbol{I} - \boldsymbol{A}_{q,1} - \boldsymbol{R}_q \boldsymbol{A}_{q,2} \right)^{-1}, & \text{if } i = 1, \\ \boldsymbol{x}_{q,1} \boldsymbol{R}_q^{i-1}, & \text{if } i > 1, \end{cases} \tag{6.11}$$

with the normalisation condition $\boldsymbol{x}_{q,0} \boldsymbol{e} + \boldsymbol{x}_{q,1} \left(\boldsymbol{I} - \boldsymbol{R}_q \right)^{-1} \boldsymbol{e} = 1$ being satisfied, and $\boldsymbol{R}_q$ is the MAM [33, 166] rate matrix expressed as:

$$\boldsymbol{R}_q = a \boldsymbol{F}_q (\boldsymbol{I} - a \boldsymbol{s}_q \boldsymbol{\beta}_q - \bar{a} \boldsymbol{F}_q - a \boldsymbol{F}_q \boldsymbol{e} \boldsymbol{\beta}_q)^{-1}. \tag{6.12}$$

Proof. Following [33, Section 4.8], to find the steady state probabilities vector, we need first to find the boundaries elements by solving the following system of equations:

$$\begin{pmatrix} \boldsymbol{x}_{q,0} & \boldsymbol{x}_{q,1} \end{pmatrix} = \begin{pmatrix} \boldsymbol{x}_{q,0} & \boldsymbol{x}_{q,1} \end{pmatrix} \begin{pmatrix} \boldsymbol{B}_q & \boldsymbol{C}_q \\ \boldsymbol{E}_q & \boldsymbol{A}_{q,1} + \boldsymbol{R}_q \boldsymbol{A}_{q,2} \end{pmatrix}.$$

Using $\boldsymbol{x}_{q,i} = \boldsymbol{x}_{q,i-1}\boldsymbol{R}_q$, the steady state probabilities of the upper levels are deduced. $\boldsymbol{R}_q$ is the minimum non-negative solution of the quadratic equation: $\boldsymbol{R}_q = \boldsymbol{A}_{q,0} + \boldsymbol{R}_q\boldsymbol{A}_{q,1} + \boldsymbol{R}_q^2\boldsymbol{A}_{q,2}$. Since $\boldsymbol{A}_{q,2}$ is of rank 1, $\boldsymbol{R}_q$ is explicitly obtained [33] as in Eq. 6.12. □

When the stability conditions mentioned in lemma 6.1 are satisfied, $\boldsymbol{R}_q$ has a spectral radius less than 1 i.e. all its eigenvalues are in the unit disk [33].

Let $\boldsymbol{\varphi}_q = [\varphi_{q,1}, \ldots \varphi_{q,m}, \ldots, \varphi_{q,(n_q+1)}]$ be the marginal distribution of the phases with nonempty data buffers where the phase $\varphi_{q,m}$ can be either the transmissible or DC states of SF_q.

Corollary 6.1. *The activity probability of SF_q is given by $\delta_q = \varphi_{q,1}$, with $\varphi_{q,1}$ is the first element of the marginal distribution $\boldsymbol{\varphi_q}$ given by:*

$$\boldsymbol{\varphi}_q = \sum_{i\geq 1} \boldsymbol{x}_{q,i} = \boldsymbol{x}_{q,1}\left(\boldsymbol{I} - \boldsymbol{R}_q\right)^{-1}. \tag{6.13}$$

Note that $\boldsymbol{\varphi}$ is a sub-stochastic vector since it does not include the empty-buffer phases.

Proof. When lemma 6.1 is satisfied, $\boldsymbol{R}_q$ has a spectral radius less than 1. Hence, the geometric series generated by $\boldsymbol{R}_q$ converges and the proof follows. □

B. Unstable LoRa System Analysis

If lemma 6.1 is not satisfied, the system is unstable which makes the buffer overflows. The probability to have empty buffer is, therefore, nullified and the marginal steady state distribution of the phases is obtained by the expression derived in lemma 6.1 i.e. $\boldsymbol{\varphi}_q = \boldsymbol{\pi}_q$ and $\delta_q = \pi_{q,1}$.

Remark 6.1. *For the case $q = 1$, the Geo/PH/1 system in Eq. 6.6 boils down to a Geo/Geo/1 with:*

$$\boldsymbol{P}_1 = \begin{pmatrix} \bar{a} & a & & & \\ \bar{a}p_1 & \bar{a}\bar{p}_1 + ap_1 & a\bar{p}_1 & & \\ & \bar{a}p_1 & \bar{a}\bar{p}_1 + ap_1 & a\bar{p}_1 & \\ & & \ddots & \ddots & \ddots \end{pmatrix}. \tag{6.14}$$

Algorithm 1: Computation of $\boldsymbol{\varphi}_q$ and $p_q \forall q$

Data: N, λ_L, Γ, a, ϵ
Initialisation: $k = 0$, $\boldsymbol{x}_{q,0}$ and $\boldsymbol{\varphi}_q$ s.t. $\boldsymbol{x}_{q,0}\boldsymbol{e} + \boldsymbol{\varphi}_q\boldsymbol{e} = 1 \forall q$;
while $\max_q\{\|\boldsymbol{\varphi_q}^{(k+1)} - \boldsymbol{\varphi_q}^{(k)}\|\} \geq \epsilon$ **do**
  for *q in Q* **do**
    1. Evaluate p_q following Theorem. 6.1 and using $\boldsymbol{\Delta}^{(k+1)}$;
    2. Construct $\boldsymbol{F}_q$ and hence $\boldsymbol{A}_q$ using p_q;
    3. Obtain $\boldsymbol{\pi}_q$ from Lemma 6.1 to check stability:
    if *Stable* **then**
      3.1 Calculate $\boldsymbol{R}_q^{(k+1)}$ using Eq. 6.12;
      3.2 Solve $\boldsymbol{x}_{q,0}$ and $\boldsymbol{x}_{q,1}$ using Theorem Theorem. 6.2;
      3.3 Compute $\boldsymbol{\varphi_q}^{(k+1)} = \boldsymbol{x}_{q,1}\left(\boldsymbol{I} - \boldsymbol{R}_q^{(k+1)}\right)^{-1}$;
    else
      3.4 Set $\boldsymbol{x}_{q,0} = 0$ and $\boldsymbol{\varphi_q}^{(k+1)} = \boldsymbol{\pi}_q$
    end
  end
  Increment k ;
end
Return $\boldsymbol{R}_q \leftarrow \boldsymbol{R}_q^{(k+1)}$, $\boldsymbol{\varphi_q} \leftarrow \boldsymbol{\varphi_q}^{(k+1)}, \forall q$

If $p_1 > a$, $\boldsymbol{P}_1$ is stable and $\boldsymbol{x}_1$ is given by:

$$x_{1,i} = \begin{cases} \frac{p_1 - a}{p_1}, & \text{if } i = 0, \\ \left(\frac{\bar{p}_1 a}{p_1 \bar{a}}\right)^i \frac{x_0}{\bar{p}_1}, & \text{if } i \geq 1. \end{cases} \tag{6.15}$$

The activity probability is $\delta_1 = \bar{x}_{1,0}$.

6.3.3 Iterative Algorithm and KPIs

The coverage probability p_q in Eq. 6.5, depends on the set of interfering nodes being concurrently active as the node of interest. The activity probability δ_q of each SF-set of nodes is obtained as outcome of the DTMC steady state analysis. At the same time, $\overline{p}_q$ is needed to construct $\boldsymbol{F}_q$. To resolve such interdependence, we propose an iterative solution with convergence criterion ϵ. The iterative solution is detailed in Algorithm. 1. Noting that Algorithm. 1 converges by virtue of the fixed point theorem.

Using the steady state statistics obtained from Algorithm. 1, we define the following performance metrics:

- **Stability frontiers:** The Pareto stability frontiers are characterised by the set of parameters $\mathcal{S}_q = \{\{\lambda_L, \gamma_q, a\} \in \mathbb{R}^2 \times [0,1]$, such that $\boldsymbol{\pi}_q \mathbf{A_{q,2}} \mathbf{e} > \boldsymbol{\pi}_q \mathbf{A_{q,0}} \mathbf{e}\}$. Operating within this region ensures a service rate higher than the arrival rate and guarantees finite packet delays.

- **Average delay:** We denote W_q the duration of a randomly selected packet from its generation to its successful delivery.

  For a stable system, the average latency per SF (including the packet on service) for Geo/PH/1 (Geo/Geo/ for $q = 1$) is obtained, following the steps in [33, Ch.5.4, Ch.5.8], as:

$$\mathbb{E}\left[W_q\right] = \begin{cases} \frac{\bar{a} a x_0}{(p_q - a)^2} + \frac{1}{p_q}, \text{for } q = 1, \\ \frac{\boldsymbol{x}_{q,1} \left(\boldsymbol{I} - \boldsymbol{R}_q\right)^{-2} \boldsymbol{e}}{a}, \text{ for } q > 1. \end{cases} \tag{6.16}$$

6.4 Numerical Results

6.4.1 Monte Carlo Simulation Setting

MC simulations, with 10^4 iterations, are used to validate p_q by spatially averaging over the active nodes. We consider a random, yet fixed instantiation of a LoRa network, where SFs are assigned following an EIB scheme. In each simulation step, channel gains are instantiated, packets arrive following a geometric distribution, devices DC states are updated, and transmissions occur whenever the device buffer is nonempty and the SF-DC restriction is satisfied. Unless otherwise stated, we use the following simulation parameters $R = 1$ km, $\eta = 3$, , $a = 0.02$ packet/slot, $\lambda_L = 10^3$ nodes/km^2, $\mathcal{P} = 14$ dBm, $\Gamma_1 = [-20, -23, -26, -29, -32, -35]$ (dB) and NF= 6 dBm.

6.4.2 Validation of the Analytical Framework

In Fig. 6.2, we plot the analytical and simulated coverage probability of the SFs (SF=9, SF=12) versus different SINR thresholds. A good agreement between

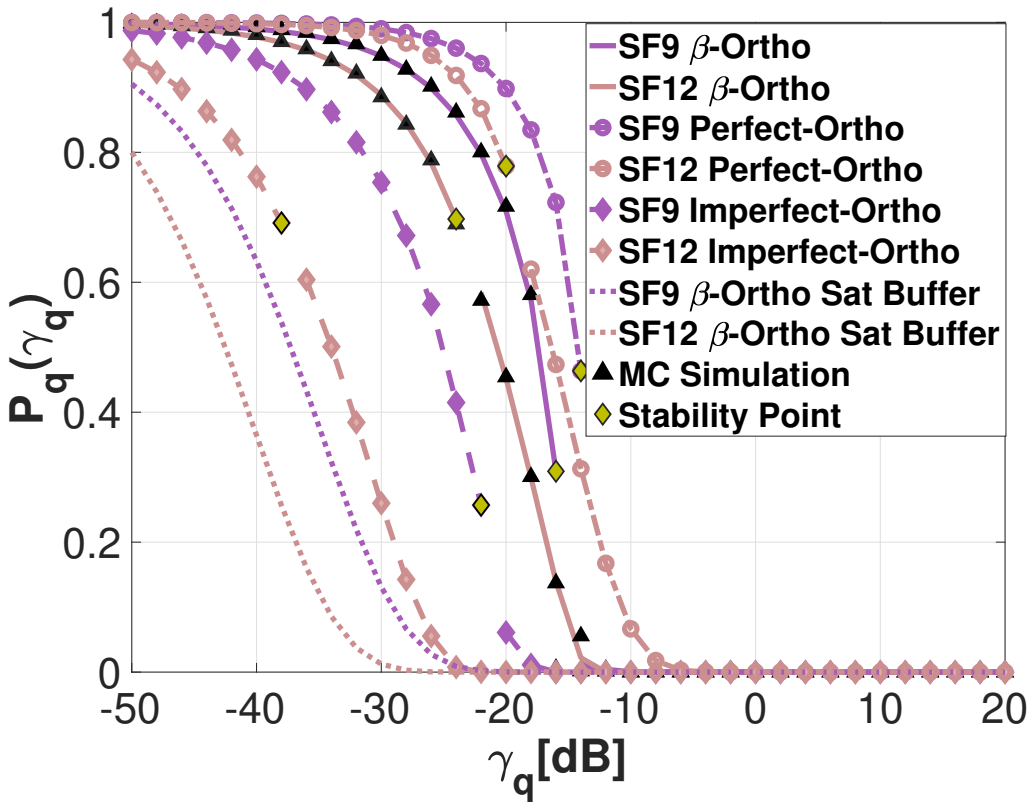

Fig. 6.2: Coverage Probability.

analytical (Lines) and simulation (Markers) is shown. Fig. 6.2 shows the achieved reliability level as the capture threshold varies. The reliability is improved as the SF decreases. To maintain stable buffers, higher SFs need lower capture thresholds. In Fig. 6.2, we also compare the coverage probability under the three assumptions of orthogonality: perfect orthogonality ($\beta_{q_1 \neq q_2} = 0$), imperfect ($\beta_{q_1,q_2} = 1 \; \forall \{q_1, q_2\}$), and $\beta_{q_1,q_2}-$orthogonality (Tab. 6.1). The perfect and imperfect orthogonality assumptions lead to either an overestimated or underestimated coverage performance. Moreover, the figure shows the coverage probability under saturated buffer which is the assumption commonly used in the literature where LoRa networks are restrictively analysed using SG tools. We can clearly see that ignoring traffic dynamics leads to an aggressive interference scenario that makes the predicted coverage very pessimistic.

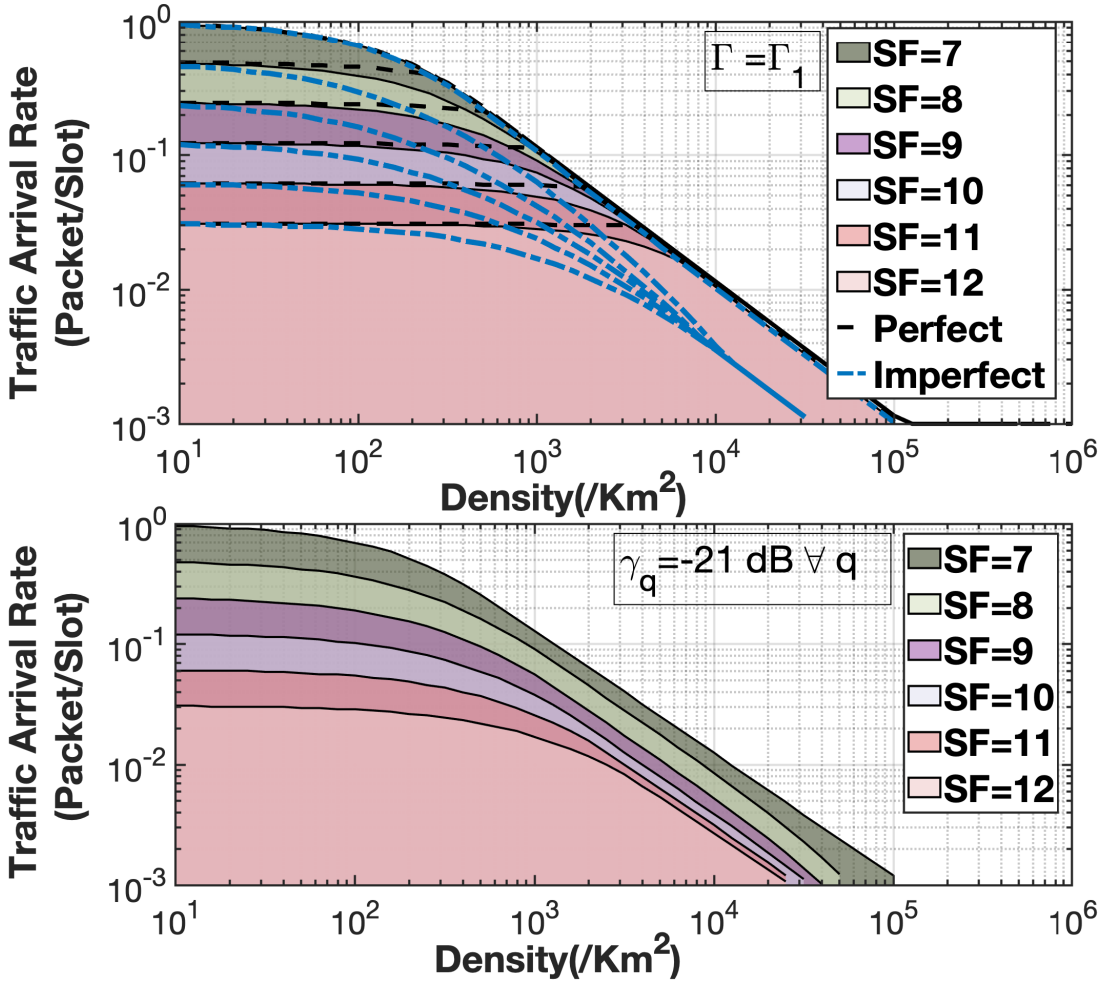

Fig. 6.3: Stability Frontiers.

6.4.3 Network Scalability-Stability Analysis

Fig. 6.3 represents the Pareto stability region for each SF. The result clearly shows the compromise between the scalability through the number of deployed devices and stability. Going for higher density requires a decrease in arrival rate to maintain unsaturated buffers and consequently finite delay to deliver packets. This further emphasizes that a comprehensive LoRa scalability analysis should take into account the underline traffic characteristics. Examining the figure we can see that even with lower sensitivities, higher SFs can drastically hinder the traffic load. Indeed, SFs> 10 fail to accommodate sensing applications with an arrival rate higher than 0.13 packets/slot, even for densities as low as 10 nodes/km^2. The

rationale behind this is that higher SFs spend a longer time in DC, leading to nodes vacating their buffers less often and consequently compromising the stability of the network.

By examining Fig. 6.3, an aspect worth analysing is that the maximal arrival rate stabilising the buffers for all the SFs converges to the same value, that of the lowest SF. Two main reasons come into play to explain this behaviour. First, the threshold distribution Γ_1 improves higher SFs' capture capabilities compared to $\gamma_q = -21$ dB. Second, as the density increases, the interference effect becomes more prominent; and although higher SFs transmit less often due to their longer DC, their spatio-temporal intensity (i.e. interferers/time) becomes comparable to that of lower SFs given the static EIB SF allocation scheme. A valuable conclusion drawn from the previousf analysis is that SF allocation is a determining factor for LoRa scalability. As such, SF assignment strategies that adapt to the nodes environment (i.e. channel conditions, interference severity, etc...) merit future scalability study.

Fig. 6.3 also illustrates the impact of different orthogonality assumptions (perfect $\beta_{q_1 \neq q_2} = 0$, and imperfect $\beta_{q_1,q_2} = 1 \ \forall\{q_1, q_2\}$) on the stability frontiers. A proper orthogonality quantification would extend the scalability limits allowing a more accurate planning for massive LoRa networks. Indeed, while the different assumptions leads to the same Per-SF maximum arrival rate for densities < 20 nodes/km^2, the difference between imperfect-orthogonality and β_{q_1,q_2}-orthogonality becomes more noteworthy for $\lambda \in [10^2 - 10^4]$ nodes/km^2, a range that spans densities in practical deployment scenarios. For a traffic arrival rate of 10^{-3} packets/slot, the maximum density is 2×10^4 nodes/km^2 with imperfect-orthogonality, instead of 10^5 nodes/km^2 with β_{q_1,q_2}.

6.4.4 Average Delay Analysis

Fig. 6.4 shows the impact of density and capture thresholds on the average latency of each SF. For SFs< 10, the average latency is resilient to the increase in density and remains less than 3 slots in all cases. The impact of higher density, implying

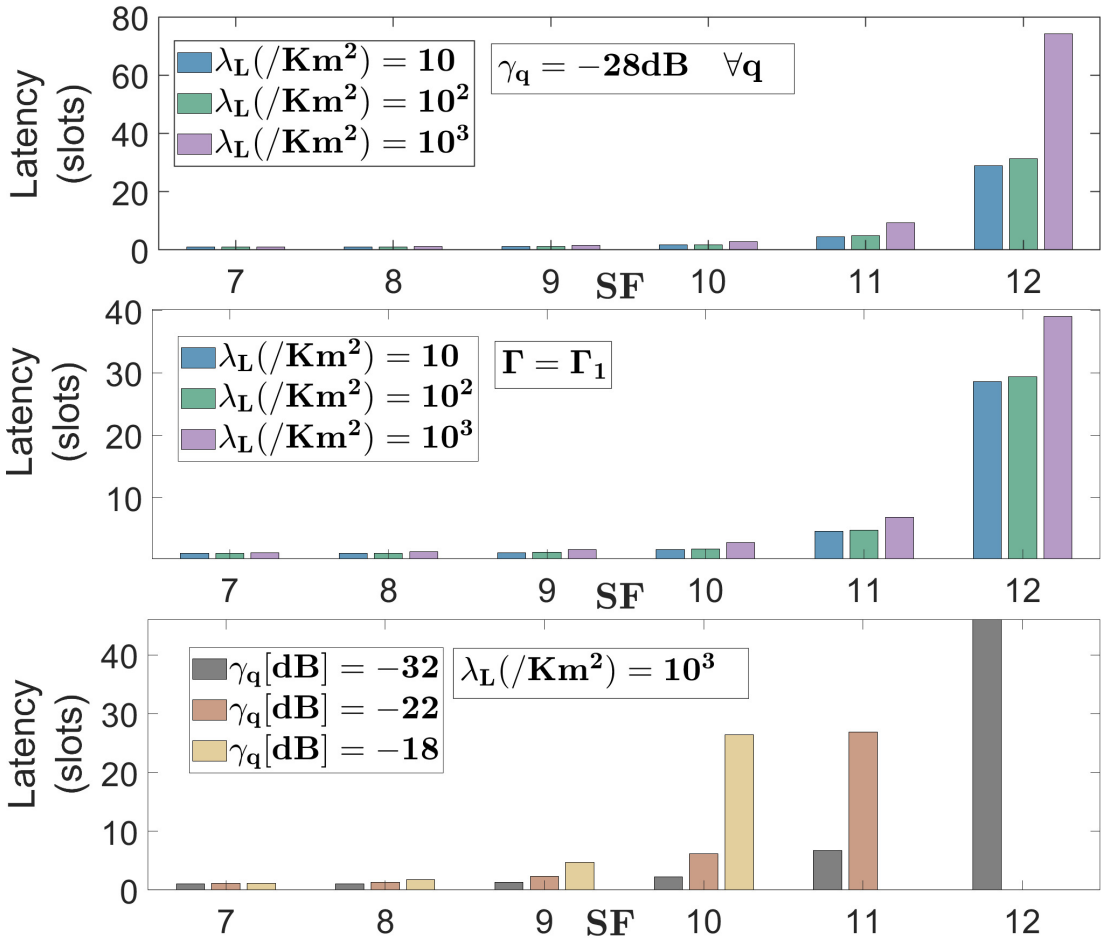

Fig. 6.4: End-To-End Latency.

more mutual interference, is more notable on SF= 12, as latency reaches 74 slots for $\lambda_L = 10^3$ nodes/km^2. A $\gamma_q \geq -18$ dB makes the buffers of devices with SF$\in \{11, 12\}$ overflow leading to unbounded delays. As such, an SF$\in \{11, 12\}$ fails to accommodate even best-effort delay-tolerant applications. Increasing γ_q from -22 dB to -18 dB makes the latency of SF= 10 jumps from 6 to 26 slots. Thus, a proper distribution of the capture thresholds among the SFs would mitigate the unfairness in terms of latency between them.

6.5 Discussion, Limitations and Future Extensions

This chapter provides useful tools to analyse the scalability-stability trade-offs, reliability, and latency in LoRa/LoRaWAN networks with static SF allocation. However, in line with the works existing in the literature, the chapter's scope was

static SF allocations, precisely the EIB scheme. Unlike static SF allocations, there is little-to-no analytical studies that address dynamic rate and SF adaption in the context of LoRa networks.This gap will be investigated in the next chapter.

6.6 Chapter Summary and Key Findings

Fusing stochastic geometry and queuing theory, this chapter has proposed a tractable analytical framework to analyse the joint scalability-stability, reliability and latency of LoRa/LoRaWAN networks with static SF allocation. The devised model accounts for various random factors that influence real deployment scenarios (channel, interference...) and incorporates key LoRa parameters (SF imperfect-orthogonal, DC...).

- A more accurate quantification of LoRa imperfect-orthogonality through cross-correlation factors is adopted in the analysis giving more accurate coverage prediction compared to the perfect and imperfect orthogonality commonly assumed in the literature.
- The stability frontiers of each LoRa SF are analysed. The results show the compromise between the network stability and scalability illustrated by the limits of nodes' density and the per-device traffic rate that a LoRa network can accommodate.
- The results also highlight that a proper distribution of capture thresholds among the SFs is a detrimental factor towards a massive LoRa network with improved latency.

CHAPTER 7

Dynamic SF-Adaptive Duty-Cycled LoRa Networks: Scalability, Reliability, and Latency Trade-offs

This chapter extends the analysis developed in Chapter. 6 from static SF to adaptive SF where LoRa nodes are assigned SFs dynamically based on their transmission experiences.

7.1 Motivation and Contribution

While LoRa is endowed with multiple tuneable parameters including the SF, the scalability analysis of LoRa/LoRaWAN networks has been often conducted under the assumption of static SF allocations whether distance-based or not as detailed in Section. 3.4. Static SF allocations assume that LoRa nodes use constantly the same fixed SF which abstracts the interaction of the nodes with their environment and neglect the impact of the environment and the network dynamics on the selection of the SF to use.

The scalability and stability of power and rate adaptation in generic IoT networks have been investigated in [10, 11, 168]. However, such generic models fail to capture

LoRa peculiarities which makes their proposed models unsuitable for analyzing the performance of LoRa networks. Closest to our research target in this chapter, the work in [169] analytically investigated adaptive rate control in LoRa class-A devices. However, the proposed model relies restrictively on a continuous Markov chain, assumes perfect orthogonality, all of which we have thoroughly discussed the limitations in Section. 3.5. Furthermore, the authors in [169] studied only the impact of the rate-up operation as they assume a fixed rate-down. They also limit the network size in their simulation setup to 25 nodes, a density that remains too low to decide on LoRa behavior in a massive connectivity context.

Therefore, in this chapter, we propose to characterize the performance of dynamic LoRa networks with adaptive SFs through a combined SG and QT model that captures device-level and network-level behaviors. Both the device-level and network-level components of the proposed model embrace the peculiarities of LoRa. From the device-level perspective, the developed DTMC exhibits the SF adaptation and accounts for LoRa regulatory DC restrictions while, from the network-level perspective, the SG analysis examines a more realistic and practically useful interference scenario thanks to the cross-correlation orthogonality coefficients between the SFs.

We derive performance metrics that quantify the scalability, reliability, and latency of the network. The trade-offs between the various metrics are studied. The provided analysis spots operational regimes achieving a stable and an adequately provisioned network according to the QoS requirements of the supported IoT application.

7.2 System Model and Assumptions

7.2.1 Spatial Distribution and Propagation Model

We consider a single-gateway LoRa network where the nodes are randomly scattered according to a homogeneous PPP Φ_L of intensity λ_L within the circumference

of radius R from the gateway. The LoRa gateway servicing area will be called hereinafter LoRa cell. Accounting for the dynamic SF assignment, the traffic requirements, and DC restrictions, let $\tilde{\Phi}_{L,q}$ be the thinned process of LoRa concurrently transmitting nodes using SF_q. The network's instantiation is random, yet static. That is, the nodes' positions are fixed, while their packet generation, the channel fading, and the communication resources (SFs), change over time. We consider a power law path-loss propagation model with Rayleigh block fading channels as described in Subsection. 6.2.2.

Taking into account the spatial distribution mentioned above, the distance between devices is characterised by the following CDF:

$$\mathcal{F}_{r_0}(r) = \frac{r^2}{R^2}, \;\; 0 < r < R. \tag{7.1}$$

LoRa devices are classified into M equi-probable distance-based regions $\{\mathcal{A}_1, ..., \mathcal{A}_M\}$ each delimited by $[d_{m-1}, d_m]$ such that d_m satisfies $d_1 = 0$, $d_M = R$ and $\mathcal{F}_{r_0}(d_{m+1}) - \mathcal{F}_{r_0}(d_m) = \frac{1}{M}$. Therefore, the quantized distances are given by $d_m = R\sqrt{\frac{m}{M}}$, $2 \leq m \leq M-1$. The subset of active nodes using SF_q $\mathcal{A}_m$ is the thinned process $\tilde{\Phi}_{L,q,m}$. The thinning probability will be obtained from the DTMC analysis and will reflect the percentage of active devices assigned to each SF at the steady state of the adaptive SF scheme. We define $\mathbf{\Delta}$, of size $M \times N$ as the activity matrix where each row $\mathbf{\Delta}^{[m]} = [\delta_1^{[m]}, \ldots, \delta_q^{[m]}, \ldots, \delta_N^{[m]}]$ represents the effective activity probability of different SFs in region $\mathcal{A}_m$ of the cell.

7.2.2 Channel Access and Queuing Model

Similarly to Subsection. 6.2.3, we assume a partitioned time window. All nodes sense for the same application characterised by packet size L and per-slot data arrival probability a. In each device, packets of size L are generated according to an i.i.d. geometric distribution with parameter $a \in [0, 1]$. Similar to Chapter. 6, the generated packets are stored in a FIFO queue. The focus of this chapter is to explore LoRa UP transmissions for confirmed traffic class$-A$ LoRa devices. The characteristics of different LoRa devices classes have been detailed in Chapter. 2.

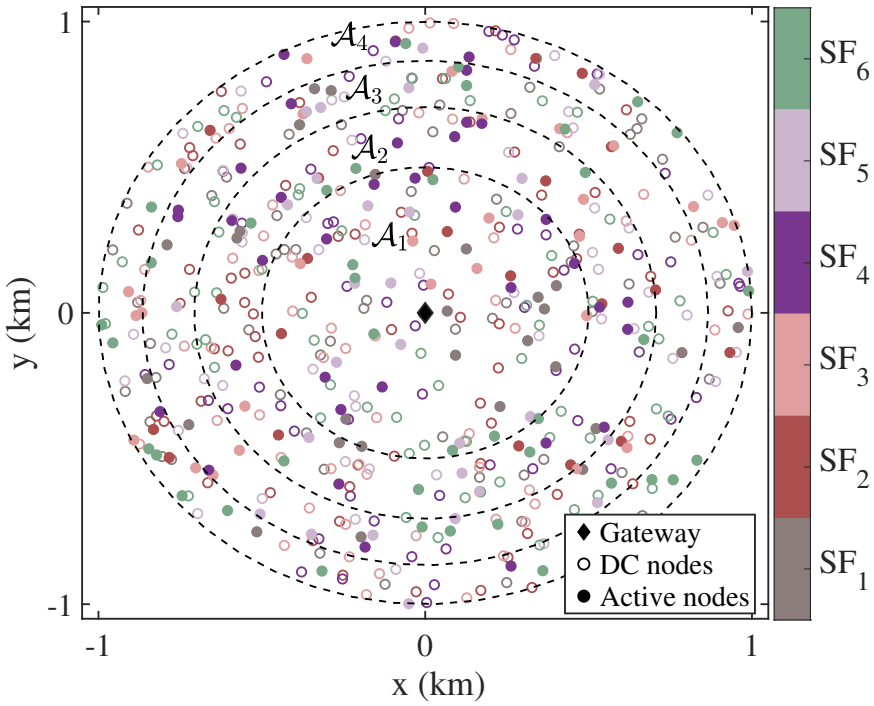

Fig. 7.1: LoRa Network discretised into $M = 4$ equiprobable regions.

Class *A* LoRa devices support both confirmed (acknowledged) and unconfirmed traffic modes. For class-A LoRa devices, DL traffic can be received during two receive windows that are open immediately after a UP transmission. The technical specifications of LoRaWAN do not specify in which window the ACKs are received, and having them duplicated would impact UP transmission success [170]. Thus, we assume error-free *Acknowledgment* (ACK)s that are instantly received during the first receive window. Error-prone acknowledgments are out of this chapter's scope and could be investigated as a future work.

7.2.3 LoRa Physical Parameters and Network Operations

A. LoRa Duty-Cycling

In the same vein as Chapter. 6, each transmission using SF$_q$ will be followed by a number of back-off slots n_q guaranteeing that the node adhere to the DC restrictions. The DC back-off state of each SF is divided into two logical states $DC_{q,s}$ and $DC_{q,f}$ that capture whether the node enters the DC after a successful or a failed

transmission, respectively. Since LoRa DC is correlated to the ToA which varies with the used SF, the logical states $DC_{q,s}$ and $DC_{q,f}$ are further discretised into a set of sub-states, $DC_{q,s} = \{DC_{q,s,1}, DC_{q,s,2}, DC_{q,s,3}, ..., DC_{q,s,n_q}\}$ where $n_q = 2^{q-1} - 1$ for $q > 1$, $n_1 = 0$ (since $T_1 = 100 \times l_1$). The same approach is applied for $DC_{q,f}$.

B. LoRa β_{q_1,q_2}−SF Orthogonality

We adopt the β_{q_1,q_2} SF-Orthogonality interference scenario detailed in Subsection. 6.2.5. Each SF experiences interference from concurrently (same and different) transmitting SFs with an orthogonality coefficient β_{q_1,q_2}. The average intensity of active devices operating at SF_q in region $\mathcal{A}_m$ is $\lambda_L \delta_q^{[m]}$. The activity probability $\delta_q^{[m]}$ is derived using the queuing theory analysis, which will be elaborated in Subsection. 7.3.2.

C. Adaptive SF Operations

We assume that all LoRa nodes send their sensed data to a LoRa gateway using the same BW and a fixed CR. Hence, the adaptation of LoRa rate, which is defined by Eq. 2.1, is mainly governed by the SF. Increasing the SF decreases the rate but at the same time improves the receiver processing gain, therefore improving the transmission coverage. Although power adaptation could also be incorporated into the proposed model, for simplicity and to have the study focus more on the impact of SF, we assumed fixed transmit power. Each node with active adaptive-SF can transmit with N different SFs; it starts by using an initial spreading factor SF_i. Then, given transmission failure/success, the node moves up/moves down, or retains its SF. Such SF adaptation is triggered by two probabilistic parameters b and d.

To satisfy the channel access limitations, each node is allowed to transmit only when the DC requirement is fulfilled. If the previous packet transmission outcome was success i.e. an ACK was successfully received during the DL received window, the node enters the $DC_{q,s}$ state. Once the required $DC_{q,s}$ is satisfied, a node reduces its SF with probability d or retains the same pre-DC SF with probability ($\overline{d} = 1 - d$).

Whereas, in case of packet failure due to missing acknowledgments, the node enters the $DC_{q,f}$ state. After satisfying the required $DC_{q,f}$, the node returns to the transmittable state while stepping-up its SF with probability b or remaining in the same SF with probability ($\overline{b} = 1 - b$). Hereinafter we describe the adaptive operations as SF−Up/SF−Down for a single step SF increase/decrease, respectively. Whenever a slot elapses, the node wakes-up to check its current state. Based on whether, the state is SF-transmittable or SF-DC, a packet has arrived, and if an ACK was received in case of transmission or not, the device performs the transitions following the Markov chain model sketched in Fig. 7.3.

Adaptation parameters b and d are design parameters that can be tailored offline at the initial phase of network design and planning taken into consideration the network performance KPIs and target QoS. These parameters can be updated during the network life-cycle and polled by the gateway/network server to LoRa devices using DL messages in the open receive windows. In the adaptation scheme, b and d reflect the speed of, respectively, SF−Up and SF−Down operations. They can be interpreted tangibly as the average number of failed/successful packet transmissions before triggering the device to perform the SF−Up/SF−Down operations. For example, consider a LoRa device having adaptive-SF scheme ON with rates $b = 0.33$ and $d = 0.25$. This means that the device performs an SF−Up operation on average every three failed transmissions to decrease its outage probability while it performs an SF-Down operation on average every four successfully transmissions assuming that the link quality and the interference level are acceptable enough to be served by lower SFs (i.e higher rates).

7.2.4 Methodology of Analysis

A two-dimensional DTMC is leveraged to model the different MAC protocol states of LoRa nodes. The number of states depends on the number of available SFs for adaptation. We can interpret LoRa devices as spatially interacting queues that adapt their SFs based on their environments. The LoRa service area centered at the gateway is discretized into M equiprobable distance-based regions $\{\mathcal{A}_1, ..., \mathcal{A}_M\}$.

For each region, the coverage probability using different SFs $\left[P_1^{[m]}, \quad P_2^{[m]}, \ldots, \quad P_N^{[m]}\right]$ is calculated, the queuing analysis is conducted, and the steady state distribution is determined. This discretization has the advantage of accounting for the spatial correlation of the received signal's quality (location dependence) and to capture any potential distance-based clustering of the SFs at the steady state of the adaptation mechanism. The discrete region number M is governed by the granularity of results we would like to reach - a high number provides more accuracy at the expense of more computation. Thus, M is chosen to ensure a balance between accuracy and complexity. The distance-independent scenario is the special case of $M = 1$ where the analysis is performed throughout the cell and an overall steady-state distribution of the allocated SFs is obtained. Fig. 7.2 details how the methodology explained in Chapter. 1 (Fig. 1.3) is applied in the context of this chapter.

7.2.5 Main Assumptions

The proposed methodology explained above has been carried out under the following approximations:

Approximation 1. *The SINR temporal correlation is negligible.*

Remark 7.1. *Incorporating DC states in DTMC makes the event of having common interfering nodes, seen at the LoRa base station throughout successive time slots, seldom. Furthermore the randomness induced by both channel fading and traffic arrival rate make the effect of interference temporal correlation negligible. Given these facts, the assumption that the SINR of a LoRa node is de-correlated across different transmission slots remains a safe conjecture.*

Approximation 2. *In each region A_m, LoRa devices experience i.i.d. steady state queues.*

Remark 7.2. *The discretization of the cell into distance-based regions accounts for the discrepancy in coverage performance, therefore in the queue departure, among nodes located at different distances from the gateway. Given that, we assume that nodes within each region experience i.i.d. steady state queue distribution.*

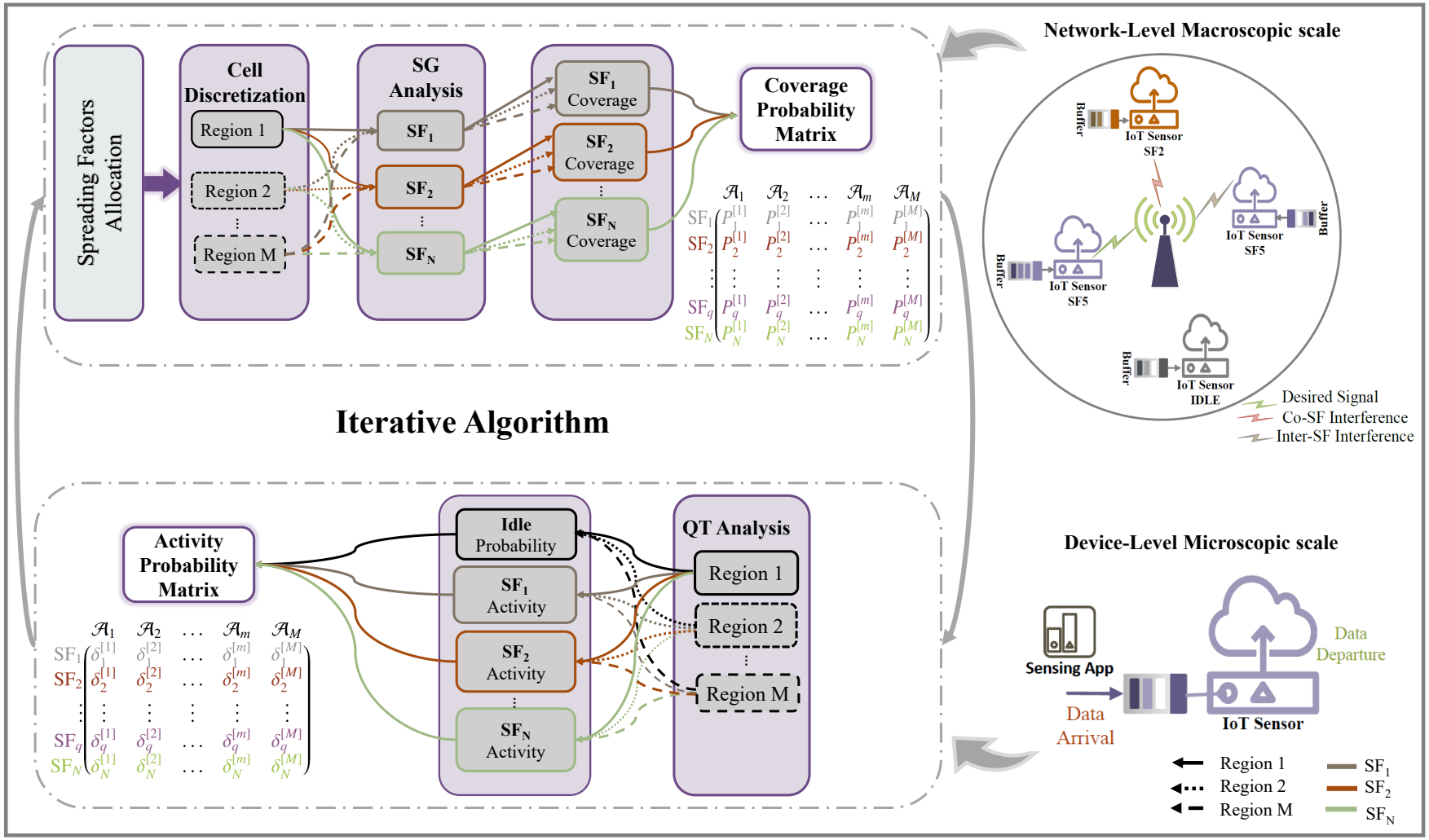

Fig. 7.2: Methodology of the proposed analysis.

7.3 Spatiotemporal Framework

7.3.1 Coverage Probability

In this section, the stochastic geometry approach detailed in Subsection. 6.3.1 is used to derive the coverage probability of each SF in each region, $P_q^{[m]}$.

Theorem 7.1. *The packet transmission success probability of the desired LoRa node is:*

$$P_s(r_0, q_0, \gamma_{q_0}) = \exp\left(-\rho_{q_0}\sigma^2\right) \prod_{q=1}^{N} \prod_{m=1}^{M} \exp\left(-2\pi\delta_q^{[m]}\lambda_L \left(\mathcal{J}_q(d_m) - \mathcal{J}_q\left(d_{m-1}\right)\right)\right), \tag{7.2}$$

where $\mathcal{J}_q(\cdot)$ *is defined by* $\mathcal{J}_q(x) = \frac{x^2}{2}\, {}_2F_1\left(1, \frac{2}{\eta}; 1 + \frac{2}{\eta}; -\frac{x^\eta}{b}\right)$ *with* $b = \gamma_{q_0} r_0^\eta \beta_{q_0,q}$.

Proof. The proof follows from applying similar steps as in Appendix Section. C.1. □

Remark 7.3. *Considering the activity matrix* $\mathbf{\Delta}$*, the orthogonality coefficients matrix* $\boldsymbol{\beta}$ *and matrix* $\boldsymbol{J}$ *defined by* $\boldsymbol{J}(m,q) = \left(\mathcal{J}_q(d_m) - \mathcal{J}_q\left(d_{m-1}\right)\right)$*, (Eq. 7.2) is vectorized into (Eq. 7.3) as*

$$P_s(r_0, q_0, \gamma_{q_0}) = \exp\left(-\rho_{q_0}\sigma^2\right) \exp\left(-2\pi\lambda_L \operatorname{Tr}\left[\mathbf{\Delta}^T \boldsymbol{J}\right]\right). \tag{7.3}$$

Remark 7.4. $\eta = 4$ *corresponds to outdoor urban environment and reduces the expression (Eq. 7.2) to:*

$$P_s(r_0, q_0, \gamma_{q_0}) \overset{(\eta=4)}{=} \exp\left(-\rho_{q_0}\sigma^2\right) \prod_{q=1}^{N} \prod_{m=1}^{M} \exp\left(-\pi\delta_q^{[m]}\lambda_L \sqrt{b}\left(\tan^{-1}\left(\frac{d_m^2}{\sqrt{b}}\right) - \tan^{-1}\left(\frac{d_{m-1}^2}{\sqrt{b}}\right)\right)\right). \tag{7.4}$$

Using the obtained transmission success probability expression for a node located in A_{m_0} and considering the device-to-gateway distance distribution f_R expressed as

$$f_R(r) = \frac{2r}{d_{m_0}^2 - d_{m_0-1}^2}, \quad d_{m_0-1} \le r \le d_{m_0}, \tag{7.5}$$

we remove the conditioning over the node's position to derive the following Per-SF coverage probability in each region A_{m_0}.

Corollary 7.1. *The Per-SF coverage probability of SF_{q_0} in region $\mathcal{A}_{m_0}$ is given by the spatially averaged transmission success probability during a generic time slot as:*

$$P_{q_0}^{[m_0]} = \int_{d_{m_0-1}}^{d_{m_0}} P_s^{[m_0]}(r, q_0, \gamma_{q_0}) f_R(r) dr. \tag{7.6}$$

7.3.2 Microscopic Device-Level Queuing Theory Analysis

Each LoRa device located in $\mathcal{A}_m$ is characterised by a QBD process (Subsection. 1.6.2) with the following transition matrix:

$$\boldsymbol{P}^{[m]} = \begin{pmatrix} \boldsymbol{B}^{[m]} & \boldsymbol{C}^{[m]} & \mathbf{0} & \mathbf{0} & \mathbf{0} & \dots \\ \boldsymbol{E}^{[m]} & \boldsymbol{A}_1^{[m]} & \boldsymbol{A}_0^{[m]} & \mathbf{0} & \mathbf{0} & \ddots \\ \mathbf{0} & \boldsymbol{A}_2^{[m]} & \boldsymbol{A}_1^{[m]} & \boldsymbol{A}_0^{[m]} & \mathbf{0} & \ddots \\ \mathbf{0} & \mathbf{0} & \boldsymbol{A}_2^{[m]} & \boldsymbol{A}_1^{[m]} & \boldsymbol{A}_0^{[m]} & \ddots \\ \vdots & \vdots & \ddots & \ddots & \ddots & \ddots \end{pmatrix}, \tag{7.7}$$

where $\boldsymbol{A}_0^{[m]}$, $\boldsymbol{A}_1^{[m]}$ and $\boldsymbol{A}_2^{[m]}$ track the buffer state when it respectively increases by one level, stays in the same level and decreases by one level, and $\boldsymbol{B}^{[m]}$, $\boldsymbol{C}^{[m]}$, and $\boldsymbol{E}^{[m]}$ track respectively the transition within, from, and to an empty buffer. An illustration of the queue-state aware DTMC for the case of adaptive scheme with $N = 3$ is sketched in Fig. 7.3. Each state in Fig. 7.3 is given by the tuple (i, j) with i being the protocol phase that can be any of the available SFs and their corresponding DC, and j is the number of packets in the device buffer.

For each $\mathcal{A}_m$, recalling the MAM [31], we construct hierarchically the block-partitioned transition matrix $\boldsymbol{P}^{[m]}$ of the queuing model as follows: $\boldsymbol{A}_1^{[m]} = a\boldsymbol{S}^{[m]} + \overline{a}\boldsymbol{F}^{[m]}$, $\boldsymbol{A}_2^{[m]} = \overline{a}\boldsymbol{S}^{[m]}$, $\boldsymbol{A}_0^{[m]} = a\boldsymbol{F}^{[m]}$, $\boldsymbol{B}^{[m]} = \overline{a}\boldsymbol{S}_0^{[m]}$, $\boldsymbol{C}^{[m]} = a\begin{bmatrix}\boldsymbol{S}_0^{[m]} & \mathbf{0}\end{bmatrix}$, $\boldsymbol{E}^{[m]} = \overline{a}\boldsymbol{S}_s^{[m]}$. The QBD process has geometric (Geo) arrival and phase (PH) type departure, denoted as Geo/Ph/1 QBD [33, Chapter 2.5.3]. The phase distribution of Geo/Ph/1 queues is built using absorbing Markov chain. Matrices $\boldsymbol{S}^{[m]}$ and $\boldsymbol{F}^{[m]}$ of size $L \times L$, where $L = 2^{N+1} - (N + 2)$, capture the dynamics of this distribution. The absorption states corresponding to packets departures from the nodes' buffers are depicted in $\boldsymbol{S}^{[m]}$

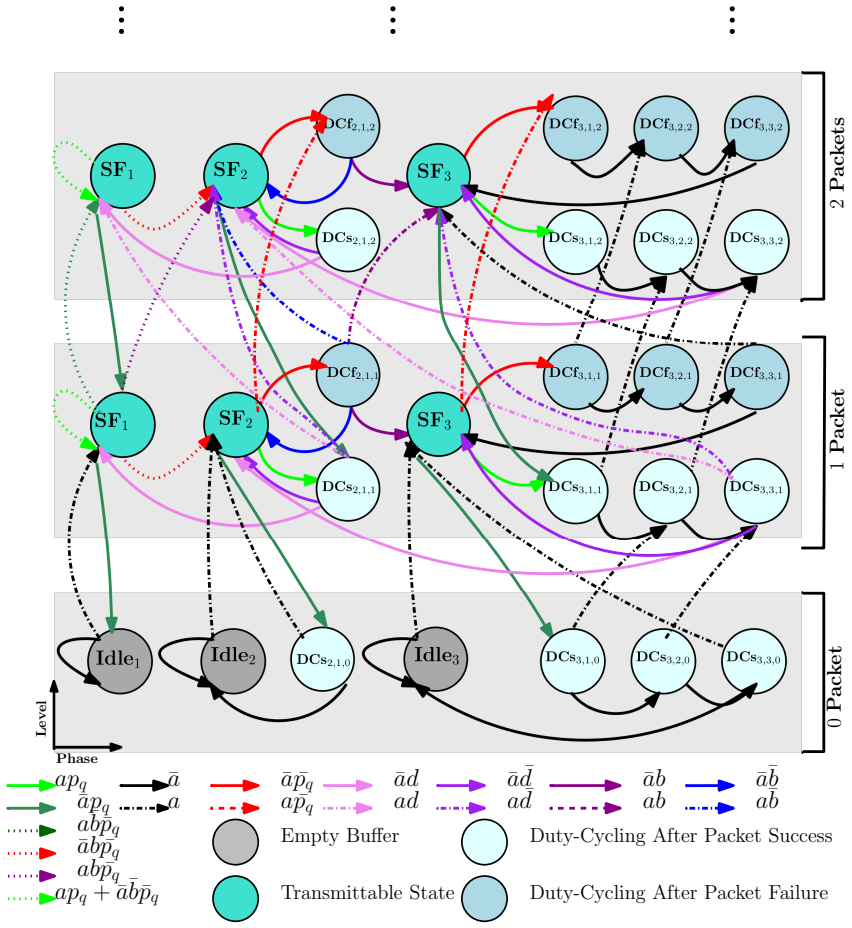

Fig. 7.3: Two-dimensional DTMC of a LoRa node under Adaptive SF for $N = 3$.

while transient states until absorption are tracked in $\boldsymbol{F}^{[m]}$:

$$\boldsymbol{F}^{[m]} = \begin{bmatrix} \boldsymbol{T}_f^{[m]} & \boldsymbol{0} & \boldsymbol{T}_{D_f}^{[m]} \\ \boldsymbol{D}_{sT}^{[m]} & \boldsymbol{D}_s^{[m]} & \boldsymbol{0} \\ \boldsymbol{D}_{fT}^{[m]} & \boldsymbol{0} & \boldsymbol{D}_f^{[m]} \end{bmatrix}, \quad \boldsymbol{S}^{[m]} = \begin{bmatrix} \boldsymbol{S}_s^{[m]} & \boldsymbol{0}_{L\times(2^N-(N+1))} \end{bmatrix}. \tag{7.8}$$

The transitions from, within, and to the idle states are captured using $\boldsymbol{S}_s^{[m]}$ and $\boldsymbol{S}_0^{[m]}$ of respective sizes $L \times (2^N - 1)$ and $(2^N - 1) \times 2^N - 1)$:

$$\boldsymbol{S}_s^{[m]} = \begin{bmatrix} \boldsymbol{T}_s^{[m]} & \boldsymbol{T}_{D_s}^{[m]} \\ \boldsymbol{0} & \boldsymbol{0} \end{bmatrix}, \quad \boldsymbol{S}_0^{[m]} = \begin{bmatrix} \boldsymbol{I}_N & \boldsymbol{0} & \boldsymbol{0} \\ \boldsymbol{0} & \boldsymbol{D}_{sT}^{[m]} & \boldsymbol{D}_s^{[m]} \end{bmatrix}. \tag{7.9}$$

$$\boldsymbol{T}_s^{[m]}(i,j) = \begin{cases} P_1^{[m]}, (i=j=1) \\ 0, \quad \text{otherwise.} \end{cases}, \qquad \boldsymbol{T}_f^{[m]}(i,j) = \begin{cases} \overline{bP}_1^{[m]}, & (i=1, j=1) \\ b\overline{P}_1^{[m]}, & (i=1, j=2) \\ 0, & \text{otherwise.} \end{cases}, \quad \boldsymbol{D}_s^{[m]} = \begin{bmatrix} \boldsymbol{V}_2 & & \\ & \ddots & \\ & & \boldsymbol{V}_N \end{bmatrix}, \tag{7.10}$$

$$\boldsymbol{D}_{sT}^{[m]} = \begin{bmatrix} d\boldsymbol{U}_2 & \overline{d}\boldsymbol{U}_2 & \boldsymbol{0} & \boldsymbol{0} & \dots & \boldsymbol{0} \\ \boldsymbol{0} & d\boldsymbol{U}_3 & \overline{d}\boldsymbol{U}_3 & \boldsymbol{0} & \dots & \boldsymbol{0} \\ \vdots & \ddots & \ddots & \ddots & \ddots & \vdots \\ \boldsymbol{0} & \dots & \boldsymbol{0} & d\boldsymbol{U}_{N-1} & \overline{d}\boldsymbol{U}_{N-1} & \boldsymbol{0} \\ \boldsymbol{0} & \boldsymbol{0} & \dots & \boldsymbol{0} & d\boldsymbol{U}_N & \overline{d}\boldsymbol{U}_N \end{bmatrix}, \qquad \boldsymbol{D}_{fT}^{[m]} = \begin{bmatrix} \boldsymbol{0} & \overline{b}\boldsymbol{U}_2 & b\boldsymbol{U}_2 & \boldsymbol{0} & \dots & \boldsymbol{0} \\ \boldsymbol{0} & \boldsymbol{0} & \overline{b}\boldsymbol{U}_3 & b\boldsymbol{U}_3 & \ddots & \vdots \\ \vdots & \vdots & \ddots & \ddots & \ddots & \boldsymbol{0} \\ \boldsymbol{0} & \boldsymbol{0} & \dots & \boldsymbol{0} & \overline{b}\boldsymbol{U}_{N-1} & b\boldsymbol{U}_{N-1} \\ \boldsymbol{0} & \boldsymbol{0} & \dots & \dots & \boldsymbol{0} & \boldsymbol{U}_N \end{bmatrix}, \tag{7.11}$$

$$\boldsymbol{T}^{[m]}{}_{D_s} = \begin{bmatrix} \boldsymbol{0} & \boldsymbol{0} & \dots & \dots & \boldsymbol{0} \\ \boldsymbol{t}_2^{[m]} & \boldsymbol{0} & \ddots & & \vdots \\ \boldsymbol{0} & \boldsymbol{t}_3^{[m]} & \ddots & \ddots & \vdots \\ \vdots & \ddots & \ddots & \ddots & \vdots \\ \vdots & & \ddots & \boldsymbol{t}_{N-1}^{[m]} & \boldsymbol{0} \\ \boldsymbol{0} & \dots & \dots & \boldsymbol{0} & \boldsymbol{t}_N^{[m]} \end{bmatrix}, \qquad \boldsymbol{T}_{D_f}^{[m]} = \begin{bmatrix} \boldsymbol{0} & \boldsymbol{0} & \dots & \dots & \boldsymbol{0} \\ \overline{\boldsymbol{t}}_2^{[m]} & \boldsymbol{0} & \ddots & & \vdots \\ \boldsymbol{0} & \overline{\boldsymbol{t}}_3^{[m]} & \ddots & \ddots & \vdots \\ \vdots & \ddots & \ddots & \ddots & \vdots \\ \vdots & & \ddots & \overline{\boldsymbol{t}}_{N-1}^{[m]} & \boldsymbol{0} \\ \boldsymbol{0} & \dots & \dots & \boldsymbol{0} & \overline{\boldsymbol{t}}_N^{[m]} \end{bmatrix}, \tag{7.12}$$

$$\boldsymbol{U}_q(i) = \begin{cases} 1, & i = 2^{(q-1)} - 1 \\ 0 & otherwise. \end{cases}, \quad \boldsymbol{t}_q^{[m]}(j) = \begin{cases} P_q^{[m]}, & j = 1 \\ 0 & otherwise. \end{cases}, \quad \boldsymbol{V}_q(i,j) = \delta_{i+1,j}, \tag{7.13}$$

Matrices $\boldsymbol{T}_f^{[m]}$, $\boldsymbol{T}_s^{[m]}$, $\boldsymbol{T}_{Ds}^{[m]}$, $\boldsymbol{T}_{Df}^{[m]}$, $\boldsymbol{D}_{fT}^{[m]}$, $\boldsymbol{D}_{sT}^{[m]}$, $\boldsymbol{D}_f^{[m]}$, and $\boldsymbol{D}_s^{[m]}$ shown in Eq. 7.10-Eq. 7.12 capture the transitions between the various DTMC states in Fig. 7.3. Below a summary of these matrices' roles.

- $\boldsymbol{T}_s^{[m]}$ and $\boldsymbol{T}_f^{[m]}$ given by Eq. 7.10 have each size $N \times N$ and track the transitions between transmittable states in case of respectively packet failure and success.
- $\boldsymbol{D}_{sT}^{[m]}$ and $\boldsymbol{D}_{fT}^{[m]}$ in Eq. 7.11 track the transitions of retaining SF_q or upgrading from SF_q to SF_{q+1} after satisfying the required DC. These matrices are built using $\boldsymbol{U}_q^{[m]}$, a column vector of size $(2^{q-1}-1)$ in Eq. 7.13. They reflect the transition from the last DC sub-state to the new transmittable state SF_q.
- $\boldsymbol{D}_s^{[m]}$ and $\boldsymbol{D}_f^{[m]}$ in Eq. 7.12 are block matrices formed by $\boldsymbol{V}_q$, a $(2^{q-1}-1)\times(2^{q-1}-1)$ matrix in Eq. 7.13 that captures the transitions until the DC restrictions of SF_q are satisfied.
- $\boldsymbol{T}_{D_s}^{[m]}$ and $\boldsymbol{T}_{D_f}^{[m]}$ shown in Eq. 7.12 keep track of the transitions from transmittable to DC states and are defined in blocks by $\boldsymbol{t}_q^{[m]}$ in Eq. 7.13. $\boldsymbol{t}_q^{[m]}$ is a row vector of size $(2^{q-1}-1)$) tracking the transition from SF_q to its first DC sub-state.

Remark 7.5. *$\boldsymbol{B}^{[m]}$, $\boldsymbol{C}^{[m]}$, and $\boldsymbol{E}^{[m]}$ have different sizes compared to $\boldsymbol{A}_0^{[m]}$, $\boldsymbol{A}_1^{[m]}$, and $\boldsymbol{A}_2^{[m]}$ because a node visits the idle state only after having a successful transmission and satisfying the DC restrictions. Thus, only $\boldsymbol{D}_s^{[m]}$ sub-states appear at level 0.*

Remark 7.6. *For $q = 1$, the device uses the lowest SF in the adaptation scheme and cannot perform SF−Down operation as depicted in matrix $T_s^{[m]}$. For $q = N$, the device reaches the highest SF and in case of failure it remains in SF_N as shown in the last transition of $D_{fT}^{[m]}$.*

A. Stability Conditions

Using Lemma. 6.1, the data buffer of a LoRa's node is stable if $\boldsymbol{\pi}^{[m]}\mathbf{A}_2^{[m]}\mathbf{e} > \boldsymbol{\pi}^{[m]}\mathbf{A}_0^{[m]}\mathbf{e}$ with

$$\boldsymbol{\pi}^{[m]} = \mathbf{e}^T(\mathbf{S}^{[m]} + \boldsymbol{F}^{[m]} - \mathbf{I} + \mathbf{e}\mathbf{e}^T)^{-1}. \tag{7.14}$$

.

B. Steady State Solution

We define the invariant probability (the steady state solution) vector with regard to $\mathbf{P}^{[m]}$ as $\mathbf{x}^{[m]} = \left[\mathbf{x}_0^{[m]} \quad \mathbf{x}_1^{[m]} \quad \mathbf{x}_2^{[m]} \dots\right]$, where $\mathbf{x}_i^{[m]} = \left[x_{i,0}^{[m]} \quad x_{i,1}^{[m]} \quad x_{i,2}^{[m]} \dots x_{i,L}^{[m]}\right]$ denotes the probability of having i packets in the buffer and $x_{i,l}^{[m]}$ is the probability of having i packets while being operating at phase l (transmittable-SF or DC-SF). The steady state solution vector $\mathbf{x}^{[m]}$ is obtained by solving the equation $\mathbf{x}^{[m]} = \mathbf{x}^{[m]}\mathbf{P}^{[m]}$ with normalisation condition $\mathbf{x}^{[m]}\mathbf{e} = 1$.

Theorem 7.2. *The steady state probabilities $\boldsymbol{x}^{[m]}$ of a LoRa node with adaptive-SF scheme is given by:*

$$\boldsymbol{x}_i^{[m]} = \begin{cases} \boldsymbol{x}_0^{[m]}\boldsymbol{C}^{[m]}\boldsymbol{G}^{[m]} \times \boldsymbol{E}^{[m]}\left(\boldsymbol{I} - \boldsymbol{B}^{[m]}\right)^{-1}, & i = 0, \\ \boldsymbol{x}_0\boldsymbol{C}^{[m]}\boldsymbol{G}^{[m]}, & i = 1, \\ \boldsymbol{x}_1\boldsymbol{R}_m^{i-1}, & i > 1, \end{cases} \tag{7.15}$$

satisfying the normalisation condition $\boldsymbol{x}_0^{[m]}\boldsymbol{e} + \boldsymbol{x}_1^{[m]}(\boldsymbol{I} - \boldsymbol{R}_m)^{-1}\boldsymbol{e} = 1$, with $\boldsymbol{R}_m$ is the MAM rate matrix being the minimum non-negative solution of the quadratic equation: $\boldsymbol{R}_m = a\boldsymbol{F}^{[m]} + \boldsymbol{R}_m\left(a\boldsymbol{S}^{[m]} + \overline{a}\boldsymbol{F}^{[m]}\right) + \overline{a}\boldsymbol{R}_m^2\boldsymbol{S}^{[m]}$, and $\boldsymbol{G}^{[m]} = \left(\boldsymbol{I} - a\boldsymbol{S}^{[m]} - \overline{a}\boldsymbol{F}^{[m]} - \overline{a}\boldsymbol{R}_m\boldsymbol{S}^{[m]}\right)^{-1}$.

Proof. The proof follows from applying a similar approach to that in Theorem. 6.2 while using the constructed matrices relative to the SF-adaptive Markov chain. □

As $\boldsymbol{A}_2^{[m]}$ and $\boldsymbol{A}_1^{[m]}$ are of ranks higher than 1, the expression of $\boldsymbol{R}_m$ cannot be explicitly obtained and the following algorithm is used to compute it.

Algorithm 2: Computation of $\boldsymbol{R}_m$

Data: m, $\boldsymbol{S}^{[m]}$, $\boldsymbol{F}^{[m]}$, ϵ
Initialisation: $k = 0$, $\boldsymbol{R}_m^{(0)} = 0$
while $\|\boldsymbol{R}_m^{(k+1)} - \boldsymbol{R}_m^{(k)}\| \geq \epsilon$ *(ϵ convergent criterion)* **do**
  $\boldsymbol{R}_m^{(k+1)} = a\boldsymbol{F}^{[m]} + \boldsymbol{R}_m^{(k)}\left(a\boldsymbol{S}^m + \overline{a}\boldsymbol{F}^{[m]}\right) + \overline{a}(\boldsymbol{R}_m^{(k)})^2\boldsymbol{S}^m$ Increment k ;
end
Return $\boldsymbol{R}_m$

C. SFs Activity Distribution

Let $\boldsymbol{\varphi}^{[m]} = [\varphi_0^{[m]}, \varphi_1^{[m]}, ...\varphi_L^{[m]}]$ be the marginal distribution vector where $\varphi_l^{[m]}$ corresponds to the MAC protocol phase of a LoRa node. This phase can be any of the available SFs or any of their corresponding DC sub-states. As a LoRa node located in $\mathcal{A}_m$ can operate with any of the N SFs, the probability to be active using SF_q, denoted hereinafter $\delta_q^{[m]}$, is given by:

$$\delta_q^{[m]} = \boldsymbol{\varphi}_q^{[m]}, \quad q \in \mathcal{Q}, \tag{7.16}$$

where $\boldsymbol{\varphi}_q^{[m]}$ is the qth element of $\boldsymbol{\varphi}^{[m]}$, the marginal distribution of the phases with nonempty data buffers. The sub-stochastic vector $\boldsymbol{\varphi}^{[m]}$ is given by:

$$\boldsymbol{\varphi}^{[m]} = \sum_{i \geq 1} \boldsymbol{x}_i^{[m]} = \boldsymbol{x}_1^{[m]} \left(\boldsymbol{I} - \boldsymbol{R}_m\right)^{-1}. \tag{7.17}$$

D. Unstable Regions

If the stability condition $\boldsymbol{\pi}^{[m]}\mathbf{A}_2^{[m]}\mathbf{e} > \boldsymbol{\pi}^{[m]}\mathbf{A}_0^{[m]}\mathbf{e}$ is not satisfied, region $\mathcal{A}_M$ is unstable and the data buffer of the nodes belonging to $\mathcal{A}_M$ infinitely grows. The probability to reach level 0 (empty buffer) is nullified and the SFs activity distribution is obtained from $\boldsymbol{\varphi}^{[m]} = \boldsymbol{\pi}^{[m]}$ where $\delta_q^{[m]} = \pi_q^{[m]}$.

7.3.3 Iterative Algorithm for SG-QT Interdependence

The iterative solution detailed in Algorithm. 1 is extended to Algorithm. 3. Algorithm. 3 accounts for the the SF adaptation and the interdependence between spatial regions.

7.3.4 Performance Assessment Metrics

The iterative solution previously detailed allows us to compute the queue distribution as well as the coverage probability at the steady state in each region of the cell. Using the obtained steady state statistics, we derive the following key performance metrics.

Algorithm 3: Computation of $\boldsymbol{\varphi}$ and $P_c(q, \gamma_q))\forall q$

Data: N, λ_L, Γ,a,b,d, ϵ
Initialisation: $k = 0$, $\boldsymbol{x}_0^{[m]}$ and $\boldsymbol{\varphi}^{[m]}$ s.t. $\boldsymbol{x}_0^{[m]}\boldsymbol{e} + \boldsymbol{\varphi}^{[m]}\boldsymbol{e} = 1\forall m$;
while $\max_m \|\boldsymbol{\varphi}_{(k+1)}^{[m]} - \boldsymbol{\varphi}_{(k)}^{[m]}\| \geq \epsilon$ *(ϵ convergence criterion)* **do**
  for $m = 1, .., M$ **do**
    1. Evaluate $P_q^{[m]}\left(q, \gamma_q\right) \forall$ q following Eq. 7.6 and using $\boldsymbol{\Delta}$;
    2. Construct $\boldsymbol{S}^{[m]}$ and $\boldsymbol{F}^{[m]}$ by Eq. 7.8;
    3. Construct $\boldsymbol{A}^{[m]}$;
    4. Obtain $\boldsymbol{\pi}^{[m]}$ (Eq. 7.14) and check the stability ($\boldsymbol{\pi}^{[m]}\mathbf{A}_2^{[m]}\mathbf{e} > \boldsymbol{\pi}^{[m]}\mathbf{A}_0^{[m]}\mathbf{e}$);
    if *Stable* **then**
      4.1 Calculate $\boldsymbol{R}_m^{(k+1)}$ using the iterative solution;
      4.2 Solve $\boldsymbol{x}_0^{[m]}$ and $\boldsymbol{x}_1^{[m]}$ using Eq. 7.15;
      4.3 Compute $\boldsymbol{\varphi}_{(k+1)}^{[m]} = \boldsymbol{x}_1^{[m]}\left(\boldsymbol{I} - \boldsymbol{R}_m^{(k+1)}\right)^{-1}$;
    else
      4.4 Set $\boldsymbol{x}_0^{[m]} = 0$ and $\boldsymbol{\varphi}_{(k+1)}^{[m]} = \boldsymbol{\pi}^{[m]}$;
    end
  end
  5. Compute $\boldsymbol{\Delta}$;
  6. Increment k ;
end
Return $\boldsymbol{R}_m \leftarrow \boldsymbol{R}_m^{(k+1)}$, $\boldsymbol{\varphi}^{[m]} \leftarrow \boldsymbol{\varphi}_{(k+1)}^{[m]}$,$\boldsymbol{x}^{[m]}$ and $p_q^{[m]}\left(\gamma_q\right)\forall q$, $\forall m$;

A. Device Coverage Probability

Using the per-SF coverage probability derived in Eq. 7.6 and the steady state SF distribution obtained by Eq. 7.16, we define the device global (SF-averaged) coverage probability in $\mathcal{A}_m$ as:

$$P^{[m]} = \sum_1^N \frac{\delta_q^{[m]}}{\sum_1^N \delta_q^{[m]}} P_q^{[m]} \tag{7.18}$$

Remark 7.7. *The device global (SF-Averaged) coverage probability metric captures the weight of each SF's activity.*

B. Delay

We use W_m to denote the number of time slots a LoRa device in $\mathcal{A}_m$ spends from a randomly selected packet generation until its successful delivery. By virtue of Little's law Subsection. 1.6.3 , the average delay is given by the ratio between the

average number of packets in the system and the packet arrival rate a and is given by:

$$\overline{W}_m = \mathbb{E}[W_m] = \frac{\overline{L}_m}{a}, \tag{7.19}$$

where $\overline{L}_m$ is the average number of packets in the system, including the packet being processed, and is given by:

$$\overline{L}_m = \mathbb{E}[L_m] = \boldsymbol{x}_1^{[m]} (\boldsymbol{I} - \boldsymbol{R}_m)^{-2} \boldsymbol{e}. \tag{7.20}$$

Considering the equi-probable discrete regions, we define the spatially averaged total latency as:

$$\overline{W} = \mathbb{E}[W] = \frac{1}{M} \sum_{1}^{M} \overline{W}_m. \tag{7.21}$$

C. ζ-Stability

For ech region, the Pareto stability frontiers are characterised by the set of system parameters $\mathcal{S}_m = \{\{\lambda_L, \Gamma, a\} \in \mathbb{R}^2 \times [0,1] \,|\, \boldsymbol{\pi}^{[m]} \mathbf{A}_2^{[\mathbf{m}]} \mathbf{e} > \boldsymbol{\pi}_m \mathbf{A}_0^{[\mathbf{m}]} \mathbf{e}\}$. LoRa nodes belonging to $\mathcal{A}_m$ and operating within $\mathcal{S}_m$ have a service rate higher than the arrival rate and deliver their packets within finite delays. The ratio/fraction of the network where stability is guaranteed is given by ζ_s.

$$\zeta_s = \frac{1}{M} \sum_{m=1}^{M} \mathbb{1}_{\left(\boldsymbol{\pi}^{[m]} \mathbf{A}_2^{[\mathbf{m}]} \mathbf{e} > \boldsymbol{\pi}_m \mathbf{A}_0^{[\mathbf{m}]} \mathbf{e}\right)} \tag{7.22}$$

Considering the adopted distance-base discretisation,we define the ζ-stability frontiers [11] of a LoRa network by the set of system parameters $\mathcal{S}_\zeta = \{\{\lambda_L, \Gamma, a, b, d\} \in \mathbb{R}^2 \times [0,1] \,|\, \zeta_s > \zeta\}$.

D. ζ-Operativity

In a similar vein as the stability, we define the ζ-operativity using the fraction of the network where a specific QoS indicator is fulfilled [11]. Taking the delay as our performance indicator and a sensing application with a delay requirement W^*, the

delay ζ-operativity region depicts the set of system parameters $O_\zeta = \{\{\lambda_L, \Gamma, a, b, d\} \in \mathbb{R}^2 \times [0,1] \,|\zeta_o > \zeta\}$ with $\zeta_{o,W}$ defined as:

$$\zeta_{o,W} = \frac{1}{M} \sum_{m=1}^{M} \mathbb{1}_{(\overline{W}_m < W^*)}. \tag{7.23}$$

Using the device (SF-averaged) coverage probability as metric of interest, the corresponding ζ-operativity region of a sensing application with coverage requirement P^* is $O_\zeta = \{\{\lambda_L, \Gamma, a, b, d\} \in \mathbb{R}^2 \times [0,1], \zeta_{o,P} > \zeta\}$ with

$$\zeta_{o,P} = \frac{1}{M} \sum_{m=1}^{M} \mathbb{1}_{(P^{[m]} > P^*)}. \tag{7.24}$$

Remark 7.8. *As the discrete regions of the LoRa cell are equiprobable, the ζ-stability metric reflects the percentage of nodes with stable queues. This also applies for ζ-operativity which gives the percentage of nodes operating with satisfied KPIs constraints.*

7.4 Numerical Results

In this section, the theoretical framework detailed in the previous section is used to study the network performance and quantify the interplays between various performance metrics. We present selected numerical results for both distance-oblivious and distance-aware scenarios according to the supplied system parameters. Unless otherwise mentioned, the system parameters are supplied according to the following setup: The SF set $\mathcal{S}$ is fixed to $\{\mathrm{SF}_1, \ldots, \mathrm{SF}_6\} = \{7, \ldots, 12\}$ with $\Gamma = [-20, -23, -26, -29, -32, -35]$ being the capture thresholds of the SFs, the transmission power of the devices is set to $\mathcal{P} = 14$ dBm, and the adaptation parameters are $d = 0.3$ and $b = 0.8$. Initially all the nodes are assigned to the lowest SF with probability 90% and start in the idle state assuming their DC requirements are satisfied.

7.4.1 Impact of SF Adaptation Cardinality N

In this subsection we fix $M = 1$ and study the impact of modifying the SF adaptation cardinality N on stability frontiers, coverage and, delay. Fig. 7.4 represents the area

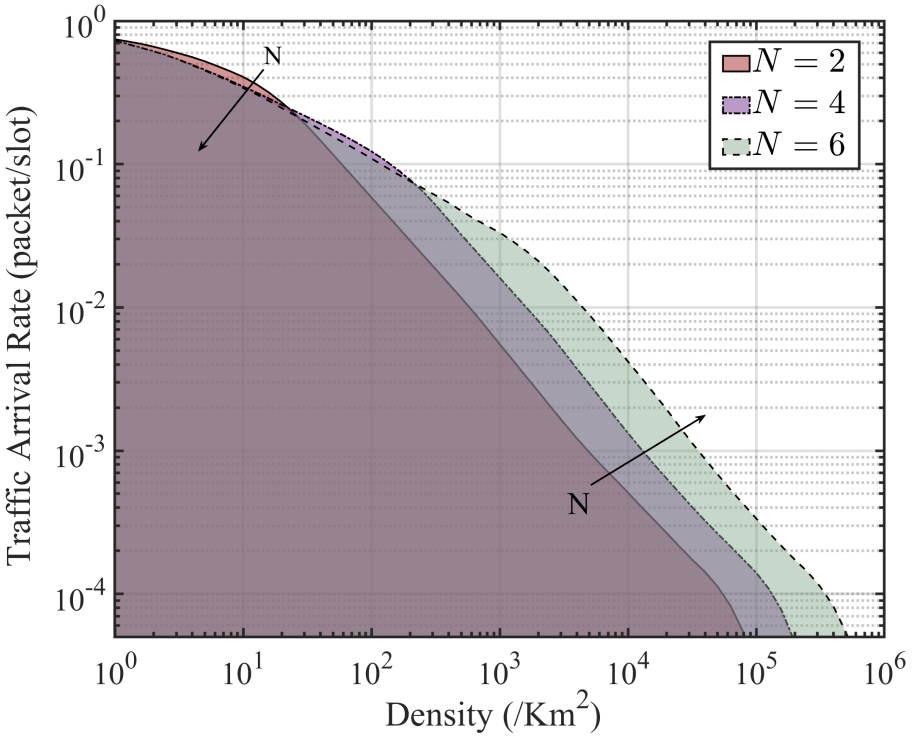

Fig. 7.4: Impact of adaptation cardinality N on stability frontiers (λ_L, a).

of system parameters pairs (λ_L, a) that guarantee stable network operations. To maintain stable network operations, the traffic arrival rate should decrease as the nodes density increases resulting in a compromise between the scalability and the stability of the network. The different areas in Fig. 7.4 show the range of sensing applications, characterised by their traffic arrival rates (i.e. sensing rates) that can be accommodated by LoRa without compromising the network stability. Two main factors can lead to unstable network operations: i) the duty cycle constraint LoRa nodes need to adhere to, and ii) interference.

Fig. 7.4 exhibits a behaviour that is worth analysing. At low-medium densities, it is shown that lower N allows the network to accommodate higher arrival rates satisfying the stability conditions, while at higher densities, higher N allows higher arrival rates. Interestingly, there exists a transition density threshold for which a higher N starts to guarantee higher arrival rates. This threshold varies between different pairs of N. Taking the example of $(2, 4)$, the transition occurs at $\lambda_L = 20$ nodes/km^2 while it occurs at $\lambda_L = 251$ nodes/km^2 for $(4, 6)$. This behaviour confirms that for low-medium densities, the limiting factor of stability is the DC.

Increasing N introduces higher SFs that spend longer time on their DC states. Longer DC periods lead to packet accumulation and make nodes vacate their buffers less often, thereby compromising network stability. At high densities, the root cause of instability is the overwhelming interference that leads to packet retransmissions. That is why increasing N alleviates the interference and extends the stability region. Within the common stability region of all Ns, for a fixed arrival rate, increasing N achieves a substantial shift in the scalability of the network since higher SFs have lower detection thresholds γ_q that improve the coverage probability of the nodes.

The behaviour manifested in Fig. 7.4 suggests that activating dynamic SF adaptation with high cardinality is not always advantageous. It also reveals that based on the characteristics of the sensing application (density and traffic arrival rate), an SF adaptation cardinality N that meets the best scalability-stability trade-off. In Fig. 7.5, we track the evolution of coverage probability for SF= 7

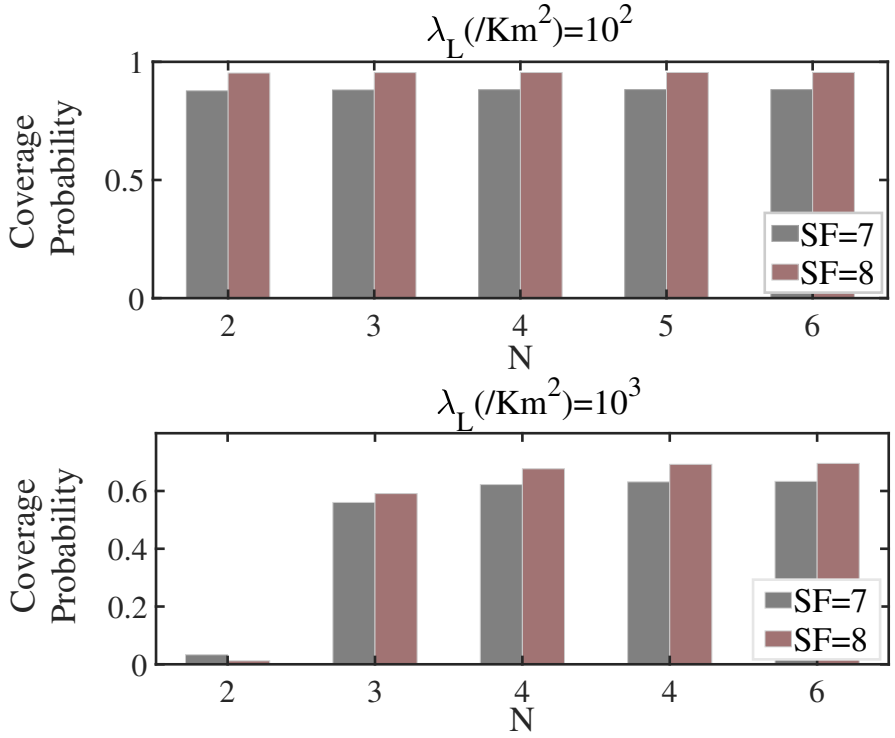

Fig. 7.5: Impact of adaptation cardinality N on coverage probability, $a = 0.01$ packets/slot, $d = 0.3$, $b = 0.8$.

and SF= 8 as N increases. We can see that for low density ($\lambda_L = 10^2$ nodes/km^2),

increasing N does not improve the coverage of SF= 7 and SF= 8 as the bars remain consistent while for higher densities ($\lambda_L = 10^3$ nodes/km^2), the improvement is more noteworthy especially as we move from $N = 2$ to $N = 3$. Based on this observation, for a dense network limiting the SF adaptation cardinality to $N = 2$ would result in overwhelming SF= 7 and SF= 8 with co-SF interference which explains their poor performance. As N increases, a sort of activity load-balancing is achieved between the SFs. This load-balancing between the SFs relieves the co-SF interference and enhances the node's coverage.

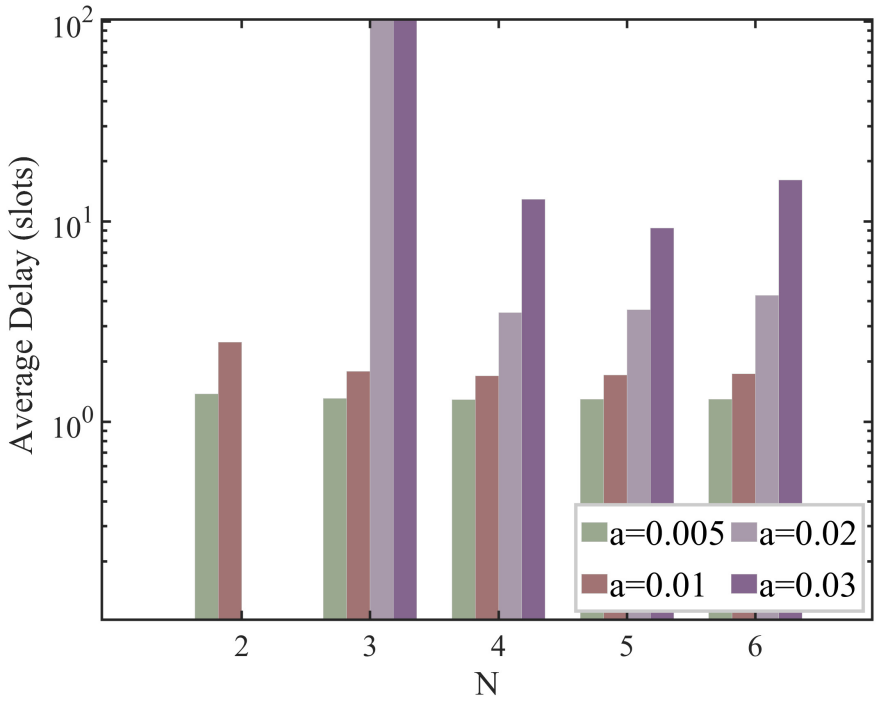

Fig. 7.6: Impact of adaptation cardinality N on average delay, $\lambda_L = 500$ nodes/Km^2, $b = 0.8$,$d = 0.3$.

In Fig. 7.6 we plot the average delay for different arrival rates while varying N. Some interesting observations follow from the examination of Fig. 7.6. For a low arrival rate ($a = 0.005$ packet/slot), the average delay is resilient to the change in N. As the traffic arrival rate increases, the average delay increases and the impact of N becomes more noteworthy. It is shown that given fixed adaptation parameters b and d and density λ_L, there exists an N that minimizes the average delay for each arrival rate. For $a = 0.01$ packet/slot the minimum delay occurs for $N = 3$, for $a = 0.02$ packet/slot, the minimum delay is obtained with $N = 4$, while for

a = 0.03 packet/slot, N = 5 guarantees a minimum delay. This clearly illustrates the importance to appropriately choose the SF cardinality in the adaptation scheme and the resulting delay trade-off.

7.4.2 Distance-Oblivious Analysis (M=1, N=6)

In this section we set the SF cardinality N = 6 and deeply examine the case of M = 1 where the analysis is devised throughout the whole LoRa cell without discretization. This distance-oblivious analysis is motivated by scenarios where the spatial correlation constraint is relaxed which might be the case of some applications like transportation, logistics, etc.

A. Stability-Scalability Frontiers

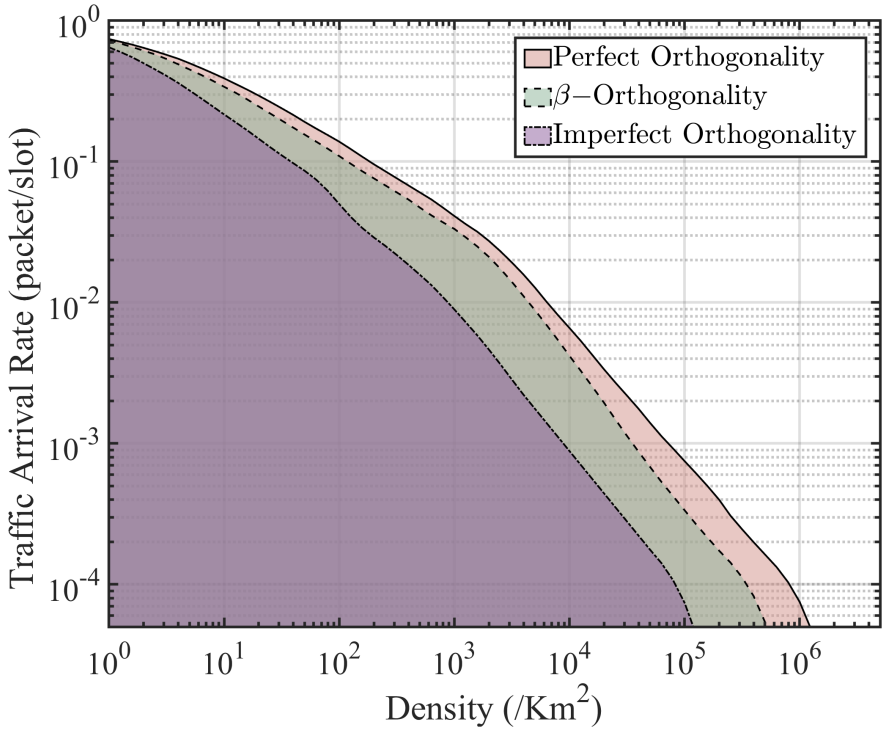

Fig. 7.7: Impact of SFs orthogonality assumption on stability frontiers (λ_L, a).

In Fig. 7.7, we plot the stability frontiers for the system parameters plane (a,λ_L) under three different orthogonality assumptions: (i) perfect orthogonality, i.e. $\beta_{q_1 \neq q_2} = 0$, (ii) imperfect orthogonality, i.e. $\beta_{q_1,q_2} = 1 \; \forall q_1, q_2$, and (iii)

β_{q_1,q_2}−orthogonality, i.e. β_{q_1,q_2} from Table Tab. 6.1. Examining Fig. 7.7, we can see that as the density increases the difference between the three orthogonality assumptions become more noticeable. For a fixed traffic arrival rate $a = 10^{-4}$ the imperfect, β_{q_1,q_2}, and perfect orthogonality assumptions give a maximum density ensuring stability of $\{ 7 \times 10^4, 3 \times 10^5, 8 \times 10^5\}$ nodes/km^2 , respectively. By overlooking the impact of inter-SF interference, the perfect orthogonality assumption overamplifies the scalability limits, while the imperfect orthogonality assumption creates an aggressive interference scenario that ends up underestimating the scalability-stability boundaries.

Fig. 7.7 clearly illustrates the impact of link-level analysis on the system's network-level performance and highlights the importance of properly quantifying the non-orthogonality of LoRa SFs in the design of scalable LoRa networks. Designing a LoRa network with the assumption of imperfect-orthogonality or perfect-orthogonality can lead to respectively over-conservative or optimistic operational regimes. Using the developed $\beta_{q1,q2}$−orthogonality characterization, we can more accurately represent the limits of scalability and gain more accurate insights into the design, planning, and dimensioning of LoRa networks.

Fig. 7.8 illustrates the impact of the SF-Up and SF-Down operations on the stability frontiers. Examining the impact of the SF-Down operations in Fig. 7.8, three density regimes can be distinguished. For a lightly loaded network $\lambda_L <= 5$ nodes/km^2, decreasing b slightly extends the stability region. As the density increases, the impact of b becomes more prominent and the increase in b substantially extends the stability region for medium densities until it reaches $\lambda_L = 4 \times 10^4$ nodes/km^2. When the network density becomes sufficiently large $\lambda_L > 4 \times 10^4$ nodes/km^2 decreasing b improves the stability region.

These density regimes can be explained by the main causes of network instability which are the DC and the interference. For a lightly loaded network, DC is the limiting factor of instability. Thus, decreasing b increases the probability of the nodes to be assigned to lower SFs which are able to accommodate higher arrival rates as they spend less time duty-cyling. As the density increases, the interference

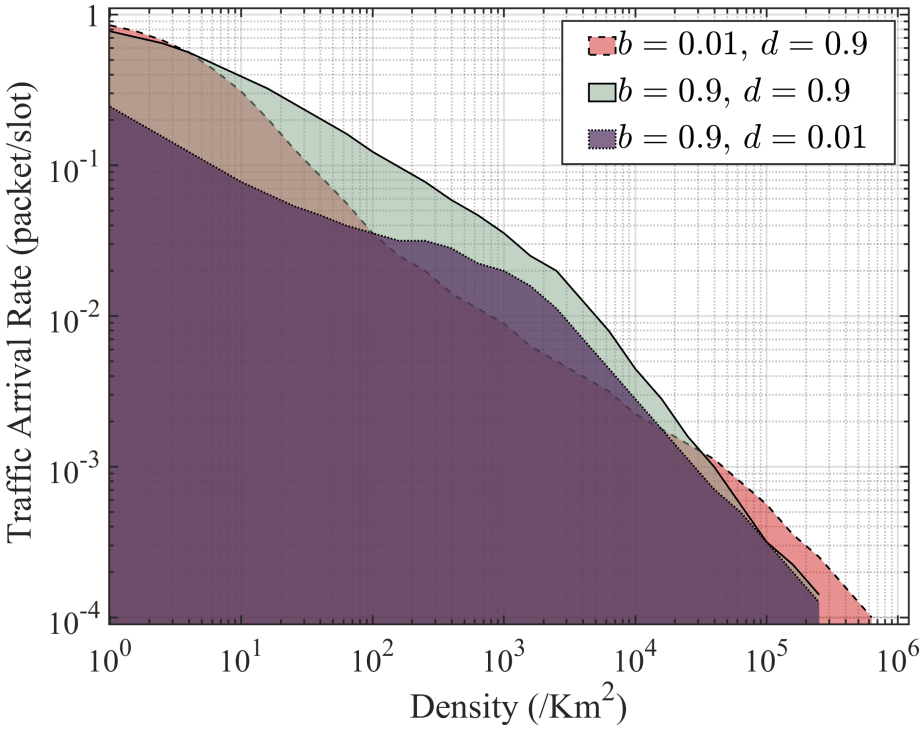

Fig. 7.8: Impact of SFs orthogonality assumption N on stability frontiers, (λ_L, a)-plane.

comes into play, and increasing b makes the node rapidly converges to a higher SF that improves its coverage. For a highly loaded network, nodes will be subject to an overwhelming interference scenario that over-speeds up the convergence to higher SFs. In such a situation, decreasing b makes the network regains the balance between the different SFs activities. With a high convergence speed to high SFs, increasing the convergence speed to lower SFs d extends the stability region with a more notable impact at for low to meidum densities $\lambda_L < 10^2$ nodes/km^2. To further understand the observed stability behaviours, next we examine the evolution of the SFs activities and the coverage probability as the traffic arrival rate and the network density increase.

B. SFs Activities Distribution, Coverage, and Delay

In Fig. 7.9 and Fig. 7.10, we track the evolution of the SFs activities and the coverage probability with the network density for a fixed traffic arrival rate while in Fig. 7.11 and Fig. 7.12, we track the evolution of the SFs activities and the coverage

probability with the arrival rate for a fixed density.

Fig. 7.9 shows that for $\lambda_L < 10^2$ nodes/km^2, SF_1 (SF= 7) clearly dominates the distribution with more than 60%. As the density increases, the activity distribution of SF_1 decreases while that of SF_q>SF_1 increases until it reaches a maximum after which it drops. Then SF_N (SF= 12) dominates for high densities. Fig. 7.10 shows that increasing SF keeps improving the coverage probability until a certain density threshold after which the coverage probability of higher SFs precisely SF= 12, and SF= 11 drops to become even lower than that of SF_1. This drop can be attributed to an overwhelming interference that leads to packet failures and retransmissions. Such aggressive congestion makes higher SFs dominate the activity distribution as demonstrated in Fig. 7.9 worsening therefore, the co-SF interference. Moreover, with high SFs, LoRa devices spend long waiting-time before being able to make any transmission attempt which leads to packet accumulation, exasperating, further, the bottleneck situation. The above analysis further justifies the impact of adaption on the stability regions observed in Fig. 7.8 and confirms that increasing the SF (i.e decreasing the rate) in a congested LoRa network could further deteriorate its performance.

Fig. 7.11 shows that for a traffic arrival rate a less than 10^{-3} packets/slot, SF_1 dominates the distribution with more than 80%. As the arrival rate increases, we notice similar behaviour as in Fig. 7.9 wherein each SF's activity increases until it reaches its maximum then drops. Fig. 7.9 and Fig. 7.11 show the existence of network density and traffic arrival rate regimes for which a transition in the activity distribution occurs and SF_{q+1} starts to dominate (highest percentage) the distribution in stead of SF_q. Fig. 7.12 shows the impact of increasing the traffic arrival rate on the coverage probability of each SF. At very low traffic arrival rate $a < 4 \times 10^{-4}$, it is shown that increasing SF has little impact on the coverage improvement. As the traffic arrival rate increases, the impact of SF adaptation on the coverage's improvement begins to be more evident. The higher the SF, the best is the coverage probability for high traffic arrival rates.

Fig. 7.9 and Fig. 7.11 coupled with Fig. 7.10 and Fig. 7.12 help identify density

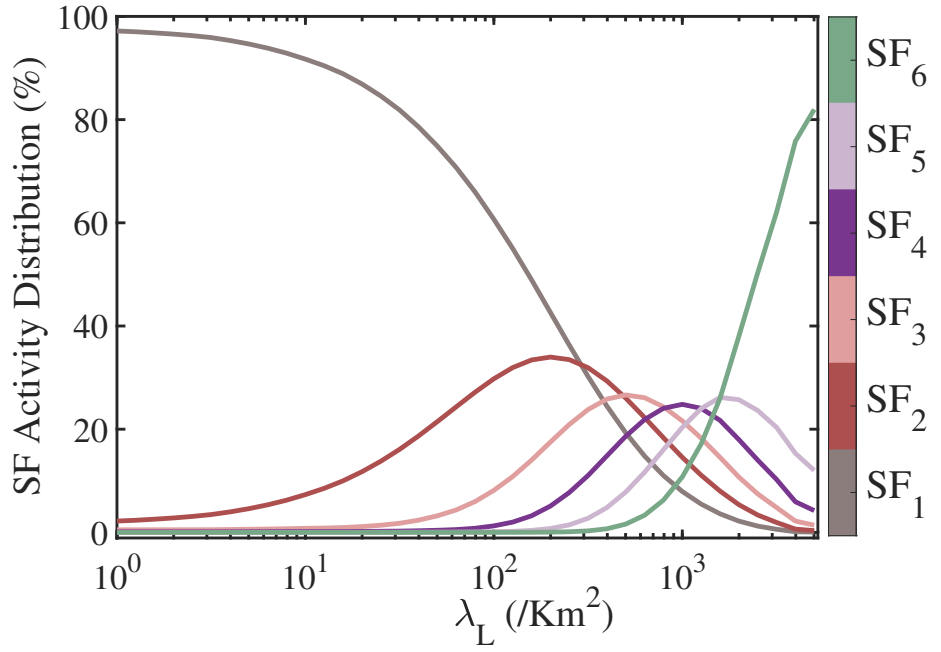

Fig. 7.9: Impact of nodes density on SF activity distribution, $a = 0.015$ (packets/slot).

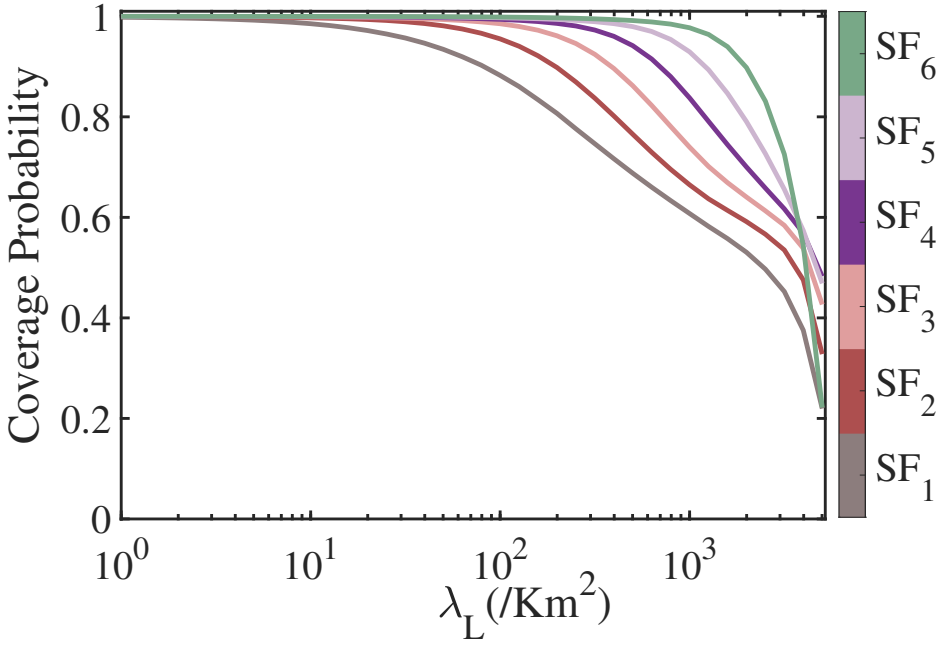

Fig. 7.10: Impact of nodes density on the Per-SF Coverage probability$a = 0.015$ (packets/slot)

and traffic load regimes where a network would take the most benefits from an SF adaptation mechanism. In what follows we study the impact of adaptation parameters b and d on the global (SF-Averaged) coverage and the average delay

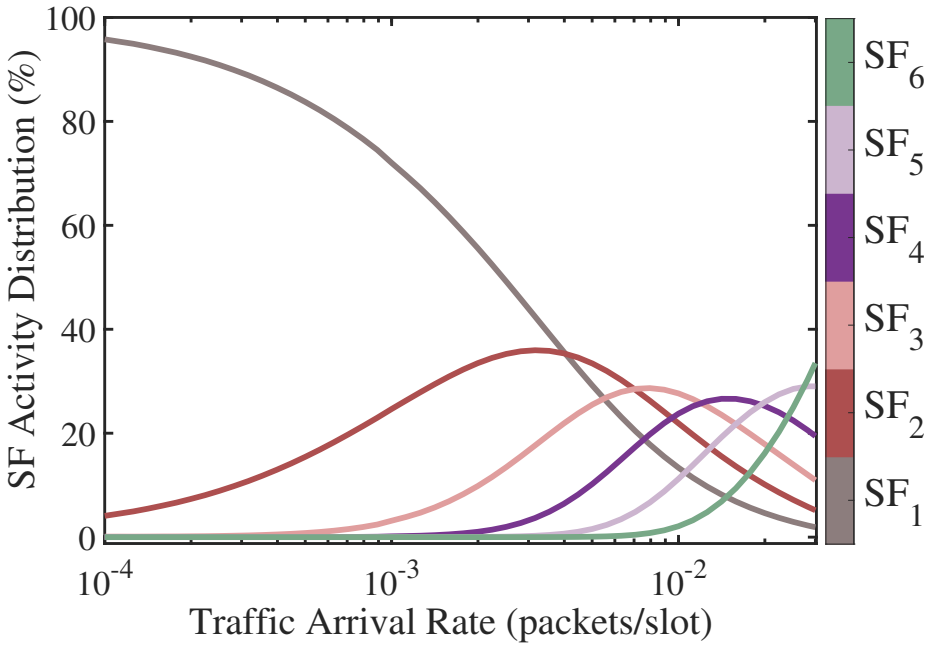

Fig. 7.11: Impact of packet arrival rate on SF activity distribution, $\lambda_L = 10^3$ nodes/km^2.

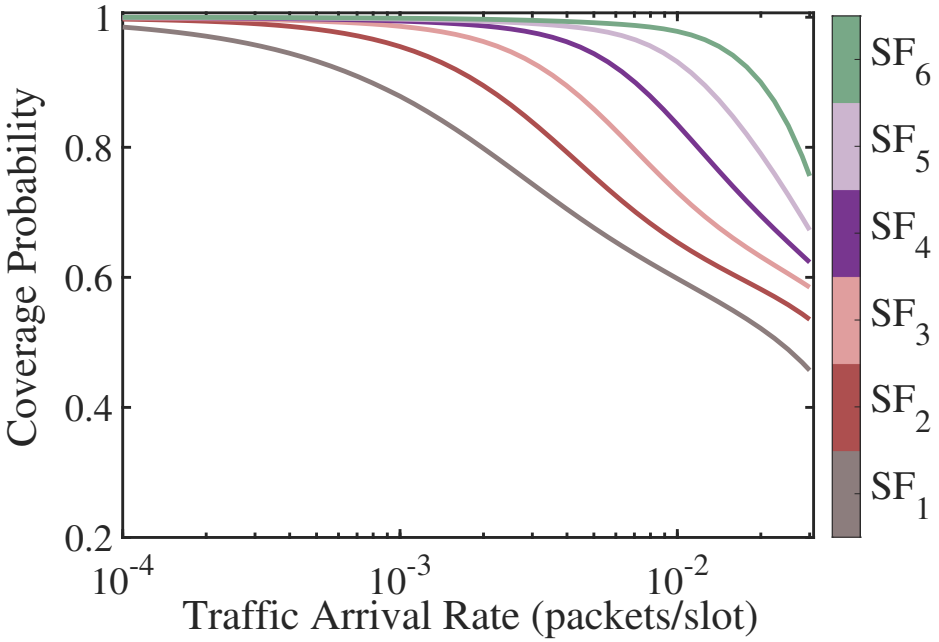

Fig. 7.12: Impact of traffic arrival rate on Per-SF Coverage probability $\lambda_L = 10^3$ nodes/km^2.

metrics given in Eq. 7.18 and Eq. 7.21, respectively.

Fig. 7.13 plots the coverage probability (SF-Averaged) at the adaptation steady state for fixed b and varying d. It shows that for a fixed b the coverage probability

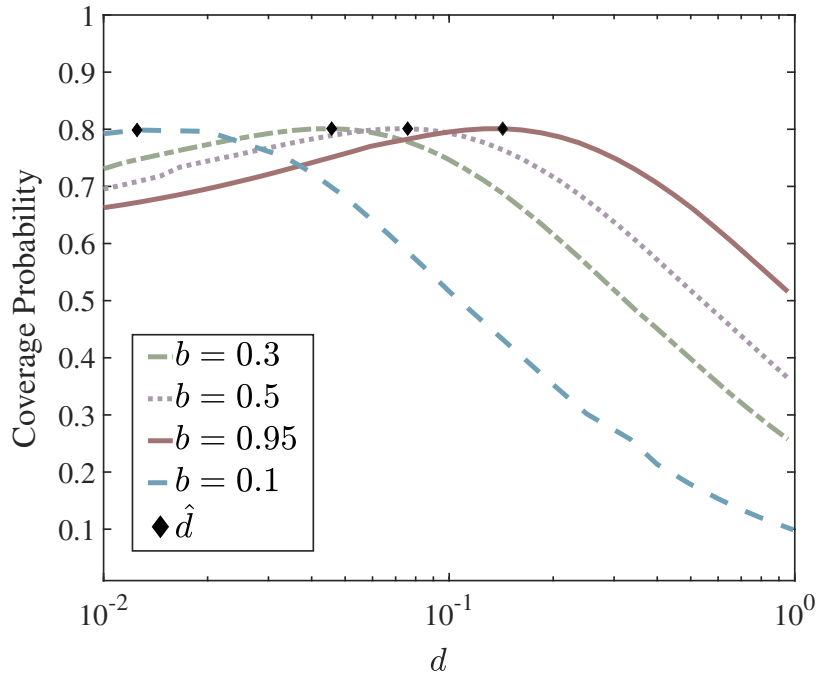

Fig. 7.13: Global (SF-Averaged) coverage probability for $\lambda_L = 10^3$ nodes/km^2 and $a = 0.02$ packet/slot.

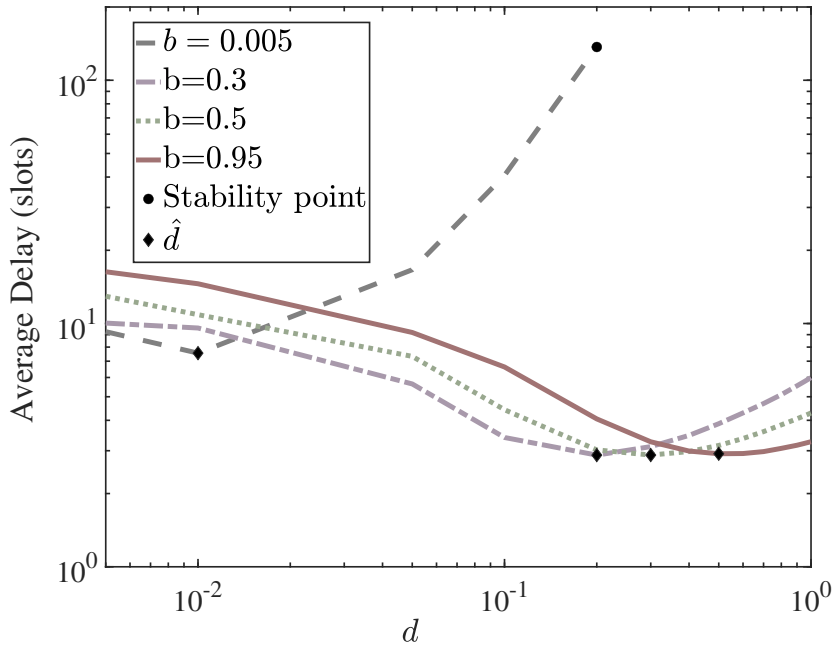

Fig. 7.14: Average delay for $\lambda_L = 10^3$ nodes/km^2 and $a = 0.02$ packet/slot.

increases with d until it reaches a maximum value then decreases which proves the existing of an optimal $\hat{d}$ that maximises the coverage probability. It can be observed that $\hat{d}$ increases with b. For instance for $b = \{0.3, 0.5, 0.95\}$, $\hat{d} = \{0.045, 0.075, 0.14\}$ corresponding on average to respectively 22, 13 and 7 successful transmissions before triggering the SF-down operation. An other compelling behaviour Fig. 7.13 shows is that for low d ($d < 10^{-1}$), the device coverage probability decreases with b, while for high d increasing b improves the coverage.

Fig. 7.14 tracks the evolution of the average delay versus the SF-Down rate d. For a fixed b, increasing d decreases the average delay until it reaches its minimum at $\hat{d}$. As d exceeds $\hat{d}$, the convergence to lower SFs becomes very fast leading to packet failure and re-transmissions which causes the delay to increase and can compromise the network stability. Fig. 7.13 and Fig. 7.14 emphasize the interplay between the SF−Up and SF−Down operations and illustrate the compromise between the coverage and the delay obtained from the SF adaptation settings.

7.4.3 Distance-Aware Analysis

In this section, we analyse the distance-aware scenario for $N = 6$ using $M > 1$ regions.

In Fig. 7.15, we plot the activity distribution and the coverage probability of the SFs among different regions A_m. The figure shows that the activity of low SFs (SF_1,SF_2) decreases as we move outward from the central region, while the activities of high SFs (SF_4,SF_5,SF_6) increases with m. It shows also that the activity distribution in region $\mathcal{A}_1$, $\mathcal{A}_2$, $\mathcal{A}_3$, and $\mathcal{A}_4$ is dominated by SF_1, SF_3, SF_3, and SF_4, respectively. We can see that the coverage probability of low SFs precisely SF$\in \{7, 8, 9\}$ decreases in the outer regions of the cell while the coverage of high SFs precisely SF$\in \{10, 11, 12\}$ remains almost consistent across the different regions.

The activity distribution and per-SF coverage probability in Fig. 7.15 give a global (SF-Averaged) coverage probability of $\{0.838, 0.75, 0.735, 0.733\}$ in $\{\mathcal{A}_1, \mathcal{A}_2, \mathcal{A}_3, \mathcal{A}_4\}$, respectively as illustrated in Fig. 7.16. We can see that the adaptation mechanism

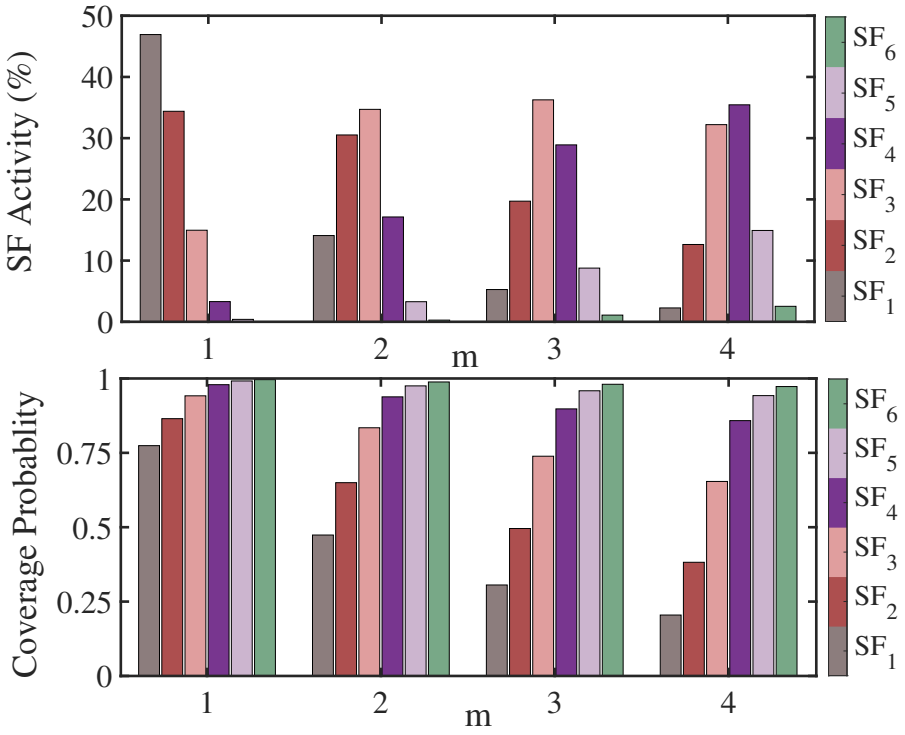

Fig. 7.15: Per-SF Activity distribution and coverage in different regions for $a = 0.01$ packet/slot, $\lambda_L = 10^3$ nodes/km^2, b) $a = 0.01$ packet/slot).

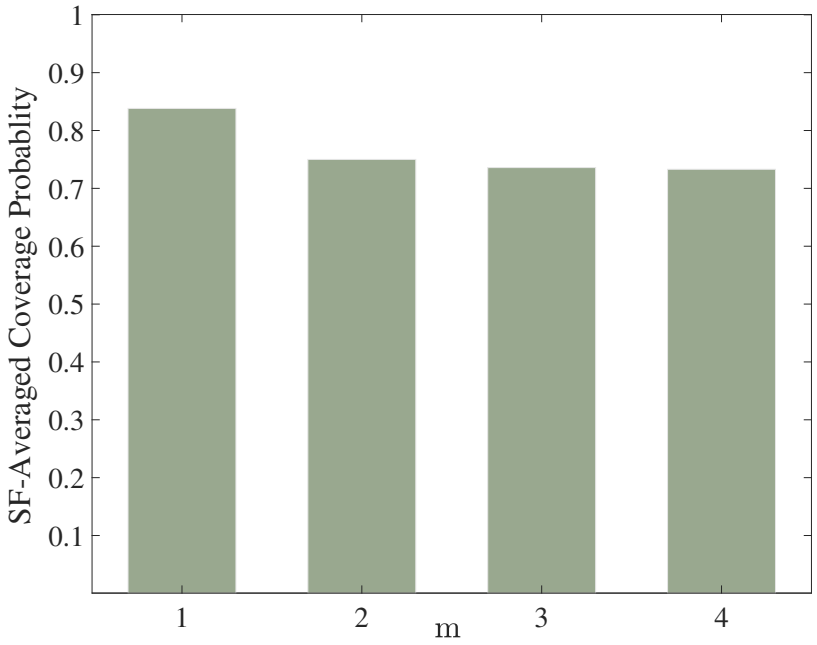

Fig. 7.16: Global (SF-Averaged) coverage probability in different regions for $a = 0.01$ packet/slot, $\lambda_L = 10^3$ nodes/km^2.

converges towards an SF distribution that ensures a sort of fairness in terms of coverage between the different regions.

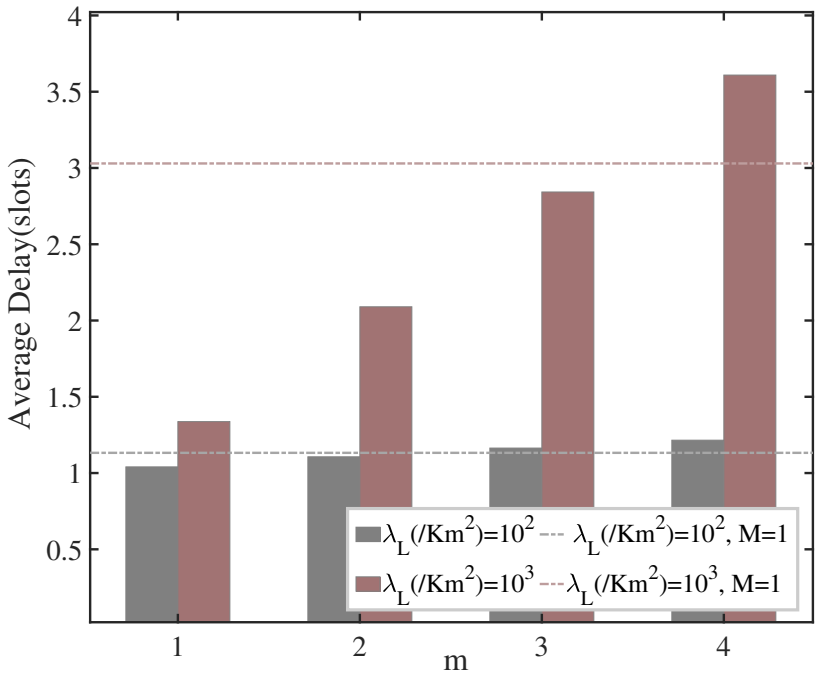

Fig. 7.17: Average delay in different regions for $\lambda_L = 10^3$ nodes/km^2 $a = 0.01$ packet/slot.

In Fig. 7.17, we plot the average delay across different regions. The figure shows the difference between the distance-oblivious analysis (lines) and the distance-based discretisation approach (bars). We can see that for $\lambda_L = 10^2$ nodes/km^2, delays across the regions are approximately equal and have small variance compared to the case of $M = 1$. As the density increases from $\lambda_L = 10^2$ nodes/km^2 to $\lambda_L = 10^3$ nodes/km^2, the difference between the per-region average delays and the single-region ($M = 1$) average delay becomes significant. Together, Fig. 7.15 and Fig. 7.17 illustrate the importance of the proposed distance-based discretisation approach in the network performance analysis, especially as the density increases.

A. ζ-Stability Analysis

In Fig. 7.18, we plot the ζ-stability regions for the systems parameter plane (d, b). The figure shows the (d, b) pairs that can be accommodated by the network subject to a stability threshold ζ. The ζ-stability metric provides more fine-grained information about the performance of individual nodes compared to distance-oblivious analysis as it allows us to determine the percentile of nodes that satisfy

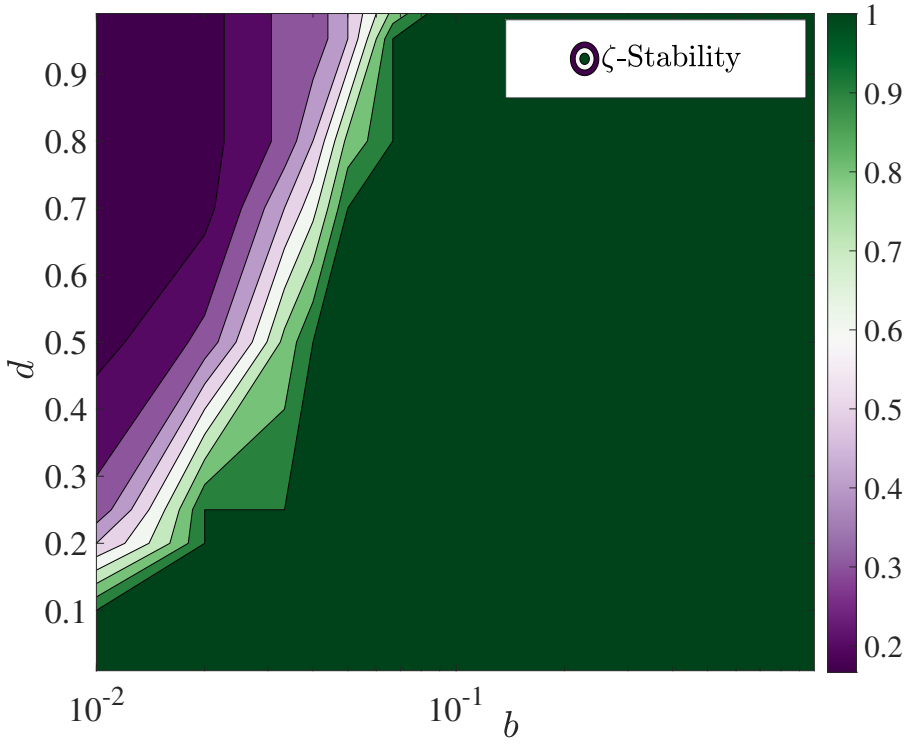

Fig. 7.18: ζ-Stability region, $M = 6$, $a = 0.01$ packet/slot, $\lambda_L = 10^3$ nodes/km^2.

a defined stability constraint. The figure shows that for a fixed density and a fixed SF-Up rate, the percentile of stable nodes satisfying the stability constraint decreases as the SF-Down rate increases.

B. ζ-Operativity Analysis

In the previous paragraph we have analysed the network performance in terms of ζ-stability. This metric is particularly useful for delay-tolerant applications where there are less constraints about the timeliness and reliability of the data to report and what matters is to deliver the sensed data within finite delay, i.e having the system stable. However, to fully characterize the network performance, we may need more information than the stability alone. For this purpose, the ζ-operativity metric comes into play. This metric intrinsically accounts for the QoS requirements of the IoT application as it gives refined information about the percentile of nodes that satisfy the desired QoS KPI constraint. Next, we study the $\zeta - operativity$ regions for two KPIs: the average delay defined in Eq. 7.23 and the

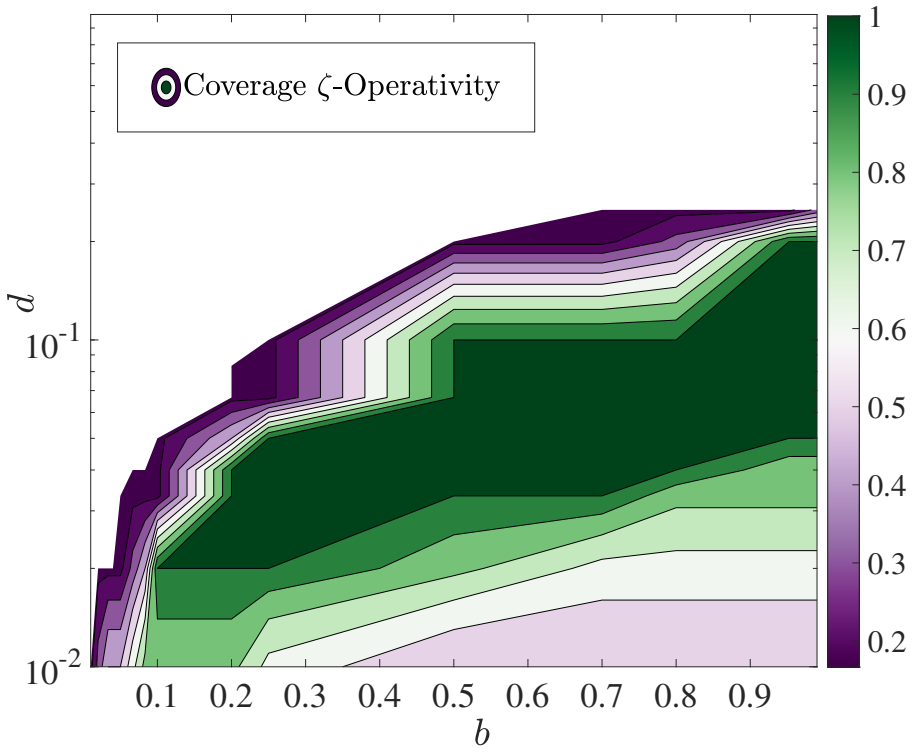

Fig. 7.19: Coverage ζ-Operativity region for $P^* = 80\%$, $M = 6$, $a = 0.01$ packet/slot, $\lambda_L = 10^3$ nodes/km^2.

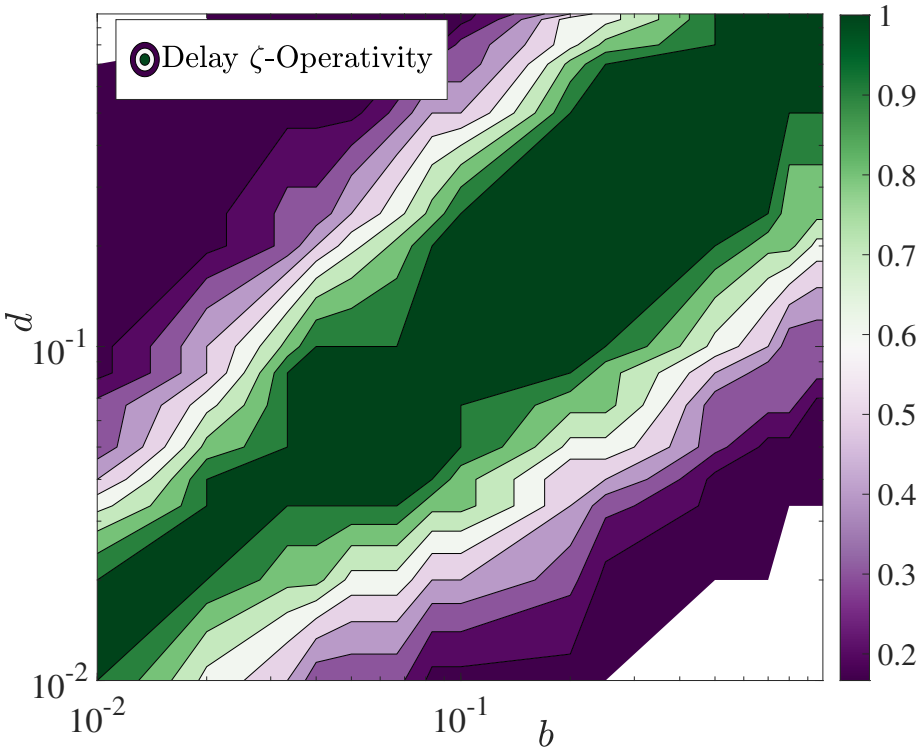

Fig. 7.20: Delay ζ-Operativity region for $W^* = 10$ slots, $M = 6$, $a = 0.01$ packet/slot, $\lambda_L = 10^3$ nodes/km^2.

global (SF-averaged) coverage obtained in Eq. 7.24.

In Fig. 7.19, we plot the operativity region subject to a coverage constraint of 80% i.e. $P > 0.8$. The figure spots the combination of adaptation parameters (b, d) that achieve this coverage constraint. Fig. 7.19 shows that for a highly loaded network ($\lambda_L = 10^3$ nodes/km^2) and $b = 0.5$ i.e. increasing the SF every 2 failed transmissions, a fast SF-Down rate larger that 0.2 i.e. decreasing the SF every 5 or less successful transmissions, leads to more than 84% of the nodes with a coverage probability less than 80 %. In Fig. 7.20, we plot the operativity region subject to a delay constraint of 10 slots. Examining Fig. 7.20, we can see that extreme regimes where a high SF-Up rate is coupled with a very low SF-Down rate and vice versa give the worst performance and make the average delay of all the nodes exceeds 10 slots.

7.5 Discussion, Limitations and Future Extensions

The results presented in Fig. 7.4, Fig. 7.7, Fig. 7.8, and Fig. 7.18 clearly illustrate the tension between the scalability and the stability of the network while Fig. 7.13, Fig. 7.14, Fig. 7.19, and Fig. 7.20 evince a tradeoff between the reliability and latency in the network. The analysis provided in this paper helps gain insights into different performance trade-offs in dynamic LoRa networks with adaptive SF allocation. It can therefore serve the development and design of application-aware decentralized or semi-decentralized SF adaptation mechanisms that could be effective both in channel fading and interference dominated environments. Extensions of the proposed analytical framework include and are not limited to:

Power-Adaptation and Energy Consumption: The proposed analytical framework can be extended further to account for power adaptation in conjunction with SF adaptation. It can also incorporate energy consumption modeling to provide a comprehensive assessment of the various trade-offs (stability, scalability, reliability, latency, and longevity).

Multiplicative SF- Up/Down Operations: A second aspect that merits future

study is to extend the developed DTMC model from one-step jump between the SFs to p-steps jump, investigate options to quantify the decision about the jump steps, and study its impact on the network performance metrics.

7.6 Chapter Summary and Key Findings

In this chapter we have proposed a probabilistic SF adaptation scheme to characterize the performance of dynamic adaptive LoRa networks through a joint use of *Stochastic Geometry* (SG) and *Queuing Theory* (QT). We have derived metrics that better reflect the performance of individual links, connecting therefore the performance analysis of LoRa networks with the application characteristics and requirements.

Key Findings

The impact of different system design parameters on the network performance have been thoroughly investigated and bellow we summarise the key findings:

- It has been shown that quantifying the imperfect orthogonality of LoRa SFs plays important role in deriving more accurate performance metrics allowing a more meticulous characterisation of the network performance boundaries.
- The evolution of the SFs distribution and coverage as the density and traffic arrival rate increase have evinced operating regimes where each of the SFs dominates and where the SF adaptation improves the performance of the network the most.
- Three operating regimes have been identified based on the impact of adaptation rates. For a lightly loaded network, increasing the SF has very little impact on the stability-scalability frontiers. For medium densities regime, increasing the SF extends the stability-scalability frontiers. While, increasing the SF has been shown to deteriorate performance in a dense congested network.

- This chapter has revealed the existence of adaptation parameters (cardinality, SF-Up probability b, SF-Down probability d,..) that minimize the average packet delay or maximises the coverage probability suggesting a number of optimisation problems that could be formulated as future extensions to this work.
- The metrics ζ-stability and ζ-operativity were introduced to characterise the percentile of nodes that satisfy the stability conditions or the desired QoS requirements. These metrics are fundamnetal for the design of IoT networks with either best-effort or delay-tolerant traffics. With the proposed methodology we can identify combinations of system parameters that achieve desired requirements in terms of coverage or latency. For a network design setting with a density $\lambda_L = 10^3$ nodes/km^2 and a traffic arrival rate of 0.01 packet/slot, given a required reliability QoS constraint of 80% , the results show that increasing the SF every 2 failed transmissions and decreasing the SF every 5 or more successful transmissions leads to more than 84% of the nodes with a coverage probability less than 80 % i.e with unsatisfied QoS requirements.

At the end of the chapter, a number of ideas that can expand the proposed analytical framework have been discussed.

CHAPTER 8

Conclusion and Future Work

8.1 Summary of Thesis Achievements

My PhD was part of a collaborative research project to assist HDB Singapore in planning and optimising their urban habitat infrastructures[1]. The research efforts throughout the PhD have started by exploring the space of IoT and smart sensing applications, their characteristics and communication requirements. Based on the conducted literature surveying and a questionnaire we distributed among IoT research teams and industrial practitioners, a taxonomy of IoT applications with their communication requirements has been proposed.

Motivated by the basic question stakeholders like HDB would ask about which technology could better answer the requirements of their sensing applications, we applied the developed taxonomy to experimentally compare the performance of LoRa and NB-IoT, the two most competing technologies in the LPWAN market. To ensure fairness, the performance comparison has been executed using the same hardware, under the same environmental conditions, against the same application profiles, and using the same application-level metrics. This preliminary study has highlighted categories of applications LoRa could fit. It has revealed how LoRa

[1]The Housing and Development Board (HDB) is Singapore's public housing authority. It plans and develops Singapore's housing estates https://www.hdb.gov.sg/cs/infoweb/homepage.

performance is highly impacted by transmission parameters and environmental conditions compared to NB-IoT.

The results of the preliminary experimental study have further motivated our focus on LoRa as a new promising license-free patented technology that merits being further explored, analysed and enhanced. We initiated our investigations about LoRa from this start point. We aimed to provide a comprehensive framework that can serve as a tool to analyse the performance LoRa/LoRaWAN networks while accounting for both spatial and temporal network dynamics. From a spatial dynamics perspective, we leveraged powerful tools from SG to model and analyse uplink asynchronous Aloha-like transmissions in single-gateway and multi-gateway LoRa networks. We derived tractable expressions for the transmission success probability and analysed the impact of different network parameters on the performance of LoRa SFs.

The concerns raised about LoRa scalability and the absence of consensus about LoRa modulation in the literature have intrinsically led us to delve into LoRa signal theory. Our goal from the LoRa signal theory investigation was to unveil the answer to how orthogonal is LoRa modulation? Therefore putting an end to the disagreement about the orthogonality (perfect, quasi, pseudo, imperfect) of LoRa modulation and devising a way to quantify it. The comprehensive analysis in Chapter. 4 provides a better understanding of LoRa signal theory, quantifies the imperfect orthogonality of LoRa modulation through the cross-correlation function analysis and reveals how LoRa orthogonality is impacted by the physical features.

Using the quantified orthogonality coefficients, we propose a more accurate interference model that was fed into the joint stochastic geometry-queuing theory framework we devised in Chapter. 6. In Chapter. 6, we have studied the coverage probability, the scalability-stability limits and the latency in static-SF LoRa networks. LoRa is endowed with multiple tuneable parameters that can be adapted to the communication requirements of the applications. Yet, the impact of this adaptation on the performance of large-scale LoRa networks is not well investigated in the

literature. This has motivated us to extend the proposed model in Chapter. 6 and explore dynamic LoRa networks with adaptive SF in Chapter. 7. Combining device-level and network-level modelling in Chapter. 7, we have leveraged a queue-aware and mutual interference-aware analytical model to study the performance of adaptive LoRa networks. Such a comprehensive model gave us the opportunity to cover various performance metrics and study the interplay between them. We have been able to spot optimal operational regimes where the QoS requirements in terms of coverage and latency are satisfied. The effect of parameters such as node density, traffic load, and adaptation rates have been analysed. The proposed analysis provides valuable insights and blueprints into the performance of dynamic LoRa networks with adaptive SF and could help the development of application-aware decentralised or semi-decentralised SF adaptation mechanisms.

At the early stage of the Ph.D., our government partner HDB teams were reticent about LoRa as it was a new technology for them. To the best of our knowledge, at the time of the experiment, the deployment detailed in Section. 2.5 was the first outdoor LoRa network in a residential area in Singapore. By the end of the Ph.D., in light of the research carried out throughout the PhD and the results of the preliminary experimental comparative study (Section. 2.5), the HDB teams have been convinced that LoRa merit being given a chance. They have even started a pilot project in HDB Punggol Northshore estate to test LoRa for some real applications, all of which have been recommended in Section. 2.5. Noting that HDB Punggol Northshore is the first smart-enabled eco-town in Singapore[2].

To conclude, this thesis focused on LPWAN, particularly on LoRa as an emerging unlicensed technology offering the opportunity for stakeholders to build private sensing infrastructures. The thesis tried to connect LoRa capabilities and performance prospects to the IoT application characteristics and needs. The frameworks developed in this thesis provide valuable analytical tools to study the performance of LoRa from link level to system level, with spatial and temporal network dynamics taken into account and under static and dynamic resource

[2] https://www.hdb.gov.sg/about-us/our-role/smart-and-sustainable-living/punggol-ecotown.

allocations. The results presented in this thesis can be extended to evaluate a broad array of system setups. The setups can be chosen according to the characteristics of the IoT application to design and plan, as well as its operational objectives and QoS requirements. With the contributions of this thesis, a better understanding of LoRa behaviours, performance boundaries and trade-offs have been achieved, delineating optimal operational regimes and sparking potential directions for making LoRa a path to scalable, ubiquitous, and adaptive connectivity.

8.2 Ongoing and Future Works

8.2.1 Energy Harvesting for Self-Powered Green LoRa Networks

Our aim has been to comprehensively evaluate the performance of LoRa towards Scalable Steady and Sustainable (3S) networks. The three dimensions, scalability, stability, and sustainability are all important for the deployment of well-provisioned smart sensing infrastructures that optimally perform their intended tasks while being sustainable and green. The scalability, stability, and reliability of the network have been investigated in Chapter. 5 Chapter. 6 and Chapter. 7. Our approach to address the remaining challenge which concerns the sustainability relies on using energy harvesting as an alternative option to power LoRa nodes. The system model and conceptual choices for this ongoing work have been prepared, and we are currently performing the necessary simulations. The outcome of this work will be submitted to IEEE Globecom 2024. In what follows, we motivate this work, outline related work, and give an overview of the system model.

Motivation: While most of the analysis focusing on LoRa were steered towards scalability analysis, throughput prediction, and spread factor allocation, only a few of them [171, 172] addressed the topic of energy efficiency, which remains a major challenge in IoT technologies and particularly in low power wide area networks including LoRa. The goal in these works was often to extend the lifetime of the sensor battery. However, relying on battery life extension would not be sufficient to avoid battery replacement, which become even more compulsory

for sensing applications deployed in harsh environments. In this regard, energy harvesting (EH) can be presented as one way to ensure sustainable operation and elongated battery life-times. In EH-enabled systems, energy can be harvested from different types of sources, including but not limited to solar, wind, electromagnetic, and radio frequency (RF) [173]. In the last RF-based harvesting technique, the energy can be obtained from dedicated transmitters (deployed specifically to provide energy) or ambient energy (transmitters that are already scattered in the environment like WiFi, cellular, etc.). Indeed, with the deployment of 5G and 6G, higher Bandwidths will be used which will increase the availability of unused frequency spectrum giving, hence, more potential for Radio Frequency (RF) energy harvesting.

Related Works: Research on EH-enabled LoRa networks is still at its infancy. In [174], a battery-less LoRa wireless sensor was designed for road condition monitoring and is powered by the vibrations harvested by an electromagnetic energy harvester based on a Halbach configuration. In [175], a novel floating device was proposed with a multi-source energy harvesting technique, which harvests solar and thermoelectric energy. The work was extended in [176], to reduce the power consumption in the listening phase. These works do not carry out energy budgeting or optimization to provide energy neutral guarantees.

Energy Harvesting Model: LoRa nodes are equipped with energy harvesters (solar panel and RF rectifier) and a rechargeable battery to store the harvested energy. They harvest energy from the ambient environment. The sources of energy that can be exploited are solar energy and RF energy from downlink cellular networks (different frequency band) or from concurrent LoRa networks (same frequency band).

The *harvest-then-transmit* protocol is considered where the LoRa node needs to harvest and store energy in the battery until the stored energy is enough to transmit one packet to the gateway. Let $P_{t,q}$ be the required power to transmit one packet using SF_q. Due to duty cycle restrictions, the total energy harvesting phase will last at least during the off-time period $\frac{1-d}{d} T_{s,q}$. In this way, each LoRa node assigned

to SF_q will be active at a given time slot if: (i) the battery has enough energy to transmit, (ii) the data buffer is not empty, and (iii) the duty cycle restrictions are met. Let δ_q be the probability that a LoRa node assigned to SF_q is active. If the i'th LoRa node is active at a given time slot with probability δ_q, the packet transmission will last during $T_{s,q}$ which represents $d2^q$ times the slot duration and then the LoRa node resets to the EH mode during at least the remaining time of the slot duration, which is $(1 - d2^q)T_1$. Otherwise, the LoRa node is in the EH mode during the whole time slot duration T_1.

Without loss of generality, we assume that the battery has a finite size and is discretized into M energy levels where the battery size corresponds to the power $P_{t,q}$ sufficient to transmit one packet. Let $\omega_q = P_{t,q}/M$ be the amount of energy corresponding to one energy level in the battery. Once a packet is transmitted, the energy is depleted from the battery and the LoRa node needs to reset to the EH mode.

8.2.2 System-Level Optimisation:

The results of Chapter. 7 have revealed the existence of multiple system parameters that minimize the delay or maximise the coverage. As a next step, optimisation problems can be formulated based on the analytical framework developed in Chapter. 7 to optimise the latency and coverage. In [6] stochastic geometry has been leveraged as a system-level optimisation tool to optimize the energy efficiency of downlink cellular networks. Extensions of the framework proposed in Chapter. 7 can further include: i) formulation of the spectral efficiency metric ii) modelling of the energy consumption, therefore being able to study and optimise the energy efficiency versus spectral efficiency trad-offs, ii) formulation of Age of Information (AoI) , which could be a very useful metric to evaluate the effectiveness of LoRa in applications with very strict timeliness constraints. In [177], a SG-based model was proposed to study peak AoI in generic IoT Uplink Networks.

8.2.3 Meta Distribution in LoRa networks:

In Chapter. 7, we discretised the cell into distance-based regions to account for the disparity of the performance across nodes placed at different distances from the serving gateway. A potential alternative to this approach is to use the Meta-Distribution metric. Meta-Distribution is an emerging metric that has been recently introduced into the performance analysis of wireless networks. It has the advantage of giving more refined information on random variables [178, 179]. [178] and [179] are seminal works where the fundamentals of this metric are presented, its properties are outlined, and its interpretations are discussed in depth. The meta-distribution metric has been widely used to study cellular networks [11, 177, 180, 181]. However, in the context of LoRa/LoRaWAN, to the best of our knowledge [135, 182] are the initial works in which analytical expressions for the SIR meta-distribution in a single-cell LoRa network with perfect orthogonality were proposed.

8.2.4 3D-SG Models:

In light of the preliminary study results obtained in Section. 2.5, the nomenclature of the urban area has been shown to affect the performance of a LoRa network. As a future extension, the proposed analytical frameworks in Chapter. 5, Chapter. 6, and Chapter. 7 can be extended to study the effect of high rising buildings. For this end, 3D stochastic geometry [183] frameworks can be leveraged to incorporate the height dimension and study its impact on network performance.

Bibliography

[1] Statistica Web site. *Internet of things (IoT) connected devices installed base worldwide from 2015 to 2025 (in billions)*. URL: https://www.statista.com/statistics/471264/iot-number-of-connected-devices-worldwide/ (visited on 02/10/2019).

[2] URL: https://lora-alliance.org/.

[3] N.Sornin(Semtech), M.Luis(Semtech), T.Eirich(IBM), T. Kramp (IBM), and O.Hersent(Actility). "LoRaWAN™ Specification". In: (2015).

[4] Yassine Hmamouche, Mustapha Benjillali, Samir Saoudi, Halim Yanikomeroglu, and Marco Di Renzo. "New Trends in Stochastic Geometry for Wireless Networks: A Tutorial and Survey". In: *Proceedings of the IEEE* 109.7 (2021), pp. 1200–1252. DOI: 10.1109/JPROC.2021.3061778.

[5] Hesham ElSawy, Ahmed Sultan-Salem, Mohamed-Slim Alouini, and Moe Z. Win. "Modeling and Analysis of Cellular Networks Using Stochastic Geometry: A Tutorial". In: *IEEE Communications Surveys & Tutorials* 19.1 (2017), pp. 167–203.

[6] Marco Di Renzo, Alessio Zappone, Thanh Tu Lam, and Mérouane Debbah. "System-Level Modeling and Optimization of the Energy Efficiency in Cellular Networks—A Stochastic Geometry Framework". In: *IEEE Transactions on Wireless Communications* 17.4 (2018), pp. 2539–2556. DOI: 10.1109/TWC.2018.2797264.

[7] Wei Lu and Marco Di Renzo. "Stochastic Geometry Modeling of Cellular Networks: Analysis, Simulation and Experimental Validation". In: *MSWiM*. 2015, pp. 1–4. DOI: 10.1109/IWMN.2015.7322991.

[8] Eleni Demarchou, Constantinos Psomas, and Ioannis Krikidis. "Wireless Powered Cognitive Communications with Asynchronous Channel Access". In: *2019 IEEE 20th International Workshop on Signal Processing Advances in Wireless Communications (SPAWC)*. Jul 2019, pp. 1–5. DOI: 10.1109/SPAWC.2019.8815517.

[9] Mohammad Gharbieh, Hesham ElSawy, Hong-Chuan Yang, Ahmed Bader, and Mohamed-Slim Alouini. "Spatiotemporal Model for Uplink IoT Traffic: Scheduling and Random Access Paradox". In: *IEEE Transactions on Wireless Communications* 17.12 (2018), pp. 8357–8372. DOI: 10.1109/TWC.2018.2876522.

[10] Mohammad Gharbieh, Hesham ElSawy, Ahmed Bader, and Mohamed-Slim Alouini. "Spatiotemporal Stochastic Modeling of IoT Enabled Cellular Networks: Scalability and Stability Analysis". In: *IEEE Transactions on Communications* 65.8 (Aug 2017), pp. 3585–3600. DOI: 10.1109/TCOMM.2017.2700309.

[11] Giovanni Chisci, Hesham Elsawy, Andrea Conti, Mohamed-Slim Alouini, and Moe Z. Win. "Uncoordinated Massive Wireless Networks: Spatiotemporal Models and Multiaccess Strategies". In: *IEEE/ACM Transactions on Networking* 27.3 (2019), pp. 918–931. DOI: 10.1109/TNET.2019.2892709.

[12] Fatma Benkhelifa, Hesham ElSawy, Julie A. McCann, and Mohamed-Slim Alouini. "Recycling Cellular Downlink Energy for Overlay Self-Sustainable IoT Networks". In: *2018 IEEE Global Communications Conference (GLOBECOM)*. Dec 2018, pp. 1–7. DOI: 10.1109/GLOCOM.2018.8647615.

[13] Qingquan Huang, Baha Eddine Youcef Belmekki, Ahmed M. Eltawil, and Mohamed-Slim Alouini. "System-Level Metrics for Non-Terrestrial Networks Under Stochastic Geometry Framework". In: *ArXiv* abs/2302.03376 (2023).

[14] Maurilio Matracia, Mustafa A. Kishk, and Mohamed-Slim Alouini. "UAV-Aided Post-Disaster Cellular Networks: A Novel Stochastic Geometry

Approach". In: *IEEE Transactions on Vehicular Technology* (2023), pp. 1–13. DOI: 10.1109/TVT.2023.3247920.

[15] Yassine Hmamouche, Mustapha Benjillali, and Samir Saoudi. "On the Role of Stochastic Geometry in Sixth Generation Wireless Networks". In: *2020 10th International Symposium on Signal, Image, Video and Communications (ISIVC)*. 2021, pp. 1–6. DOI: 10.1109/ISIVC49222.2021.9487542.

[16] Wei Lu and Marco Di Renzo. "Stochastic geometry modeling of mmWave cellular networks: Analysis and experimental validation". In: *2015 IEEE International Workshop on Measurements Networking (M N)*. 2015, pp. 1–4.

[17] Joonas Kokkoniemi, Josep M. Jornet, and Markku Juntti. "Stochastic Geometry Framework for THz Satellite-Airplane Network Analysis". In: *2021 IEEE International Symposium on Dynamic Spectrum Access Networks (DySPAN)*. Los Angeles, CA, USA: IEEE Press, 2021, pp. 67–72. DOI: 10.1109/DySPAN53946.2021.9677325. URL: https://doi.org/10.1109/DySPAN53946.2021.9677325.

[18] Dorsaf Ghozlani, Aymen Omri, Seifeddine Bouallegue, Hela Chamkhia, and Ridha Bouallegue. "Stochastic Geometry-based Analysis of Joint Radar and Communication-Enabled Cooperative Detection Systems". In: *2021 17th International Conference on Wireless and Mobile Computing, Networking and Communications (WiMob)*. 2021, pp. 325–330. DOI: 10.1109/WiMob52687.2021.9606367.

[19] Yongxu Zhu, Gan Zheng, and Kai-Kit Wong. "Stochastic Geometry Analysis of Large Intelligent Surface-Assisted Millimeter Wave Networks". In: *IEEE Journal on Selected Areas in Communications* 38.8 (2020), pp. 1749–1762. DOI: 10.1109/JSAC.2020.3000806.

[20] Martin Haenggi. *Stochastic Geometry for Wireless Networks*. Cambridge University Press, 2012. DOI: 10.1017/CBO9781139043816.

[21] Bartłomiej Błaszczyszyn and Dhandapani Yogeshwaran. "Clustering Comparison of Point Processes, with Applications to Random Geometric Models". In: *Stochastic Geometry, Spatial Statistics and Random Fields: Models and*

Algorithms. Ed. by Volker Schmidt. Cham: Springer International Publishing, 2015, pp. 31–71. ISBN: 978-3-319-10064-7. DOI: 10.1007/978-3-319-10064-7_2. URL: https://doi.org/10.1007/978-3-319-10064-7_2.

[22] Martin Haenggi. *Stochastic Geometry for Wireless Networks*. Cambridge University Press, 2012. DOI: 10.1017/CBO9781139043816.

[23] Ihor Tereikovskiy, Ivan Parkhomenko, Serhii Toliupa, and Liudmyla Tereikovska. "Markov model of normal conduct template of computer systems network objects". In: *2018 14th International Conference on Advanced Trends in Radioelecrtronics, Telecommunications and Computer Engineering (TCSET)*. 2018, pp. 498–501. DOI: 10.1109/TCSET.2018.8336250.

[24] Salvatore Scrivano and Tullio Tolio. "A Markov Chain model for the performance evaluation of manufacturing lines with general processing times". In: *Procedia CIRP* 103 (2021). 9th CIRP Global Web Conference – Sustainable, resilient, and agile manufacturing and service operations : Lessons from COVID-19, pp. 20–25. ISSN: 2212-8271. DOI: https://doi.org/10.1016/j.procir.2021.10.002. URL: https://www.sciencedirect.com/science/article/pii/S221282712100843X.

[25] Margot Wagner, Thomas M. Bartol, Terrence J. Sejnowski, and Gert Cauwenberghs. "Markov Chain Abstractions of Electrochemical Reaction-Diffusion in Synaptic Transmission for Neuromorphic Computing". In: *Frontiers in Neuroscience* 15 (). DOI: 10.3389/fnins.2021.698635. URL: https://par.nsf.gov/biblio/10326452.

[26] Pietro Cipresso, Francesca Borghesi, and Alice Chirico. "Affects affect affects: A Markov Chain". eng. In: *Frontiers in psychology* 14 (2023), pp. 1162655–1162655. ISSN: 1664-1078.

[27] Amel Salem Omer and Dereje Hailemariam Woldegebreal. "Review of Markov Chain and Its Applications in Telecommunication Systems". In: *e-Infrastructure and e-Services for Developing Countries*. Ed. by Yahya H. Sheikh, Idris A. Rai, and Abubakar D. Bakar. Cham: Springer International Publishing, 2022, pp. 366–385. ISBN: 978-3-031-06374-9.

[28] S. Lall, A. S. Alfa, and B. T. Maharaj. "The role of queueing theory in the design and analysis of wireless sensor networks: An insight". In: *2016 IEEE 14th International Conference on Industrial Informatics (INDIN)*. 2016, pp. 1191–1194. DOI: 10.1109/INDIN.2016.7819347.

[29] Bartłomiej Błaszczyszyn and Mohamed Kadhem Karray. "Performance Analysis of Cellular Networks With Opportunistic Scheduling Using Queueing Theory and Stochastic Geometry". In: *IEEE Transactions on Wireless Communications* 18.12 (2019), pp. 5952–5966. DOI: 10.1109/TWC.2019.2940938.

[30] Krati Rastogi, Anurag Barthwal, Divya Lohani, and Debopam Acharya. "An IoT-based Discrete Time Markov Chain Model for Analysis and Prediction of Indoor Air Quality Index". In: *2020 IEEE Sensors Applications Symposium (SAS)*. 2020, pp. 1–6. DOI: 10.1109/SAS48726.2020.9220077.

[31] Srinvas R. Chakravarthy. *Introduction to matrix-analytic methods in queues. 1, Analytical and simulation approach - basics*. eng. Mathematics and statistics series. Hoboken, NJ: John Wiley & Sons, Inc., 2022. ISBN: 1-394-16542-0.

[32] R. M. Loynes. "The stability of a queue with non-independent inter-arrival and service times". In: *Mathematical Proceedings of the Cambridge Philosophical Society* 58.3 (1962), pp. 497–520. DOI: 10.1017/S0305004100036781.

[33] Attahiru S. Alfa. *Applied Discrete-Time Queues*. 2nd. Springer Publishing Company, Incorporated, 2015. ISBN: 149393418X.

[34] Y. P. E. Wang, X. Lin, A. Adhikary, A. Grovlen, Y. Sui, Y. Blankenship, J. Bergman, and H. S. Razaghi. "A Primer on 3GPP Narrowband Internet of Things". In: *IEEE Communications Magazine* 55.3 (Mar 2017), pp. 117–123. ISSN: 0163-6804.

[35] Joseph Finnegan and Stephen Brown. "A Comparative Survey of LPWA Networking". In: *ArXiv* abs/1802.04222 (2018). URL: https://api.semanticscholar.org/CorpusID:3656886.

[36] Min Chen, Yiming Miao, Yixue Hao, and Kai Hwang. "Narrow Band Internet of Things". In: *IEEE Access* 5 (2017), pp. 20557–20577. DOI: 10.1109/ACCESS.2017.2751586.

[37] Collins Burton Mwakwata, Hassan Malik, Muhammad Mahtab Alam, Yannick Le Moullec, Sven Parand, and Shahid Mumtaz. "Narrowband Internet of Things (NB-IoT): From Physical (PHY) and Media Access Control (MAC) Layers Perspectives". In: *Sensors* 19.11 (2019). ISSN: 1424-8220. DOI: 10.3390/s19112613.

[38] Borja Martinez, Ferran Adelantado, Andrea Bartoli, and Xavier Vilajosana. "Exploring the Performance Boundaries of NB-IoT". In: *IEEE Internet of Things Journal* 6.3 (2019), pp. 5702–5712. DOI: 10.1109/JIOT.2019.2904799.

[39] Sigfox Web site. *Technology Overview*. URL: https://www.sigfox.com/en/sigfox-iot-technology-overview (visited on 09/17/2019).

[40] Claire Goursaud and Jean-Marie Gorce. "Dedicated networks for IoT: PHY / MAC state of the art and challenges". In: *EAI Endorsed Transactions on Internet of Things* 1.1 (2015), p. 150597. DOI: 10.4108/eai.26-10-2015.150597.

[41] *Semtech*. URL: https://www.semtech.com (visited on 01/12/2021).

[42] URL: https://www.semtech.com/products/wireless-rf/lora-24ghz/sx1281.

[43] Olivier Bernard, André Seller, and Nicolas Sornin. *Low power long range transmitter*. 2014.

[44] Juha Petäjäjärvi, Konstantin Mikhaylov, Marko Pettissalo, Janne Janhunen, and Jari Iinatti. "Performance of a Low-Power Wide-Area network based on LoRa technology: Doppler robustness, scalability, and coverage". In: *International Journal of Distributed Sensor Networks* 13.3 (2017). DOI: 10.1177/1550147717699412.

[45] Aloÿs Augustin, Jiazi Yi, Thomas Clausen, and William Mark Townsley. "A Study of LoRa: Long Range and Low Power Networks for the Internet of Things". In: *Sensors* 16.9 (2016). ISSN: 1424-8220. DOI: 10.3390/s16091466.

[46] *LoRa Modulation Basics - AN1200.22, Revision 2*. AN1200.22. Semtech Corporation. May 2015.

[47] The Things Network. *LoRa Physical Layer Packet Format*. URL: https://www.thethingsnetwork.org/docs/lorawan/lora-phy-format (visited on 05/01/2022).

[48] *RP002-1.0.2 LoRaWAN® Regional Parameters*. RP002-1.0.2. LoRa Allicance. Oct 2020.

[49] Phui San Cheong, Johan Bergs, Chris Hawinkel, and Jeroen Famaey. "Comparison of LoRaWAN classes and their power consumption". In: *2017 IEEE Symposium on Communications and Vehicular Technology (SCVT)*. Oct 2017, pp. 1–6. DOI: 10.1109/SCVT.2017.8240313.

[50] *LoRa ADR*. https://www.thethingsnetwork.org/docs/lorawan/adaptive-data-rate/. Accessed: 2021-04-20.

[51] U. Raza, P. Kulkarni, and M. Sooriyabandara. "Low Power Wide Area Networks: An Overview". In: *IEEE Communications Surveys & Tutorials* 19.2 (2017), pp. 855–873. ISSN: 1553-877X. DOI: 10.1109/COMST.2017.2652320.

[52] Rashmi Sharan Sinha, Yiqiao Wei, and Seung-Hoon Hwang. "A survey on LPWA technology: LoRa and NB-IoT". In: *ICT Express* 3.1 (2017), pp. 14–21. ISSN: 2405-9595. DOI: https://doi.org/10.1016/j.icte.2017.03.004.

[53] Augustine Ikpehai, Bamidele Adebisi, Khaled M. Rabie, Kelvin Anoh, Ruth E. Ande, Mohammad Hammoudeh, Haris Gacanin, and Uche M. Mbanaso. "Low-Power Wide Area Network Technologies for Internet-of-Things: A Comparative Review". In: *IEEE Internet of Things Journal* 6.2 (2019), pp. 2225–2240. DOI: 10.1109/JIOT.2018.2883728.

[54] Claire Goursaud and Jean-Marie Gorce. "Dedicated networks for IoT : PHY / MAC state of the art and challenges". In: *EAI endorsed transactions on Internet of Things* (Oct 2015). DOI: 10.4108/eai.26-10-2015.150597.

[55] Franck Muteba, Karim Djouani, and Thomas Olwal. In: *Procedia Computer Science* 155 (2019), pp. 636–641. ISSN: 1877-0509. DOI: https://doi.org/10.1016/j.procs.2019.08.090.

[56] Sarah Ruepp, Alba Carrillo Mateo, Krzysztof Mateusz Malarski, Jakob Thrane, and Martin Nordal Petersen. "Internet of Things Connectivity in Deep-Indoor Environments". In: *2018 9th International Conference on the Network of the Future (NOF)*. 2018, pp. 96–100. DOI: 10.1109/NOF.2018.8597871.

[57] B. Vejlgaard, M. Lauridsen, H. Nguyen, I. Z. Kovacs, P. Mogensen, and M. Sorensen. "Coverage and Capacity Analysis of Sigfox, LoRa, GPRS, and NB-IoT". In: *2017 IEEE 85th Vehicular Technology Conference (VTC Spring)*. Jun 2017, pp. 1–5. DOI: 10.1109/VTCSpring.2017.8108666.

[58] Transaction Processing Performance Council. *TPC EXPRESS BENCHMARK IoT, Standard Specification Version 1.0.5*. URL: http://www.tpc.org/tpc_documents_current_versions/pdf/tpcx-iot_v1.0.5.pdf.

[59] Embedded Microprocessor Benchmark Consortium. *IoTMark*. URL: https://www.eembc.org/iotmark/.

[60] Embedded Microprocessor Benchmark Consortium. *SecureMark-TLS*. URL: https://www.eembc.org/securemark/.

[61] Filippo Malandra, Steven Rochefort, Pascal Potvin, and Brunilde Sansò. "A Case Study for M2M Traffic Characterization in a Smart City Environment". In: *Proceedings of the 1st International Conference on Internet of Things and Machine Learning*. IML '17. Liverpool, United Kingdom: ACM, 2017, 48:1–48:9. ISBN: 978-1-4503-5243-7. DOI: 10.1145/3109761.3109809.

[62] Jozef Mocnej. "Network Traffic Characteristics of the IoT Application Use Cases". In: 2018. URL: https://api.semanticscholar.org/CorpusID:198181520.

[63] Saber Talari, Miadreza Shafie-khah, Pierluigi Siano, Vincenzo Loia, Aurelio Tommasetti, and João P. S. Catalão. "A Review of Smart Cities Based on the Internet of Things Concept". In: vol. 10. 4. 2017. DOI: 10.3390/en10040421. URL: https://www.mdpi.com/1996-1073/10/4/421.

[64] Arunan Sivanathan, Daniel Sherratt, Hassan Habibi Gharakheili, Adam Radford, Chamith Wijenayake, Arun Vishwanath, and Vijay Sivaraman. "Characterizing and classifying IoT traffic in smart cities and campuses". In: *2017 IEEE Conference on Computer Communications Workshops (INFOCOM WKSHPS)*. 2017, pp. 559–564. DOI: 10.1109/INFCOMW.2017.8116438.

[65] Andrea Zanella, Nicola Bui, Angelo Castellani, Lorenzo Vangelista, and Michele Zorzi. "Internet of Things for Smart Cities". In: *IEEE Internet of Things Journal* 1.1 (2014), pp. 22–32. DOI: 10.1109/JIOT.2014.2306328.

[66] Wenpeng Luan, Duncan Sharp, and Sol Lancashire. "Smart grid communication network capacity planning for power utilities". In: (2010), pp. 1–4. DOI: 10.1109/TDC.2010.5484223.

[67] Gunawan Wibisono and Nofiandri Badruzzaman. "Strategy of smart meter infrastructure implementation using LPWAN technology, pilot project PLN Bali Case Study". In: *MATEC Web Conf.* 218 (2018), p. 03013. DOI: 10.1051/matecconf/201821803013. URL: https://doi.org/10.1051/matecconf/201821803013.

[68] Murat Kuzlu, Manisa Pipattanasomporn, and Saifur Rahman. "Communication network requirements for major smart grid applications in HAN, NAN and WAN". In: *Computer Networks* 67 (2014), pp. 74–88. ISSN: 1389-1286. DOI: https://doi.org/10.1016/j.comnet.2014.03.029.

[69] Libelium. *Smart Parking Technical Guide*. URL: http://www.libelium.com/development/smart-parking/documentation/plug-sense-smart-parking-technical-guide/ (visited on 09/15/2019).

[70] Imad Jawhar, Nader Mohamed, and Jameela Al-Jaroodi. "Networking architectures and protocols for smart city systems". In: *Journal of Internet Services and Applications* 9.1 (Dec 2018), p. 26. ISSN: 1869-0238. DOI: 10.1186/s13174-018-0097-0. URL: https://doi.org/10.1186/s13174-018-0097-0.

[71] Sowmya Ravidas, Alexios Lekidis, Federica Paci, and Nicola Zannone. "Access control in Internet-of-Things: A survey". In: *Journal of Network and Computer Applications* 144 (2019), pp. 79–101. ISSN: 1084-8045. DOI: https://doi.org/10.1016/j.jnca.2019.06.017. URL: https://www.sciencedirect.com/science/article/pii/S108480451930222X.

[72] Nausheen Shoaib and Jawwad A. Shamsi. "Understanding Network Requirements for Smart City Applications: Challenges and Solutions". In: *IT Professional* 21.3 (2019), pp. 33–40. DOI: 10.1109/MITP.2018.2883047.

[73] Daniel Minoli, Benedict Occhiogrosso, and Xi Chen. "Practical Aspects for the Integration of 5G Networks and IoT Applications in Smart Cities Environments". In: *Wirel. Commun. Mob. Comput.* 2019 (Jan 2019). ISSN: 1530-8669. DOI: 10.1155/2019/5710834. URL: https://doi.org/10.1155/2019/5710834.

[74] Andres Laya, Charalampos Kalalas, Francisco Vazquez-Gallego, Luis Alonso, and Jesus Alonso-Zarate. "Goodbye, ALOHA!" In: *IEEE Access* (2016).

[75] Sokratis Kartakis, Babu D. Choudhary, Alexander D. Gluhak, Lambros Lambrinos, and Julie A. McCann. "Demystifying Low-Power Wide-Area Communications for City IoT Applications". In: WiNTECH '16. New York City, New York: Association for Computing Machinery, 2016, pp. 2–8. ISBN: 9781450342520. DOI: 10.1145/2980159.2980162. URL: https://doi.org/10.1145/2980159.2980162.

[76] Guus Leenders, Gilles Callebaut, Geoffrey Ottoy, Liesbet Van der Perre, and Lieven De Strycker. "Multi-RAT for IoT: The Potential in Combining LoRaWAN and NB-IoT". In: *IEEE Communications Magazine* 59.12 (2021), pp. 98–104. DOI: 10.1109/MCOM.008.2100382.

[77] L. Vangelista. "Frequency Shift Chirp Modulation: the LoRa Modulation". In: *IEEE Signal Processing Letters* 24.12 (2017), pp. 1818–1821.

[78] B. Reynders and S. Pollin. "Chirp spread spectrum as a modulation technique for long range communication". In: *2016 Symposium on Communications and Vehicular Technologies (SCVT)*. 2016, pp. 1–5.

[79] M. Chiani and A. Elzanaty. "On the LoRa Modulation for IoT: Waveform Properties and Spectral Analysis". In: *IEEE Internet of Things Journal* 6.5 (2019), pp. 8463–8470. DOI: 10.1109/JIOT.2019.2919151.

[80] Guillaume Ferré and Audrey Giremus. "LoRa Physical Layer Principle and Performance Analysis". In: *2018 25th IEEE International Conference on Electronics, Circuits and Systems (ICECS)*. 2018, pp. 65–68. DOI: 10.1109/ICECS.2018.8617880.

[81] Tallal Elshabrawy and Joerg Robert. "Closed-Form Approximation of LoRa Modulation BER Performance". In: *IEEE Communications Letters* 22.9 (2018), pp. 1778–1781. DOI: 10.1109/LCOMM.2018.2849718.

[82] Giuseppe Baruffa, Luca Rugini, Vanni Mecarelli, Lorenzo Germani, and Fabrizio Frescura. "Coded LoRa Performance in Wireless Channels". In: *2019 IEEE 30th Annual International Symposium on Personal, Indoor and Mobile Radio Communications (PIMRC)*. 2019, pp. 1–6. DOI: 10.1109/PIMRC.2019.8904298.

[83] Giuseppe Baruffa, Luca Rugini, Lorenzo Germani, and Fabrizio Frescura. "Error probability performance of chirp modulation in uncoded and coded LoRa systems". In: *Digital Signal Processing* 106 (2020), p. 102828. ISSN: 1051-2004. DOI: https://doi.org/10.1016/j.dsp.2020.102828.

[84] Tallal Elshabrawy and Joerg Robert. "Analysis of BER and Coverage Performance of LoRa Modulation under Same Spreading Factor Interference". In: *2018 IEEE 29th Annual International Symposium on Personal, Indoor and Mobile Radio Communications (PIMRC)*. 2018, pp. 1–6. DOI: 10.1109/PIMRC.2018.8581011.

[85] Orion Afisiadis, Matthieu Cotting, Andreas Burg, and Alexios Balatsoukas-Stimming. "On the Error Rate of the LoRa Modulation With Interference". In: *IEEE Transactions on Wireless Communications* 19.2 (2020), pp. 1292–1304. DOI: 10.1109/TWC.2019.2952584.

[86] Clément Demeslay, Philippe Rostaing, and Roland Gautier. "Theoretical Performance of LoRa System in Multipath and Interference Channels". In: *IEEE Internet of Things Journal* 9.9 (2022), pp. 6830–6843. DOI: 10.1109/JIOT.2021.3114439.

[87] O. Afisiadis, M. Cotting, A. Burg, and A. Balatsoukas-Stimming. "On the Error Rate of the LoRa Modulation with Interference". In: *IEEE Transactions on Wireless Communications* 19.2 (2020), pp. 1292–1304.

[88] Anders Carlsson, Ievgeniia Kuzminykh, Robin Franksson, and Alexander Liljegren. "Measuring a LoRa Network: Performance, Possibilities and Limitations". In: *Internet of Things, Smart Spaces, and Next Generation Networks and Systems*. Cham: Springer International Publishing, 2018, pp. 116–128. ISBN: 978-3-030-01168-0.

[89] Jansen C. Liando, Amalinda Gamage, Agustinus W. Tengourtius, and Mo Li. "Known and Unknown Facts of LoRa: Experiences from a Large-Scale Measurement Study". In: *ACM Trans. Sen. Netw.* 15.2 (Feb 2019). ISSN: 1550-4859. DOI: 10.1145/3293534.

[90] Lukas Gregora, Lukas Vojtech, and Marek Neruda. "Indoor signal propagation of LoRa technology". In: *2016 17th International Conference on Mechatronics - Mechatronika (ME)*. 2016, pp. 1–4.

[91] Paul Prasanna Kumar, Partha Sarathi Paul, and Manjunath Ananda. "Development of LoRa Communication System for Effective Transmission of Data from Underground Coal Mines". In: *Processes* 11.6 (2023). ISSN: 2227-9717. DOI: 10.3390/pr11061691. URL: https://www.mdpi.com/2227-9717/11/6/1691.

[92] Nikola Jovalekic, Vujo Drndarevic, Ermanno Pietrosemoli, Iain Darby, and Marco Zennaro. "Experimental Study of LoRa Transmission over Seawater". In: *Sensors* 18.9 (2018). ISSN: 1424-8220. DOI: 10.3390/s18092853.

[93] Jorge Navarro-Ortiz, Juan J. Ramos-Munoz, Juan M. Lopez-Soler, Cristina Cervello-Pastor, and Marisa Catalan. "A LoRaWAN Testbed Design for Supporting Critical Situations: Prototype and Evaluation". In: *Wireless*

Communications and Mobile Computing 2019 (Feb 2019), p. 1684906. ISSN: 1530-8669. DOI: 10.1155/2019/1684906. URL: https://doi.org/10.1155/2019/1684906.

[94] Hedi Krishna, I Ketut Agung Enriko, Tri Alhudi, Dandy Fabian, Hery Santoso, Guntur Supriadi, and Dimas Aji. "Smart Meter over LoRaWAN". In: *2022 8th International Conference on Wireless and Telematics (ICWT)*. 2022, pp. 1–4. DOI: 10.1109/ICWT55831.2022.9935466.

[95] Daeun Yim, Jiwon Chung, Yulim Cho, Hyunji Song, Daehan Jin, Sojeong Kim, Sungwook Ko, Anthony Smith, and Austin Riegsecker. "An experimental LoRa performance evaluation in tree farm". In: *IEEE Sensors Applications Symposium (SAS'2018)*. 2018, pp. 1–6. DOI: 10.1109/SAS.2018.8336764.

[96] Mohamed Saban, Mostapha Bekkour, Ibtisam Amdaouch, Jaouad El Gueri, Badiaa Ait Ahmed, Mohamed Zied Chaari, Juan Ruiz-Alzola, Alfredo Rosado-Muñoz, and Otman Aghzout. "A Smart Agricultural System Based on PLC and a Cloud Computing Web Application Using LoRa and LoRaWan". In: *Sensors* 23.5 (2023). ISSN: 1424-8220. DOI: 10.3390/s23052725. URL: https://www.mdpi.com/1424-8220/23/5/2725.

[97] S. J. Suji Prasad, M. Thangatamilan, M. Suresh, Hitesh N. Panchal, C. Christober Asir Rajan, C. Sagana, B. Gunapriya, Aditi Sharma, Tusharkumar Panchal, and Kishor kumar Sadasivuni. "An efficient LoRa-based smart agriculture management and monitoring system using wireless sensor networks". In: *International Journal of Ambient Energy* (2021).

[98] S. J. Suji Prasad, M. Thangatamilan, M. Suresh, Hitesh Panchal, Christober Asir Rajan, C. Sagana, B. Gunapriya, Aditi Sharma, Tusharkumar Panchal, and Kishor Kumar Sadasivuni. "An efficient LoRa-based smart agriculture management and monitoring system using wireless sensor networks". In: *International Journal of Ambient Energy* 43.1 (2022), pp. 5447–5450. DOI: 10.1080/01430750.2021.1953591.

[99] L. Gallego Manzano, Hamza Boukabache, Salvatore Danzeca, Natalie Heracleous, Fabrizio Murtas, Daniel Perrin, Vasja Pirc, Alejandro Ribagorda

Alfaro, Alessandro Zimmaro, and Marco Silari. "An IoT LoRaWAN Network for Environmental Radiation Monitoring". In: *IEEE Transactions on Instrumentation and Measurement* 70 (2021), pp. 1–12. DOI: 10.1109/TIM.2021.3089776.

[100] Lidia Pocero Fraile, Stelios Tsampas, Georgios Mylonas, and Dimitrios Amaxilatis. "A Comparative Study of LoRa and IEEE 802.15.4-Based IoT Deployments Inside School Buildings". In: *IEEE Access* 8 (2020), pp. 160957–160981. DOI: 10.1109/ACCESS.2020.3020685.

[101] Georgios Z. Papadopoulos, Kosmas Kritsis, Antoine Gallais, Periklis Chatzimisios, and Thomas Noel. "Performance evaluation methods in ad hoc and wireless sensor networks: a literature study". In: *IEEE Communications Magazine* 54.1 (2016), pp. 122–128. DOI: 10.1109/MCOM.2016.7378437.

[102] Romain Jacob, Carlo Alberto Boano, Usman Raza, Marco Zimmerling, and Lothar Thiele. "Towards a Methodology for Experimental Evaluation in Low-Power Wireless Networking". In: CPS-IoTBench '19. Montreal, Quebec, Canada: Association for Computing Machinery, 2019, pp. 18–23. ISBN: 9781450366939. DOI: 10.1145/3312480.3313173. URL: https://doi.org/10.1145/3312480.3313173.

[103] Carlo Alberto Boano, Simon Duquennoy, Anna Förster, Omprakash Gnawali, Romain Jacob, Hyung-Sin Kim, Olaf Landsiedel, Ramona Marfievici, Luca Mottola, Gian Pietro Picco, Xavier Vilajosana, Thomas Watteyne, and Marco Zimmerling. "IoTBench: Towards a Benchmark for Low-Power Wireless Networking". In: *2018 IEEE Workshop on Benchmarking Cyber-Physical Networks and Systems (CPSBench)*. 2018, pp. 36–41. DOI: 10.1109/CPSBench.2018.00013.

[104] Martin C. Bor, Utz Roedig, Thiemo Voigt, and Juan M. Alonso. "Do LoRa Low-Power Wide-Area Networks Scale?" In: *Proceedings of the 19th ACM International Conference on Modeling, Analysis and Simulation of Wireless and Mobile Systems*. MSWiM '16. Malta, Malta: Association for Computing

Machinery, 2016, pp. 59–67. ISBN: 9781450345026. DOI: 10.1145/2988287.2989163.

[105] Floris Van den Abeele, Jetmir Haxhibeqiri, Ingrid Moerman, and Jeroen. Hoebeke. "Scalability Analysis of Large-Scale LoRaWAN Networks in NS-3". In: *IEEE Internet of Things Journal* 4.6 (2017), pp. 2186–2198. DOI: 10.1109/JIOT.2017.2768498.

[106] Martina Capuzzo, Davide Magrin, and Andrea Zanella. "Confirmed traffic in LoRaWAN: Pitfalls and countermeasures". In: *2018 17th Annual Mediterranean Ad Hoc Networking Workshop (Med-Hoc-Net)*. 2018, pp. 1–7. DOI: 10.23919/MedHocNet.2018.8407095.

[107] Ibrahima Faye, Pape Abdoulaye Fam, and Mamadou Lamine Ndiaye. "Energy consumption of IoT devices: An accurate evaluation to better predict battery lifetime". In: *Radio Science* 57.12 (2022), pp. 1–10. DOI: 10.1029/2021RS007423.

[108] Brecht Reynders, Qing Wang, and Sofie Pollin. "A LoRaWAN Module for Ns-3: Implementation and Evaluation". In: *Proceedings of the 2018 Workshop on Ns-3*. WNS3 '18. Surathkal, India: Association for Computing Machinery, 2018, pp. 61–68. ISBN: 9781450364133. DOI: 10.1145/3199902.3199913. URL: https://doi.org/10.1145/3199902.3199913.

[109] Floris Van den Abeele, Jetmir Haxhibeqiri, Ingrid Moerman, and Jeroen Hoebeke. "Scalability Analysis of Large-Scale LoRaWAN Networks in ns-3". In: *IEEE Internet of Things Journal* 4.6 (2017), pp. 2186–2198. DOI: 10.1109/JIOT.2017.2768498.

[110] Khaled Q. Abdelfadeel, Victor Cionca, and Dirk Pesch. "Fair Adaptive Data Rate Allocation and Power Control in LoRaWAN". In: *2018 IEEE 19th International Symposium on "A World of Wireless, Mobile and Multimedia Networks" (WoWMoM)*. 2018, pp. 14–15. DOI: 10.1109/WoWMoM.2018.8449737.

[111] S. Li, U. Raza, and A. Khan. "How Agile is the Adaptive Data Rate Mechanism of LoRaWAN?" In: *2018 IEEE Global Communications Conference (GLOBECOM)*. Dec 2018, pp. 206–212. DOI: 10.1109/GLOCOM.2018.8647469.

[112] Joseph Finnegan, Ronan Farrell, and Stephen Brown. "Analysis and Enhancement of the LoRaWAN Adaptive Data Rate Scheme". In: *IEEE Internet of Things Journal* 7.8 (2020), pp. 7171–7180. DOI: 10.1109/JIOT.2020.2982745.

[113] Mariusz Slabicki, Gopika Premsankar, and Mario Di Francesco. "Adaptive configuration of lora networks for dense IoT deployments". In: *NOMS 2018 - 2018 IEEE/IFIP Network Operations and Management Symposium*. 2018, pp. 1–9. DOI: 10.1109/NOMS.2018.8406255.

[114] Francesca Cuomo, Manuel Campo, Alberto Caponi, Giuseppe Bianchi, Giampaolo Rossini, and Patrizio Pisani. "EXPLoRa: Extending the performance of LoRa by suitable spreading factor allocations". In: *2017 IEEE 13th International Conference on Wireless and Mobile Computing, Networking and Communications (WiMob)*. 2017, pp. 1–8. DOI: 10.1109/WiMOB.2017.8115779.

[115] Inaam Ilahi, Muhammad Usama, Muhammad Omer Farooq, Muhammad Umar Janjua, and Junaid Qadir. "LoRaDRL: Deep Reinforcement Learning Based Adaptive PHY Layer Transmission Parameters Selection for LoRaWAN". In: *2020 IEEE 45th Conference on Local Computer Networks (LCN)*. 2020, pp. 457–460. DOI: 10.1109/LCN48667.2020.9314772.

[116] Thanh-Hai To and Andrzej Duda. "Simulation of LoRa in NS-3: Improving LoRa Performance with CSMA". In: *2018 IEEE International Conference on Communications (ICC)*. 2018, pp. 1–7. DOI: 10.1109/ICC.2018.8422800.

[117] Gyeongheon Lee and Joosang Youn. "Group-based Transmission Scheduling Scheme for Building LoRa-based Massive IoT". In: *2020 International Conference on Artificial Intelligence in Information and Communication (ICAIIC)*. 2020, pp. 583–586. DOI: 10.1109/ICAIIC48513.2020.9065273.

[118] Sadiq Idris, Thenuka Karunathilake, and Anna Förster. "Survey and Comparative Study of LoRa-Enabled Simulators for Internet of Things and Wireless Sensor Networks". In: *Sensors* 22.15 (2022). ISSN: 1424-8220. DOI: 10.3390/s22155546.

[119] Sérgio Francisco, Pedro Pinho, and Miguel Luís. "Improving LoRa Network Simulator for a More Realistic Approach on LoRaWAN". In: *2021 Telecoms Conference (ConfTELE)*. 2021, pp. 1–6. DOI: 10.1109/ConfTELE50222.2021.9435570.

[120] Sahel Alouneh, Ala' Khalifeh, Dhiah El Diehn I. Abou-Tair, Khaled Aldahdouh, and Feras Al-Hawari. "An Open Source LoRaWAN Simulator Framework for the Internet of Things Applications". In: *2021 8th International Conference on Internet of Things: Systems, Management and Security (IOTSMS)*. 2021, pp. 1–5. DOI: 10.1109/IOTSMS53705.2021.9704982.

[121] Aikaterini I. Griva, Achilles D. Boursianis, Shaohua Wan, Panagiotis Sarigiannidis, Konstantinos E. Psannis, George Karagiannidis, and Sotirios K. Goudos. "LoRa-Based IoT Network Assessment in Rural and Urban Scenarios". In: *Sensors* 23.3 (2023). ISSN: 1424-8220. DOI: 10.3390/s23031695. URL: https://www.mdpi.com/1424-8220/23/3/1695.

[122] Antoine Waret, Megumi Kaneko, Alexandre Guitton, and Nancy El Rachkidy. "LoRa Throughput Analysis With Imperfect Spreading Factor Orthogonality". In: *IEEE Wireless Communications Letters* 8.2 (2019), pp. 408–411. DOI: 10.1109/LWC.2018.2873705.

[123] Rene Brandborg Sorensen, Nasrin Razmi, Jimmy Jessen Nielsen, and Petar Popovski. "Analysis of LoRaWAN Uplink with Multiple Demodulating Paths and Capture Effect". In: *ICC 2019 - 2019 IEEE International Conference on Communications (ICC)*. 2019, pp. 1–6. DOI: 10.1109/ICC.2019.8761142.

[124] Daniele Croce, Michele Gucciardo, Stefano Mangione, Giuseppe Santaromita, and Ilenia Tinnirello. "LoRa Technology Demystified: From Link Behavior to Cell-Level Performance". In: *IEEE Transactions on Wireless Communications* 19.2 (2020), pp. 822–834. DOI: 10.1109/TWC.2019.2948872.

[125] Dmitry Bankov, Evgeny Khorov, and Andrey Lyakhov. "Mathematical model of LoRaWAN channel access". In: *2017 IEEE 18th International Symposium on A World of Wireless, Mobile and Multimedia Networks (WoWMoM)*. 2017, pp. 1–3. DOI: 10.1109/WoWMoM.2017.7974300.

[126] Dmitry Bankov, Evgeny Khorov, and Andrey Lyakhov. "Mathematical model of LoRaWAN channel access with capture effect". In: *2017 IEEE 28th Annual International Symposium on Personal, Indoor, and Mobile Radio Communications (PIMRC)*. 2017, pp. 1–5. DOI: 10.1109/PIMRC.2017.8292748.

[127] Tallal Elshabrawy and Joerg Robert. "Capacity Planning of LoRa Networks With Joint Noise-Limited and Interference-Limited Coverage Considerations". In: *IEEE Sensors Journal* 19.11 (2019), pp. 4340–4348. DOI: 10.1109/JSEN.2019.2897156.

[128] Orestis Georgiou and Usman Raza. "Low Power Wide Area Network Analysis: Can LoRa Scale?" In: *IEEE Wireless Communications Letters* 6.2 (2017), pp. 162–165. DOI: 10.1109/LWC.2016.2647247.

[129] Bartłtomiej Błaszczyszyn and Paul Mühlethaler. "Analyzing LoRa Long-Range, Low-Power, Wide-Area Networks Using Stochastic Geometry". In: *Proceedings of the 12th EAI International Conference on Performance Evaluation Methodologies and Tools*. Palma, Spain: Association for Computing Machinery, 2019, pp. 119–126. ISBN: 9781450365963. DOI: 10.1145/3306309.3306327.

[130] Zhijin Qin, Yuanwei Liu, Geoffrey Ye Li, and Julie A. McCann. "Modelling and analysis of Low-Power Wide-Area Networks". In: *IEEE International Conference on Communications (ICC'2017)*. May 2017, pp. 1–7. DOI: 10.1109/ICC.2017.7996589.

[131] Romain Chevillon, Guillaume Andrieux, Laurent Clavier, and Jean-François Diouris. "Stochastic Geometry-Based Analysis of the Impact of Underlying Uncorrelated IoT Networks on LoRa Coverage". In: *IEEE Access* 10 (2022), pp. 8790–8803. DOI: 10.1109/ACCESS.2022.3141540.

[132] Arliones Hoeller, Richard Demo Souza, Samuel Montejo-Sánchez, and Hirley Alves. "Performance Analysis of Single-Cell Adaptive Data Rate-Enabled LoRaWAN". In: *IEEE Wireless Communications Letters* 9.6 (Jun 2020), pp. 911–914. ISSN: 2162-2345. DOI: 10.1109/LWC.2020.2975604.

[133] Lam-Thanh Tu, Abbas Bradai, Yannis Pousset, and Alexis I. Aravanis. "Energy Efficiency Analysis of LoRa Networks". In: *IEEE Wireless Communications Letters* 10.9 (2021), pp. 1881–1885. DOI: 10.1109/LWC.2021.3084996.

[134] Orestis Georgiou, Constantinos Psomas, and Ioannis Krikidis. "Coverage Scalability Analysis of Multi-Cell LoRa Networks". In: *ICC 2020 - 2020 IEEE International Conference on Communications (ICC)*. 2020, pp. 1–7. DOI: 10.1109/ICC40277.2020.9149081.

[135] Orestis Georgiou, Constantinos Psomas, Christodoulos Skouroumounis, and Ioannis Krikidis. "Optimal Non-Uniform Deployments of LoRa Networks". In: *IEEE Wireless Communications Letters* 9.11 (2020), pp. 1919–1923. DOI: 10.1109/LWC.2020.3008103.

[136] Aamir Mahmood, Emiliano Sisinni, Lakshmikanth Guntupalli, Raúl Rondón, Syed Ali Hassan, and Mikael Gidlund. "Scalability Analysis of a LoRa Network Under Imperfect Orthogonality". In: *IEEE Transactions on Industrial Informatics* 15.3 (2019), pp. 1425–1436. DOI: 10.1109/TII.2018.2864681.

[137] J. Lim and Y. Han. "Spreading Factor Allocation for Massive Connectivity in LoRa Systems". In: *IEEE Communications Letters* 22.4 (2018), pp. 800–803. DOI: 10.1109/LCOMM.2018.2797274.

[138] L. Beltramelli, A. Mahmood, M. Gidlund, P. Österberg, and U. Jennehag. "Interference Modelling in a Multi-Cell LoRa System". In: *14th International Conference on Wireless and Mobile Computing, Networking and Communications (WiMob'2018)*. Oct 2018, pp. 1–8. DOI: 10.1109/WiMOB.2018.8589100.

[139] Orestis Georgiou, Constantinos Psomas, Eleni Demarchou, and Ioannis Krikidis. "LoRa Network Performance Under Ambient Energy Harvesting and Random Transmission Schemes". In: *ICC 2021 - IEEE International Conference on Communications*. 2021, pp. 1–6. DOI: 10.1109/ICC42927.2021.9500756.

[140] Luca Beltramelli, Aamir Mahmood, Patrik Österberg, and Mikael Gidlund. "LoRa Beyond ALOHA: An Investigation of Alternative Random Access

Protocols". In: *IEEE Transactions on Industrial Informatics* 17.5 (2021), pp. 3544–3554. DOI: 10.1109/TII.2020.2977046.

[141] Jeffrey G. Andrews, Abhishek K. Gupta, and Harpreet S. Dhillon. "A Primer on Cellular Network Analysis Using Stochastic Geometry". In: *ArXiv* abs/1604.03183 (2016).

[142] Barłomiej Błaszczyszyn and Paul Mühlethaler. "Interference and SINR Coverage in spatial non-slotted Aloha networks". In: *Anals of Telecommunications* 70.7 (Aug 2015), pp. 345–358. ISSN: 1958-9395. DOI: 10.1007/s12243-014-0455-2.

[143] D. Croce, M. Gucciardo, S. Mangione, G. Santaromita, and I. Tinnirello. "Impact of LoRa Imperfect Orthogonality: Analysis of Link-Level Performance". In: *IEEE Communications Letters* 22.4 (Apr 2018), pp. 796–799. DOI: 10.1109/LCOMM.2018.2797057.

[144] Fatma Benkhelifa, Zhijin Qin, and Julie A. McCann. "User Fairness in Energy Harvesting-Based LoRa Networks with Imperfect SF Orthogonality". In: *IEEE Transactions on Communications* (2021), pp. 1–1. DOI: 10.1109/TCOMM.2021.3068304.

[145] Fatma Benkhelifa and Julie McCann. "Resource Allocation for NOMA-based LPWA Networks Powered by Energy Harvesting". In: *2021 IEEE Wireless Communications and Networking Conference (WCNC)*. 2021, pp. 1–6. DOI: 10.1109/WCNC49053.2021.9417507.

[146] Khaled Q. Abdelfadeel, Victor Cionca, and Dirk Pesch. "Fair Adaptive Data Rate Allocation and Power Control in LoRaWAN". In: *2018 IEEE 19th International Symposium on "A World of Wireless, Mobile and Multimedia Networks" (WoWMoM)*. 2018, pp. 14–15. DOI: 10.1109/WoWMoM.2018.8449737.

[147] René Brandborg Sørensen, Dong Min Kim, Jimmy Jessen Nielsen, and Petar Popovski. "Analysis of Latency and MAC-Layer Performance for Class A LoRaWAN". In: *IEEE Wireless Communications Letters* 6.5 (2017), pp. 566–569. DOI: 10.1109/LWC.2017.2716932.

[148] Imane Cheikh, Essaid Sabir, Rachid Aouami, Mohamed Sadik, and Sébastien Roy. "Throughput-Delay Tradeoffs for Slotted-Aloha-based LoRaWAN Networks". In: *2021 International Wireless Communications and Mobile Computing (IWCMC)*. 2021, pp. 2020–2025. DOI: 10.1109/IWCMC51323.2021.9498969.

[149] Furqan Hameed Khan, Raja Jurdak, and Marius Portmann. "A Model for Reliable Uplink Transmissions in LoRaWAN". In: *2019 15th International Conference on Distributed Computing in Sensor Systems (DCOSS)*. 2019, pp. 147–156. DOI: 10.1109/DCOSS.2019.00042.

[150] Ruben M Sandoval, Antonio-Javier Garcia-Sanchez, and Joan Garcia-Haro. "Performance optimization of LoRa nodes for the future smart city/industry". eng. In: *EURASIP journal on wireless communications and networking* 1 (2019), pp. 1–13. ISSN: 1687-1499. DOI: https://doi.org/10.1186/s13638-019-1522-1.

[151] Francois Delobel, Nancy El Rachkidy, and Alexandre Guitton. "Analysis of the Delay of Confirmed Downlink Frames in Class B of LoRaWAN". In: *2017 IEEE 85th Vehicular Technology Conference (VTC Spring)*. 2017, pp. 1–6. DOI: 10.1109/VTCSpring.2017.8108412.

[152] Martin C. Bor, Utz Roedig, Thiemo Voigt, and Juan M. Alonso. "Do LoRa Low-Power Wide-Area Networks Scale?" In: *Proceedings of the 19th ACM International Conference on Modeling, Analysis and Simulation of Wireless and Mobile Systems (MSWiM '2016)*. Nov 2016, pp. 59–67.

[153] Thiemo Voigt, Martin Bor, Utz Roedig, and Juan Alonso. "Mitigating Inter-Network Interference in LoRa Networks". In: *Proceedings of the 2017 International Conference on Embedded Wireless Systems and Networks*. EWSN '17. Uppsala, Sweden: Junction Publishing, 2017, pp. 323–328. ISBN: 9780994988614.

[154] J. Tapparel, O. Afisiadis, P. Mayoraz, A. Balatsoukas-Stimming, and A. Burg. "An Open-Source LoRa Physical Layer Prototype on GNU Radio". In: *2020 IEEE 21st International Workshop on Signal Processing Advances in Wireless Communications (SPAWC)*. 2020, pp. 1–5.

[155] Jung Suk Joo. "A study on the interleaving scheme of LoRa PHY layer". In: *International Research Journal of Computer Science*. 2020.

[156] Zhenqiang Xu, Shuai Tong, Pengjin Xie, and Jiliang Wang. "From Demodulation to Decoding: Toward Complete LoRa PHY Understanding and Implementation". In: *ACM Trans. Sen. Netw.* 18.4 (Jan 2023). ISSN: 1550-4859. DOI: 10.1145/3546869.

[157] URL: https://www.semtech.com/products/wireless-rf/lora-24ghz.

[158] NUS urban analytic lab. *HDB Map*. URL: https://ual.sg/post/2019/08/25/release-of-3d-building-open-data-of-hdbs-in-singapore/.

[159] Lam-Thanh Tu, Abbas Bradai, Yannis Pousset, and Alexis I. Aravanis. "On the Spectral Efficiency of LoRa Networks: Performance Analysis, Trends and Optimal Points of Operation". In: *IEEE Transactions on Communications* 70.4 (2022), pp. 2788–2804. DOI: 10.1109/TCOMM.2022.3148784.

[160] Alan Jeffrey, Daniel Zwillinger, I.S. Gradshteyn, and I.M. Ryzhik, eds. *Table of Integrals, Series, and Products (Seventh Edition)*. 7th Edition. Boston: Academic Press, 2007, pp. 1063–1068. ISBN: 978-0-12-373637-6. DOI: https://doi.org/10.1016/B978-0-08-047111-2.50019-4.

[161] Muhammad Omer Farooq and Dirk Pesch. "Analyzing LoRa: A Use Case Perspective". In: *2018 IEEE 4th World Forum on Internet of Things (WF-IoT)*. 2018, pp. 355–360. DOI: 10.1109/WF-IoT.2018.8355224.

[162] Jinchuan Tang, Gaojie Chen, Justin P. Coon, and David E. Simmons. "Distance distributions for Matérn cluster processes with application to network performance analysis". In: *2017 IEEE International Conference on Communications (ICC)*. 2017, pp. 1–6. DOI: 10.1109/ICC.2017.7997055.

[163] Fatma Benkhelifa, Zhijin Qin, and Julie McCann. "Minimum Throughput Maximization in LoRa Networks Powered by Ambient Energy Harvesting". In: *ICC 2019 - 2019 IEEE International Conference on Communications (ICC)*. 2019, pp. 1–7. DOI: 10.1109/ICC.2019.8761478.

[164] Yasin Kabalci. "A survey on smart metering and smart grid communication". In: *Renewable and Sustainable Energy Reviews* 57 (2016), pp. 302–318. ISSN: 1364-0321. DOI: https://doi.org/10.1016/j.rser.2015.12.114.

[165] Rong Du, Paolo Santi, Ming Xiao, Athanasios V. Vasilakos, and Carlo Fischione. "The Sensable City: A Survey on the Deployment and Management for Smart City Monitoring". In: *IEEE Communications Surveys & Tutorials* 21.2 (2019), pp. 1533–1560. DOI: 10.1109/COMST.2018.2881008.

[166] G. Latouche and V. Ramaswami. *Introduction to Matrix Analytic Methods in Stochastic Modeling*. Society for Industrial and Applied Mathematics, 1999. DOI: 10.1137/1.9780898719734.

[167] Ioannis Krikidis, Themistoklis Charalambous, and John S. Thompson. "Buffer-Aided Relay Selection for Cooperative Diversity Systems without Delay Constraints". In: *IEEE Transactions on Wireless Communications* 11.5 (2012), pp. 1957–1967. DOI: 10.1109/TWC.2012.032712.111970.

[168] Hesham Elsawy. "Rate Adaptation and Latency in Heterogeneous IoT Networks". In: *IEEE Communications Letters* 25.2 (2021), pp. 660–664. DOI: 10.1109/LCOMM.2020.3031630.

[169] Wha Sook Jeon and Dong Geun Jeong. "Adaptive Uplink Rate Control for Confirmed Class A Transmission in LoRa Networks". In: *IEEE Internet of Things Journal* 7.10 (2020), pp. 10361–10374. DOI: 10.1109/JIOT.2020.2986494.

[170] Martina Capuzzo, Davide Magrin, and Andrea Zanella. "Mathematical Modeling of LoRaWAN Performance with Bi-directional Traffic". In: *2018 IEEE Global Communications Conference (GLOBECOM)*. 2018, pp. 206–212. DOI: 10.1109/GLOCOM.2018.8647351.

[171] M. Costa, T. Farrell, and L. Doyle. "On energy efficiency and lifetime in low power wide area network for the Internet of Things". In: *IEEE Conference on Standards for Communications and Networking (CSCN'2017)*. Sep 2017, pp. 258–263. DOI: 10.1109/CSCN.2017.8088631.

[172] Binbin Su, Zhijin Qin, and Qiang Ni. "Energy Efficient Uplink Transmissions in LoRa Networks". In: *IEEE Transactions on Communications* 68.8 (2020), pp. 4960–4972. DOI: 10.1109/TCOMM.2020.2993085.

[173] Bruno Clerckx, Rui Zhang, Robert Schober, Derrick Wing Kwan Ng, Dong In Kim, and H. Vincent Poor. "Fundamentals of Wireless Information and Power Transfer: From RF Energy Harvester Models to Signal and System Designs". In: *IEEE Journal on Selected Areas in Communications* 37.1 (Jan 2019), pp. 4–33. ISSN: 1558-0008. DOI: 10.1109/JSAC.2018.2872615.

[174] F. Orfei, C. Benedetta Mezzetti, and F. Cottone. "Vibrations powered LoRa sensor: An electromechanical energy harvester working on a real bridge". In: *2016 IEEE SENSORS*. Oct 2016, pp. 1–3. DOI: 10.1109/ICSENS.2016.7808752.

[175] Wai-Kong Lee, Martin J. W. Schubert, Boon-Yaik Ooi, and Stanley Jian-Qin Ho. "Multi-Source Energy Harvesting and Storage for Floating Wireless Sensor Network Nodes With Long Range Communication Capability". In: *IEEE Transactions on Industry Applications* 54.3 (May 2018), pp. 2606–2615. ISSN: 0093-9994. DOI: 10.1109/TIA.2018.2799158.

[176] Michele Magno, Fayçal Ait Aoudia, Matthieu Gautier, Olivier Berder, and Luca Benini. "WULoRa: An energy efficient IoT end-node for energy harvesting and heterogeneous communication". In: *Design, Automation Test in Europe Conference Exhibition (DATE'2017)*. Mar 2017, pp. 1528–1533. DOI: 10.23919/DATE.2017.7927233.

[177] Mustafa Emara, Hesham ElSawy, and Gerhard Bauch. "A Spatiotemporal Framework for Information Freshness in IoT Uplink Networks". In: *2020 IEEE 92nd Vehicular Technology Conference (VTC2020-Fall)*. 2020, pp. 1–6. DOI: 10.1109/VTC2020-Fall49728.2020.9348865.

[178] Martin Haenggi. "Meta Distributions—Part 1: Definition and Examples". In: *IEEE Communications Letters* 25.7 (2021), pp. 2089–2093. DOI: 10.1109/LCOMM.2021.3069662.

[179] Martin Haenggi. "Meta Distributions—Part 2: Properties and Interpretations". In: *IEEE Communications Letters* 25.7 (2021), pp. 2094–2098. DOI: 10.1109/LCOMM.2021.3069681.

[180] Praful D. Mankar and Harpreet S. Dhillon. "Meta Distribution for Downlink NOMA in Cellular Networks with 3GPP-Inspired User Ranking". In: *2019 IEEE Global Communications Conference (GLOBECOM)*. 2019, pp. 1–6. DOI: 10.1109/GLOBECOM38437.2019.9013825.

[181] Martin Haenggi. "The Meta Distribution of the SIR in Poisson Bipolar and Cellular Networks". In: *IEEE Transactions on Wireless Communications* 15.4 (2016), pp. 2577–2589. DOI: 10.1109/TWC.2015.2504983.

[182] Yuanjie Wang, Martin Haenggi, and Zhenhui Tan. "The Meta Distribution of the SIR for Cellular Networks With Power Control". In: *IEEE Transactions on Communications* 66 (2017), pp. 1745–1757.

[183] Alexandre Mouradian. "Modeling dense urban wireless networks with 3D stochastic geometry". In: *Performance Evaluation* 121-122 (2018), pp. 1–17. ISSN: 0166-5316. DOI: 10.1109/IWCMC.2016.7577036.

[184] Kenneth I. Gross and Donald St. P. Richards. *Algebraic Methods Toward Higher-Order Probability Inequalities*. Ed. by Ioannis Karatzas, Balram S. Rajput, and Murad S. Taqqu. Boston, MA: Birkhäuser Boston, 1998, pp. 185–206. ISBN: 978-1-4612-2030-5. DOI: 10.1007/978-1-4612-2030-5_10.

APPENDIX A

Appendices for Chapter 4

A.1 Proof of Theorem. 4.1 By Dr. Fatma Benkhelifa (co-author in [P1])

The cross-correlation expression obtained in Theorem. 4.1 follows from the expression of the integral below:

$$
\begin{aligned}
I_{k_1,k_2}(\tau,t_1,t_2) &= \int_{t_1}^{t_2} e^{2j\pi\left(f_1+\mu_1\left(\frac{t}{2T_1}+k_1\right)\right)t} e^{-2j\pi\left(f_2+\mu_2\left(\frac{t-\tau}{2T_2}+k_2\right)\right)(t-\tau)} dt \\
&= e^{2j\pi\left(f_2+\mu_2 k_2-\frac{\mu_2\tau}{2T_2}\right)\tau} \int_{t_1}^{t_2} e^{2j\pi\left(\mu_1 k_1-\mu_2 k_2+f_1-f_2+\frac{\mu_2\tau}{T_2}\right)t} e^{j\pi\left(\frac{\mu_1}{T_1}-\frac{\mu_2}{T_2}\right)t^2} dt \qquad \text{(A.1)} \\
&= e^{2j\pi c_{k_2}} \int_{t_1}^{t_2} e^{j\pi\left(2b_{k_1,k_2}t+a_{12}t^2\right)} dt \qquad \text{(A.2)} \\
&= \begin{cases} e^{j\pi\left(2c_{k_2}-\frac{b_{k_1,k_2}^2}{a_{12}}\right)} \int_{t_1}^{t_2} e^{j\pi a_{12}\left(t+\frac{b_{k_1,k_2}}{a_{12}}\right)^2} dt, & \text{if } a_{12}\neq 0, \\ e^{2j\pi c_{k_2}} \int_{t_1}^{t_2} e^{2j\pi b_{k_1,k_2}t} dt, & \text{if } a_{12}=0, \end{cases} \qquad \text{(A.3)} \\
&= \begin{cases} \sqrt{\frac{j}{\pi a_{12}}} e^{j\pi\left(2c_{k_2}-\frac{b_{k_1,k_2}^2}{a_{12}}\right)} \int_{\sqrt{\frac{\pi a_{12}}{j}}\left(t_1+\frac{b_{k_1,k_2}}{a_{12}}\right)}^{\sqrt{\frac{\pi a_{12}}{j}}\left(t_2+\frac{b_{k_1,k_2}}{a_{12}}\right)} e^{-x^2} dx, & \\ & \text{if } a_{12}\neq 0, \\ e^{2j\pi c_{k_2}} e^{j\pi b_{k_1,k_2}(t_1+t_2)} & \\ \times sinc\left(\pi b_{k_1,k_2}\left(t_2-t_1\right)\right)\left(t_2-t_1\right), & \text{if } a_{12}=0, \end{cases} \qquad \text{(A.4)}
\end{aligned}
$$

$$= \begin{cases} \frac{\sqrt{j}}{2\sqrt{a_{12}}} e^{j\pi\left(2c_{k_2} - \frac{b_{k_1,k_2}^2}{a_{12}}\right)} \Bigg[\operatorname{erf}\left(\sqrt{\frac{\pi a_{12}}{j}}\left(t_2 + \frac{b_{k_1,k_2}}{a_{12}}\right)\right) \\ - \operatorname{erf}\left(\sqrt{\frac{\pi a_{12}}{j}}\left(t_1 + \frac{b_{k_1,k_2}}{a_{12}}\right)\right)\Bigg], & \text{if } a_{12} \neq 0, \\ e^{2j\pi c_{k_2}} e^{j\pi b_{k_1,k_2}(t_1+t_2)} \\ \times sinc\left(\pi b_{k_1,k_2}\left(t_2 - t_1\right)\right)\left(t_2 - t_1\right), & \text{if } a_{12} = 0, \end{cases} \tag{A.5}$$

with $a_{12} = \frac{\mu_1}{T_1} - \frac{\mu_2}{T_2}$, $b_{k_1,k_2} = \mu_1 k_1 - \mu_2 k_2 + f_1 - f_2 + \frac{\mu_2 \tau}{T_2}$, $c_{k_2} = \left(f_2 + \mu_2 k_2 - \frac{\mu_2 \tau}{2T_2}\right)\tau$.

A.2 Proof of Theorem. 4.2

Let T_d be the sampling time and let $B_1 = 2^{s_1}/T_d$, $B_2 = 2^{s_2}/T_d$, and $\mathrm{SF}_2 = SF_1 + s_3$. Let $m_0 = \frac{t_0}{T_d}$, and $m_1 = \frac{\tau}{T_d}$. The cross-correlations between two discrete transmitted waveforms is given by:

$$\mathcal{R}^{\mathcal{D}}_{k_1,k_2}(\tau, f_d) = \sum_{n=\frac{t_0}{T_d}+\frac{\tau}{T_d}}^{\frac{t_0}{T_d}+\frac{T_{s,1}}{T_d}-1} s^{\mathcal{D}}_{k_1}(nT_d)\left(s^{\mathcal{D}}_{k_2}(nT_d - \tau)\right)^* \tag{A.6}$$

$$= \frac{e^{2j\pi c_{k_2}}}{\sqrt{2^{SF_1}2^{SF_2}}} \sum_{n=\frac{\tau}{T_d}}^{2^{SF_1-s_1}-1} e^{j\pi 2^{-s_1-SF_1}\left(\left(2^{s_1}-2^{-s_1+2s_2-s_3}\right)n\right)n} e^{j\pi 2^{-s_1-SF_1}\left(2\left(A-2^{s_1}1\left(nT_d \geq t_{k_1}\right)+2^{s_2}1\left(nT_d \geq t_{k_2}+\tau\right)\right)\right)n} \tag{A.7}$$

$$= \begin{cases} \frac{e^{2j\pi c_{k_2}}}{\sqrt{2^{SF_1}2^{SF_2}}} \sum_{n=\frac{\tau}{T_d}}^{\frac{T_{s,1}}{T_d}-1} e^{j\pi a_{12}(nT_d)^2} e^{2j\pi\left(b_{k_1,k_2} - B_1 1\left(nT_d \geq t_{k_1}\right)+B_2 1\left(nT_d \geq t_{k_2}+\tau\right)\right)nT_d}, & \text{if } a_{12} \neq 0, \\ \frac{e^{2j\pi c_{k_2}}}{\sqrt{2^{SF_1}2^{SF_2}}} \sum_{n=\frac{\tau}{T_d}}^{\frac{T_{s,1}}{T_d}-1} e^{2j\pi\left(b_{k_1,k_2} - B_1 1\left(nT_d \geq t_{k_1}\right)\right)nT_d} e^{2j\pi B_2 1\left(nT_d \geq t_{k_2}+\tau\right)nT_d}, & \text{if } a_{12} = 0, \end{cases} \tag{A.8}$$

$$= \begin{cases} \frac{e^{2j\pi c_{k_2}}}{\sqrt{2^{SF_1}2^{SF_2}}} \sum_{n=\frac{\tau}{T_d}}^{2^{SF_1-s_1}-1} e^{j\pi\left(a_{12}nT_d + 2b_{k_1,k_2}\right)nT_d}, & \text{if } a_{12} \neq 0, \\ \frac{e^{2j\pi c_{k_2}}}{\sqrt{2^{SF_1}2^{SF_2}}} \sum_{n=\frac{\tau}{T_d}}^{2^{SF_1-s_1}-1} e^{2j\pi b_{k_1,k_2} nT_d}, & \text{if } a_{12} = 0, \end{cases} \tag{A.9}$$

$$= \begin{cases} \frac{e^{2j\pi c_{k_2}} e^{-j\pi a_{12}\left(\frac{b_{k_1,k_2}}{a_{12}}\right)^2}}{\sqrt{2^{SF_1}2^{SF_2}}} \sum_{n'=0}^{2^{SF_1-s_1}-m_1-1} e^{j\pi a_{12}\left(n'T_d + m_1 T_d + \frac{b_{k_1,k_2}}{a_{12}}\right)^2}, & \text{if } a_{12} \neq 0, \\ \frac{e^{2j\pi c_{k_2}} e^{2j\pi b_{k_1,k_2} T_d m_1} e^{j\pi\left(2^{SF_1-s_1}-m_1-1\right)b_{k_1,k_2}T_d}}{\sqrt{2^{SF_1}2^{SF_2}}} \sin\left(\pi\left(2^{SF_1-s_1} - m_1\right)b_{k_1,k_2}T_d\right) \\ \times cosec\left(\pi b_{k_1,k_2} T_d\right), & \text{if } a_{12} = 0 \,\&\, b_{k_1,k_2} \neq 0, \\ \frac{e^{2j\pi c_{k_2}}}{\sqrt{2^{SF_1}2^{SF_2}}} \frac{T_{s,1}-\tau}{T_d}, & \text{if } a_{12} = 0 \,\&\, b_{k_1,k_2} = 0, \end{cases} \tag{A.10}$$

with $m_1 = \frac{\tau}{T_d}$, $a_{12} = \frac{\mu_1}{T_1} - \frac{\mu_2}{T_2} = \left(1 - 2^{2(-s_1+s_2)-s_3}\right)\frac{\mu_1}{T_1}$, $c_{k_2} = \left(f_2 + \mu_2 k_2 - \frac{\tau\mu_2}{2T_2}\right)\tau$,
and $b_{k_1,k_2} = \mu_1\left(k_1 - 2^{2(-s_1+s_2)-s_3}k_2 + 2^{2(-s_1+s_2)-s_3}\frac{\tau}{T_1} - \frac{f_d 2^{SF_1}}{B_1}\right)$,

A.3 Tables of LoRa Cross-Correlation Factors

In this section, we provide in Tables III-IX the numerical values of the maximum and mean cross-correlation factors that were validated analytically using our expressed cross-correlation functions and which are the object of the plotted figures Fig. 4.4 and Fig. 4.5 with $\tau = 0$, $f_d = 0$, and $B_1 = B_2$.

Table A.1: Maximum of cross-correlations functons in continuous time domain.

	5	6	7	8	9	10	11	12
5	1	0.253	0.149	0.098	0.068	0.048	0.034	0.024
6	0.253	1	0.182	0.104	0.068	0.048	0.034	0.024
7	0.149	0.182	1	0.126	0.072	0.047	0.033	0.024
8	0.098	0.104	0.126	1	0.089	0.051	0.033	0.023
9	0.068	0.068	0.072	0.089	1	0.063	0.036	0.023
10	0.048	0.048	0.047	0.051	0.063	1	0.044	0.025
11	0.034	0.034	0.033	0.033	0.036	0.044	1	0.031
12	0.024	0.024	0.024	0.023	0.023	0.025	0.031	1

Table A.2: Maximum of cross-correlation functions in discrete time domain.

	5	6	7	8	9	10	11	12
5	1	0.204	0.127	0.084	0.059	0.042	0.030	0.021
6	0.204	1	0.147	0.088	0.059	0.042	0.030	0.021
7	0.126	0.147	1	0.104	0.062	0.041	0.029	0.021
8	0.084	0.088	0.104	1	0.073	0.043	0.029	0.020
9	0.059	0.059	0.062	0.073	1	0.052	0.030	0.020
10	0.042	0.042	0.041	0.043	0.052	1	0.037	0.021
11	0.030	0.030	0.029	0.029	0.030	0.037	1	0.026
12	0.021	0.021	0.021	0.020	0.020	0.021	0.026	1

Table A.3: Mean of crosscorrelation functions in continuous time domain.

	5	6	7	8	9	10	11	12
5	0.069	0.103	0.080	0.059	0.042	0.030	0.021	0.015
6	0.103	0.037	0.071	0.057	0.042	0.030	0.022	0.015
7	0.081	0.071	0.020	0.049	0.040	0.030	0.021	0.015
8	0.059	0.057	0.049	0.010	0.034	0.028	0.021	0.015
9	0.042	0.042	0.040	0.034	0.006	0.024	0.020	0.015
10	0.030	0.030	0.030	0.028	0.024	0.003	0.016	0.014
11	0.021	0.021	0.021	0.021	0.020	0.016	0.002	0.012
12	0.015	0.015	0.015	0.015	0.015	0.014	0.012	0.001

Table A.4: Mean of crosscorrelation functions in discrete time domain.

	5	6	7	8	9	10	11	12
5	0.031	0.022	0.016	0.011	0.008	0.006	0.004	0.003
6	0.022	0.016	0.011	0.008	0.006	0.004	0.003	0.002
7	0.016	0.011	0.008	0.006	0.004	0.003	0.002	0.001
8	0.011	0.008	0.006	0.004	0.003	0.002	0.001	0.001
9	0.008	0.006	0.004	0.003	0.002	0.001	0.001	0.001
10	0.006	0.004	0.003	0.002	0.001	0.001	0.001	0.001
11	0.004	0.003	0.002	0.001	0.001	0.001	0.001	0.0003
12	0.003	0.002	0.001	0.001	0.001	0.001	0.0003	0.0002

APPENDIX B

Appendices for Chapter 5

B.1 Proof of Lemma 5.1

Assuming an interfering node located at x_{ij} that starts transmitting its packet of duration l_q at instant T_{ij} randomly in a contention window $[-T_c, T_c]$. Then, the collision time overlap between x_j and the typical user starting transmission at $T_{00} = 0$ is given by:

- If $l_q \leq l_{q_0}$,

$$h_{q_0,q}(T_{ij}) = \begin{cases} \frac{l_{q_0}-T_{ij}}{l_{q_0}}, & \text{if } l_{q_0} - l_q \leq T_{ij} \leq l_{q_0}, \\ \frac{l_q}{l_{q_0}}, & \text{if } 0 \leq T_{ij} \leq l_{q_0} - l_q, \\ \frac{l_q+T_{ij}}{l_{q_0}}, & \text{if } -l_q \leq T_{ij} \leq 0, \\ 0 & \text{if } -T_c \leq T_{ij} < -l_q \quad \text{or} \quad l_{q_0} < T_{ij} \leq T_c. \end{cases}$$

- If $l_q > l_{q_0}$,

$$h_{q_0,q}(T_{ij}) = \begin{cases} \frac{l_{q_0}-T_{ij}}{l_{q_0}}, & \text{if } 0 \leq T_{ij} \leq l_{q_0}, \\ 1, & \text{if } l_{q_0} - l_q \leq T_{ij} \leq 0, \\ \frac{l_q+T_{ij}}{l_{q_0}}, & \text{if } -l_q \leq T_{ij} \leq l_{q_0} - l_q, \\ 0 & \text{if } -T_c \leq T_{ij} < -l_q \quad \text{or} \quad l_{q_0} < T_{ij} \leq T_c. \end{cases}$$

B.2 Proof of Corollary 5.1

Assuming that the transmission start time of LoRa active nodes follows a uniform distribution $T_{ij} \overset{Dist}{=} U(-T_c, T_c)$ and using Lemma. 5.1, we evaluate $\mathbb{E}_{T_{ij}}\left[\frac{1}{1+sh_{q_0,q}(T_{ij})}\right]$ for $l_q \leq l_{q_0}$ as

$$\begin{aligned}\mathbb{E}_t\left[\frac{1}{1+uh_{q_0,q}(T_{ij})}\right] &= \frac{1}{2T_c}\Bigg[\int_{-T_c}^{-l_q} dt + \int_{-l_q}^{0} \frac{1}{1+u\frac{t+l_q}{l_{q_0}}}dt \\ &+ \int_{0}^{l_{q_0}-l_q} \frac{1}{1+u\frac{l_q}{l_{q_0}}}dt + \int_{l_{q_0}-l_q}^{l_{q_0}} \frac{1}{1+u\frac{l_{q_0}-t}{l_{q_0}}}dt + \int_{l_{q_0}}^{T_c} dt\Bigg] \\ &= 1 - \frac{l_{q_0}+l_q}{2T_c} + \frac{l_{q_0}}{T_c u}\log\left(\frac{ul_q}{l_{q_0}}+1\right) + \frac{l_{q_0}-l_q}{2T_c\left(1+u\frac{l_q}{l_{q_0}}\right)}. \end{aligned} \tag{B.1}$$

Similarly, we show for $l_q > l_{q_0}$, that

$$\mathbb{E}_t\left[\frac{1}{1+uh_{q_0,q}(T_{ij})}\right] = 1 - \frac{l_{q_0}+l_q}{2T_c} + \frac{l_{q_0}\log(u+1)}{T_c u} - \frac{l_{q_0}-l_q}{2T_c(1+u)}. \tag{B.2}$$

Grouping the two expressions above, we obtain the expression in Lemma. 5.1.

B.3 Proof of Theorem 5.1

$$\begin{aligned}\mathfrak{L}_{I_{intra}}\{s\} &= \mathbb{E}_{x,G,t}\left[\exp\left(-s\sum_{q\in Q}\sum_{x_j\in\tilde{\Phi}_{ED,0,q}\setminus x_0} P_q h_{q_0,q}(T_{ij})\alpha\|x_{0,j}\|^{-\eta}g_{0j}\right)\right] \\ &= \mathbb{E}_{x,G,t}\left[\prod_{q\in Q}\prod_{x_j\in\tilde{\Phi}_{ED,0,q}\setminus x_0}\exp\left(-sP_q h_{q_0,q}(T_{ij})\alpha\|x_{0,j}\|^{-\eta}g_{0j}\right)\right] \\ &\overset{(a)}{=} \mathbb{E}_{x,t}\left[\prod_{q\in Q}\prod_{x_j\in\tilde{\Phi}_{ED,0,q}\setminus x_0}\frac{1}{1+sP_q h_{q_0,q}(T_{ij})\alpha\|x_{0,j}\|^{-\eta}}\right] \\ &\overset{(b)}{\approx} \prod_{q\in Q}\left[\mathbb{E}_{x,t}\prod_{x_j\in\tilde{\Phi}_{ED,0,q}\setminus x_0}\frac{1}{1+sP_q h_{q_0,q}(T_{ij})\alpha\|x_{0,j}\|^{-\eta}}\right] \\ &\overset{(c)}{=} \prod_{q\in Q}\left[\exp\left(-2\pi a\lambda_{ED}\int_{d_{q-1}}^{d_q}\left(1-\mathbb{E}_t[\frac{1}{1+sP_q h_{q_0,q}(T_{ij})\alpha r^{-\eta}}]rdr\right)\right)\right],\end{aligned} \tag{B.3}$$

where (a) is explained by the independence of channel gains from both the spatial and temporal dimensions and is obtained using the moment generating function

(MGF) of the exponential distribution with mean 1, (b) is an approximation obtained using Fortuin–Kasteleyn–Ginibre (FKG) inequality [184] for $T_{ij} > 0$ and extended to $\forall\ T_{ij}$ through validation by MC simulations, and (c) is obtained by applying the PGFL of $\tilde{\Phi}_{ED,i}$ and the change of integration coordinates from Cartesian to polar. Recalling the expressions obtained in Corollary 5.1, we obtain the expression in (Eq. 5.8).

B.4 Proof of Theorem 5.2

$$\begin{aligned}
\mathfrak{L}_{I_{inter}}\{s\} &\overset{(a)}{=} \mathbb{E}_{y,x,t}\left[\prod_{q\in Q}\prod_{y_i\in\Phi_G}\prod_{x_j\in\tilde{\Phi}_{ED,i,q}}\frac{1}{1+sP_q h_{q_0,q}(T_{ij})\alpha\|y_i+x_{ij}\|^{-\eta}}\right] \\
&\overset{(b)}{\approx} \prod_{q\in Q}\mathbb{E}_{y,x,t}\left[\prod_{y_i\in\Phi_G\setminus y_0}\prod_{x_j\in\tilde{\Phi}_{ED,i,q}}\frac{1}{1+sP_q h_{q_0,q}(T_{ij})\alpha\|y_i+x_{ij}\|^{-\eta}}\right] \\
&\overset{(c)}{=} \prod_{q\in Q}\exp\left(-2\pi\lambda_G\int_0^{\infty}(1-\xi_q(s,y))ydy\right),
\end{aligned}$$

(a) and (b) follow from applying similar steps to $\mathfrak{L}_{I_{intra}}$, and (c) is obtained using the PGFL of the MCP [162] with

$$\xi_q(s,y) = \exp\left(-\lambda_{ED}a\int_{d_{q-1}}^{d_q}\int_0^{2\pi}\left(1-E_t\left(\frac{1}{1+sP_q h_{q_0,q}(T_{ij})\alpha\beta(x,y,\theta)^{-\eta}}\right)\right)xdxd\theta\right), \quad \text{(B.4)}$$

where $\beta(x,y,\theta) = \sqrt{y^2+x^2-2xycos(\theta)}$.

For a highly clustered network, $x << y$. Using the approximation in [130, Corollary 2], we have $\beta(x,y,\theta) \approx y$ and after a Taylor series expansion weobtain:

$$\begin{aligned}
\mathfrak{L}_{I_{inter}}\{s\} &= \prod_{q\in Q}\exp\left(-2\pi\lambda_G aN_q\int_0^{\infty}\int_{-\infty}^{+\infty}\left(\frac{sP_q h_{q_0,q}(t)\alpha y^{-\eta}}{1+sP_q h_{q_0,q}(t)\alpha y^{-\eta}}\right)f_{T_{ij}(t)}ydtdy\right) \\
&\overset{(d)}{=} \prod_{q\in Q}\exp\left(-2\pi\lambda_G aN_q\frac{\pi(sP_q\alpha)^{\frac{2}{\eta}}}{\eta\sin(\pi\frac{2}{\eta})}\int_{-\infty}^{+\infty}(h_{q_0,q}(t))^{\frac{2}{\eta}}f_{T_{ij}(t)}dt\right),
\end{aligned}$$

where (d) is obtained using [160, (3.241)].

Recalling Lemma. 5.1, we evaluate $\int_{-\infty}^{+\infty}(h_{q_0,q}(t))^{\frac{2}{\eta}}f_{T_{ij}(t)}dt$. For $s=\rho$, we obtain the final expression obtained in Eq. 5.15.

APPENDIX C

Appendices for Chapter 6

C.1 Proof of Theorem. 6.1

During a generic time slot, we have:

$$\begin{aligned}
\mathcal{L}_I\{s\} &= \mathbb{E}_{\phi,G}\left[\exp\left(-s\sum_{q\in Q}\sum_{x_j\in\tilde{\Phi}_{L,q}\setminus x_0}\mathcal{P}\alpha\|^{-\eta}\beta_{q_0,q}g_j\|x_j\right)\right] \\
&\overset{(a)}{=} \mathbb{E}_{\phi}\left[\prod_{q=1}^{N}\prod_{x_j\in\tilde{\Phi}_{L,q}\setminus x_0}\frac{1}{1+s\mathcal{P}\beta_{q_0,q}\alpha\|x_j\|^{-\eta}}\right] \\
&\overset{(b)}{\approx} \prod_{q=1}^{N}\left[\mathbb{E}_{x}\prod_{x_j\in\tilde{\Phi}_{L,q}\setminus x_0}\frac{1}{1+s\mathcal{P}\beta_{q_0,q}\alpha\|x_j\|^{-\eta}}\right] \\
&\overset{(c)}{=} \prod_{q=1}^{N}\exp\left(-2\pi\delta_q\lambda_L\int_{d_{q-1}}^{d_q}\left(\frac{s\mathcal{P}\beta_{q_0,q}\alpha r^{-\eta}}{1+s\mathcal{P}\beta_{q_0,q}\alpha r^{-\eta}}\right)rdr\right),
\end{aligned} \tag{C.1}$$

where (a) follows the moment generating function (MGF) of the unit-mean exponential distribution with independence of channel gains from the space and time (b) is obtained using Fortuin–Kasteleyn–Ginibre (FKG) inequality [184], (c) follows the PGFL of $\tilde{\Phi}_L$.

APPENDIX D

Attributions

- London experimental setup in Section. 2.5: Mr. Denver Boon (Imperial College London), Dr. Mike Preza (Imperial College London), Dr. Laksh Bhatia (Imperial College London).
- Singapore experimental setup in Section. 2.5: Mr. Denver Boon (Imperial College London), Mr. Teo Keng Boon (I2R, A*Star), Mr. Chia Weei Chew (APAQ Group, Singapore).
- Data for experimental PDR evaluation in Chapter. 4: Dr. Laksh Bhatia.